Lecture Notes in Electrical Engineering 669

Farhad Shahnia
Sara Deilami *Editors*

# ICPES 2019

## Selected Articles from the 9th International Conference on Power and Energy Systems, Perth, Australia

Springer

# Lecture Notes in Electrical Engineering

## Volume 669

The book series *Lecture Notes in Electrical Engineering* (LNEE) publishes the latest developments in Electrical Engineering—quickly, informally and in high quality. While original research reported in proceedings and monographs has traditionally formed the core of LNEE, we also encourage authors to submit books devoted to supporting student education and professional training in the various fields and applications areas of electrical engineering. The series cover classical and emerging topics concerning:

- Communication Engineering, Information Theory and Networks
- Electronics Engineering and Microelectronics
- Signal, Image and Speech Processing
- Wireless and Mobile Communication
- Circuits and Systems
- Energy Systems, Power Electronics and Electrical Machines
- Electro-optical Engineering
- Instrumentation Engineering
- Avionics Engineering
- Control Systems
- Internet-of-Things and Cybersecurity
- Biomedical Devices, MEMS and NEMS

For general information about this book series, comments or suggestions, please contact leontina.dicecco@springer.com.

To submit a proposal or request further information, please contact the Publishing Editor in your country:

**China**

Jasmine Dou, Associate Editor (jasmine.dou@springer.com)

**India, Japan, Rest of Asia**

Swati Meherishi, Executive Editor (Swati.Meherishi@springer.com)

**Southeast Asia, Australia, New Zealand**

Ramesh Nath Premnath, Editor (ramesh.premnath@springernature.com)

**USA, Canada:**

Michael Luby, Senior Editor (michael.luby@springer.com)

**All other Countries:**

Leontina Di Cecco, Senior Editor (leontina.dicecco@springer.com)

**** Indexing: The books of this series are submitted to ISI Proceedings, EI-Compendex, SCOPUS, MetaPress, Web of Science and Springerlink ****

More information about this series at http://www.springer.com/series/7818

Farhad Shahnia · Sara Deilami
Editors

# ICPES 2019

## Selected Articles from the 9th International Conference on Power and Energy Systems, Perth, Australia

Springer

*Editors*
Farhad Shahnia
Discipline of Engineering and Energy
Murdoch University
Perth, WA, Australia

Sara Deilami
School of Engineering
Macquarie University
Sydney, NSW, Australia

ISSN 1876-1100 ISSN 1876-1119 (electronic)
Lecture Notes in Electrical Engineering
ISBN 978-981-15-5373-8 ISBN 978-981-15-5374-5 (eBook)
https://doi.org/10.1007/978-981-15-5374-5



This Springer imprint is published by the registered company Springer Nature Singapore Pte Ltd.
The registered company address is: 152 Beach Road, #21-01/04 Gateway East, Singapore 189721, Singapore

# Contents

# About the Editors

**A/Prof. Farhad Shahnia** received his Ph.D. in Electrical Engineering from Queensland University of Technology (QUT), Brisbane, in 2012. He is currently an A/Professor at Murdoch University. Before that, he was a Lecturer at Curtin University (2012–2015), a Research Scholar at QUT (2008–2011), and an R&D Engineer at the Eastern Azarbayjan Electric Power Distribution Company, Iran (2005–2008). He is a senior member of IEEE, Chair of IEEE Western Australia Section and a member of the Engineers Australia and the Australasian Association for Engineering Education. He was the General Chair of the 9th International Conference on Power and Energy Systems at Perth, Australia on December 2019. A/Professor Shahnia's research focuses on distribution networks, and microgrid and smart grid concepts. He has authored one book, 11 book chapters and over 100 peer-reviewed articles in international conferences and journals, and has also edited six books.

**Dr. Sara Deilami** received her Master's and Ph.D. degrees in Electrical Engineering from Curtin University. She has over ten years of industry experience, and she is currently a Senior Lecturer at the School of Electrical Engineering, Macquarie University. Before joining Macquarie, she was a Lecturer at Curtin University (2014–2020), at the School of Computing and Mathematical Sciences, Curtin University. Her research interests are smart grids, renewable energy, power quality, and power system protection. She has published over 40 papers including high citation journal articles, book chapters and peer reviewed conferences. Dr. Deilami is currently a member of the IEEE PES/PELS and the IEEE Women in Engineering (WIE). She was the Vice Chair and the Chair of the IEEE WIE, WA section, in 2016 and 2017, respectively.

She was the publication chair of the 9th International Conference on Power and Energy Systems at Perth, Australia on December 2019. She was also the technical chair and women in engineering chair of CMD 2018 conference and AUPEC 2014 conference, respectively.

# Two-Layer Energy Sharing Strategy in Distribution Network with Hybrid Energy Storage System


**Xiao Han, Lingling Sun, Guozhong Liu, Li Kang, Fenglei Zheng, and Jing Qiu**

**Abstract** This paper addresses an energy sharing strategy in a two-layer microgrid with the renewable distributed generation and hybrid energy storage system considered to minimize the total energy bill purchased from the utility grid and reduce the peak time consumption from the utility grid. This approach considers the energy operation management of thermal energy loads and electrical energy loads, in which the thermal energy loads are supplied by electrical energy and gas energy. Moreover, this energy sharing model is designed to allow the operation with different types of end-user modes, and the participants are divided into different layers based on their characteristics. Furthermore, the modified trading method is based on the trading model of stock opening with the maximum transaction volume. The proposed two-layer model is tested in 18-bus IEEE system with the real historical data in the Australia energy market. With the proposed two-layer energy sharing strategy, the simulation results show that the two-layer energy sharing model provides economic profits to participants and encourages load schedule.

X. Han (✉) · J. Qiu
School of Electrical and Information Engineering, University of Sydney, Camperdown, NSW 2006, Australia
e-mail: xhan2702@uni.sydney.edu.au

J. Qiu
e-mail: qiujing0322@gmail.com

L. Sun (✉)
School of Electrical Engineering and Telecommunications, University of New South Wales, Kensington, NSW 2052, Australia
e-mail: lingling.sun@unsw.edu.au

G. Liu · L. Kang
School of Electrical Engineering and Intelligentization, Dongguan University of Technology, No. 1 Daxue Rd., 523808 Dongguan, China
e-mail: liugz@dgut.edu.cn

L. Kang
e-mail: kangl@dgut.edu.cn

F. Zheng
Dongguan Power Supply Bureau, 523808 Dongguan, China
e-mail: zhengfl@csg.cn



F. Shahnia and S. Deilami (eds.), *ICPES 2019*, Lecture Notes in Electrical Engineering 669, https://doi.org/10.1007/978-981-15-5374-5_1

**Keywords** Two-layer energy sharing strategy · Hybrid energy storage system · Energy market

## Abbreviations

| | |
|---|---|
| $\beta_n^{bat,ch}$ & $\beta_n^{bat,dch}$ | Charging and discharging coefficient of BESS |
| $\beta_n^{bat}$ | Coefficient of BESS degradation cost |
| $\beta_c^{th}$ & $\beta_l^{th}$ | Coefficients of the thermal energy capacity and loss |
| $\gamma_n^{bat,loss}$ | Coefficient of BESS loss |
| A | Price of electrical and gas energy |
| B | Benefit and profit |
| C | Cost |
| E | Energy |
| P | Power |
| t | Time |
| T | Temperature |
| bat | Battery energy storage system (BESS) |
| ch | Energy charging of BESS |
| dch | Energy discharging of BESS |
| ele | Electrical energy |
| rate | Rate value of variable |
| th | Thermal energy |
| $A_{n,t}^{buy}$, $A_{n,t}^{sell}$ | Planning buying and selling price |
| $\boldsymbol{A}_t^{buy}$ & $\boldsymbol{A}_t^{sell}$ | Sorted matrixes of buying price $A_{n,t}^{buy}$ and selling price $A_{n,t}^{sell}$ |
| $B_{n,t}^{ele}$ | Benefit from electrical energy sharing |
| $E_{n,}^{th,loss}$ | Loss energy of thermal energy |
| $E_{n,t}^{rdg}$ & $E_{n,t}^{dem}$ | DRG energy and demand energy for the n-th participant at time t |
| $E_{n,t}^{buy}$ & $E_{n,t}^{sell}$ | Planning buying and selling energy |
| $E_{n,t}^{t-b}$ & $E_{n,t}^{t-s}$ | Traded buying and selling energy for the n-th trading player at time t |
| $\boldsymbol{E}_t^{buy}$, $\boldsymbol{E}_t^{sell}$ | Sorted matrixes of buying energy $E_{n,t}^{buy}$ and selling energy $E_{n,t}^{sell}$ |
| $f_{A_{n,t}^{buy}}\left\{E_{n,t}^{buy}\right\}$ | Function to sort the buying energy $E_{n,t}^{buy}$ by the same with the same sorting sequence of the buying price $A_{n,t}^{buy}$ |
| $f'_{A_{n,t}^{buy}}\left\{\boldsymbol{E}_t^{'buy}\right\}$ | Function to sort the energy $\boldsymbol{E}_t^{'buy}$ with the inverse sequence of $f_{A_{n,t}^{buy}}\left\{E_{n,t}^{buy}\right\}$ |
| $M_t^{buy}$ & $M_t^{sell}$ | Amount energy of the buying and selling energy |
| $N_{n,lc}^{bat}$ | Charging numbers during the battery lifetime |
| $P_{n,t}^{waste}$ | Waste energy generated by RDG |
| $P_{n,t}^{dem}$ | Demand energy of the n-th participant at time t |

| | |
|---|---|
| $P_i$, $Q_i$, $V_i$ | Active power, reactive power and voltage in the i-th branch |
| $T_{amb}^{th}$ | Ambient temperature |

## 1 Introduction

With the development of the Renewable Distributed Generation (RDG) and the energy storage system, several existing works focus on the energy management strategy of distribution network with RDG and energy storage system [1]. The distributed energy storage system can mitigate the RDG fluctuation and increase the RDG penetration [2, 3]. Because of this significant role and the high investment cost of DESS in the distribution network, this paper focuses on the energy sharing strategy with Hybrid Energy Storage System (HESS).

Based on the increasing trend of the energy trading method applied in the energy market [4], the two-layer energy sharing model is developed on the energy trading method [5–7] and the energy management method of the energy storage system [3, 8, 9]. A real-time energy trading system is improved with rational aggregator in microgrids for the most currently energy market [5]. Another application of energy trading is proposed for the end-user and energy resources in the energy market [5]. Moreover, the energy sharing provider is proposed with the dynamic internal pricing and the demand response in microgrids [7]. Furthermore, a hierarchical energy management method is proposed to coordinate multiple groups of energy storage system [8]. Meanwhile, there is an optimal sizing model to provide the services of RDG fluctuation smoothing and the peak-time power supplying in the distributed network [3]. At last, A novel model of household energy management is applied with the energy storage devices for demand response [9]. In this paper, we are interested in the application of distributed network within the energy trading method, especially considering different end-users. Our motivation is to reduce the requirement of the capacity of the energy storage system, increase the utilization of RDG, and reduce the energy bill. To achieve these aims, HESS is operated in this model including the distributed Battery Energy Storage System (BESS) and the Thermal Energy Storage System (TESS), and the energy sharing model is modified on the energy trading method. In this paper, we discuss the two-layer energy sharing strategy with the consideration of the maximum transaction volume in the trading algorithm. The contributions of the two-layer energy sharing strategy are as follows.

- The proposed framework of the two-layer energy sharing model classifies different end-users into different communities based on the different characteristics, such as the RDG & load characteristics and geographical location.
- Based on the trading method of stock opening, the trading model is modified with the maximum transaction volume for this two-layer energy sharing model to achieve the aims of increasing RDG utilization, reducing energy bill, and saving HESS cost.

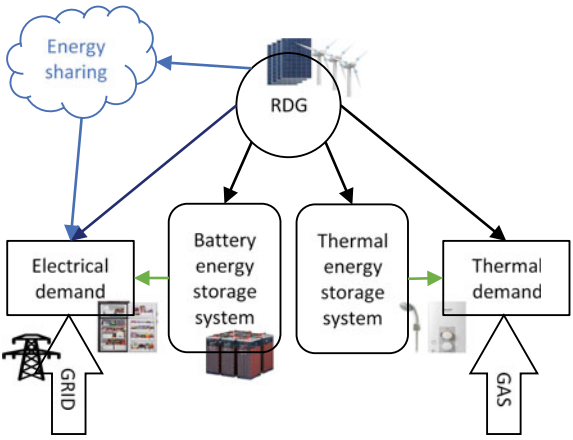


**Fig. 1** Frame structure of the energy sharing model for one participant

This frame structure of the proposed two-layer energy sharing strategy has been shown in Fig. 1. It is not independent of the traditional energy networks, and any kind end-users can be connected to. The rest of this paper is organized as follows. Section 2 introduces an overview of the proposed model. The model functions are presented in Sect. 3. Section 4 shows the case study simulated with the real-world data in the Australia electricity market,and conclusions are discussed in Section 5.

## 2 Energy Sharing Model Overview

In this paper, we propose a two-layer energy sharing strategy for the end-users in the distribution network. Users are classified into different communities based on their different characteristics, and a single end-user can be a community. In this two-layer energy sharing strategy, all participants are classed into two layers. Firstly, the demand is supplied by RDG, HESS, sharing with other participants and buying from the utility grid for each user in the first layer. Moreover, the participants in 1-layer are geographically adjacent and in the same sub-network. There are several groups in 1-layer and energy sharing is operated in each group. After the group-energy-sharing, the energy sharing between groups and other participants are in 2-layer. By this way, there is no network limitation in 1-layer, the energy sharing can be more efficient, and the utilization of RDG is maximized.

The model structure is shown in Fig. 2. It shows the operation in each group of 1-layer, and the energy sharing between groups and other participants in 2-layer. The 1-layer is operated in every community, in which the energy is shared with the participants who have the same load characteristics or are geographically close. After the 1-layer energy sharing, the remaining RDG or the shortage of demand is transferred to participate in the 2-layer energy sharing progressing. For each participant, the energy management model with the HESS operation could calculate

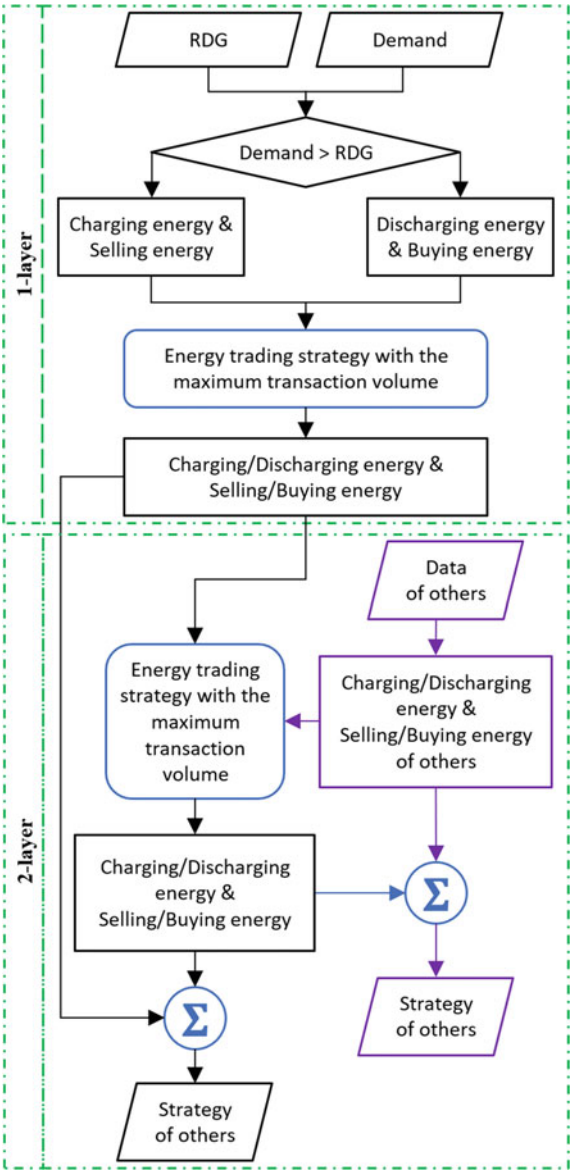


**Fig. 2** The flow chart of two-layer energy sharing model

the charging/discharging/selling/buying energy. According to the calculation, customers could share their selling/buying energy with other participants in the same layer based on the energy trading system. Moreover, the energy trading model is based on the trading method of stock opening, and the maximum transaction volume as the trading principle will increase the energy utilization of RDG and reduce the costs.

# 3 Model and Function

## 3.1 Energy Management Model

The energy storage system plays an important role in energy trading of the distribution network [10]. In this paper, the Battery Energy Storage System (BESS) and Thermal Energy Storage System (TESS) are considered for participants. The management strategy is based on the forecast data of RDG, demand and energy trading, in which the predictive data is referred by the method of the minimization optimization of empirical mean absolute percentage error [11].

The cost of BESS $C_{n,t}^{ele}$ is assumed to be the depreciation cost for every participant. The cost of TESS $C_{n,t}^{th}$ is the Operation and Management (O&M) cost in which the cost considers the thermal energy loss to the ambient. The HESS cost is the sum of costs of BESS and TESS, which the cost functions are expressed as,

$$C_{n,t}^{ele} = \beta_n^{bat} \Delta t \sum P_{n,t}^{ch,e} + P_{n,t}^{dch,e} + \gamma_n^{bat,loss} E_{n,t}^{bat} \tag{1}$$

$$\beta_n^{bat} = \frac{C_{n,inv}^{bat}}{E_{n,rate}^{bat} N_{n,lc}^{bat}} \tag{2}$$

$$C_{n,t}^{th} = \beta_n^{th} \sum P_{n,t}^{ch,th} + P_{n,t}^{dch,th} + A_{gas}^{buy,th} \sum E_{n,}^{th,loss} \tag{3}$$

$$E_n^{th,loss}\left(t_j - t_i\right) = \beta_c^{th}\left(\frac{T_n^{th}\left(t_j\right) - T_n^{th}(t_i)}{t_j - t_i}\right) + \beta_l^{th}\left(\frac{T_n^{th}\left(t_j\right) + T_n^{th}(t_i)}{2} - T_{amb}^{th}\right) \tag{4}$$

Based on the energy balance, the aim of the energy management model is to reduce the costs of BESS and TESS $\left(\mathrm{C}_{\mathrm{n,t}}^{\mathrm{th}}, \mathrm{C}_{\mathrm{n,t}}^{\mathrm{ele}}\right)$, increase the benefit of energy sharing $\left(\mathrm{B}_{\mathrm{n,t}}^{\mathrm{ele}}\right)$ and decrease the energy waste of RDG $\left(\mathrm{P}_{\mathrm{n,t}}^{\mathrm{waste}}\right)$, the objective function of the energy model is expressed as,

$$\underset{P_{n,t}^{th},\, P_{n,t}^{e},\, P_{n,t}^{waste}}{argmin} \left\{A_{grid}^{buy,e} P_{n,t}^{waste} + C_{n,t}^{th} + C_{n,t}^{ele} - B_{n,t}^{ele}\right\} \tag{5}$$

$$B_{n,t}^{ele} = \sum A_{grid}^{buy,e} P_{n,ele,t}^{rdg,e} + \sum A_{grid}^{buy,e} \frac{P_{n,t}^{dch,e}}{\beta_n^{dch,e}} + \sum \left(A_{grid}^{buy,e} - A_{n,t}^{buy,e}\right) P_{n,t}^{buy,e} + \sum A_{n,t}^{sell,e} P_{n,t}^{sell,e} \tag{6}$$

$$P_{n,t}^{rdg} + P_{n,t}^{dch,e} + P_{n,t}^{dch,th} + P_{n,t}^{buy,th} + P_{n,t}^{buy,e} = P_{n,t}^{dem,e} + P_{n,t}^{dem,th} + P_{n,t}^{ch,e} + P_{n,t}^{ch,th} + P_{n,t}^{sell,th} + P_{n,t}^{sell,e} + P_{n,t}^{waste} \tag{7}$$

$$\sum E_{n,t}^{ren} + E_{n,t}^{ch} + E_{n,t}^{buy} = \sum E_{n,t}^{dem} + E_{n,t}^{dch} + E_{n,t}^{sell} \tag{8}$$

$$P_{i+1}(t) = \sum_{h=i+2}^{N} R_h(t) \tag{9}$$

$$Q_{i+1}(t) = \sum_{h=i+2}^{N} Q_h(t) \tag{10}$$

$$V_{i+1}(t)^2 = V_i(t) - \frac{r_i P_i(t) + s_i Q_i(t)}{V_{i,0}} \tag{11}$$

$$V_{i,\min} \le V_i(t) \le V_{i,\max} \tag{12}$$

$$P_{i,\min} \le P_i(t) \le P_{i,\max} \tag{13}$$

$$G_i = \frac{f_{g,i} K_g \Gamma_0}{\rho_0} \sqrt{\frac{f_{g,i}\left(\rho_x^2 - \rho_y^2\right) D_{g,i}^5}{g F_i L_i \Gamma_i Z_g}} \tag{14}$$

$$f_{g,i} = \begin{cases} +1, \rho_x - \rho_y > 0 \\ -1, \rho_x - \rho_y < 0 \end{cases} \tag{15}$$

$$T_{n,\min} \le T_{n,th}(t) \le T_{n,\max} \tag{16}$$

$$S_{n,\min}^{BESS} \le S_{n,t}^{BESS} \le S_{n,\max}^{BESS} \tag{17}$$

$$S_{n,\min}^{TESS} \le S_{n,t}^{TESS} \le S_{n,\max}^{TESS} \tag{18}$$

where Eq. (6) denotes the benefit of energy sharing; Eqs. (7)–(8) denote the power balance; Eqs. (9)–(13) denote the power flow and the boundaries of the voltage and power; Eqs. (14)–(15) denote the gas power flow; Eqs. (16)–(18) denote the maximum and minimum values of temperature $\left(\mathrm{T_{n,th}}\right)$ and SOC $\left(S_{n,t}^{BESS}, S_{n,t}^{TESS}\right)$ of BESS and TESS.

## 3.2 Energy Trading

The energy sharing strategy is based on the call-action method with the maximum transaction volume. For the energy sharing mechanism in the same sharing layer, the sharing energy data is shown by the trading players based on the energy management strategy. The pricing model is not the main focus in this paper, the prices

$\left(A_{n,t}^{sell}, A_{n,t}^{buy}\right)$ are assumed to the forecast price based on the method of the minimization optimization of empirical mean absolute percentage error [11]. In this paper, there is a uniform trading price (clearing price) for every trading player. As the power energy is the homogeneous product in the current energy market, the price is the only factor for the energy sharing mechanism, and the trading principle is to achieve the maximum transaction volume. The trading price $\left(A_{n,t}^{trade}\right)$ is represented as

$$\begin{cases} A_{\min}^{trade} \le A_t^{trade} \le A_{\max}^{trade} \\ A_{\max}^{trade} = \max\left\{\max\left(A_{n,t}^{buy}\right), \max\left(A_{n,t}^{sell}\right)\right\} \\ A_{\min}^{trade} = \min\left\{\min\left(A_{n,t}^{buy}\right), \min\left(A_{n,t}^{sell}\right)\right\} \\ n \in [1, N] \end{cases} \tag{18}$$

$$A_t^{trade} \in \left\{ argmax\left\{ \min\left( \sum_{n=1}^{\mathrm{N}} E_{n,t}^{buy} \gamma_{n,t}^{buy}, \sum_{n=1}^{\mathrm{N}} E_{n,t}^{sell} \gamma_{n,t}^{sell} \right) \right\} \right\}, \tag{19}$$

$$\begin{cases} \gamma_{n,t}^{buy} = \begin{cases} 1, & A_{n,t}^{buy}(t) \ge A_{n,t}^{trade}(t) \\ 0, & others \end{cases} \\ \gamma_{n,t}^{sell} = \begin{cases} 1, & A_{n,t}^{sell}(t) \le A_{n,t}^{trade}(t) \\ 0, & others \end{cases} \end{cases} \tag{20}$$

where the Eqs. (18)–(20) denote the mathematical algorithm of the energy trading, in which $\gamma_n^{sell}, \gamma_n^{buy}$ denote the coefficients of selling/buying, they are binary variables. To achieve the principle of the maximum transaction volume, the trading amount with the same clearing price is processed as

$$\boldsymbol{A}_t^{buy} = descend\left\{A_{n,t}^{buy}\right\}, \boldsymbol{A}_t^{sell} = ascend\left\{A_{n,t}^{sell}\right\} \tag{21}$$

$$\boldsymbol{E}_t^{buy} = f_{A_{n,t}^{buy}}\left\{E_{n,t}^{buy}\right\}, \boldsymbol{E}_t^{sell} = f_{A_{n,t}^{sell}}\left\{E_{n,t}^{sell}\right\} \tag{22}$$

$$M_t^{buy} = \sum E_{n,t}^{buy}, M_t^{sell} = \sum E_{n,t}^{sell} \tag{23}$$

$$M_t^{trade} = \min\left\{M_t^{buy}, M_t^{sell}\right\} \tag{24}$$

$$\begin{aligned} m_t^{buy} &= 1 + \underset{i}{\operatorname{argmin}} \left\{ M_t^{trade} - \sum_{n=1}^{i} \boldsymbol{E}_t^{buy}(n:i) \right\}, \\ &if\ M_t^{trade} - \sum_{n=1}^{i} \boldsymbol{E}_t^{buy}(n:i) \ge 0, i \in [1, N] \end{aligned} \tag{25}$$

$$m_t^{sell} = 1 + \underset{j}{\operatorname{argmin}} \left\{ M_t^{trade} - \sum_{n=1}^{j} \boldsymbol{E}_t^{sell}(n:j) \right\},$$
$$if\ M_t^{trade} - \sum_{n=1}^{j} \boldsymbol{E}_t^{sell}(n:j) \geq 0,\ j \in [1, N] \tag{26}$$

$$\boldsymbol{E}_t^{'buy}(m) = \begin{cases} \boldsymbol{E}_t^{buy}(m), & m \leq \left(m_t^{buy} - 1\right) \\ M_t^{trade} - \sum_{1}^{m_t^{buy}-1} \boldsymbol{E}_t^{buy}(1:m), & m = m_t^{buy} \\ 0, & m > m_t^{buy} \end{cases} \tag{27}$$

$$\boldsymbol{E}_t^{'sell}(m) = \begin{cases} \boldsymbol{E}_t^{sell}(m), & m \leq \left(m_t^{sell} - 1\right) \\ M_t^{trade} - \sum_{1}^{m_t^{sell}-1} \boldsymbol{E}_t^{sell}(1:m), & m = m_t^{sell} \\ 0, & m > m_t^{sell} \end{cases} \tag{28}$$

$$\boldsymbol{E}_t^{t-b} = f'_{A_{n,t}^{buy}}\left\{\boldsymbol{E}_t^{'buy}\right\},\ \boldsymbol{E}_t^{t-s} = f'_{A_{n,t}^{buy}}\left\{\boldsymbol{E}_t^{'sell}\right\} \tag{29}$$

$$E_{n,t}^{t-b} = \boldsymbol{E}_t^{t-b}(n),\ E_{n,t}^{t-s} = \boldsymbol{E}_t^{t-s}(n) \tag{30}$$

where the Eqs. (21)–(22) denote the ordering based on the prices; the Eqs. (23)–(26) denote the total buying and selling transaction volume; the Eqs. (27)–(30) denote the selling or buying energy for each trading players. By the processing the equations, the trading energy for every trading player $\left(E_{n,t}^{t-b}, E_{n,t}^{t-s}\right)$ can be calculated.

## 4 Case Study

In this paper, the two-layer energy sharing strategy is proposed to possess end-users with different load characteristics and different HESS capacities in the distribution network. The participants 1–11 are the residential end-users, based on the geographical location they are classed into three communities (1–6, 7–9, 10–11) in the 1-layer. The participants 12–18 are the business and industry energy users, each of them is assumed to be one community and only progress in the 2-layer. The HESS capacities of participants 10–15 are zero, which is no HESS; the TESS capacities of participants 2 and 6–8 are the lowest value, which is the no extra TESS. The case study is operated in Matlab® on a PC with Intel Core i7-6600 CPU @ 2.80 GHZ with 8.00 GB RAM. All the data of the participants is the real historical data in the Australia national electricity market [12].

1. *Simulation in 1-layer*

With energy management model, the energy sharing strategy is operated for participants 1–11 in three communities. As shown in Fig. 3, the energy strategies for 11 participants are operated in 1-layer. The purple bar denotes the electrical buying

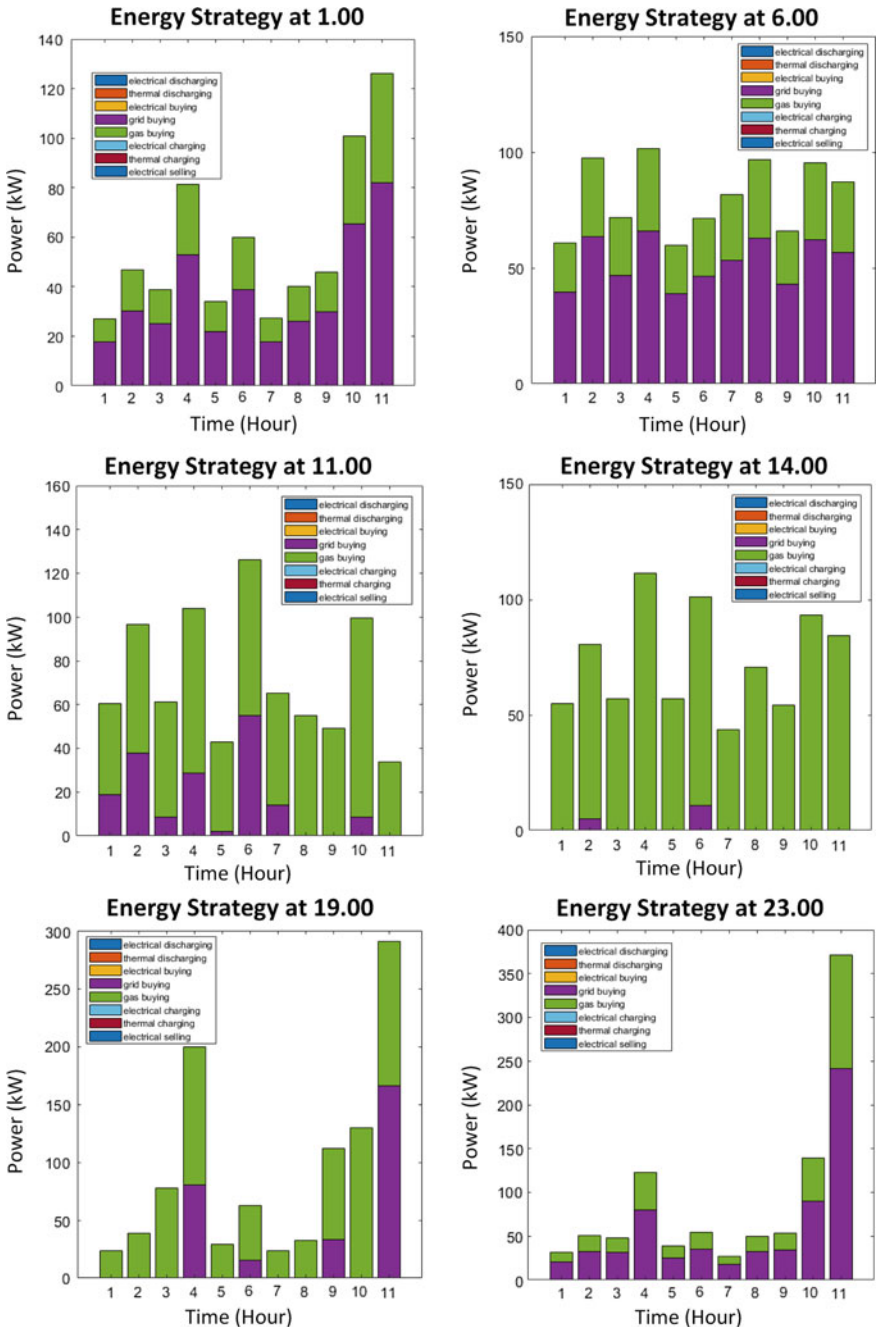


**Fig. 3** The simulation results of the energy strategies in 1-layer at time 1 am, 6 am, 11 am, 2 pm, 7 pm and 11 pm

energy from the utility grid, the green bar denotes the gas buying energy to supply the thermal demand. For the residential under-users, the investment costs of RDG and HESS is very high, the capacities of them are low, the supplying energy for electrical demand and thermal demand are main buying from the main grid. For the residential under-users, the investment costs of RDG and HESS is very high, the capacities of them are low, the supplying energy for electrical demand and thermal demand are main buying from the main grids. Figure 4 shows the hourly simulation results of three communities in 1-layers, this data is the transferring data for 2-layer.

2. *Simulation in Two-Layer Energy Sharing Strategy*

With the transferring data of three communities from 1-layer, the simulation results are calculated for the three communities and the participants 12–18. The energy sharing strategies in 2-layer of participants 12–18 are shown in Fig. 5. Because of the demand and generation characteristics of participants 12–18, the capacities of RDG and HESS are higher than the residential und-users in 1-layer, the energy charging is from 12.00 to 18.00, because that the PV panels generation is higher, and the energy sharing volume is much lower than the remaining energy, since the remaining energy is used as the HESS charging energy. Based on all the simulation data, the priority of energy management in this two-layer energy sharing strategy is shown in Fig. 6. There is the charging energy of HESS after energy sharing. By this way, the utilization of RDG can be provided, and the requirement of HESS is reduced.

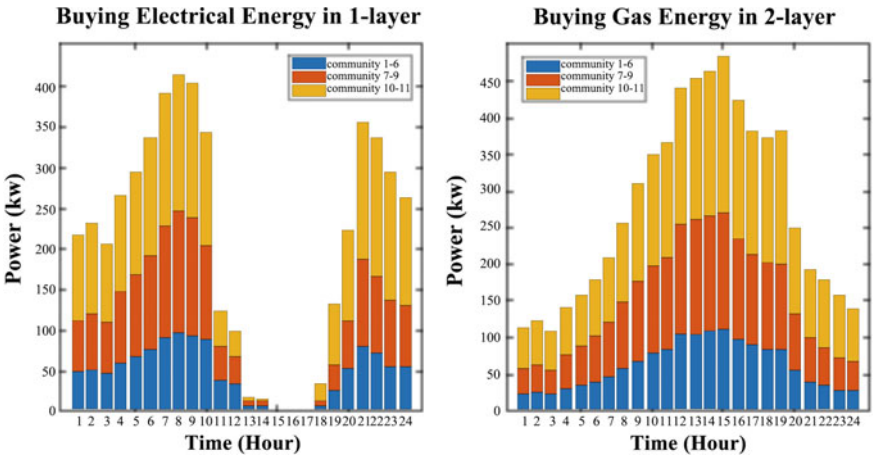


**Fig. 4** The energy data of 1-layer is transferred for 2-layer energy sharing of 24 h

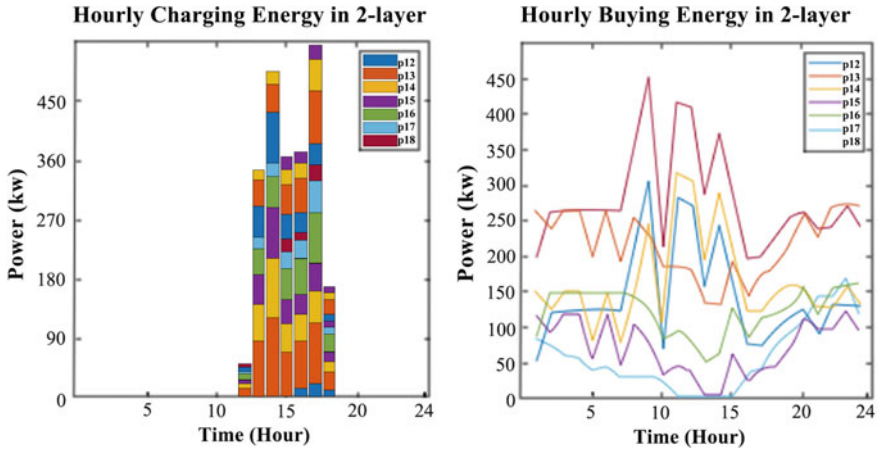


**Fig. 5** The hourly simulation results of 2-layer for participants 12–18

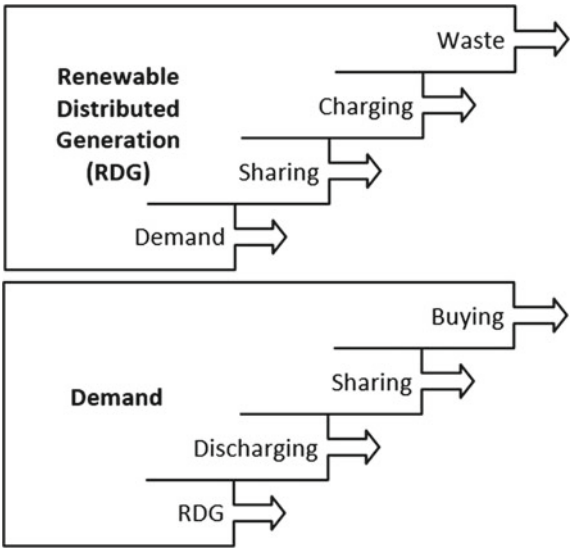


**Fig. 6** The energy management priority in this proposed two-layer energy sharing model

## 5 Conclusion

The two-layer energy sharing strategy is proposed to improve the utilization of RDG, reduce the energy cost of end-users, and decrease the investment of energy storage devices. Moreover, the HESS model is used in this paper, which includes BESS and TESS. The power flow and gas flow are considered in the energy management model under the energy nodal balance. Furthermore, the energy trading model with the maximum transaction volume is proposed as the energy sharing mechanism based

on the stock trading method of stock opening. In the future, our work will focus on the trading player complete and the pricing model generalization works.

**Acknowledgements** This work was supported by the National Key Research and Development Program of China (2017YFB0903205) and was also supported by the ARC Research Hub for Integrated Energy Storage Solutions (IH180100020), FEIT Early Career Researcher and Newly Appointed Staff Development Scheme, The University of Sydney and Sir William Tyree Foundation-Distributed Power Generation Research Fund.

## References

1. Kang J, Yu R, Huang X, Maharjan S, Zhang Y, Hossain E (2017) Enabling localized peer-to-peer electricity trading among plug-in hybrid electric vehicles using consortium blockchains. IEEE Trans Industr Inf 13(6):3154–3164
2. Li Q, Choi SS, Yuan Y et al (2011) On the determination of battery energy storage capacity and short-term power dispatch of a wind farm. IEEE Trans Sustain Energy 2(2):148–158
3. Zhang F, Xu Z, Meng K (2016) Optimal sizing of substation-scale energy storage station considering seasonal variations in wind energy. IET Gener Transm Distrib 10(13):3241–3250
4. Castaneda J, Enslin J, Elizondo D, Abed N, Teleke S (2010) Application of statcom with energy storage for wind farm integration. In: Proceedings IEEE PES transmission and distribution conference and exposition, pp 1–6
5. Zhang C, Wang Q, Wang J, Pinson P, Morales JM, Østergaard J (2018) Real-time procurement strategies of a proactive distribution company with aggregator-based demand response. IEEE Trans Smart Grid 9(2):766–776
6. Nguyen DT, Le LB (2015) Risk-constrained profit maximization for microgrid aggregators with demand response. IEEE Trans Smart Grid 6(1):135–146
7. Zhang C, Xu Y, Dong ZY, Ma J (2017) Robust operation of microgrids via two-stage coordinated energy storage and direct load control. IEEE Trans Power Syst 32(4):2858–2868
8. Wang D, Meng K, Gao X, Qiu J, Lai LL, Dong ZY (2018) Coordinated dispatch of virtual energy storage systems in LV grids for voltage regulation. IEEE Trans Indust Inf 14(6):2452–2462
9. Wang Z, Gu C, Li F, Bale P, Sun H (2013) Active demand response using shared energy storage for household energy management. IEEE Trans Smart Grid 4(4):1888–1897
10. Castaneda J, Enslin J, Elizondo D, Abed N, Teleke S (2010) Application of statcom with energy storage for wind farm integration. In: Proceeding IEEE PES transmission and distribution conference and exposition, pp 1–6
11. Kong W, Dong ZY, Hill DJ, Luo F, Xu Y (2018) Short-term residential load forecasting based on resident behaviour learning. IEEE Trans Power Syst 33(1):1087–1088
12. AEMO: http://www.aemo.com.au

# Effects of PV Modules Temperature Variations on the Characteristic of PV Array


**Gholamreza Farahani**

**Abstract** This paper simulates the effects of photovoltaic (PV) module temperature variations on the different characteristic of PV array with MATLAB/Simulink software. Four classification for temperature variations of PV module have been defined that are soft uniform, hard uniform, soft nonuniform and hard nonuniform temperature variations. The changes of five parameters of the PV array that are maximum output power (MOP), open circuit voltage ($V_{OC}$), short circuit current ($I_{SC}$), fill factor (F.F.) and efficiency have been investigated under four temperature classification. The results are shown that in the two first classes and different scenarios in each class, the MOP, $V_{OC}$, F.F. and efficiency are monotonically increasing with decreasing the uniform temperature while the $I_{SC}$ of PV array decreases with decreasing the uniform temperature. For nonuniform temperature variations, the MOP, $V_{OC}$ and efficiency have reverse relationship with temperature variations but for two other parameters $I_{SC}$ and F.F., there is not any direct relationship. Also for all classes, always the relationship of five parameters with temperature variations is nonlinear.

**Keywords** PV array · Efficiency · Maximum output power · Shading

## Abbreviations

| | |
|---|---|
| F.F. | Fill Factor |
| $I_{SC}$ | Short Circuit Current |
| I-V | Current-Voltage |
| MOP | Maximum Output Power |
| MPP | Maximum Power Point |
| PV | PhotoVoltaic |
| P-V | Power-Voltage |
| $V_{OC}$ | Open Circuit Voltage |

G. Farahani (✉)
Department of Electrical Engineering and Information Technology, Iranian Research Organization for Science and Technology, Tehran, Iran
e-mail: farahani.gh@irost.org



F. Shahnia and S. Deilami (eds.), *ICPES 2019*, Lecture Notes in Electrical Engineering 669, https://doi.org/10.1007/978-981-15-5374-5_2

## 1 Introduction

One of the best and reliable source of renewable energy is the solar system. The solar energy is pollution free with less maintenance and recyclable. Energy demand in the world is increasing every day which it cannot be met only by the fuel sources. As a result, there are several alternative energy sources that solar energy is one of them with great potential to meet the energy growing requirement. Photovoltaic (PV) technology consists of an array of solar panels to generate electricity using energy of sun [1].

Several applications for PV panels are developed such as alternative energy generation, solar vehicle construction, battery charging, water pumping and satellite grid. It is very common to find solar cells which have lower output than the maximum one, due to several causes such as manufacturing defects, degradation of cells, high temperatures on the solar cell, or shading. Shading is one of the bottlenecks that PV arrays are facing with it. The shading on the PV panels may occur by the passing clouds, shadows of tress, neighbor buildings, dirt, debris, bird droppings, different orientation, tilt angles, and other PV panels [2]. The partial or overall shading on the PV array causes not only reduction in output power but also leads to hot-spot and causes damage to these cells.

A cell can be modeled as a combination of a current generator and a diode. The photo current goes in the reverse direction of the diode. This means that if one cell is shaded, it will produce less current than the other cells in the string, and the other cells will try to push more current through the poor cell than the poor cell deliver. This is however not possible since then the cell acts as a diode in the reverse direction. Thus the current produced in the poor cell will limit the current in the string. Bypass diodes have to be installed in order to avoid the current losses either to avoid the restriction of the current and also to avoid heat stress on the shaded cells [3]. Bypass diodes enable the current to flow through an alternative path through them and skip modules that cannot contribute to the power production. Shading impact depends on the module specifications, placement of the bypass diode, string configuration and shading severity. The general effects of shading on the PV module are power loss, current mismatch within a PV string and voltage mismatch between parallel strings [4].

In the studies to assess the effects of shading conditions in PV systems take on many different forms. In some studies, the position of the PV modules and obstacles in the environment with respect to the position of the sun are used to map shadows onto the panels [5]. Other methods involve using simulated shading conditions to explore the impact of shading on the PV characteristics [6]. Different factors that influence the PV system performance like PV array configuration, are irradiance of the solar and the temperature. It is mandatory to classify the relation between these factors with the performance of the PV system [7]. In the next section, the PV cell model will describe. The effects of the shadow on the PV array will explain in the Sect. 3. Section 4 includes the simulation to analyze the temperature effects on the PV characteristic. Finally, Sect. 5 concludes the paper.

## 2 PV Cell Model

The solar cell is the semiconductor device that directly converts the light energy to the electricity. A solar cell has nearly the same behavior as a diode. The most conventional model of a solar cell is the one diode, a photo current ($I_L$), a series resistor ($R_S$), and a shunt resistor ($R_{SH}$) that is shown in Fig. 1. Equation (1) describe the I-V characteristic of diode D.

$$I_D = I_0 \times \left[\exp(V_d / nV_T) - 1\right] \tag{1}$$

where $I_D$ is diode current (A), $V_d$ is diode voltage (V), $I_0$ is diode saturation current (A), $n$ is the ideality factor of the diode D and $V_T$ is temperature voltage and will calculate as (2):

$$V_T = k \times T/q \tag{2}$$

where $T$ is cell temperature (K), $k = 1.3806 \times 10^{-23}$ J/K is Boltzman constant and $q = 1.6022 \times 10^{-19}$ C is electron charge. The current at the output terminal of the solar cell is formulated as (3) [8]:

$$I = I_L - I_0\left[\exp\left(q\frac{(V + I.R_S}{k.T.n}\right) - 1\right] - \frac{V + I.R_S}{R_{SH}} \tag{3}$$

The PV cell efficiency is defined as the ratio of peak power output to input solar power and is calculated as (4).

$$\eta(\%) = \frac{V_{mp} \times I_{mp}}{G \times A} \times 100 \tag{4}$$

where $V_{mp}$ is the voltage at peak power, $I_{mp}$ is the current at peak power, $G$ is the solar intensity per square meter and $A$ is the area on which solar radiation falls. The fill factor was estimated using the (5).

$$F.F. = \frac{V_{mp} \times I_{mp}}{I_{sc} \times V_{oc}} \tag{5}$$

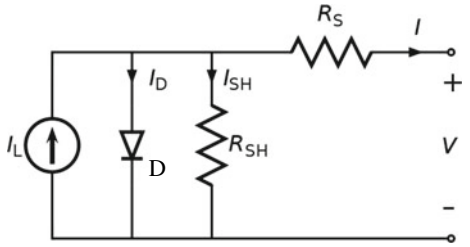


**Fig. 1** Equivalent circuit of a PV cell

where $V_{OC}$ is the open circuit voltage and $I_{SC}$ is the short circuit current. An ideal PV panel should have a perfectly rectangular current-voltage (I-V) curve such that the maximum power point (MPP) coincided with ($I_{SC}$, $V_{OC}$), therefore F.F. will be 1.

## 3 Effects of Temperature Variations on the PV Array

The performance of PV system is mostly affected by solar irradiation, module temperature and array configuration. The knowledge of the impact of the temperature variations and its relationship with the output powers of the PV array is very important in order to find the best performance of the PV system. In temperature variations that its main reason is partial shading, different PV modules of the PV array received a different irradiance level. Therefore, the temperature of the modules will be different and characteristic of PV array will change.

Temperature is a significant design factor affecting the performance of many PV systems. Measuring the extent of temperature variations on a solar array can be challenging due to the fact that it depends on the environmental conditions. The temperature variations which are happened based on partial shading are more complicated by the changes in the source of shade itself. For example, the shade of tree can sway in the wind or lose its leaves during the winter, therefore the type of shade and temperature variations profile on a solar array will change [9].

Severity of temperature variations depends on the shade severity and area of the shade. In this paper, the effect of uniform and nonuniform temperature variations on the five parameters maximum output power (MOP), open circuit voltage ($V_{OC}$), short circuit current ($I_{SC}$), Fill Factor (F.F.) and efficiency ($\eta$) of PV panel is investigated. Also the effects of uniform and nonuniform temperature variations on the I-V and power-voltage (P-V) characteristics of the PV array with use of Matlab/Simulink software have been analyzed.

## 4 Simulation

In simulation, 8 PV modules that their configuration is as Fig. 2 are connected in series and parallel. According to Fig. 2, the output voltage of PV system is connected to the voltage source to simulate the output voltage of PV array.

During the simulations, 4 different class of temperature variations are defined as below:

- class A: Soft uniform temperature variations
- class B: Hard uniform temperature variations
- class C: Soft nonuniform temperature variations
- class D: Hard nonuniform temperature variations.

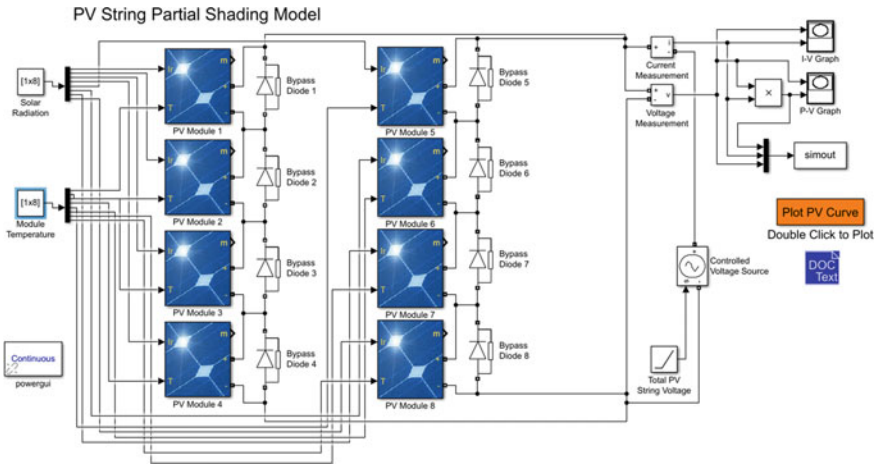


**Fig. 2** The simulation block diagram of the PV array in different temperature variations condition

In each class, different scenarios are defined. For each classes A & D, six scenarios and each classes B & C, 5 scenarios are defined. Each module receives the numerical irradiance and temperature in Simulink software. The mono-crystalline PV cells were used in the simulation. At Table 1 the characteristics of the simulated PV module are illustrated. Table 2 shows the PV cell model parameters.

A. *Effect of uniform temperature variations on the characteristics of the PV Array*

In this section, two types of uniform temperature variations (class A and class B) with different scenarios will be analyzed. At the class A, only one PV string

**Table 1** Module data

| Name | Value |
|---|---|
| Module manufacture | SunPower |
| Module type | SPR-X20-250-BLK |
| Maximum power (W) | 249.952 |
| Open circuit voltage ($V_{OC}$) (V) | 50.93 |
| Voltage at maximum power point $V_{mp}$ (V) | 42.8 |
| Temperature coefficient of $V_{OC}$ (%/°C) | −0.35602 |
| Cells per module ($N_{\text{cell}}$) | 72 |
| Short-circuit current ($I_{SC}$) (A) | 6.2 |
| Current at maximum power point ($I_{mp}$) (A) | 5.84 |
| Temperature coefficient of $I_{SC}$ (%/°C) | 0.07 |
| Parallel strings | 1 |
| Series-connected modules per string | 1 |

**Table 2** PV cell model parameters

| Parameter | Value |
|---|---|
| Light-generated current ($I_L$) (A) | 6.2073 |
| Diode saturation current ($I_0$) (A) | $1.8536e^{-10}$ |
| Diode ideality factor | 1.1367 |
| Shunt resistance ($R_{SH}$) ($\Omega$) | 621.2034 |
| Series resistance ($R_S$) ($\Omega$) | 0.301 |

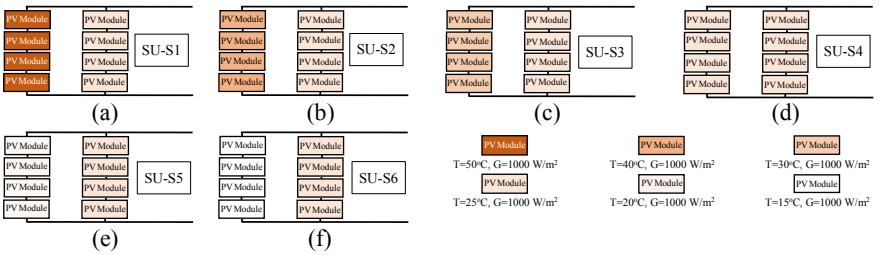


**Fig. 3** Different scenarios for soft uniform temperature variations (SU-S1 to SU-S6)

have the temperature variations while at class B, both strings will have a temperature variation.

1. *Soft uniform temperature variations (class A):* As shown in Fig. 3, at class A, one string has a STC temperature (25 °C) and other string temperature will change, thus uniform temperature variations will happen. In this class, 6 scenarios named soft uniform scenario (SU-S1 to SU-S6) are defined. Figure 4 illustrates the I-V and P-V curves of these scenarios.

In spite of the solar irradiation effects on the I-V and P-V curves, the variations of the five recorded parameters MOP, $V_{OC}$, $I_{SC}$, F.F. and $\eta$ are very low. The numerical vales of these parameters are shown in Table 3. According to Fig. 5, with decreasing the PV panel temperature, the MOP, $V_{OC}$, F.F. and $\eta$ will increase slowly and $I_{SC}$ will decrease slowly too.

2. *Hard uniform temperature variations (class B):* At class B, the both strings in the simulation have a same temperature. 5 scenarios named hard uniform scenario (HU-S1 to HU-S5) are defined in this class (Fig. 6). The I-V and P-V curves of these scenarios are shown in Fig. 7. To get the quantitative values of parameters for comparison, Table 4 shows the five PV array parameters that are MOP, $V_{OC}$, $I_{SC}$, F.F. and $\eta$.

The changes in these five parameters are shown in Fig. 8. As expected like as class A, the variation of MOP, $V_{OC}$, $I_{SC}$, F.F. and $\eta$ are like as class A but their variations are faster than class A.

B. *Effect of nonuniform temperature variations on the characteristics of the PV Array*

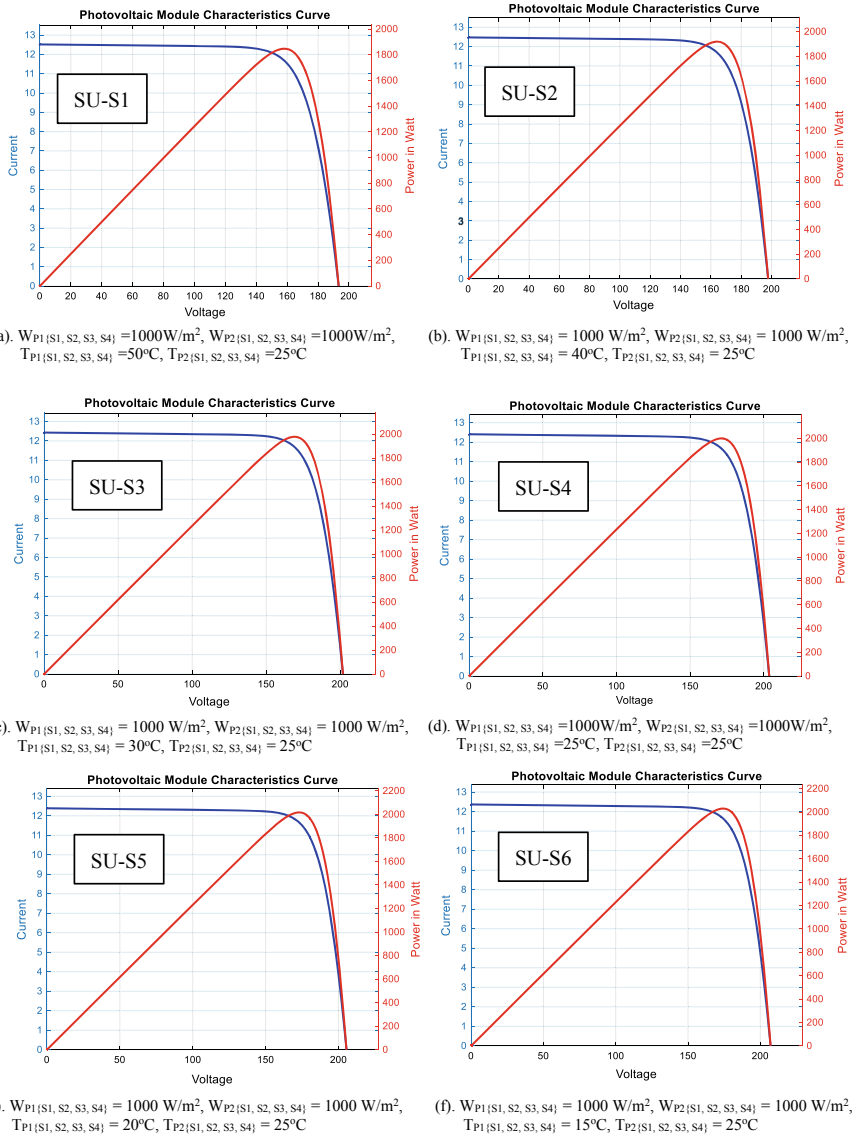


(a). $W_{P1\{S1, S2, S3, S4\}}$ =1000W/m$^2$, $W_{P2\{S1, S2, S3, S4\}}$ =1000W/m$^2$, $T_{P1\{S1, S2, S3, S4\}}$ =50ºC, $T_{P2\{S1, S2, S3, S4\}}$ =25ºC

(b). $W_{P1\{S1, S2, S3, S4\}}$ = 1000 W/m$^2$, $W_{P2\{S1, S2, S3, S4\}}$ = 1000 W/m$^2$, $T_{P1\{S1, S2, S3, S4\}}$ = 40ºC, $T_{P2\{S1, S2, S3, S4\}}$ = 25ºC

(c). $W_{P1\{S1, S2, S3, S4\}}$ = 1000 W/m$^2$, $W_{P2\{S1, S2, S3, S4\}}$ = 1000 W/m$^2$, $T_{P1\{S1, S2, S3, S4\}}$ = 30ºC, $T_{P2\{S1, S2, S3, S4\}}$ = 25ºC

(d). $W_{P1\{S1, S2, S3, S4\}}$ =1000W/m$^2$, $W_{P2\{S1, S2, S3, S4\}}$ =1000W/m$^2$, $T_{P1\{S1, S2, S3, S4\}}$ =25ºC, $T_{P2\{S1, S2, S3, S4\}}$ =25ºC

(e). $W_{P1\{S1, S2, S3, S4\}}$ = 1000 W/m$^2$, $W_{P2\{S1, S2, S3, S4\}}$ = 1000 W/m$^2$, $T_{P1\{S1, S2, S3, S4\}}$ = 20ºC, $T_{P2\{S1, S2, S3, S4\}}$ = 25ºC

(f). $W_{P1\{S1, S2, S3, S4\}}$ = 1000 W/m$^2$, $W_{P2\{S1, S2, S3, S4\}}$ = 1000 W/m$^2$, $T_{P1\{S1, S2, S3, S4\}}$ = 15ºC, $T_{P2\{S1, S2, S3, S4\}}$ = 25ºC

**Fig. 4** I-V and P-V characteristic curves of SU-S1 to SU-S6

In this section, two types of nonuniform temperature variations (class C and class D) with 5 and 6 scenarios are defined respectively. These scenarios have been used to analyze the effect of the nonuniform temperature variations on the PV array.

1. Soft *nonuniform temperature variations (class C):* In the class C, one string has a fixed temperature with 25 °C and other string temperature will grow up

**Table 3** Maximum power, open circuit voltage, short circuit current, fill factor and efficiency values of different scenarios for soft uniform temperature variation

| Scenario | MOP (W) | $V_{OC}$ (V) | $I_{SC}$ (A) | F.F. | $\eta$(%) |
|---|---|---|---|---|---|
| SU-S1 | 1846.50 | 195.02 | 12.52 | 0.756 | 18.55 |
| SU-S2 | 1918.60 | 198.88 | 12.48 | 0.773 | 19.28 |
| SU-S3 | 1976.90 | 203.50 | 12.44 | 0.781 | 19.86 |
| SU-S4 | 1999.60 | 205.71 | 12.41 | 0.783 | 20.09 |
| SU-S5 | 2017.10 | 206.74 | 12.39 | 0.787 | 20.27 |
| SU-S6 | 2029.60 | 208.38 | 12.37 | 0.787 | 20.39 |

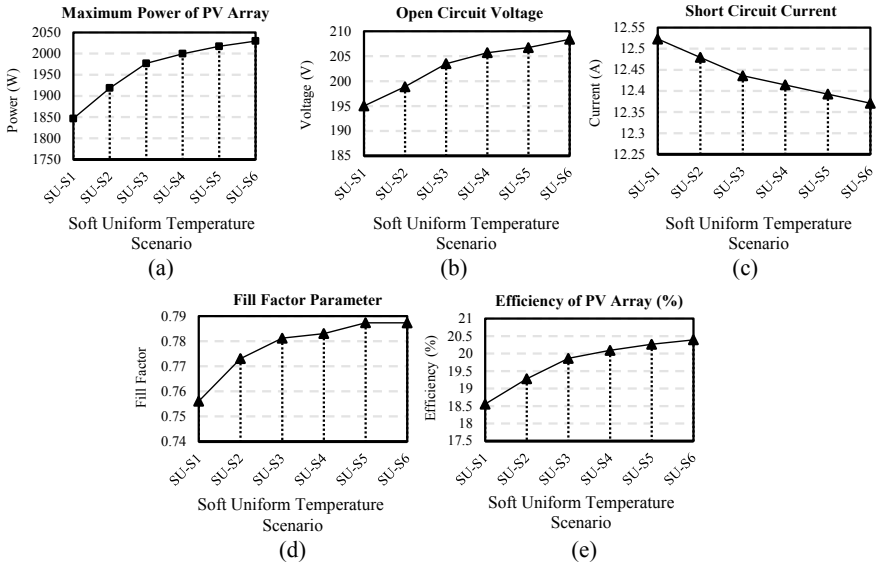


**Fig. 5** **a** Maximum power, **b** open circuit voltage, **c** short circuit current, **d** fill factor and **e** efficiency of the PV array for class A

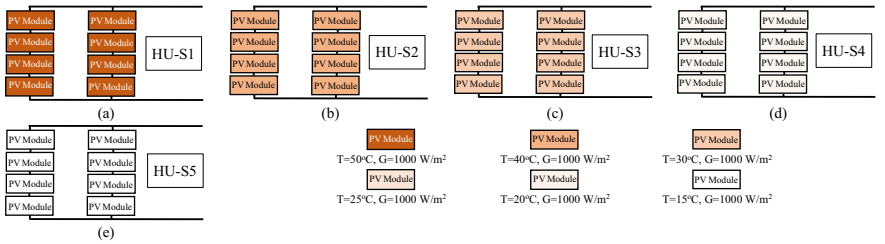


**Fig. 6** Different scenarios for hard uniform temperature variations (HU-S1 to HU-S5)

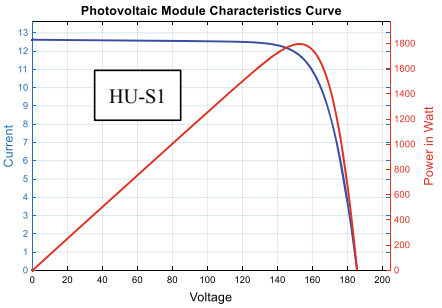


(a). $W_{P1\{S1,S2,S3,S4\}}$ =1000W/m$^2$, $W_{P2\{S1,S2,S3,S4\}}$ =1000W/m$^2$, $T_{P1\{S1,S2,S3,S4\}}$ =50ºC, $T_{P2\{S1,S2,S3,S4\}}$ =50ºC

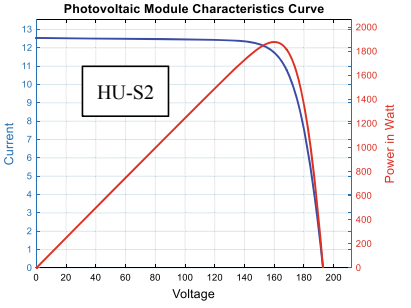


(b). $W_{P1\{S1,S2,S3,S4\}}$ = 1000 W/m$^2$, $W_{P2\{S1,S2,S3,S4\}}$ = 1000 W/m$^2$, $T_{P1\{S1,S2,S3,S4\}}$ = 40ºC, $T_{P2\{S1,S2,S3,S4\}}$ = 40ºC

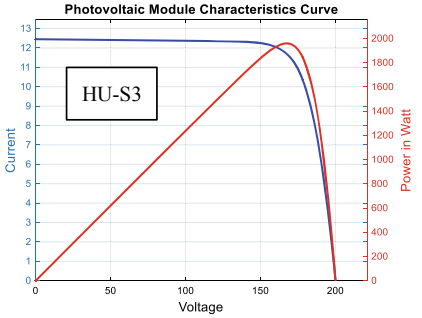


(c). $W_{P1\{S1,S2,S3,S4\}}$ = 1000 W/m$^2$, $W_{P2\{S1,S2,S3,S4\}}$ = 1000 W/m$^2$, $T_{P1\{S1,S2,S3,S4\}}$ = 30ºC, $T_{P2\{S1,S2,S3,S4\}}$ = 30ºC

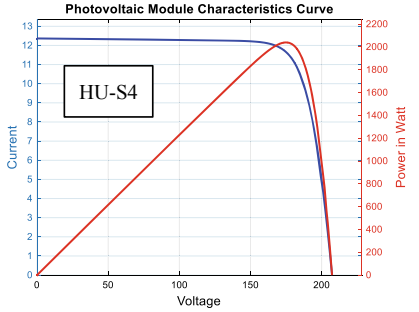


(d). $W_{P1\{S1,S2,S3,S4\}}$ = 1000 W/m$^2$, $W_{P2\{S1,S2,S3,S4\}}$ = 1000 W/m$^2$, $T_{P1\{S1,S2,S3,S4\}}$ = 20ºC, $T_{P2\{S1,S2,S3,S4\}}$ = 20ºC

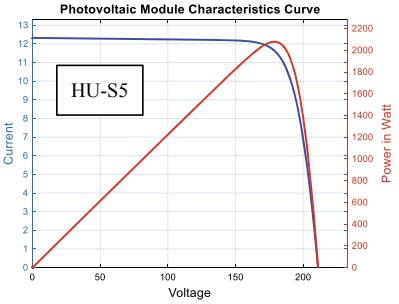


(e). $W_{P1\{S1,S2,S3,S4\}}$ = 1000 W/m$^2$, $W_{P2\{S1,S2,S3,S4\}}$ = 1000 W/m$^2$, $T_{P1\{S1,S2,S3,S4\}}$ = 15ºC, $T_{P2\{S1,S2,S3,S4\}}$ = 15ºC

**Fig. 7** I-V and P-V characteristic curves of HU-S1 to HU-S5

module by module to the 50 °C. As shown in Fig. 9, these 5 scenarios are named soft nonuniform scenario (SNU-S1 to SNU-S5). Figure 10 illustrates the I-V and P-V curves of the class C for different scenarios. The numerical values of the MOP, $V_{OC}$, $I_{SC}$, F.F. and $\eta$ parameters are listed at the Table 5. Because of nonuniformity of temperature variations, these parameters changes are more nonlinear than class A and class B (Fig. 11).

**Table 4** Maximum power, open circuit voltage, short circuit current, fill factor and efficiency values of different scenarios for hard uniform temperature variation

| Scenario | MOP (W) | $V_{OC}$ (V) | $I_{SC}$ (A) | F.F. | $\eta$(%) |
|---|---|---|---|---|---|
| HU-S1 | 1769.30 | 185.84 | 12.63 | 0.754 | 17.78 |
| HU-S2 | 1877.80 | 192.93 | 12.54 | 0.776 | 18.87 |
| HU-S3 | 1959.20 | 201.07 | 12.46 | 0.782 | 19.69 |
| HU-S4 | 2039.40 | 207.53 | 12.37 | 0.794 | 20.49 |
| HU-S5 | 2078.90 | 211.82 | 12.33 | 0.796 | 20.89 |

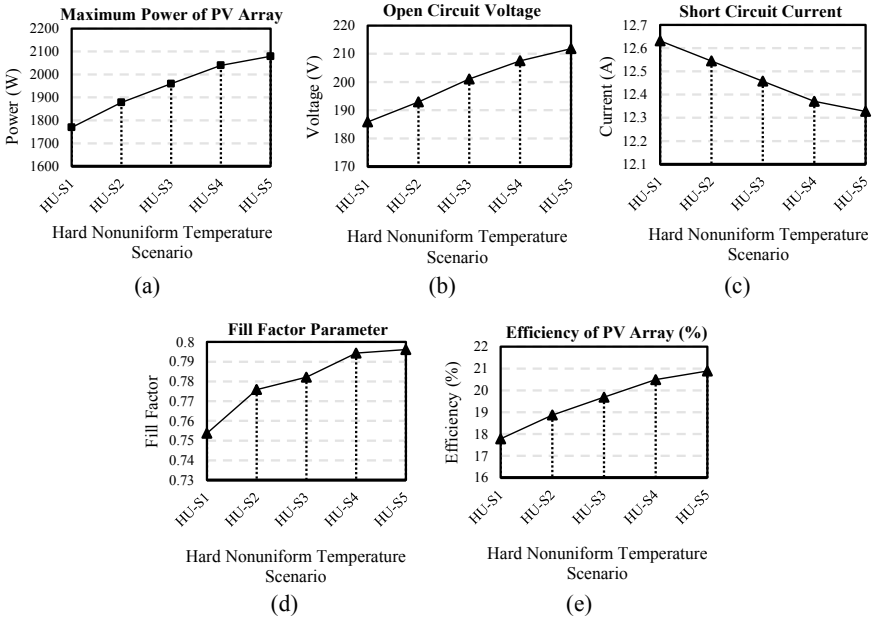


**Fig. 8** **a** Maximum power, **b** open circuit voltage, **c** short circuit current, **d** fill factor and **e** efficiency of the PV array for class B

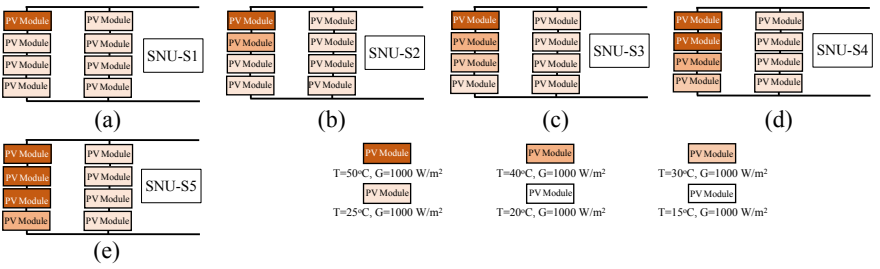


**Fig. 9** Different scenarios for soft nonuniform temperature variations (SNU-S1 to SNU-S5)

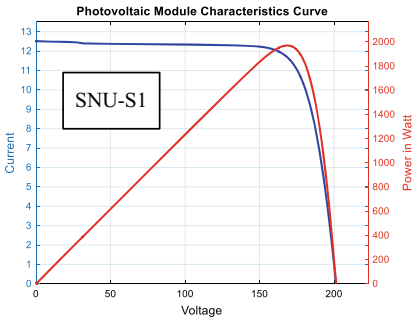


(a). $W_{P1\{S1, S2, S3, S4\}}$ = 1000 W/m$^2$, $W_{P2\{S1, S2, S3, S4\}}$ = 1000 W/m$^2$,
$T_{P1\{S1, S2, S3, S4\}}$ = {50, 25, 25, 25} ºC,
$T_{P2\{S1, S2, S3, S4\}}$ = {25, 25, 25, 25} ºC

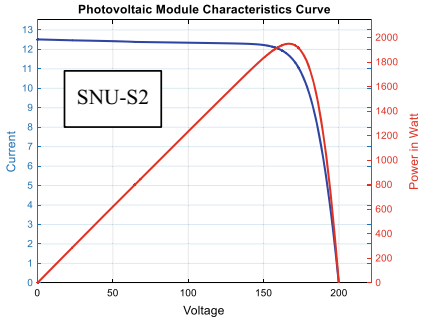


(b). $W_{P1\{S1, S2, S3, S4\}}$ = 1000 W/m$^2$, $W_{P2\{S1, S2, S3, S4\}}$ = 1000 W/m$^2$,
$T_{P1\{S1, S2, S3, S4\}}$ = {50, 40, 25, 25} ºC,
$T_{P2\{S1, S2, S3, S4\}}$ = {25, 25, 25, 25} ºC

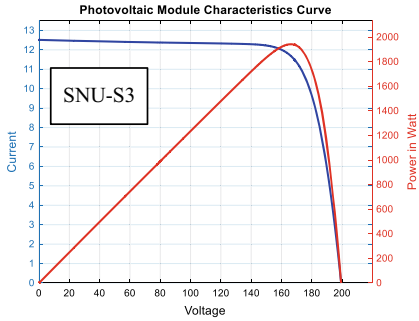


(c). $W_{P1\{S1, S2, S3, S4\}}$ = 1000 W/m$^2$, $W_{P2\{S1, S2, S3, S4\}}$ = 1000 W/m$^2$,
$T_{P1\{S1, S2, S3, S4\}}$ = {50, 40, 30, 25} ºC,
$T_{P2\{S1, S2, S3, S4\}}$ = {25, 25, 25, 25} ºC

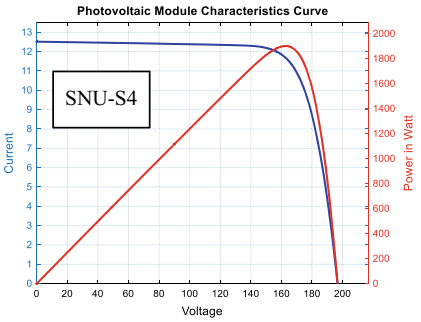


(d). $W_{P1\{S1, S2, S3, S4\}}$ = 1000 W/m$^2$, $W_{P2\{S1, S2, S3, S4\}}$ = 1000 W/m$^2$,
$T_{P1\{S1, S2, S3, S4\}}$ = {50, 50, 40, 30} ºC,
$T_{P2\{S1, S2, S3, S4\}}$ = {25, 25, 25, 25} ºC

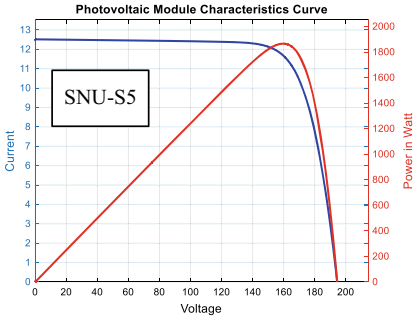


(e). $W_{P1\{S1, S2, S3, S4\}}$ = 1000 W/m$^2$, $W_{P2\{S1, S2, S3, S4\}}$ = 1000 W/m$^2$,
$T_{P1\{S1, S2, S3, S4\}}$ = {50, 50, 50, 40} ºC,
$T_{P2\{S1, S2, S3, S4\}}$ = {25, 25, 25, 25} ºC

**Fig. 10** I-V and P-V characteristic curves of SNU-S1 to SNU-S5

**Table 5** Maximum power, open circuit voltage, short circuit current, fill factor and efficiency values of different scenarios for soft nonuniform temperature variation

| Scenario | MOP (W) | $V_{OC}$ (V) | $I_{SC}$ (A) | F.F. | $\eta$(%) |
|---|---|---|---|---|---|
| SNU-S1 | 1970.40 | 201.78 | 12.518 | 0.780 | 19.80 |
| SNU-S2 | 1949.50 | 201.36 | 12.518 | 0.773 | 19.59 |
| SNU-S3 | 1942.30 | 199.40 | 12.518 | 0.778 | 19.52 |
| SNU-S4 | 1901.60 | 197.70 | 12.521 | 0.768 | 19.11 |
| SNU-S5 | 1865.70 | 194.55 | 12.522 | 0.766 | 18.75 |

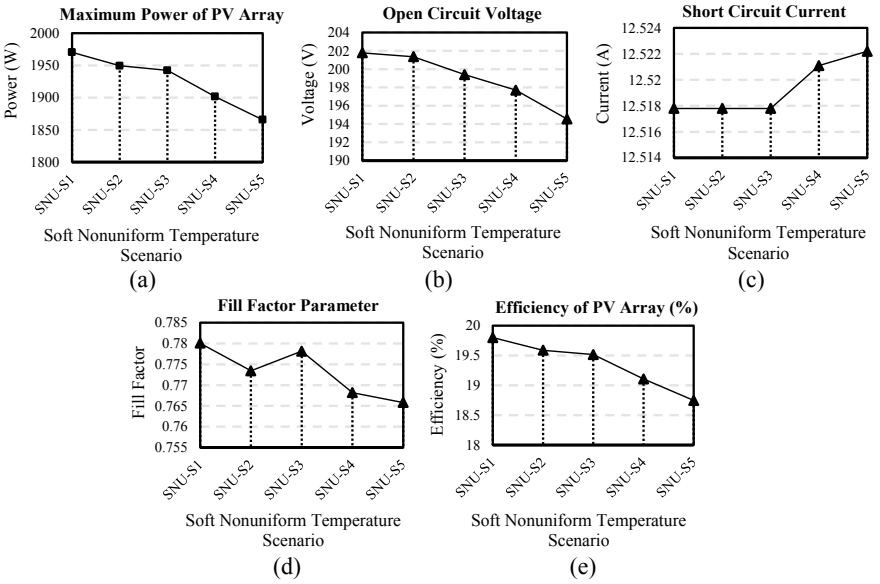


**Fig. 11** **a** Maximum power, **b** open circuit voltage, **c** short circuit current, **d** fill factor and **e** efficiency of the PV array for class C

2. *Hard nonuniform temperature variations (class D):* For class D, 6 scenarios named hard nonuniform scenario (HNU-S1 to HNU-S6) are defined. In this class, both strings will change their temperature and grow up to 50 °C as shown in Fig. 12. The I-V and P-V curves (Fig. 13), numerical value of MOP, $V_{OC}$, $I_{SC}$, F.F. and $\eta$ parameters (Table 6) and these parameters variations (Fig. 14) have shown that effect of temperature variations on the class D parameters is near to class C but with faster slop.

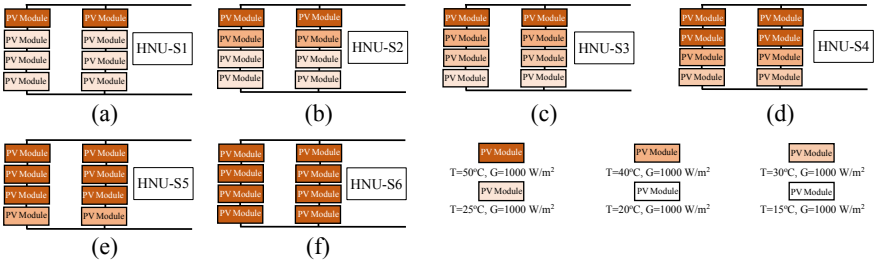


**Fig. 12** Different scenarios for hard nonuniform temperature variations (HNU-S1 to HNU-S6)

## 5 Conclusions

With rising the solar radiation on the PV panel, the temperature of the PV panel will increase. In this paper with simulation the effect of temperature variations on the five parameters of the PV array was studied. These parameters were MOP, $V_{OC}$, $I_{SC}$, F.F. and $\eta$ of the PV array. The results showed that temperature variation has a direct effect on short circuit current of PV array and has a reverse effect on the maximum output power, open circuit voltage, fill factor and efficiency.

In uniform temperature variations, the variations of these five parameters are not too much and I-V and P-V curves have a small change, but in the nonuniform temperature variations, these five PV array parameters have the larger changes than uniform temperature variations. Therefor with increasing the nonuniform temperature variations, the efficiency and output power of PV array will decrease much than uniform temperature changes.

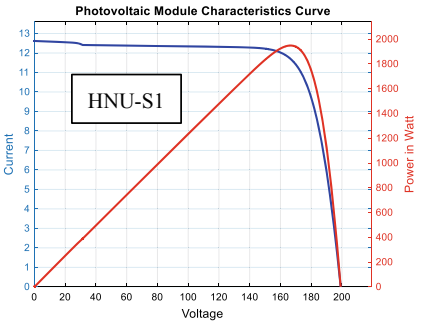


(a). $W_{P1\{S1,\,S2,\,S3,\,S4\}} = 1000$ W/m$^2$, $W_{P2\{S1,\,S2,\,S3,\,S4\}} = 1000$ W/m$^2$, $T_{P1\{S1,\,S2,\,S3,\,S4\}} = \{50, 25, 25, 25\}$ ºC, $T_{P2\{S1,\,S2,\,S3,\,S4\}} = \{50, 25, 25, 25\}$ ºC

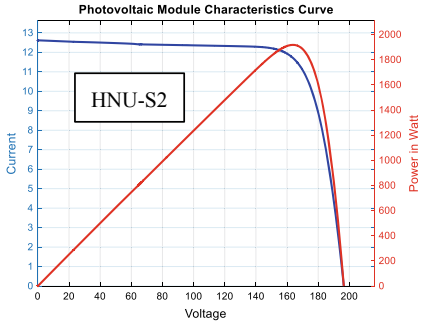


(b). $W_{P1\{S1,\,S2,\,S3,\,S4\}} = 1000$ W/m$^2$, $W_{P2\{S1,\,S2,\,S3,\,S4\}} = 1000$ W/m$^2$, $T_{P1\{S1,\,S2,\,S3,\,S4\}} = \{50, 40, 25, 25\}$ ºC, $T_{P2\{S1,\,S2,\,S3,\,S4\}} = \{50, 40, 25, 25\}$ ºC

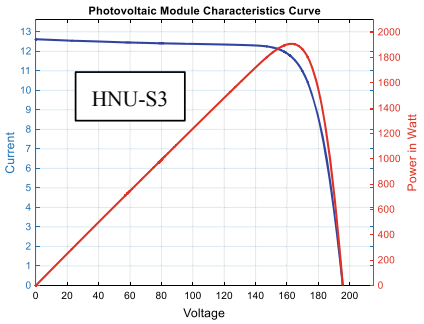


(c). $W_{P1\{S1,\,S2,\,S3,\,S4\}} = 1000$ W/m$^2$, $W_{P2\{S1,\,S2,\,S3,\,S4\}} = 1000$ W/m$^2$, $T_{P1\{S1,\,S2,\,S3,\,S4\}} = \{50, 40, 30, 25\}$ ºC, $T_{P2\{S1,\,S2,\,S3,\,S4\}} = \{50, 40, 30, 25\}$ ºC

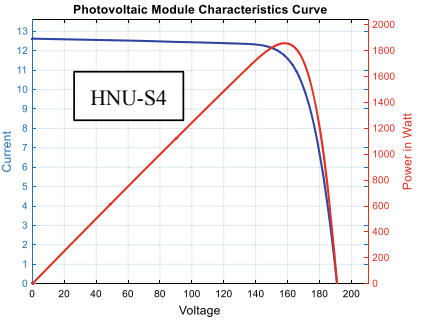


(d). $W_{P1\{S1,\,S2,\,S3,\,S4\}} = 1000$ W/m$^2$, $W_{P2\{S1,\,S2,\,S3,\,S4\}} = 1000$ W/m$^2$, $T_{P1\{S1,\,S2,\,S3,\,S4\}} = \{50, 50, 40, 30\}$ ºC, $T_{P2\{S1,\,S2,\,S3,\,S4\}} = \{50, 50, 40, 30\}$ ºC

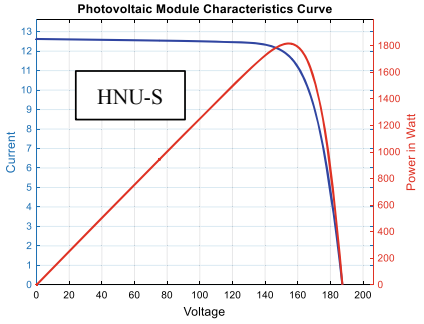


(e). $W_{P1\{S1,\,S2,\,S3,\,S4\}} = 1000$ W/m$^2$, $W_{P2\{S1,\,S2,\,S3,\,S4\}} = 1000$ W/m$^2$, $T_{P1\{S1,\,S2,\,S3,\,S4\}} = \{50, 50, 50, 40\}$ ºC, $T_{P2\{S1,\,S2,\,S3,\,S4\}} = \{50, 50, 50, 40\}$ ºC

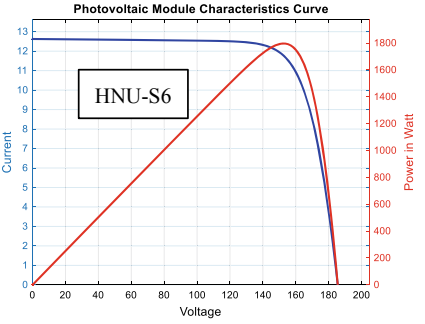


(f). $W_{P1\{S1,\,S2,\,S3,\,S4\}} = 1000$ W/m$^2$, $W_{P2\{S1,\,S2,\,S3,\,S4\}} = 1000$ W/m$^2$, $T_{P1\{S1,\,S2,\,S3,\,S4\}} = \{50, 50, 50, 50\}$ ºC, $T_{P2\{S1,\,S2,\,S3,\,S4\}} = \{50, 50, 50, 50\}$ ºC

**Fig. 13** I-V and P-V characteristic curves of HNU-S1 to HNU-S7 scenarios

**Table 6** MOP, $V_{OC}$, $I_{SC}$, F.F. and $\eta$ values of different scenarios for hard nonuniform temperature variation

| Scenario | MOP (W) | $V_{OC}$ (V) | $I_{SC}$ (A) | F.F. | $\eta$(%) |
|---|---|---|---|---|---|
| HNU-S1 | 1948.60 | 199.68 | 12.621 | 0.7732 | 19.58 |
| HNU-S2 | 1918.30 | 196.50 | 12.621 | 0.7735 | 19.27 |
| HNU-S3 | 1908.20 | 195.69 | 12.621 | 0.7726 | 19.17 |
| HNU-S4 | 1857.50 | 191.21 | 12.628 | 0.7693 | 18.66 |
| HNU-S5 | 1816.60 | 187.87 | 12.630 | 0.7656 | 18.25 |
| HNU-S6 | 1796.30 | 185.84 | 12.631 | 0.7652 | 18.05 |

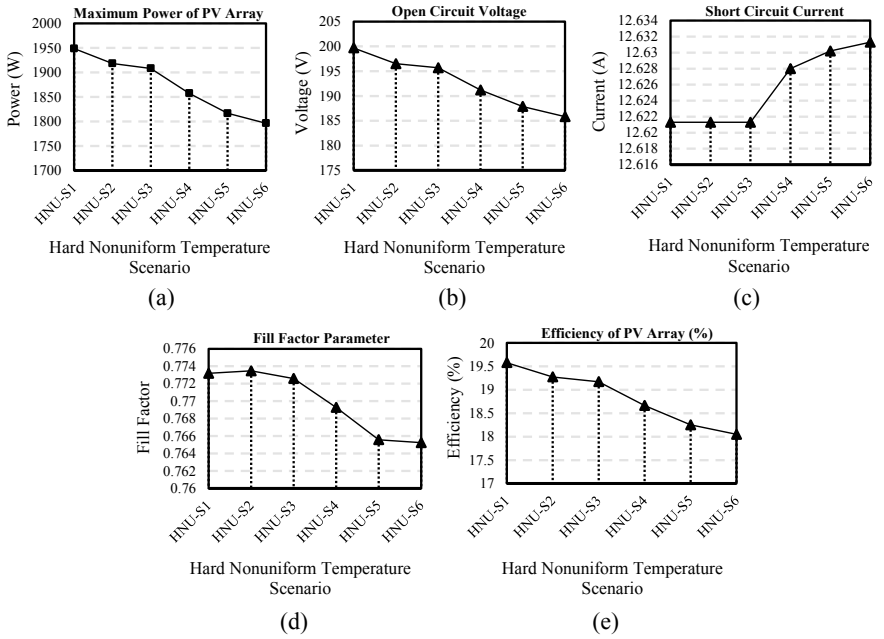


**Fig. 14** **a** Maximum power, **b** open circuit voltage, **c** short circuit current, **d** fill factor and **e** efficiency of the PV array for class D

## References

1. Mughal S, Sood YR, Jarial RK (2018) A review on solar photovoltaic technology and future trends. Int J Sci Res Comput Sci Eng Inf Technol 4:227–235
2. Teo JC, Tan RHG, Mok VH, Ramachandaramurthy VK, Tan C (2018) Impact of partial shading on the P-V characteristics and the maximum power of a photovoltaic string. Energies 11(1860):1–22
3. Fadliondi F, Isyanto H, Budiyanto B (2018) Bypass diodes for improving solar panel performance. Int J Electr Comput Eng 8(5):2703–2708

4. Al Mansur A, Amin Md R, Islam KK (2019) Performance comparison of mismatch power loss minimization techniques in series-parallel PV array configurations. Energies 12(874)
5. Goss B, Cole I, Betts T, Gottschalg R (2014) Irradiance modelling for individual cells of shaded solar photovoltaic arrays. Sol Energy 110:410–419
6. Patel H, Agarwal V (2008) MATLAB-based modeling to study the effects of partial shading on PV array characteristics. IEEE Trans Energy Convers 23(1)
7. Mandadapu U, Vedanayakam SV, Thyagarajan K (2017) Effect of temperature and irradiance on the electrical performance of a PV module. Int J Adv Res 5(3):2018–2027
8. Bikaneria J, Joshi SP, Joshi AR (2013) Modeling and simulation of PV cell using one-diode model. Int J Sci Res Publ 3(10)
9. Davies L, Thornton R, Hudson P, Ray B (2018) Automatic detection and characterization of partial shading in PV system. In: IEEE 7th world conference on photovoltaic energy conversion, HI, 10–15 June 2018

# Effects of PV Module Shading on the Efficiency of the PV Array


**Gholamreza Farahani**

**Abstract** Among the renewable energies, solar energy is an important source due to the easy access to it. One weakness of the photovoltaic (PV) system is achieving the maximum efficiency of the system. The PV cell is the essential part of PV system for power conversion. The maximum output power of PV cell reduces when it exposes to shading because of lack of solar insolation. In this paper, PV modules under several shading conditions using Matlab/Simulink software are simulated. The uniform and nonuniform shading of PV modules are considered in the simulation. Results have shown that the power-voltage (P-V) and current-voltage (I-V) characteristic of PV modules will change under shading but P-V and I-V characteristic curves for nonuniform shading have several local maximum power points (MPP). Therefore, nonuniform shading is more complicated than uniform shading but in both uniform and nonuniform conditions, the PV array efficiency noticeably will decrease and its relation with severity of shading is nonlinear and is not monotonically decreasing.

**Keywords** Nonuniform shading · Uniform shading · Partial shading · PV · MPP

## Abbreviations

| | |
|---|---|
| F.F. | Fill Factor |
| $I_{SC}$ | Short Circuit Current |
| I-V | Current-Voltage |
| MOP | Maximum Output Power |
| MPP | Maximum Power Point |
| MPPT | Maximum Power Point Tracking |
| PV | PhotoVoltaic |

G. Farahani (✉)
Department of Electrical Engineering and Information Technology, Iranian Research Organization for Science and Technology, Tehran, Iran
e-mail: farahani.gh@irost.org



F. Shahnia and S. Deilami (eds.), *ICPES 2019*, Lecture Notes in Electrical Engineering 669, https://doi.org/10.1007/978-981-15-5374-5_3

P-V Power-Voltage
STC Standard Condition
$V_{OC}$ Open Circuit Voltage

## 1 Introduction

Nowadays, solar energy as a clean and renewable source that can be used because of environmental problems of humanity life. In the world, there is many places that they have good condition for sun radiation, therefore this condition make them suitable to use for photovoltaic (PV) arrays. However, the PV arrays will affect by two main parameters that are temperature and solar irradiation. When the panels are in the shadow, their performance will change [1]. Shading that wholly or partially is caused by moving clouds, trees, adjacent buildings, towers or other PV panels during the day affects the cell temperature and the incident solar radiation [2].

PV arrays characterized by their nonlinear current voltage (I-V) and power-voltage (P-V) curves. With changes in the environmental conditions, these curves will change that is one of the main challenges in the PV arrays, and it becomes more complicated when the PV arrays perch in nonuniform irradiance such as partial shadow conditions [3]. Investigators are trying to optimize the usage of PV system because of high initial cost [4]. Although improving the PV cell efficiency and fabrication are essential issues, the improvement of the overall performance of the PV system has the same importance.

Shading will reduce the PV array output power and also causes a safety hazard. Under partially shaded conditions, because of the existence of multiple maxima in the P-V and I-V curves, it makes the PV array characteristics more complicated. The main problem in multiple maxima in the P-V and I-V curves is in the reduction of the PV efficiency at the maximum power point tracking (MPPT) systems that weakness of these tracking systems is the inability to differentiate between the local and global peaks, therefore the output power will reduce [5]. Understanding the shading effects on the efficiency of PV arrays is important as it leads to better design and obtain better power from PV panels. During the years, many researchers considered the PV arrays characteristics and the impact of many factors on the PV array efficiency [6]. However, each researcher has considered some limitation and hypothesis to study the shadow effect on the PV array efficiency. In this paper, the effect of shading is considered as the uniform and nonuniform on the PV panels. Therefore, different scenarios are considered and effect of different irradiance on the series, parallel and series-parallel PV panels with certain temperature is studied.

## 2 PV Equivalent Model

PV panel consists of solar cell stacks. The duty of solar cells is to turn light into electricity. The equivalent circuit of solar cell is shown in Fig. 1. The I-V characteristic of diode $D$ can be described by the Shockley diode as (1).

$$I_D = I_0 \times [\exp(V_d / nV_T) - 1] \tag{1}$$

where $I_D$ is diode current (A), $V_d$ is diode voltage (V), $I_0$ is diode saturation current (A), $n$ is the ideality factor of the diode D and $V_T$ is temperature voltage and will calculate as (2):

$$V_T = k \times T/q \tag{2}$$

where $T$ is cell temperature ($K$), $k = 1.3806 \times 10^{-23}$ J/k is Boltzman constant and $q = 1.6022 \times 10^{-19}$ C is electron charge. Solar cell model consists of a diode, a photo current ($I_L$), a series resistor ($R_S$), and a shunt resistor ($R_{SH}$) (Fig. 1). The current at the terminal of the solar cell is formulated as (3) [7]:

$$I = I_L - I_0\left[\exp\left(q\frac{(V + I.R_S)}{k.T.n}\right) - 1\right] - \frac{V + I.R_S}{R_{SH}} \tag{3}$$

In the simple model of PV cell, $R_S$ =0 and $R_{SH} = \infty$ that is impossible practically. Researches are work to reduce the effects of the series and shunt resistance in PV cells. Because of low power of one PV cell, to get larger output power, PV cells will connect in series and parallel to make a PV module. Also PV modules will connect in series and parallel arrangement to make a PV array. The capacity of PV cell can be estimated by cell efficiency and fill factor (F.F.) parameters. The PV cell efficiency is defined as the ratio of peak power output to input solar power and is calculated as (4).

$$\eta(\%) = \frac{V_{mp} \times I_{mp}}{G \times A} \times 100 \tag{4}$$

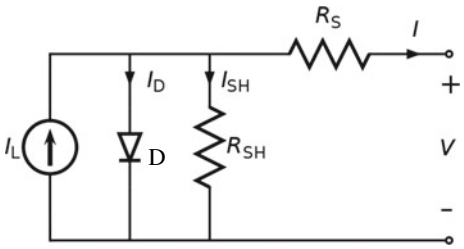


**Fig. 1** Equivalent circuit of a PV cell

where $V_{mp}$ is the voltage at peak power, $I_{mp}$ is the current at peak power, $G$ is the solar intensity per square meter and $A$ is the area on which solar radiation falls. If the PV cell delivers maximum power for the right combination of environmental conditions of irradiance and temperature, then the efficiency will become highest [8]. The fill factor estimate using the (5).

$$F.F. = \frac{V_{mp} \times I_{mp}}{I_{sc} \times V_{oc}} \tag{5}$$

where $V_{OC}$ is the open circuit voltage and $I_{SC}$ is the short circuit current. The fill factor of a PV panel is an important performance indicator. Although fill factor parameter physically unrealizable, an ideal PV panel should have a perfectly rectangular I-V curve such that the maximum power point (MPP) coincided with ($I_{SC}$, $V_{OC}$).

## 3 Effects of Shadow on PV Array

There are many parameters that effect on the PV array output power. One of these parameter is solar insolation changes on the PV modules which its main reason is shading [9]. In this paper, different condition of shading on the PV arrays will discuss that may occur due to shadows of different objects such as trees, clouds, building or other PV panels.

The P-V curve of PV array at standard condition (STC) (irradiance = 1000 W/m$^2$, temperature = 25 °C) exhibits nonlinear with one MPP, but with changing isolation conditions because of shading, P-V curve will have more MPP. Under partial shading conditions, in the series structure, a uniform current will pass in each cell, thus the shaded cells should run in reverse biasing and bypass diode will turn to have equal current that decrease the value of MPP [10].

The usage of bypass diodes will change the characteristic of the PV array. With use of bypass diode, under partial shading conditions, many local MPP will create. The bypass diode will create a short circuit around the shaded cells that allow the shaded cells to follow current from unshaded cells, thus heating and array current loss will reduce. In this paper, with use of Matlab/Simulink software, characteristic curves of PV arrays under different shading circumstances are investigated.

## 4 Simulation

In simulation, 8 PV modules are used. These modules are connected in series and parallel configuration as shown in Fig. 2. According to Fig. 2, the output voltage of PV system is connected to the voltage source to simulate the output voltage of PV array.

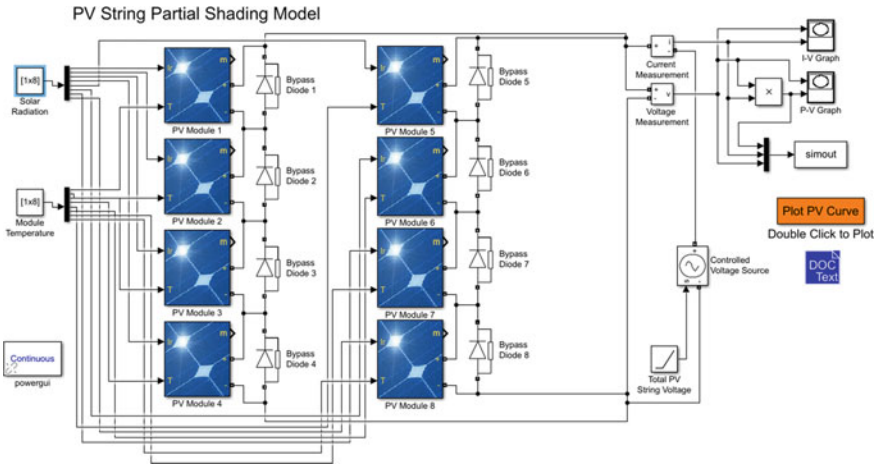


**Fig. 2** The simulink block diagram of the PV array in different shading conditions

**Table 1** Module data

| Name | Value |
|---|---|
| Module manufacture | SunPower |
| Module type | SPR-X20-250-BLK |
| Maximum power (W) | 249.952 |
| Open circuit voltage ($V_{OC}$) (V) | 50.93 |
| Voltage at maximum power point $V_{mp}$ (V) | 42.8 |
| Temperature coefficient of $V_{OC}$ (%/°C) | −0.35602 |
| Cells per module ($N_{\text{cell}}$) | 72 |
| Short-circuit current ($I_{SC}$) (A) | 6.2 |
| Current at maximum power point ($I_{mp}$) (A) | 5.84 |
| Temperature coefficient of $I_{SC}$ (%/°C) | 0.07 |
| Parallel strings | 1 |
| Series-connected modules per string | 1 |

**Table 2** PV cell model parameters

| Parameter | Value |
|---|---|
| Light-generated current ($I_L$) (A) | 6.2073 |
| Diode saturation current ($I_0$) (A) | $1.8536e^{-10}$ |
| Diode ideality factor | 1.1367 |
| Shunt resistance ($R_{SH}$) (Ω) | 621.2034 |
| Series resistance ($R_S$) (Ω) | 0.301 |

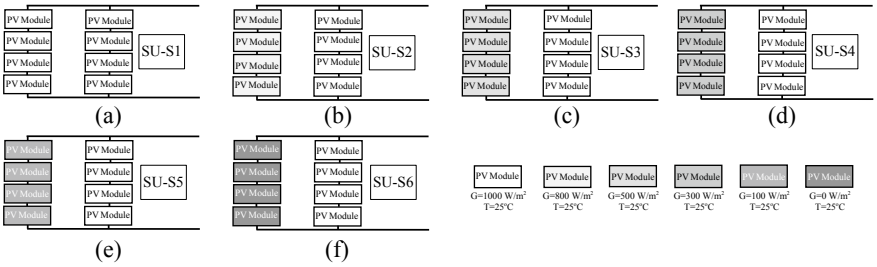


**Fig. 3** Different scenarios for soft uniform shading (SU-S1 to SU-S6)

Each module receives the numerical irradiance and temperature. The used PV cells in the simulation are mono-crystalline PV cells. Table 1 illustrates the characteristics of the studied PV module. Table 2 illustrates the PV cell model parameters. In the simulation, different scenarios for uniform and nonuniform shading have been considered.

1. *Effect of uniform shading on the characteristics of PV array*

In this section, two types of uniform shading will be investigated. In the soft uniform shading, only one PV string have the shadow but in the hard uniform shading, both strings will be shaded.

(a) *Soft uniform shading:* In simulation, for soft uniform shading condition, six scenarios have been designed and named soft uniform-scenario (SU-S1 to SU-S6). In Fig. 3, these six scenarios are shown schematically. SU-S1 is under STC, but in the other scenarios, the half of the PV modules experience shading and others are in the STC. As it is clear from Fig. 4, by increasing the severity of soft uniform shading (SU-S1 to SU-S6), the maximum output power (MOP) will decrease but fortunately there is just one MPP. Therefore, finding this MPP is easier than more local and global MPPs together (In the next subsection will happen with nonuniform shading).

The numerical values of other PV array parameters include $V_{OC}$, $I_{SC}$, F.F. and efficiency ($\eta$) are listed at Table 3. In Fig. 5, the results of uniform irradiance on the PV array parameters are shown MOP (Fig. 5a) parameter reduces linearity with reduction of irradiance but value reduction of the other parameters include $V_{OC}$ (Fig. 5b), $I_{SC}$ (Fig. 5c) and $\eta$ (Fig. 5e) is not linear. All of the parameters will decrease with increasing the severity of soft uniform shading except the F.F. parameter (Fig. 5d) which is reverse. Also the slop variations of F.F. parameter is not always positive and there is fluctuation on this parameter while the slop variations in other parameters is always negative.

(b) *Hard uniform shading:* In the Fig. 6, four different scenarios for hard uniform shading (HUS1-HU-S4) is shown. In the hard uniform shading, all PV modules have a same irradiance reduction for shading. Therefore, in comparison to the

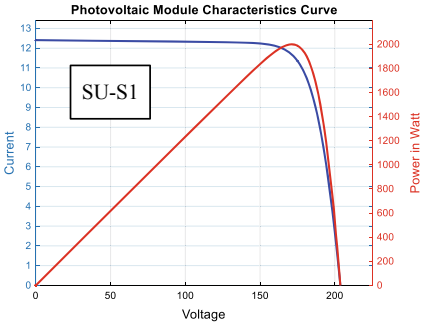


(a). $W_{P1\{S1, S2, S3, S4\}}$ =1000W/m$^2$,
$W_{P2\{S1, S2, S3, S4\}}$ =1000W/m$^2$,
$T_{P1\{S1, S2, S3, S4\}}$ =25ºC, $T_{P2\{S1, S2, S3, S4\}}$ =25ºC

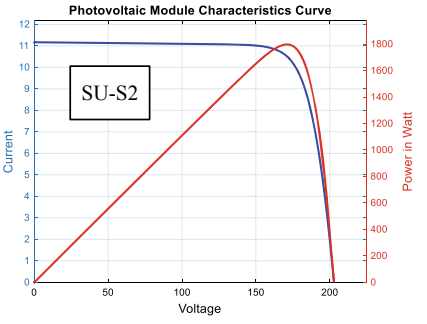


(b). $W_{P1\{S1, S2, S3, S4\}}$ =800W/m$^2$,
$W_{P2\{S1, S2, S3, S4\}}$ =1000W/m$^2$,
$T_{P1\{S1, S2, S3, S4\}}$ =25ºC, $T_{P2\{S1, S2, S3, S4\}}$ =25ºC

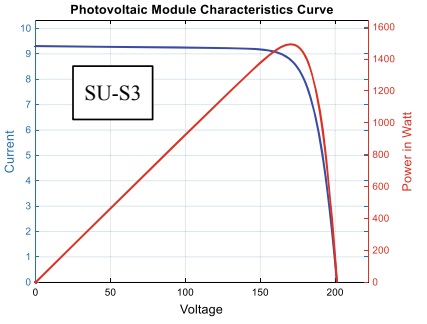


(c). $W_{P1\{S1, S2, S3, S4\}}$ =500W/m$^2$,
$W_{P2\{S1, S2, S3, S4\}}$ =1000W/m$^2$,
$T_{P1\{S1, S2, S3, S4\}}$ =25ºC, $T_{P2\{S1, S2, S3, S4\}}$ =25ºC

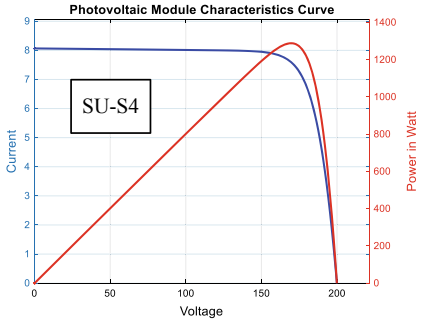


(d). $W_{P1\{S1, S2, S3, S4\}}$ =300W/m$^2$,
$W_{P2\{S1, S2, S3, S4\}}$ =1000W/m$^2$,
$T_{P1\{S1, S2, S3, S4\}}$ =25ºC, $T_{P2\{S1, S2, S3, S4\}}$ =25ºC

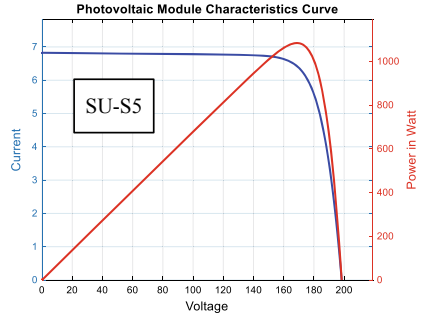


(h). $W_{P1\{S1, S2, S3, S4\}}$ =100W/m$^2$,
$W_{P2\{S1, S2, S3, S4\}}$ =1000W/m$^2$,
$T_{P1\{S1, S2, S3, S4\}}$ =25ºC, $T_{P2\{S1, S2, S3, S4\}}$ =25ºC

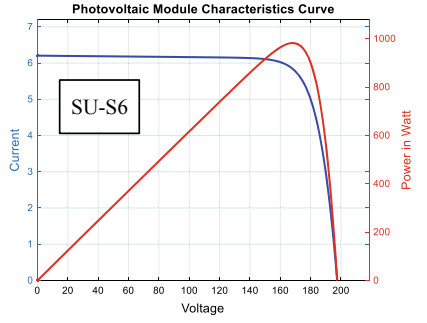


(j) $W_{P1\{S1, S2, S3, S4\}}$ =0W/m$^2$,
$W_{P2\{S1, S2, S3, S4\}}$ =1000W/m$^2$,
$T_{P1\{S1, S2, S3, S4\}}$ =25ºC, $T_{P2\{S1, S2, S3, S4\}}$ =25ºC

**Fig. 4** I-V and P-V characteristic curves of SU-S1 to SU-S6

**Table 3** Maximum power, open circuit voltage, short circuit current, fill factor and efficiency values of different scenarios for soft uniform shading

| Scenario | MOP (W) | $V_{OC}$ (V) | $I_{SC}$ (A) | F.F. | $\eta$ (%) |
|---|---|---|---|---|---|
| SU-S1 | 1999.60 | 205.71 | 12.41 | 0.783 | 20.09 |
| SU-S2 | 1797.50 | 203.14 | 11.17 | 0.792 | 40.13 |
| SU-S3 | 1492.30 | 202.67 | 9.31 | 0.791 | 39.98 |
| SU-S4 | 1288.20 | 200.71 | 8.07 | 0.795 | 39.82 |
| SU-S5 | 1084.00 | 198.59 | 6.83 | 0.799 | 39.61 |
| SU-S6 | 982.05 | 198.75 | 6.21 | 0.796 | 39.47 |

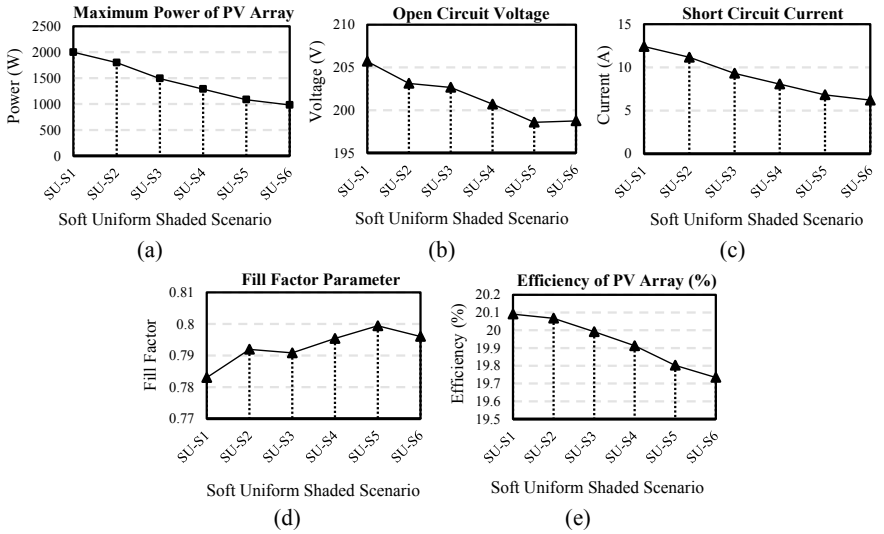


**Fig. 5** **a** Maximum power, **b** open circuit voltage, **c** short circuit current, **d** fill factor and **e** efficiency of PV array under soft uniform shading

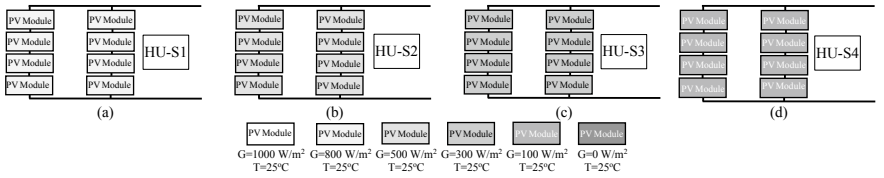


**Fig. 6** Four different scenarios for hard uniform shading

soft uniform shading (Fig. 4), the MOP will reduce dramatically than soft uniform shading (Fig. 7). The MOP, $V_{OC}$, $I_{SC}$, F.F. and\$eta$ values of hard uniform shading for different scenarios are shown in Table 4.

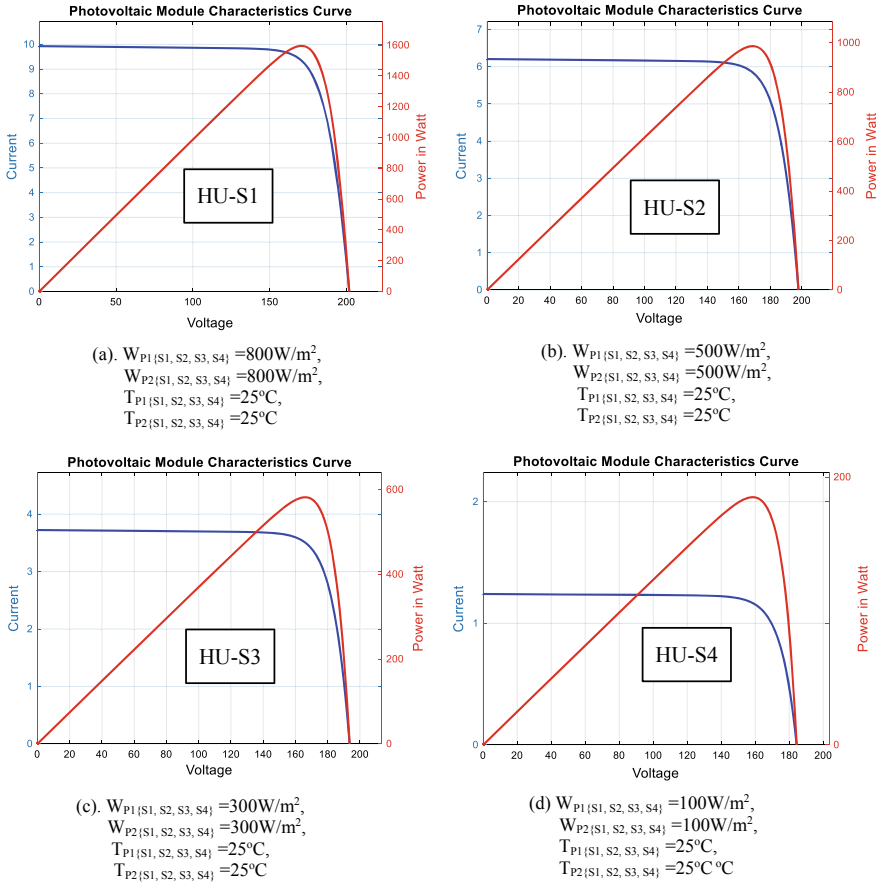


(a). $W_{P1\{S1, S2, S3, S4\}}$ =800W/m$^2$, $W_{P2\{S1, S2, S3, S4\}}$ =800W/m$^2$, $T_{P1\{S1, S2, S3, S4\}}$ =25°C, $T_{P2\{S1, S2, S3, S4\}}$ =25°C

(b). $W_{P1\{S1, S2, S3, S4\}}$ =500W/m$^2$, $W_{P2\{S1, S2, S3, S4\}}$ =500W/m$^2$, $T_{P1\{S1, S2, S3, S4\}}$ =25°C, $T_{P2\{S1, S2, S3, S4\}}$ =25°C

(c). $W_{P1\{S1, S2, S3, S4\}}$ =300W/m$^2$, $W_{P2\{S1, S2, S3, S4\}}$ =300W/m$^2$, $T_{P1\{S1, S2, S3, S4\}}$ =25°C, $T_{P2\{S1, S2, S3, S4\}}$ =25°C

(d) $W_{P1\{S1, S2, S3, S4\}}$ =100W/m$^2$, $W_{P2\{S1, S2, S3, S4\}}$ =100W/m$^2$, $T_{P1\{S1, S2, S3, S4\}}$ =25°C, $T_{P2\{S1, S2, S3, S4\}}$ =25°C °C

**Fig. 7** I-V and P-V characteristic curves of PV array under hard uniform shading

**Table 4** MOP, $V_{OC}$, $I_{SC}$, F.F. and $\eta$ values of different scenarios for hard uniform shading

| Scenario | MOP (W) | $V_{OC}$ (V) | $I_{SC}$ (A) | F.F. | $\eta$ (%) |
|---|---|---|---|---|---|
| HU-S1 | 1595.00 | 203.29 | 9.93 | 0.790 | 20.03 |
| HU-S2 | 986.49 | 197.96 | 6.21 | 0.803 | 19.82 |
| HU-S3 | 582.01 | 194.62 | 3.72 | 0.803 | 19.49 |
| HU-S4 | 184.00 | 184.45 | 1.24 | 0.804 | 18.49 |

The curves for different parameter of PV array for four hard uniform shading are shown in Fig. 8. According to Fig. 8, the variation of MOP and $I_{SC}$ have linear relation with severity of the hard uniform shading approximately but other parameters include $V_{OC}$, F.F. and $\eta$ have a nonlinear relation with hard uniform shading. $V_{OC}$

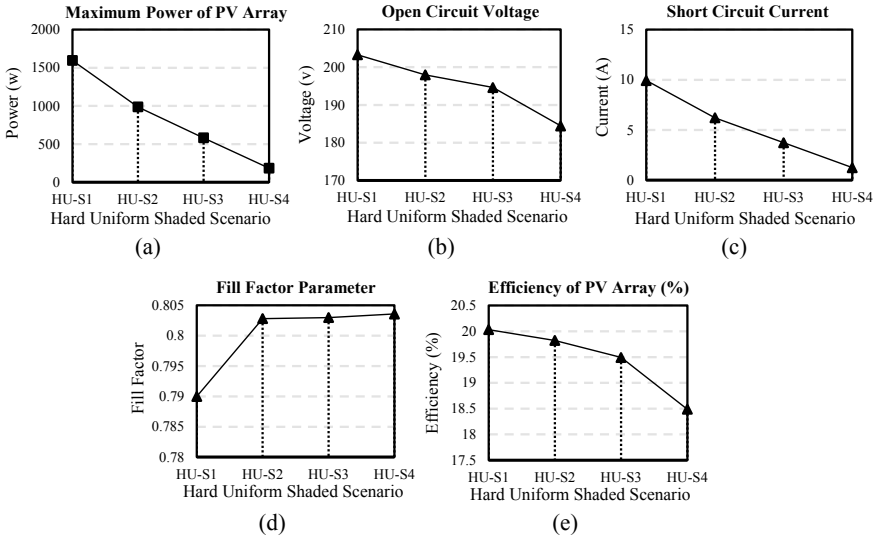


**Fig. 8** **a** Maximum power, **b** open circuit voltage, **c** short circuit current, **d** fill factor and **e** efficiency of PV array under hard uniform shading

and F.F. are always decreasing and increasing respectively in spite of the soft uniform shading.

2. *Effect of nonuniform shading on the characteristics of PV Array*

In this section, two types of nonuniform shading is described. The soft and hard nonuniform shading. In the soft nonuniform shading, just one PV string will change its irradiance but in hard nonuniform shading, both PV strings will change their irradiance and there is a more nonuniformity in the hard nonuniform shading than soft nonuniform shading.

(a) *Soft nonuniform shading:* In this subsection, the three scenarios for soft nonuniform shading (SNU-S1 to SNU-3) will be described. As shown in Fig. 9, the PV modules in one string have a different shading and therefore each PV module will produce different current.

Figure 10 shows the **I-V** and **P-V** characteristic curves of the soft nonuniform shading for these three scenarios. As it is clear from Fig. 10, in the nonuniform

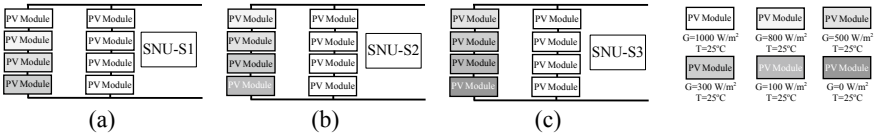


**Fig. 9** Different soft nonuniform shading scenarios

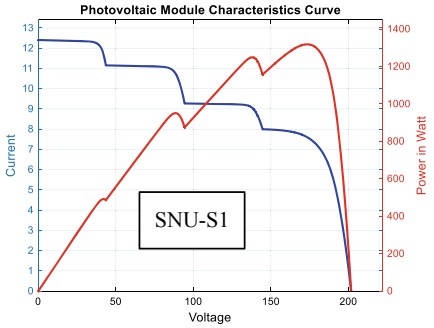


a). $W_{P1\{S1, S2, S3, S4\}}$ = {1000, 800, 500, 300} W/m$^2$, $W_{P2\{S1, S2, S3, S4\}}$ =1000W/m$^2$, $T_{P1\{S1, S2, S3, S4\}}$ =25ºC, $T_{P2\{S1, S2, S3, S4\}}$ =25ºC

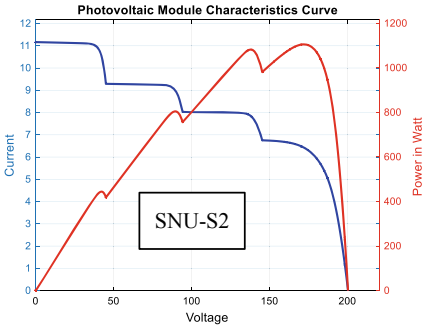


b). $W_{P1\{S1, S2, S3, S4\}}$ = {800, 500, 300, 100} W/m$^2$, $W_{P2\{S1, S2, S3, S4\}}$ =1000W/m$^2$, $T_{P1\{S1, S2, S3, S4\}}$ =25ºC, $T_{P2\{S1, S2, S3, S4\}}$ =25ºC

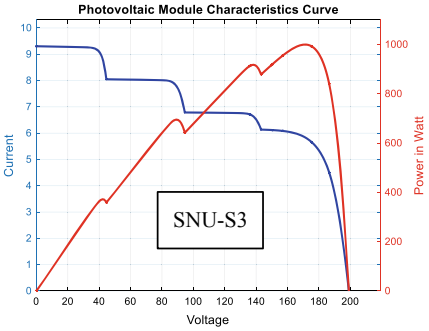


c). $W_{P1\{S1, S2, S3, S4\}}$ = {500, 300, 100, 0} W/m$^2$, $W_{P2\{S1, S2, S3, S4\}}$ =1000W/m$^2$, $T_{P1\{S1, S2, S3, S4\}}$ =25ºC, $T_{P2\{S1, S2, S3, S4\}}$ =25ºC

**Fig. 10** I-V and P-V characteristic curves of soft nonuniform shading

shading, there are more than one peak on the I-V and P-V curves that one of them is global and others are local. Thus, finding the global maximum power point is the challenging subject between researches.

Table 5, shows the numerical values of different PV array parameters includes MOP, $V_{OC}$, $I_{SC}$, F.F. and $\eta$ for these three scenarios. Figure 11 illustrates curves for variations of MOP, $V_{OC}$, $I_{SC}$, F.F. and $\eta$ parameters with soft nonuniform shading.

**Table 5** MOP, $V_{OC}$, $I_{SC}$, F.F. and $\eta$ values of different scenarios for soft nonuniform shading

| Scenario | MOP (W) | $V_{OC}$ (V) | $I_{SC}$ (A) | F.F. | $\eta$ (%) |
|---|---|---|---|---|---|
| SNU-S1 | 1318.40 | 201.97 | 12.41 | 0.526 | 16.06 |
| SNU-S2 | 1105.60 | 200.48 | 11.17 | 0.494 | 15.59 |
| SNU-S3 | 999.77 | 199.32 | 9.31 | 0.539 | 16.40 |

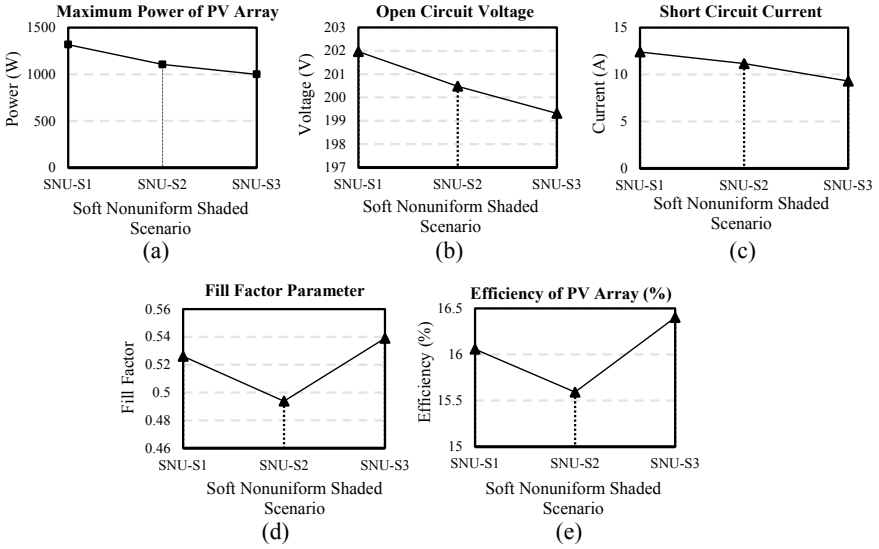


**Fig. 11** **a** MOP, **b** $V_{OC}$, **c** $I_{SC}$, **d** F.F. and **e** $\eta$ of PV array under soft nonuniform shading

Based on the Fig. 11, the MOP, $V_{OC}$ and $I_{SC}$ are decreasing with increasing soft nonuniform shading on the PV modules and approximately linear but other parameters are nonlinear with soft nonuniform shading and are not decreasing monotonically.

(b) *Hard nonuniform shading:* In hard nonuniform shading, seven scenarios have been considered and named hard nonuniform shading (HNU-S1 to HNU-S7). In these scenarios, the shading will happen on the both strings simultaneously as shown in Fig. 12. Therefore, the effect of this type of shading is too much than soft nonuniform shading. The hard nonuniform shading has many maxima in P-V curve in spite of uniform shading (Fig. 13). Thus finding the global maximum power point in this condition is too hard. Also in hard nonuniform

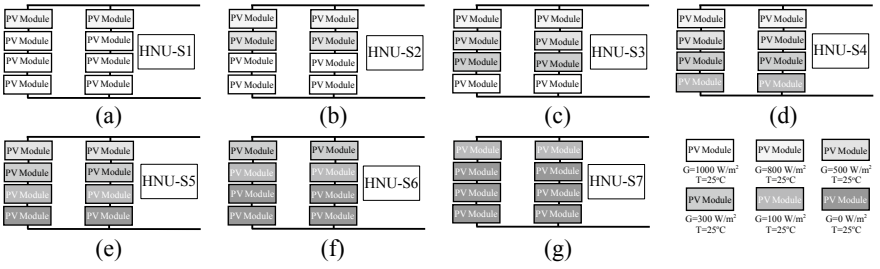


**Fig. 12** Different hard nonuniform shading scenarios

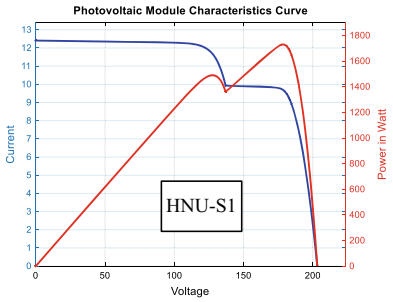


a). $W_{P1\{S1, S2, S3, S4\}}$ = {800, 1000, 1000, 1000} W/m$^2$, $W_{P2\{S1, S2, S3, S4\}}$ = {800, 1000, 1000, 1000} W/m$^2$, $T_{P1\{S1, S2, S3, S4\}}$ =25ºC, $T_{P2\{S1, S2, S3, S4\}}$ =25ºC

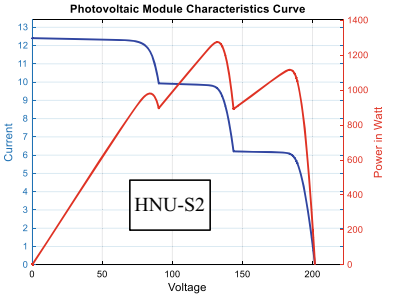


b) $W_{P1\{S1, S2, S3, S4\}}$ = {800, 500, 1000, 1000} W/m$^2$, $W_{P2\{S1, S2, S3, S4\}}$ = {800, 500, 1000, 1000} W/m$^2$, $T_{P1\{S1, S2, S3, S4\}}$ =25ºC, $T_{P2\{S1, S2, S3, S4\}}$ =25ºC

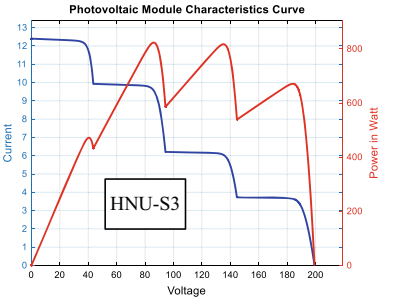


c) $W_{P1\{S1, S2, S3, S4\}}$ = {800, 500, 300, 1000} W/m$^2$, $W_{P2\{S1, S2, S3, S4\}}$ = {800, 500, 300, 1000} W/m$^2$, $T_{P1\{S1, S2, S3, S4\}}$ =25ºC, $T_{P2\{S1, S2, S3, S4\}}$ =25ºC

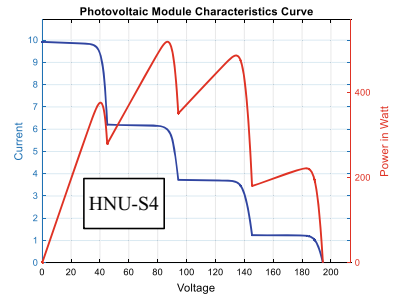


d). $W_{P1\{S1, S2, S3, S4\}}$ = {800, 500, 300, 100} W/m$^2$, $W_{P2\{S1, S2, S3, S4\}}$ = {800, 500, 300, 100} W/m$^2$, $T_{P1\{S1, S2, S3, S4\}}$ =25ºC, $T_{P2\{S1, S2, S3, S4\}}$ =25ºC

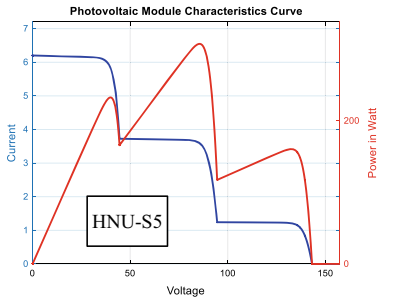


e). $W_{P1\{S1, S2, S3, S4\}}$ = {500, 300, 100, 0} W/m$^2$, $W_{P2\{S1, S2, S3, S4\}}$ = {500, 300, 100, 0} W/m$^2$, $T_{P1\{S1, S2, S3, S4\}}$ =25ºC, $T_{P2\{S1, S2, S3, S4\}}$ =25ºC

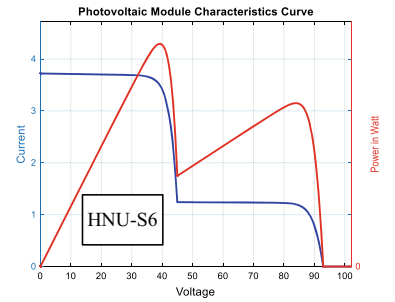


f) $W_{P1\{S1, S2, S3, S4\}}$ = {300, 100, 0, 0} W/m$^2$, $W_{P2\{S1, S2, S3, S4\}}$ = {300, 100, 0, 0} W/m$^2$, $T_{P1\{S1, S2, S3, S4\}}$ =25ºC, $T_{P2\{S1, S2, S3, S4\}}$ =25ºC

**Fig. 13** I-V and P-V characteristic curves of HNU-S1 to HNU-S7 scenarios

**Fig. 13** (continued)

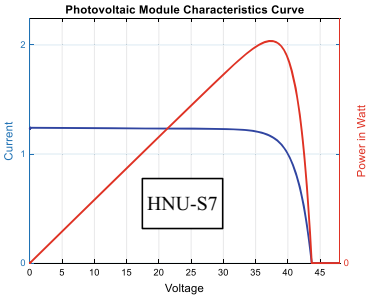


g) $W_{P1\{S1, S2, S3, S4\}} = \{100, 0, 0, 0\}$ W/m$^2$, $W_{P2\{S1, S2, S3, S4\}} = \{100, 0, 0, 0\}$ W/m$^2$, $T_{P1\{S1, S2, S3, S4\}}$ =25°C, $T_{P2\{S1, S2, S3, S4\}}$ =25°C

**Table 6** MOP, $V_{OC}$, $I_{SC}$, F.F. and $\eta$ values of different scenarios for hard nonuniform shading

| Scenario | MOP (W) | $V_{OC}$ (V) | $I_{SC}$ (A) | F.F. | $\eta$ (%) |
|---|---|---|---|---|---|
| HNU-S1 | 1730.00 | 203.25 | 12.41 | 0.686 | 18.30 |
| HNU-S2 | 1275.50 | 201.80 | 12.41 | 0.509 | 15.53 |
| HNU-S3 | 823.22 | 199.31 | 12.40 | 0.333 | 12.73 |
| HNU-S4 | 519.65 | 194.48 | 9.92 | 0.269 | 12.29 |
| HNU-S5 | 307.50 | 143.17 | 6.20 | 0.346 | 13.73 |
| HNU-S6 | 137.09 | 92.90 | 3.72 | 0.397 | 13.77 |
| HNU-S7 | 43.45 | 43.70 | 1.24 | 0.802 | 17.46 |

shading, the MOP will intensely drop and therefore the efficiency of the PV array will fall significantly (Table 6).

In Fig. 14 the curves for variations of MOP, $V_{OC}$, $I_{SC}$, F.F. and $\eta$ parameters under hard nonuniform shading are shown.

According to Fig. 13a–g, it is clear that the structure of I-V and P-V curves become more complicated with hard nonuniform shading effects where several local MPP and one global MPP appear. Also nonuniform shading will cause a large reduction on the MOP of PV array that does not comparable with the output power of uniform shading.

Based on Fig. 14, the MOP and $V_{OC}$ are always decreasing while $I_{SC}$, F.F. and $\eta$ have a different slop during the changes of hard nonuniform shading severity on the PV modules.

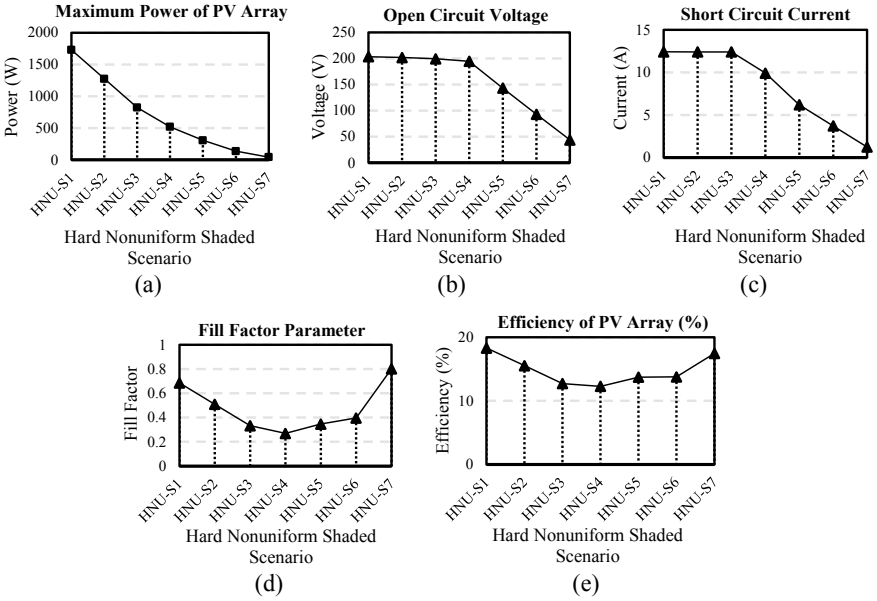


**Fig. 14** **a** MOP, **b** $V_{OC}$, **c** $I_{SC}$, **d** F.F. and **e** $\eta$ of PV array under hard nonuniform shading

## 5 Conclusions

In this paper, the effects of the four different shading conditions include soft/hard uniform and soft/hard nonuniform shading with predefined scenarios on the PV modules parameters are investigated. Simulation are carried out in Matlab/Simulink software. For the simulation, the data from SunPower SPR-X20-250-BLK panel are extracted. The results are shown that the MOP in all shading condition have a negative slop with increasing the shading severity but other $V_{OC}$, $I_{SC}$, F.F. and $\eta$ parameters have not always positive/negative slop in all condition. Also nonuniform shading conditions on the PV array makes the output power curve more complex with the existence of multiple local MPPs instead of unique MPP in the case of uniform shading.

## References

1. Djalab A, Rezaoui MM, Bessous N, Merzouk I (2018) Study of the effects of partial shading on PV array. In: International conference on communications and electrical engineering, Babel Oued Alger, Algeria, 17–18 Dec 2018
2. Bimenyimana S, Asemota GNO, Kemunto MC, Li L (2017) Shading effects in photovoltaic modules: Simulation and experimental results. In: 2nd international conference on power and renewable energy, Chengdu, China, 20–23 Sep 2017

3. Jena D, Ramana VV (2015) Modeling of photovoltaic system for uniform and non-uniform irradiance: a critical review. Renew Sust Energy Rev 52:400–417
4. Gioutsos DM, Blok K, van Velzen L, Moorman S (2018) Cost-optimal electricity systems with increasing renewable energy penetration for islands across the globe. Appl Energy 226:437–449
5. Gosumbonggot J, Fujita G (2019) Partial shading detection and global maximum power point tracking algorithm for photovoltaic with the variation of irradiation and temperature. Energies 12
6. Yi T, Tong L, Qiu M, Liu J (2019) Analysis of driving factors of photovoltaic power generation efficiency: a case study in China. Energies 12
7. Tamrakar V, Gupta SC, Sawle Y (2015) Single-diode PV cell modeling and study of characteristics of single and two-diode equivalent circuit. Electr Electron Eng Int J 4(3):13–24
8. Zhang L, Yu SS, Fernando T, Iu HH-C, Wong KP (2019) An online maximum power point capturing technique for high-efficiency power generation of solar photovoltaic systems. J Mod Power Syst Clean Energy 7(2):357–368
9. Kumar VR, Singh SK (2018) Solar photovoltaic modeling and simulation: as a renewable energy solution. Energy Rep 4:701–712
10. Islam H, Mekhilef S, Shah NBM, Soon TK, Seyedmahmousian M, Horan B, Stojcevski A (2018) Performance evaluation of maximum power point tracking approaches and photovoltaic systems. Energies 11

# Grid Inertia Reconfiguration Strategy and Tech Solution Suggestions for South Australia Blackouts


**Jianlong Bai**

**Abstract** This paper delivers a unique strategy—inertia re-configuration, and provides viable tech schemes of innovation to solve the blackouts, especially like that frequently happen in South Australia due to wind power. Flywheel will directly participate in grid stabilization, but not be only an energy storage device any more. Confidently, new energy will become the main power of state grid in the future.

**Keywords** Inertia · Strategy · Suggestion · Blackout · Flywheel

## 1 Introduction

Carbon emission is a focal issue nowadays. New energy is expected to become the major power in grid or substitute carbonaceous fossil energy. But the former, such as wind, solar, is much less continuous, controllable and steady than the latter. It is hesitating to full use for safety of power consumption. A significant case is the blackout in South Australia (SA) on Sep. 28, 2016. Reliability and safety of the new energy to grid will have to be solved if it becomes the main power of grid.

The decisive factor of SA blackouts is inertia power in grid, as many researchers point out. Inertia power usually comes from hydro and thermo generators that direct couple with grid. To recover capacity of thermal power station is obviously equivalent to veto the previous decision. It seems an intractable challenge.

In order to solve the puzzle, a series of creative methods or techs and the inertia reconfiguration strategy based on them are proffered in this paper.

1. PVSEM (pure variable speed electric machine). It will be the base tech element of many new electrical systems. Publication or patent application has not been decided.
2. NCWPP (non-convertor wind power plant), with power convert-set based on PVSEM.

J. Bai (✉)
Generator Tech Dep., CSSC-CMXD, Zhenjiang, China
e-mail: baijianlong@aliyun.com



F. Shahnia and S. Deilami (eds.), *ICPES 2019*, Lecture Notes in Electrical Engineering 669, https://doi.org/10.1007/978-981-15-5374-5_4

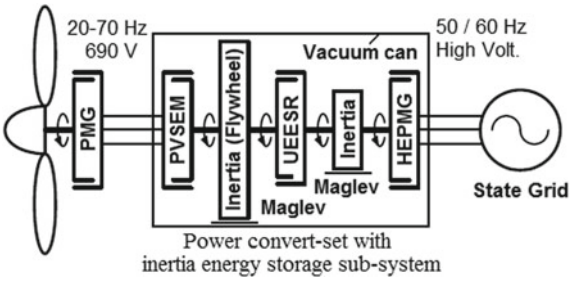


**Fig. 1** Typical techs in grid inertia reconfiguration strategy

3. Unique design methods of PMG (permanent magnet generator), HEPMG (hybrid excitation PMG), and other EM (electric machine) operating in vacuum.
4. Lean maglev, vacuum and flywheel.
5. UEESR (ultra-high efficient electromagnetic speed regulator), based on techs of PVSEM and UEEM (ultra-high efficient EM) with lossless idling.
6. Functions of distributed inertia energy storage system in grid of conventional WPPs (wind power plants).
7. Low power WPPs and functions in grid.

All mentioned above are based on feasibility and significant improvements to the conventional techs.

The typical strategy scheme is shown as Fig. 1.

## 2 Description of Main Techs

### *2.1 Smart Motor: PVSEM, A Creationary and Significant Tech*

PVSEM feeds no harmonic back to grid. And on the premise of high power factor and efficiency, PVSEM can operate forward-backward at any speed within the synchronous and change speed according to the requirement. It operates with brushless and no convertor. Emphatically, it is different from EM with convertor, IM (induction machine) with adjustable resistance or rotor chopper control, or DFIM (double-fed IM). Zinc oxide will be a vital material.

### *2.2 NCWPP—Inertia Power WPP*

As shown in Fig. 2, the typical NCWPP power-train is constructed of wind turbine, PMG, power convert-set of PVSEM and high voltage HEPMG, state or local grid.

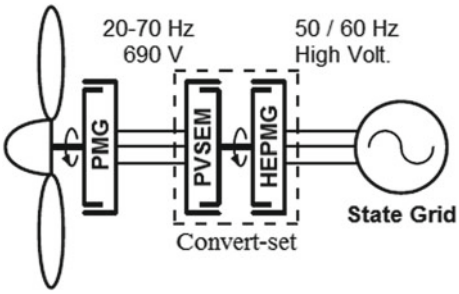


**Fig. 2** NCWPP (inertia power WPP)

In nature, power convert-set based on PVSEM is a convertor. Here, convert-set is named directly for difference from power electronic convertor.

NCWPP features are as following:

1. Reliable, simple and high efficient due to convert-set.
2. Sine AC power (no harmonic pollution) provided to grid, no L-C-L filter as in Figs. 3 and 4.
3. Direct couple with grid via HEPMG of high voltage design, no transformer as in Figs. 3 and 4.
4. No off-grid problem, especially no disconnecting due to convertor like conventional WPPs.
5. Expected operation range up to more than 35 m/s.
6. PVSEM owns natural buffer function to deal gust and high wind, and ensures NCWPP superiority.

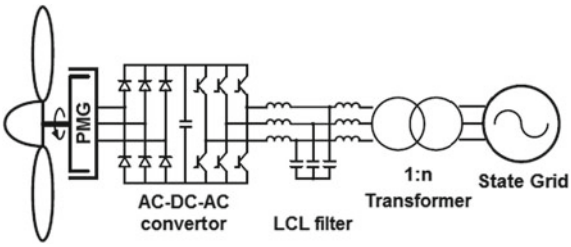


**Fig. 3** Full power convertor WPP

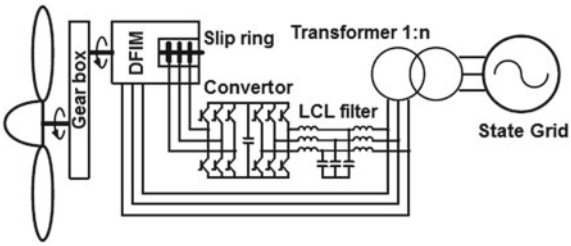


**Fig. 4** Section power convertor WPP

## 2.3 Inertia, Maglev, Vacuum and Cooling

Both vacuum and maglev shown in Fig. 1 are for efficiency, or in order to reduce the loss of friction.

- Inertia: With the strategy aim, flywheel is mainly for grid stability, especially avoiding blackout, though generally it is only applied to energy storage. So high speed and capacity is not the primary goal in design. Medium speed flywheel of super high strength steel alloy (or high strength steel alloy instead of carbon fiber [1]) is suitable considering cost and EM rotor design. Inclusively, it will store and regulate the energy from wind.
- Maglev: Hybrid maglev will be lean in design if the steel alloy is applied to flywheel. In structure, it seems some similar to a 10 kW FESS proposed in [2]. It will be improved significantly and applied in products.
- Cooling and vacuum: There will always be a bit of air remained in a can because it is impossible to gain absolute vacuum on the Earth. Air friction will lead to extra energy loss. It is unable to be eliminated, but can be reduced via light gas (hydrogen or helium). Hydrogen will eliminate carbon element in steel due to its particularity of high infiltration and deoxidization, and then steel will become soft and damaged, though it is an excellent coolant to EM. As to the better method for EM cooling, lubricating oil of vacuum pump will be considered into the design. And helium will be filled into vacuum can to drive air and then pumped out to get vacuum, for less friction as possible. So flywheel energy storage system (FESS) will get ideally high efficiency.

Less than 4% energy loss per day of FESS is expected via the methods of vacuum and maglev.

Advantages of FESS with techs mentioned in this paper exhibit in Table 1. And it will benefit the grid with new energy as main power.

Smart grid with energy storage has been proposed and put in practice in recent years. Battery as storage device has been applied, but the cost is some high. PSPS has popularized quite a few years, but needs suitable site. High speed FESS of carbon fiber is high in cost though it owns high energy storage density. As a general energy storage device, steel FESS has no advantage with low energy storage density in one-side view and less than 80–85% [3] efficiency with bearing at current lagged tech level.

## 2.4 UEESR and UEEM

Essentially, UEESR is an integration of PMG, PVSEM and edge current clutch. Design of ultra-high efficiency with only real-time copper loss will ensure its application in visible speed gap between inertia and HEPMG.

All EMs can own ultra-high efficiency with lossless idling design, i.e. UEEM.

**Table 1** Comparison of 3 energy storage devices

| | Inertia[a] | PSPS[b] | Battery |
|---|---|---|---|
| Life time | ≥25 years[c] | ≥25 years[d] | ≤2000 cycles[e] |
| Efficiency | $\geq 0.96^2 \times 0.96$ (days) | ≤0.8[f] | 0.7–0.9[g] |
| Reliability | High | Medium | Low |
| Inertia power | Yes | Yes | – |
| Response | Quick | Slow | – |
| Sharp discharge | Yes | No | No |
| Site nearby | Yes | No | Yes |
| EEIIGR[h] | 1 | 0.6 | 0.3[i] |

[a]FESS as shown in Fig. 1
[b]*PSPS* Pumped storage power station
[c]Reference lifetime of other FESS: 20 years in [3, 13] etc., $10^7$ cycles in [14]
[d]Reference: 40 years in [15]
[e]Reference: Max. 3000 cycles in [14], dubious 4000 cycles and cycles of other storage devices in [16], 2000 cycles in [3], 2–10 years in [17] etc., lead acid battery only with 200–400 cycles in many papers
[f]Reference: 0.8 in [15], 0.6–0.75 in [18], $0.85 \times 0.85$ in [19], 0.734–0.891 in [20] etc.
[g]Reference: 0.6–0.9 in [15]
[h]*EEIIGR* Expected economic integration index to grid robustness
[i]Battery connects grid via convertor

### *2.5 HEPMG*

HEPMG has not been popular as plain PMG for tech reason, though it has been expatiated in a good many literatures in recent decades years. But the state will change owing to the HEPMG with viable paw-pole tech scheme of odd design. Advantages of high efficiency and adjustable voltage will popularize it in FESS, NCWPP, diesel engine generator set, etc.

## 3 Description of Strategy

Basic background: On 28th of September 2016, fierce storms and lightning strikes caused multiple faults on the SA transmission system and 456 MW of wind generation tripped off-line as a result of low voltage ride through protection feature of wind turbines. This loss of generation and lack of load shedding activities led to a significant blackout in the area [4].

The power constitution of SA in 2016 is shown as Table 2. Nearly 50% came from wind (and solar) energy. Inertia power that grid stability depends on had been cut down drastically.

Another reference data: SA has developed approximately 1600 MW wind [5] and 730 MW photovoltaic generation [6], with around 2900 MW peak load [7].

**Table 2** Pre-blacout network operating condition [21]

| Source | Generation (MW) |
|---|---|
| Synchronous generators (TIPS and LGPS) | 330 |
| Wind + Solar | 683 + 50 |
| Import from Victoria via Heywood | 700 |
| Import from Victoria via Murraylink | 113 |
| Total load (including losses) | 1826 |

The installed capacity is redundant, but the grid is weak. Problems of current WPP is obvious. Convertor of power electronic devices is allergic to instantaneous overload from grid, such as limited short circuit, and too fragile to endure the surge power due to sudden chop wind. WPPs will have to disconnect from grid when hurricane comes. Then the fragility will trigger protection measures of correlative and additional devices in grid at the same time which lead to difficult recovery.

There are 2 popular kinds of high power WPP (HPWPP) nowadays. In order to differentiate from NCWPP presented in this paper, they are defined as the conventional.

The popular 1 is with full power convertor, i.e. all power via the convertor in power-train (or Type 4 full converter connected generation mentioned in [8] etc.). Usually, PMG is directly driven by wind turbine. As shown in Fig. 3, typical power-train of full power convertor WPP is constructed of wind turbine, PMG, convertor with harmonic filter, step-up transformer, state or local grid.

The popular 2 is with section power convertor, i.e. section power via the convertor in power-train (or Type 3 in [8] etc.). DFIM coupled with speed-up gear box is adopted. Its power-train is shown as Fig. 4.

Harmonic will be inevitably input into grid due to convertor in the output power of 2 HPWPPs. Though the latter harmonic remnant is less than the former, gear box is fragile, makes noise and will pollute environment if lubricating oil leaks. So there is a tendency that the former will substitute the latter at more than 3 MW level.

## *3.1 Strategy 1: NCWPP Substituting the Conventional WPP*

Inertia power in grid decides the frequency and stabilizes the voltage [9] because online generators have natural ability to synchronize each other. Convertor has no those abilities in nature.

As inertia power of grid, direct coupled generator can be on grid continuously, even when drastic grid drop of voltage and frequency comes. And the generators have ability and will try their best to recover the grid power even if blackout happens. So they can stabilize both frequency and voltage of grid in function. While conventional WPP will have to cut off at that case.

NCWPP owns direct coupled grid generator with same function as that of thermal or hydro power plant. PVSEM and UEESR are equivalent to the very excellent power conversion buffers respectively.

Undoubtedly, NCWPP, especially that shown as Fig. 1, will be highly recommended in the next WPP installations. Its inertia energy storage sub-system can be directly as a part of grid sometimes if necessary.

The conventional WPP is not suitable to be the main power in state grid and should go out of use step by step.

## *3.2 Strategy 2: Remediation to the Current Grid*

Because the conventional HPWPPs could not go out of use and bulk installations of NCWPP are impossible in near future, the feasible remediation method can be extracted from NCWPP shown as Fig. 1. That is non-convertor power convert-set with inertia energy storage sub-system. And distributed FESS is recommended. A scheme for reference is shown as Fig. 5.

Distributed FESS is nearly same as that of NCWPP and remedies the disability of the conventional WPP. The advantages are listed as following:

1. To avoid potential blackouts and quickly recover after blackout.
2. To ensure grid supply economic and sufficient power. It will balance peak-valley power demand and absorb superfluous wind power as extra storage for emergencies.
3. To improve power factor efficiently and smartly.
4. No harmonic pollution to grid during charge-discharge.
5. Competitive reliability, lifetime and operation cost.

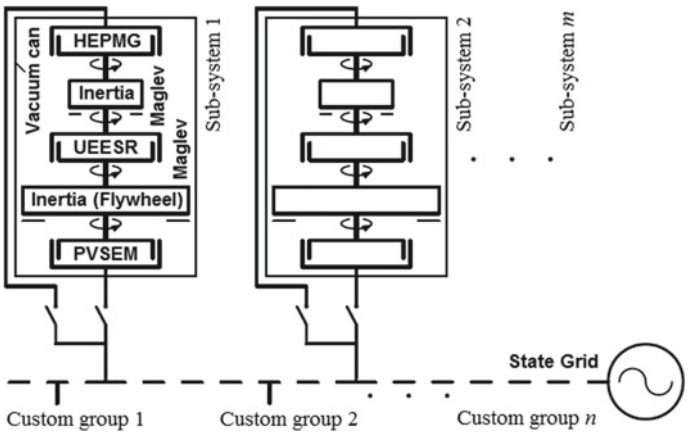


**Fig. 5** Distributed inertia energy storage system

### 3.3 *Strategy 3: Low Power WPP Joining the Grid*

It seems to be neglected to develop low power WPP (LPWPP) in many years recently, though there are many demands in quite a few countries. Most techs of HPWPP cannot be used in LPWPP because of complexity. The complex means lack of reliability and high cost. And the current tech is obviously lagged. Most LPWPPs, as shown in Fig. 6, are independent from grid.

The status will change from now on. Grid LPWPP has been researched a few years. It is developed for families and named as Grid Home Wind Power Plant (GHWPP). And it will be much simpler than HPWPP.

2 types of grid GHWPP for are provided in this paper.

GHWPP 1 with power range from 2 to 5 kW, shown as Fig. 7, is mainly for city buildings. Yawing motor is outside, has no obvious nacelle. Building-top type is defined due to its site.

**Fig. 6** Typical LPWPPs at present

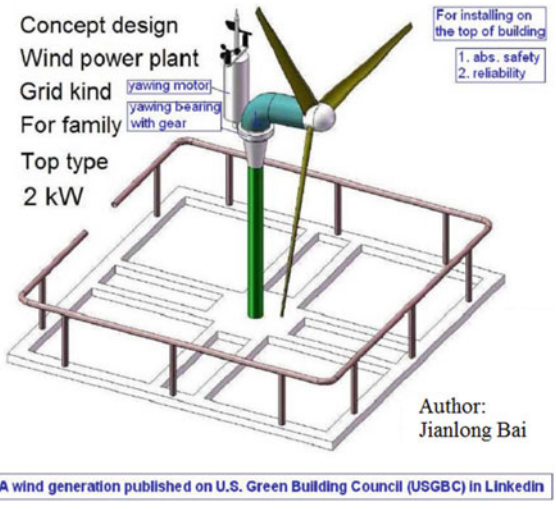


**Fig. 7** Building-top GHWPP

**Fig. 8** Villa-farm GHWPP

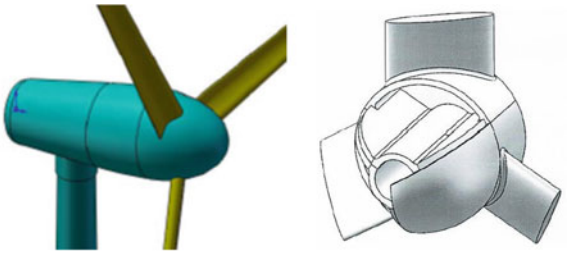

GHWPP 2 with power range of 10–100 kW as Fig. 8 is for villa and farm. So Villa-farm is named.

GHWPP will be much more advantageous than HPWPP:

1. PVSEM is also included. And the powertrains are almost same as Fig. 1 or 2.
2. Simple layout can reduce potential failures.
3. Integration of fraction-hub and blade will be adopted for much higher mechanical strength.
4. Ropes between blades gain more strength; and in case of blade break-off, some strings per blade are inside.
5. Wind intake regulation is via yawing. Wind speed operation range of GHWPP will be from 3 to more than 25 m/s, factually up to 35 m/s depending on tolerance of grid cable.
6. Ecological and environmental protection is considered: turbine with much smaller radius can avoid killing birds; hub-blades and nacelle are made of recyclable aluminum instead of resin fiberglass.
7. No risk of fire there will be.

Reliable GHWPPs are flexible in installation and can be smartly distributed in cities, towns, villages and open country.

Potential market demand of GHWPPs can be foreseen. Widely distribution and considerable power volume in total will benefit grid further.

## *3.4 Strategy 4: Smart Connecting Grid of New Energy*

Many small solar power stations and mini gas turbine power stations have been installed, and there will be more in the future. How to manage the discontinuous power from them has become an issue nowadays.

A suggestion of local smart grid is given as Fig. 9. When state grid fails, local grid disconnects from it and continues to power the local for a while.

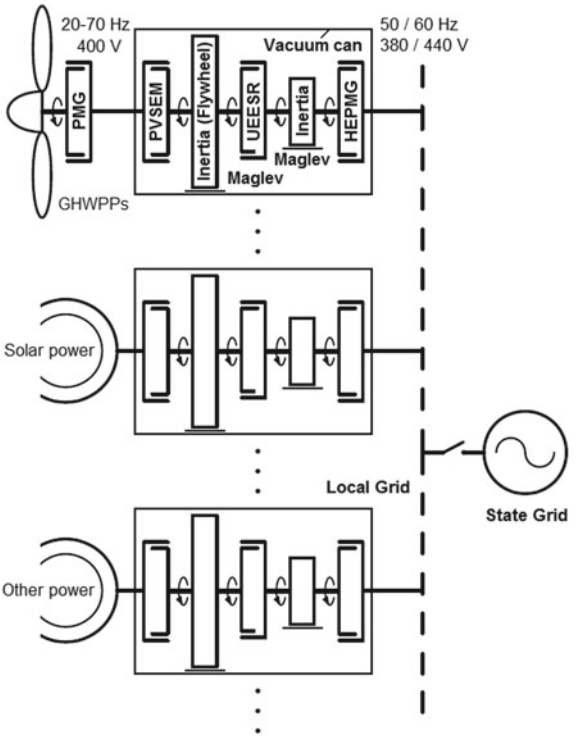


**Fig. 9** Local smart grid with inertia power and energy storage

## 4 Discussion

There are many papers about grid stability with inertia. Virtual inertia [10], factually, is a gigantic DC energy storage with rapid or sharp discharge. A large rotating mass like a synchronous generator connected synchronously to the grid has some stored kinetic energy which is defined at the nominal frequency [9]. To mitigate possibilities of unforeseeable SA blackout events, a solution using synchronous condensers proposed in [11, 12] is a good suggestion, but it has to be at the price of additional energy loss and cost.

For full power convertor WPP, there is a remediation method specially, as shown in Fig. 10: a set of IM and high voltage HEPMG substituting transformer. Few poles are suitable for EM economic size. The set can turn discrete "switch" power into continuous inertia power.

In grid, to accelerate flywheel with more than 3000 or 3600 r/min, EM with convertor is more suitable than PVSEM.

It is necessary to research inertia reconfiguration strategy further, to optimize schemes and perfect techs mentioned in this paper.

There should be strategies and techs to deal with high wind and gust for WPP normal operation.

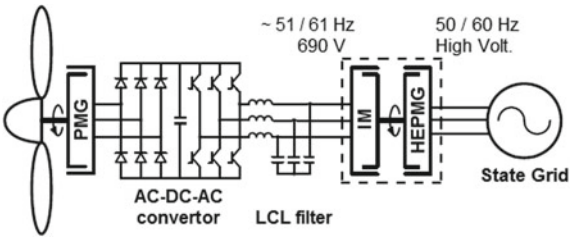


**Fig. 10** IM-HEPMG in full power convertor WPP

Hybrid of EM and maglev is viable in design, with lossless idling tech for high efficiency. While the hybrid with super conductor is difficult due to characteristic, cooling and maintenance.

High tech does not mean complexity.

On Mars, GHWPP may be the optimum device for power.

## 5 Conclusion

This paper proffers a viable blackout solution mode, and consummates the previous thesis with only analysis, model theory or suggestion.

Grid inertia reconfiguration is an effectual strategy to solve the blackout problems like that in SA.

Via grid inertia reconfiguration, new energy will be much more advantageous than carbonaceous fossil energy, can substitute it perfectly, and smart grid will be veritable.

GHWPPs will be welcome. GHWPP power will be an indispensable component of state grid in the future.

## References

1. Navarro G, Torres J, Moreno-Torres P, Blanco M, Lafoz M (2015) Technology description and characterization of a low-cost flywheel for energy management in microgrids. In: 17th European conference on power electronics and applications (EPE'15 ECCE-Europe), pp 1–10
2. Zhang J (2005) Research on flywheel energy storage system using in power network. In: 2005 International conference on power electronics and drives systems, vol 2, pp 1344–1347
3. Smith SC, Sen PK Sr., Member IEEE, Kroposki B, Sr. Member IEEE (2008) Advancement of energy storage devices and applications in electrical power system. In: 2008 IEEE power and energy society general meeting—Conversion and delivery of electrical energy in the 21st century, pp 1–8
4. Jamborsalamati1 P, Moghimi M, Hossain1 MJ, Taghizadeh1 S, Lu J, Konstantinou G (2018) A framework for evaluation of power grid resilience case study: 2016 South Australian blackout. In: 2018 IEEE international conference on environment and electrical engineering and 2018 ieee industrial and commercial power systems Europe (EEEIC/I & CPS Europe), pp 1–6

5. AEMO Generation Information Page (2017) https://www.aemo.com.au/Electricity/-/National-Electricity-Market-NEM/Planning-and-forecasting/Generation-information
6. Australian Photovoltaic Institute (2017) Solar PV status. http://pv-map.apvi.org.au/historical#4/-26.67/134.12
7. AEMO (2016) South Australian demand forecasts. http://www.aemo.com.au/media/Files/Electricity/NEM/-/Market_Notices_and_Events/Power_System_Incident_Reports/2017/Integrated-Final-Report-SA-Black-System-28-September-2016.pdf. Accessed on 10 Oct 2017
8. Adrees A, Milanović JV, Mancarella P (2018) The influence of location of distributed energy storage systems on primary frequency response of low inertia power systems. In: 2018 IEEE power & energy society general meeting (PESGM), pp 1–5
9. Spahic E, Varma D, Beck G, Kuhn G, Hild V (2016) Impact of reduced system inertia on stable power system operation and an overview of possible solutions. In: 2016 IEEE power and energy society general meeting (PESGM), pp 1–5
10. Benidris M, Student Member IEEE, Mitra J, Senior Member IEEE (2012) Enhancing stability performance of renewable energy generators by utilizing virtual inertia. In: 2012 IEEE power and energy society general meeting, pp 1–6
11. Al-Masood N, Yan R, Kumar Saha T (2018) Cascading contingencies in a renewable dominated power system: risk of blackouts and its mitigation. In: 2018 IEEE power & energy society general meeting (PESGM), pp 1–5
12. Al-Masood N, Modi N, Yan R (2016) Low inertia power systems: frequency response challenges and a possible solution. In: 2016 Australasian universities power engineering conference (AUPEC), pp 1–6
13. Chatzivasileiadi A, Ampatzi E, Knight I (2013) Characteristics of electrical energy storage technologies and their applications in buildings. Renew Sustain Energy Rev 25:814–830
14. Li X, Erd N, Binder A (2016) Evaluation of flywheel energy storage systems for residential photovoltaic installations. In: 2016 International symposium on power electronics, electrical drives, automation and motion (SPEEDAM), pp 255–260
15. Faias S, Santos P, Matos F, Sousa J, Castro R, Evaluation of energy storage devices for renewable energies integration: application to a Portuguese wind farm. In: 5th International conference on the european electricity market, pp 1–7
16. Elgenedy MA, Massoud AM, Ahmed S (2015) Energy in smart grid: strategies and technologies for efficiency enhancement. In: 2015 First workshop on smart grid and renewable energy (SGRE), pp 1–6
17. Beardsall JC, Gould CA, Al-Tai M (2015) Energy storage systems: a review of the technology and its application in power systems. In: 50th International universities power engineering conference (UPEC), pp 1–6
18. Busca-Forcos A, Marinescu C (2014) Pumped storage system for wind energy in variable operating conditions. In: 2014 International symposium on fundamentals of electrical engineering (ISFEE), pp 1–6
19. Yang T, Wu D, Stoorvogel AA, Stoustrup J (2016) Distributed coordination of energy storage with distributed generators. In: 2016 IEEE power and energy society general meeting (PESGM), pp 1–5
20. Zhao C, Yin H, Noguchi Y, Ma C (2014) Quantitative analysis on energy efficiency of a battery-ultracapacitor hybrid system. In: 23rd International symposium on industrial electronics (ISIE), pp 1829–1835
21. AEMO (2017) Integrated final report SA black system 28 September 2016. http://www.aemo.com.au/media/-/Files/Electricity/NEM/Market_Notices_and_Events/Power_System_Incident_Reports/2017/Integrated-Final-Report-SA-Black-System-28-September-2016.pdf. Accessed on 10 Oct 2017

# Robust Least Mean Logarithmic Square Control of Multifunctional PV Battery Grid Tied System


**Mukul Chankaya, Ikhlaq Hussain, and Aijaz Ahmad**

**Abstract** This paper describes the control of grid-tied PV-Battery system using robust least mean logarithmic square (RLMLS) algorithm with bidirectional converter control. The proposed control provides faster control and batter controlling capabilities than conventional control over sporadic nature of photovoltaic (PV). The battery current control and DC voltage control provided by the bidirectional converter. The presented system operates satisfactorily under variable power mode i.e. varying load and insolation and peak power demand mode. The results of MATLAB simulation are satisfactory according to IEEE519 standards.

**Keywords** Robust least mean logarithmic square (RLMLS) · Grid-tied · Photovoltaic (PV) · Battery

## 1 Introduction

Renewable energy systems (RES) are attaining their acclaim in the modern power system. With the shrinking reserves of non-renewable resources and ever-growing demand for power, penetration of RES is increasing promptly in the power system [1]. As the cost of photovoltaic (PV) is declining and soaring awareness towards global warming issues, makes the PV system a viable choice [2]. The capacity of the PV system ranges from a few kW rooftop plants to mega solar plant of 1000 MW that makes it versatile enough to uphold any load, in both grid-tied and autonomous mode of operation. The PV power generation is affected by the sporadic nature of solar insolation. Due to the erratic nature of solar irradiations power fluctuation takes place, which is a serious concern for the stability of the connected system,

M. Chankaya (✉) · A. Ahmad
Electrical Engineering Department, NIT Srinagar, Srinagar, India
e-mail: mukulchankaya@gmail.com

A. Ahmad
e-mail: aijaz54@nitsri.net

I. Hussain
Electrical Engineering Department, Kashmir University, Srinagar, India
e-mail: ikhlaqiitd2015@gmail.com



F. Shahnia and S. Deilami (eds.), *ICPES 2019*, Lecture Notes in Electrical Engineering 669, https://doi.org/10.1007/978-981-15-5374-5_5

load accountability and the safety of personnel. The PV system may be connected to the grid by a single stage or dual stage topologies. The single-stage connects the PV array straight to the DC bus and provides better efficiency than the dual-stage [3]. Whereas, dual-stage topology involves a boost converter that provides control over the DC bus voltage and makes it constant irrespective of the insolation variation [4]. Maximum power point tracking (MPPT) ensures the PV system operation at the maximum power point (MPP). Many MPPT algorithms have been spotlighted in the literature so far [5].

PV system faces a flaw of able to work during sunlight only. This shortcoming of the PV system somewhat can be overcome by using a battery energy storage system (BESS) for maintaining the power continuity throughout the day. With the help of a bidirectional converter, battery bank stores auxiliary power generated during off-peak load by the PV system and utilizes it during peak load interval. Considering the depth of discharge (DOD) limit, lead-acid battery is most suited for standstill operation. The bidirectional converter between DC bus and battery is highly serviceable when DC bus voltage ($V_{dc}$) is <750 V [6].

Several conventional control algorithms have been suggested by the researchers like synchronous reference frame (SRF), power balance theory (PBT), $I - \cos\emptyset$ technique and instantaneous reactive power theory (IRPT) [7]. The adaptive controls have unique characteristics of self modification with each iteration and provides faster convergence during dynamic operation [8]. The Kalman filter, weiner filter and recursive least square (RLS) algorithm were proposed for optimal performance [9–11]. The least mean square (LMS) algorithm is more famous due to its simple design and lack from substantial performance degradation [12, 13]. Several variant of LMS have been developed like normalized LMS (NLMS), modified normalized LMS (MN-LMS), leaky LMS, Block LMS, Sign error LMS, robust LMS (RLMS), robust least mean logarithmic square (RLMLS), variable step size LMS (VS-LMS), Hybrid LMS (H-LMS) and many more [14–21]. The proposed RLMLS algorithm for control is less complex and requires less computation per iteration than the various variant of LMS. The Artificial intelligence (AI) based control [22]. With proper control, voltage source converter (VSC) mitigates the power quality problems at the point of common coupling (PCC). Multifunctional operation of VSC with proposed control involves operation under steady-state, unbalanced, dynamic i.e. varying load and insolation [23].

The proposed system introduces a PV-battery 3-phase 3-wire grid-tied AC system. The controls are provided for maximum power point tracking (MPPT) of PV power, $V_{dc}$, and VSC. The main contribution of the work as follows

1. Combination of the PV and battery complement each other in satisfying the load requirements while keeping the system stable.
2. The proposed system can operate in both fixed and variable power mode. During fixed power mode a fixed amount of power is to be contributed to the grid by the combined PV and battery system irradiation changes. The battery discharges while supplying the peak load. Whereas, in variable power mode, variable power is contributed to the grid and excess energy charges the battery.

3. The VSC is controlled by a robust least mean logarithmic square (RLMLS). Adaptive control algorithm RLMLS is picked for its less complexity, reduced mean square error and better control capability over conventional control.

## 2 Proposed Topology

The proposed PV-battery-grid-tied system is depicted in Fig. 1. PV system with a boost converter has one degree of freedom and batteries with a bidirectional buck-boost converter have dual degrees of freedom. Both are connected in parallel to each other, on DC bus. MPPT based on IC algorithm is implemented. Moreover, interfacing inductance and RC filter are employed to reduce the voltage and current ripples at the PCC.

The RC filter is tuned for a resonant frequency capable of eliminating switching harmonics. The simulated load is of non-linear nature.

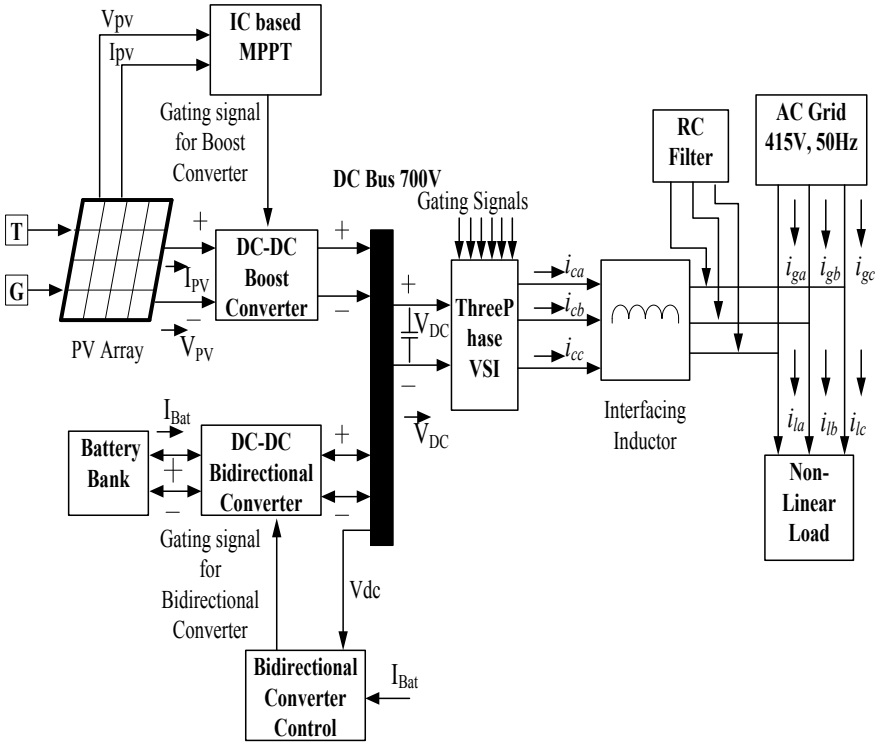


**Fig. 1** Block diagram of the proposed topology

## 3 Control Strategy

The proposed controls are depicted in Fig. 2. The boost control matches the varying impedance of the PV and remaining system. Bidirectional converter control of battery executes the DC link voltage control. VSC control performs multiple functions during the steady-state and dynamic state.

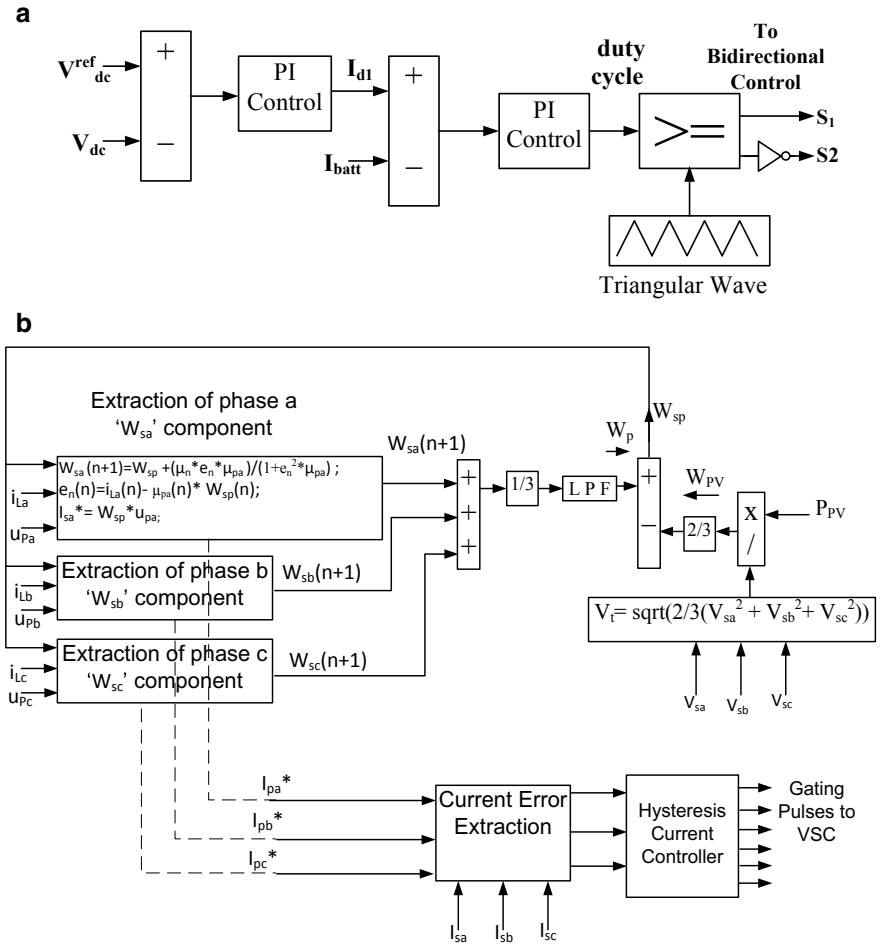


**Fig. 2** **a** Bidirectional converter control. **b** Voltage source converter control

### 3.1 MPPT Control

The IC algorithm is based on instantaneous sensing of the PV power $P_{PV}$ and voltage $V_{PV}$ [23].

$$\frac{dP_{PV}}{dV_{PV}} = i_{PV} + V_{PV} * \frac{di_{PV}}{dV_{PV}} = 0, \tag{1}$$

$$\frac{di_{PV}}{dV_{PV}} = -\frac{i_{PV}}{V_{PV}} \tag{2}$$

The duty cycle is increased or decreased depending on the slope of the PV curve is positive and negative as per (1). The PV curve at MPP has zero slopes as per (2). The controlling signal for boost converter is generated at 20 kHz.

### 3.2 Bidirectional Buck-Boost Converter Control

The charging and discharging of the battery along with $V_{dc}$ is controlled by bidirectional buck-boost control [23] as depicted in Fig. 2a. The control equations of two variables are as follows (3) and (4). Where $K_{Pdc}$, $K_{idc}$ are the proportional and integral (PI) gains of $V_{dc}$ control loop and $K_{Pb}$, $K_{ib}$ are the PI gains for the battery current $I_{batt}$ control loop.

$$I_{d1} = \left(V_{dc}^{ref} - V_{dc}\right) * \left(K_{Pdc} + \frac{K_{idc}}{s}\right) \tag{3}$$

$$I_{d2} = (I_{d1} - I_{batt}) * \left(K_{Pb} + \frac{K_{ib}}{s}\right) \tag{4}$$

### 3.3 VSC Control

The VSC control for variable power mode is depicted in Fig. 2b. Error signal $e_n$ is calculated by negating the calculated signal from the desired signal as (5). $\mu_{pa}$, $\mu_{pb}$, $\mu_{pc}$ are the unit template signals of each phase [18]. The $\mu_n$ is the step size chosen to stabilize the system. The feed-forward (FF) term of the PV system $W_{pv}$ is created as per (6). The three weight signals of each phase are $[W_{sa}(n+1), W_{sb}(n+1), W_{sc}(n+1)]$ and their average weight $W_p$ is negated with the $W_{PV}$ to produce $W_{sp}$ as per (7)–(11). The $W_{sp}$ is the weight signal further multiplied with the unit template of each phase to produce the reference current signal $I_{sa}^*$, $I_{sb}^*$, $I_{sc}^*$ as per (12). Whereas, in the fixed power mode $W_{sp_{fix}}$ and $I_{sa_{fix}}^*$, $I_{sb_{fix}}^*$, $I_{sc_{fix}}^*$ are computed as per (13) and (14) to generate

switching sequence of VSC. During fixed power mode, a fixed amount of power is supplied to the grid.

$$\mathrm{e_n} = \mathrm{i_{La}} - \mu_{\mathrm{pa}} * \mathrm{W_{sp}} \tag{5}$$

$$W_{pv} = \frac{2}{3}\left(\frac{P_{PV}}{\sqrt{\frac{2}{3}\left(V_{sa}^2 + V_{sb}^2 + V_{sc}^2\right)}}\right) \tag{6}$$

$$W_{sa}(n+1) = \mathrm{W_{sp}} + \left(\mu_{\mathrm{n}} * \mathrm{e_n} * \mu_{\mathrm{pa}}\right)/\left(1 + \mathrm{e_n^2} * \mu_{\mathrm{pa}}\right) \tag{7}$$

$$W_{sb}(n+1) = \mathrm{W_{sp}} + \left(\mu_{\mathrm{n}} * \mathrm{e_n} * \mu_{\mathrm{pa}}\right)/\left(1 + \mathrm{e_n^2} * \mu_{\mathrm{pa}}\right) \tag{8}$$

$$W_{sc}(n+1) = \mathrm{W_{sp}} + \left(\mu_{\mathrm{n}} * \mathrm{e_n} * \mu_{\mathrm{pa}}\right)/\left(1 + \mathrm{e_n^2} * \mu_{\mathrm{pa}}\right) \tag{9}$$

$$W_p = 1/3(W_{sa} + W_{sb} + W_{sc}) \tag{10}$$

$$W_{sp} = W_p - W_{pv} \tag{11}$$

$$\mathrm{I_{sa}^*} = W_{sp} * \mu_{\mathrm{pa}};\ \mathrm{I_{sb}^*} = W_{sp} * \mu_{\mathrm{pb}};\ \mathrm{I_{sc}^*} = W_{sp} * \mu_{\mathrm{pc}} \tag{12}$$

$$W_{sp_{fix}} = \frac{2}{3}\left(\frac{P_{fix}}{\sqrt{\frac{2}{3}\left(V_{sa}^2 + V_{sb}^2 + V_{sc}^2\right)}}\right) \tag{13}$$

$$\mathrm{I_{sa_{fix}}^*} = W_{sp_{fix}} * \mu_{\mathrm{pa}};\ \mathrm{I_{sa_{fix}}^*} = W_{sp_{fix}} * \mu_{\mathrm{pb}};\ \mathrm{I_{sa_{fix}}^*} = W_{sp_{fix}} * \mu_{\mathrm{pc}} \tag{14}$$

The proposed adaptive control algorithm provides faster response considering the insolation variation and better-controlling capabilities during variable and fixed power mode.

## 4 System Performance

The proposed system is operating with 32 kW of PV system along with a battery of 7200 Ah capacity and a non-linear load of 15.5 kW. The system is subjected to steady-state and dynamic conditions with non-linear load under which its performance is observed.

### 4.1 Steady-State Performance

During steady-state operation, solar insolation is kept at 1000 W/m$^2$. The system performance remains balanced, stable and maintains unity power factor (UPF) between source voltage ($v_{sabc}$) and current ($i_{sabc}$) in phase opposition as the power is delivered to the grid. Around 11 kW of power $P_g$ is delivered to grid from the PV system as the power generated is more than the load requirement depicted in Fig. 3a. The waveshape of phase 'a' of the load current $i_{La}$ shows the non-linear nature of the load as it is non sinusoidal. The compensation current from converter $i_{Ca}$ trying to compensate the non-linearity of load current to make the overall current requirement of load sinusoidal. The $V_{DC}$ is regulated and remains at 700 V as shown in Fig. 3b. The PV voltage $V_{PV}$ and current $I_{PV}$ remains constant with fixed irradiation level so as the PV power $P_{PV}$. The battery is charging as the $I_{Bat}$ is negative and battery voltage $V_{Bat}$ is gradually increasing. The Total harmonics distortion (THD) of phase 'a' of source current $i_{Sa}$, source voltage $v_{Sa}$ and load current $i_{La}$ are depicted in Fig. 4a–c and are accepted as per IEEE 519 standards.

### 4.2 Dynamic Performance Under Fixed Power Mode

During the dynamic performance of the proposed system under a fixed power mode is implemented by supplying fixed power to the grid. The VSC maintains the $v_{sabc}$ and $i_{sabc}$ at UPF in phase opposition. The system have to deliver $P_g$ around 13 kW to the grid before 0.4 s of simulation time. A change in $i_{sabc}$ is visible before and after 0.4 s of simulation time in Fig. 5a. The $i_{Ca}$, $i_{La}$ are same as they were in steady state. The reactive power $Q_g$ delivered to grid is maintained at zero as the VSC satisfy the reactive power requirement of the system. The $V_{PV}$, $I_{PV}$, $P_{PV}$ remains same as steady state with fixed irradiation as shown in Fig. 5b. Before 0.4 s of simulation time battery is charging at a slower rate than steady state as more amount of power to be delivered to the grid. After 0.4 s of simulation time $P_g$ delivered to the grid become around 7 kW and $I_{Bat}$ become more negative results into battery charging at a faster rate. The $V_{DC}$ is preserved at 700 V throughout the operation as depicted in Fig. 5b. The $V_{DC}$ control is provided by the voltage control loop of the bidirectional buck-boost converter.

### 4.3 Dynamic Performance with Varying Insolation

During the dynamic performance, the asserted system the solar irradiations are changed from 1000 to 600 W/m$^2$. The $v_{Sabc}$, $i_{Sabc}$ remains in UPF in phase opposition. Before 0.6 s of simulation time, with the irradiation level at 600 W/m$^2$ the $P_g$ delivered to the grid reduces to few hundred watts only. After 0.6 s of simulation time

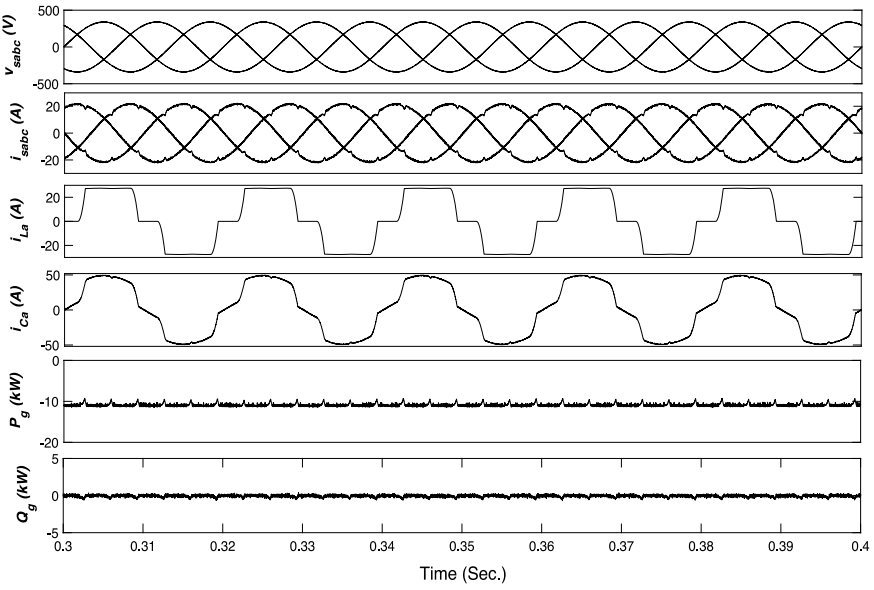


*(a)*

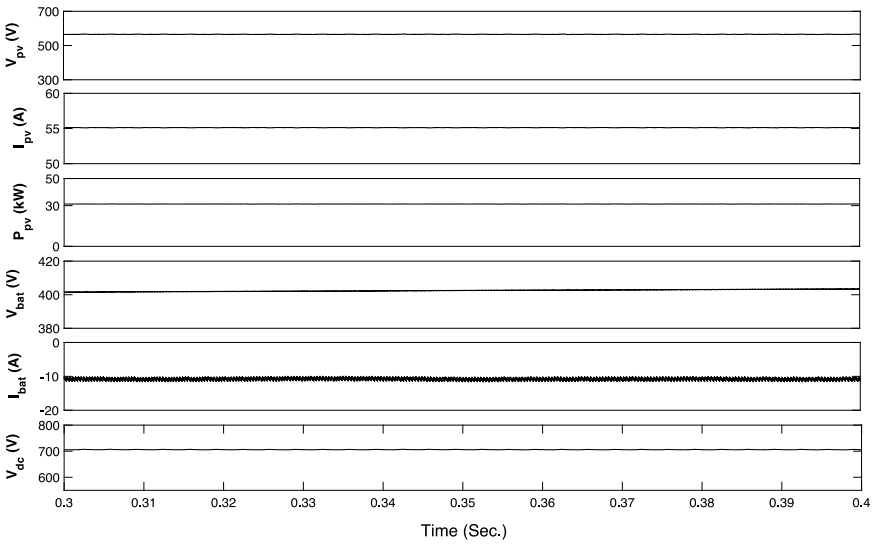


*(b)*

**Fig. 3** Steady-state performance of **a** $v_{sabc}$, $i_{sabc}$, $i_{La}$, $i_{Ca}$, $P_g$ and $Q_g$, **b** $V_{PV}$, $I_{PV}$, $P_{PV}$, $V_{Bat}$, $I_{Bat}$ and $V_{dc}$

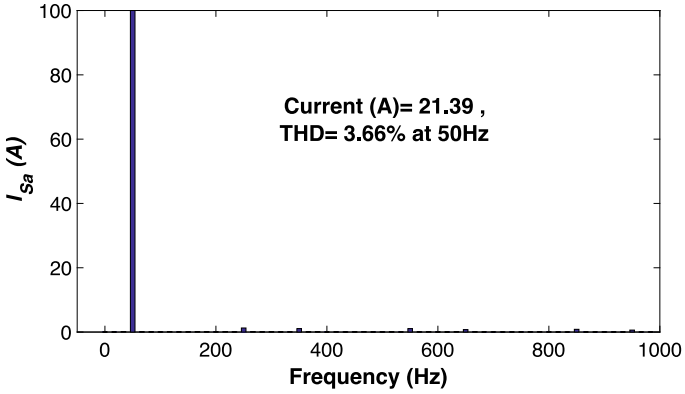


*(a)*

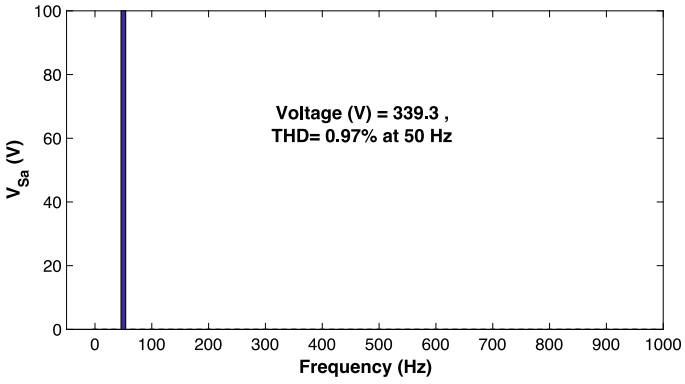


*(b)*

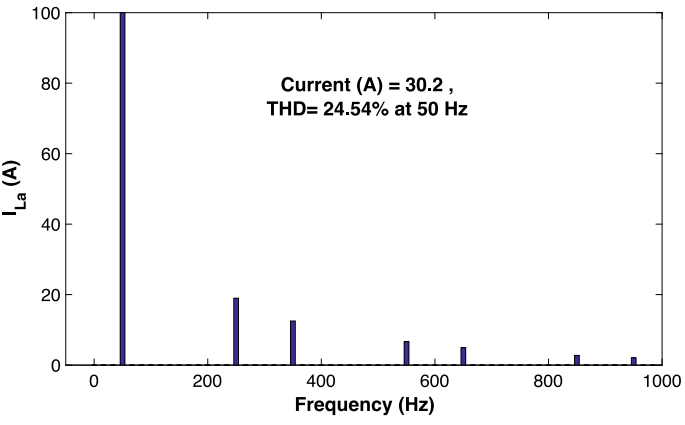


*(c)*

**Fig. 4** Harmonic content of **a** $i_{sa}$, **b** $v_{sa}$ and **c** $i_{La}$ during steady-state

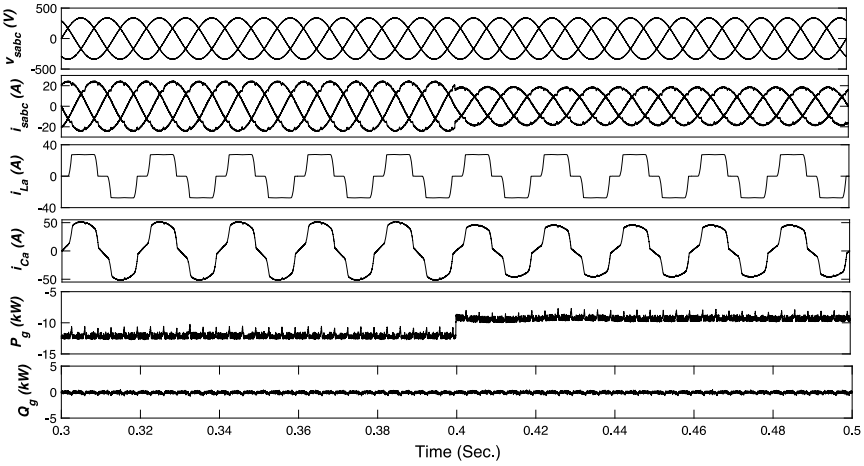


*(a)*

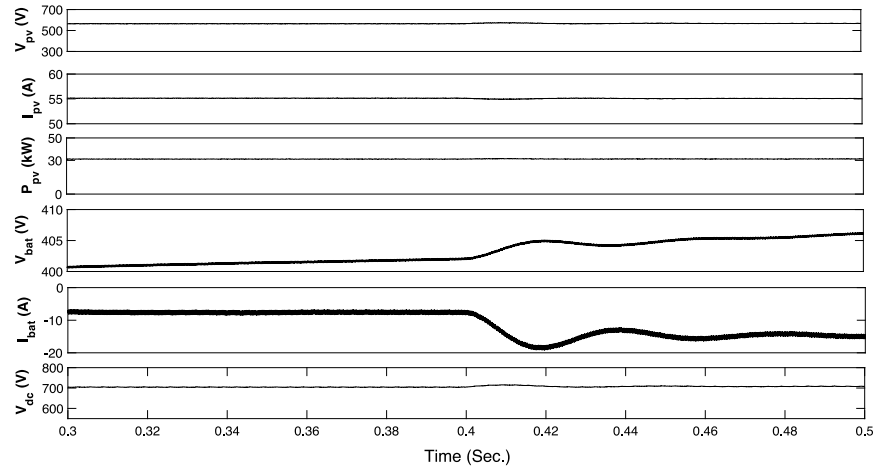


*(b)*

**Fig. 5** Dynamic performance under fixed power mode of **a** $v_{sabc}, i_{sabc}, i_{La}, i_{Ca}, P_g$ and $Q_g$ **b** $V_{PV}$, $I_{PV}$, $P_{PV}$, $V_{Bat}$, $I_{Bat}$ and $V_{dc}$

at 1000 W/m$^2$ the $P_g$ become 11 kW. The variation in $i_{Sabc}$ with irradiation variation are shown in Fig. 6a. The $i_{La}$ remains the same as steady state whereas $i_{Ca}$ changes as power coming from the PV changes. The $Q_g$ supplied from the grid remains zero. The $V_{PV}$ remains constant due to boost converter. The variation in $P_{PV}$ and $I_{PV}$, before 0.6 s of simulation time at irradiation level at 600–1000 W/m$^2$ after 0.6 s of simulation time is shown in Fig. 6b. The $V_{DC}$ remains constant due to bidirectional converter control. The gradual change in $V_{Batt}$ and $I_{Batt}$ are visible as it is charging.

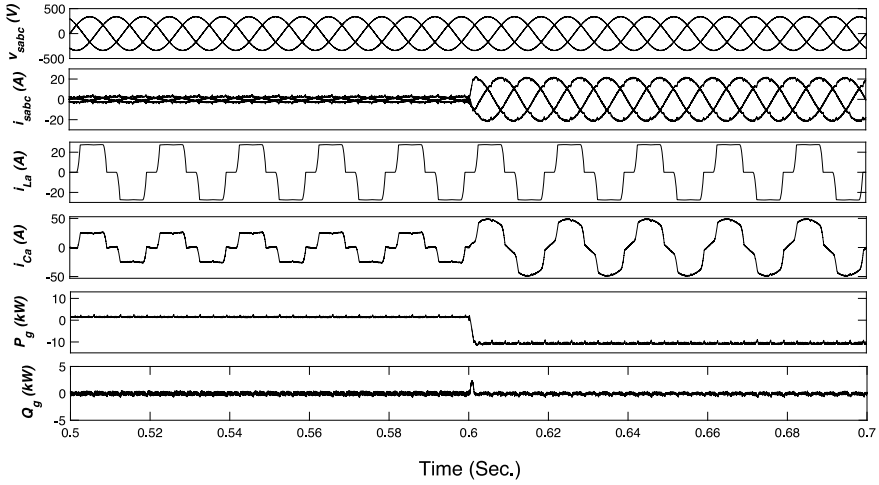


*(a)*

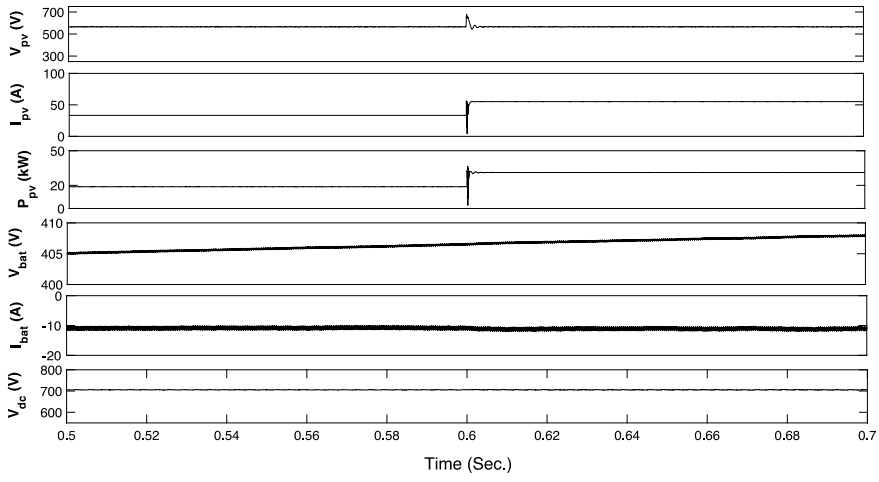


*(b)*

**Fig. 6** Dynamic performance under varying solar irradiations of **a** $v_{sabc}$, $i_{sabc}$, $i_{La}$, $i_{Ca}$, $P_g$ and $Q_g$, **b** $V_{PV}$, $I_{PV}$, $P_{PV}$, $V_{Bat}$, $I_{Bat}$ and $V_{dc}$

## *4.4 Dynamic Performance Under Load Unbalancing*

The load unbalancing is simulated by detaching phase-*a* of a load resulting into $i_{La} = 0$ from 0.3 to 0.5 s of simulation time. The proposed system maintains its stability while keeping source unaffected from load variations. The $v_{sabc}$ and $i_{sabc}$ operates at UPF in phase opposition as depicted in Fig. 7a. The $i_{Ca}$ from the converter

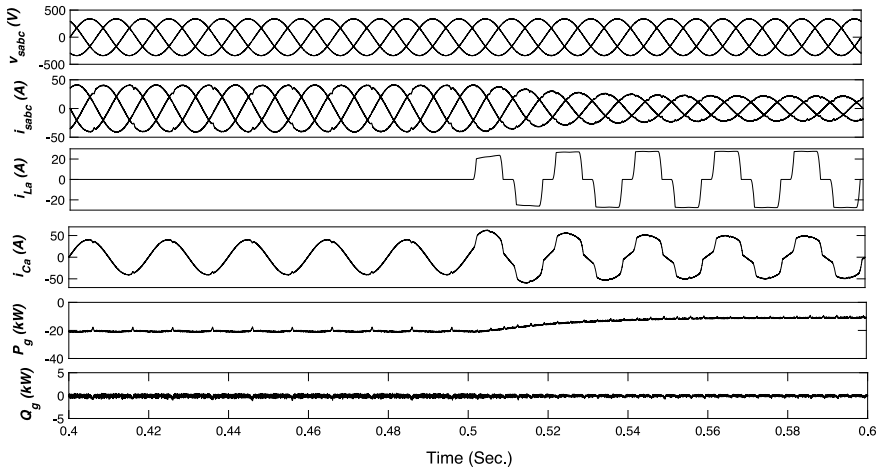


*(a)*

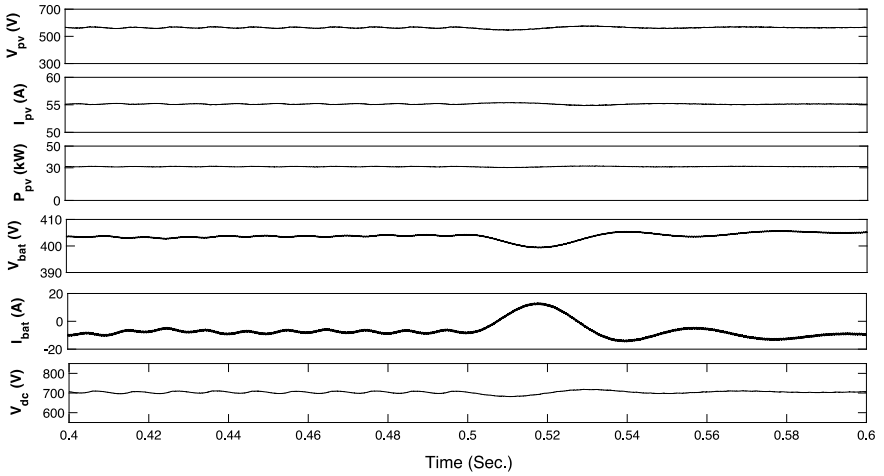


*(b)*

**Fig. 7** Dynamic performance under load unbalancing of **a** $v_{sabc}, i_{sabc}, i_{La}, i_{Ca}, P_g$ and $Q_g$ **b** $V_{PV}$, $I_{PV}$, $P_{PV}$, $V_{Bat}$, $I_{Bat}$ and $V_{dc}$

is almost sinusoidal during load unbalancing. The $P_g$ delivered to the grid reaches to 20 kW due to reduction of load requirement for the time in which phase 'a' of the load is disconnected. The $Q_g$ remains zero as VSC provides the reactive power for the system during load unbalancing also. The $V_{DC}$ is preserved at 700 V during load unbalancing as depicted the Fig. 7b. The $V_{PV}$, $I_{PV}$ and $P_{PV}$ remains same during unbalanced and balanced load as irradiation level remains at 1000 W/m$^2$. The unit template $\mu_{pa}$, weight signals $W_{sa}$, $W_p$, $W_{PV}$, $W_{sp}$ and reference current component of each phase $I^*_{sa}$,$I^*_{sb}$ and $I^*_{sc}$ are depicted in Fig. 8 during load unbalancing. The $\mu_{pa}$

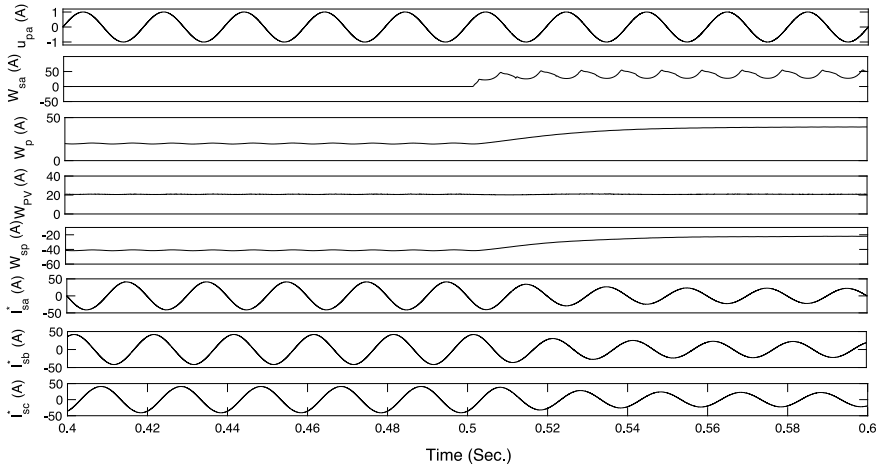


**Fig. 8** Dynamic performance under load unbalancing of $\mu_{pa}$, $W_{sa}$, $W_p$, $W_{PV}$, $W_{sp}$, $I^*_{sa}$, $I^*_{sb}$ and $I^*_{sc}$

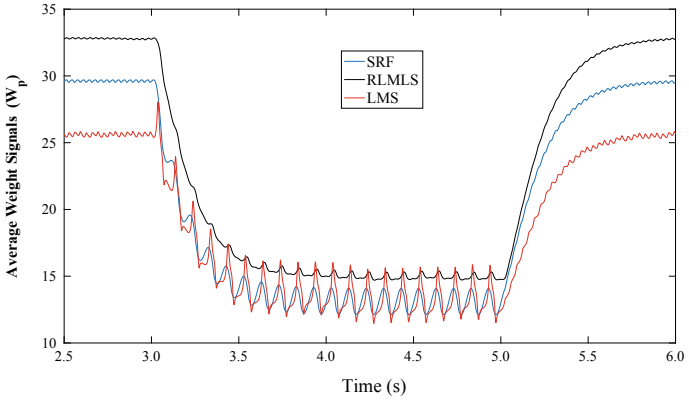


**Fig. 9** Comparision of controlling strategies

and $I^*_{sa}$,$I^*_{sb}$ and $I^*_{sc}$ remains sinusoidal during load unbalancing also to maintain the system stability. The weight component of phase 'a' $W_{sa}$ remains zero during load unbalancing and $W_p$ changes accordingly as per (10). The $W_{PV}$ remains constant during the operation.

The LMS algorithm is preferred over the several conventional and advanced version of LMS algorithm due to its less complexities and better stability. The RLMLS algorithm is chosen over LMS as it produces less mean square error due to logarithmic function and provides better stability, though it is slightly over complex than

LMS. The comparison of the $W_p$ of VSC control with SRF, LMS & RLMLS algorithm during load unbalancing is shown in Fig. 9. The $W_p$ with RLMLS control have minimum ripples and provides better results overall.

## 5 Conclusion

The PV-battery grid-tied 3-phase 3-wire system has been working satisfactorily under variable and fixed power mode. During fixed power, peak demand can be fulfilled by discharging battery whereas battery stores energy during off-peak demand when electricity is cheaper. The overall cost of electricity can be reduced while making the load curve and load duration curve flatter. The proposed system has handled the critical load under various steady-state and dynamic conditions and most suited for household application. An adaptive VSC control has performed multifunctional capability. The proposed system is robust, feasible and working satisfactorily under the steady-state and dynamic state.

## Appendix

***Experimental System Parameters*** The PV module voltage, $V_{mpp} = 26.3$ V; PV module current, $I_{mpp} = 7.614$ A; no. of parallel module, $n_p = 7$; no. of series module, $n_s = 23$; PV array voltage, $V_{pv} = 605$ V; PV array current, $I_{pv} = 53.29$ A; PV array power, $P_{pv} = 32$ kW; boost inductor,$L_b = 4$ mH; DC link capacitor, $C_{dc} = 10,000\,\mu$F; battery capacity = 400 V, 18 Ah; bidirectional converter inductor, $L_i = 7$ mH; DC link voltage PI control, $K_{Pdc} = 2$ and $K_{idc} = 0.5$; battery current PI control, $K_{Pb} = 0.18$ and $K_{ib} = 0$; DC bus voltage, $V_{dc} = 700$ V; VSC = 35 kVA; adaptive filter constant, $\mu_n = 0.01$; interfacing inductance, $L_f = 4$ mH; 3-phase grid voltage, $V_{sabc} = 415$ V (rms); RC filter, $R_f = 10\ \Omega$ and $C_f = 10\,\mu$F; 3-phase non-linear load = 15.5 kW, sampling time, $T_s = 10\,\mu$s.

## References

1. Obi M, Bass R (2016) Trends and challenges of grid-connected photovoltaic systems—A review. Renew Sustain Energy Rev 58:1082–1094
2. Hasan R, Mekhilef S, Seyedmahmoudian M, Horan B (2017) Grid-connected isolated PV microinverters: a review. Renew Sustain Energy Rev 67:1065–1080
3. Barnes AK, Balda JC, Stewart CM (2012) Selection of converter topologies for distributed energy resources. In: 2012 Twenty-seventh annual IEEE application of power electronics conference exposition, pp 1418–1423

4. Singh AK, Hussain I, Singh B (2018) Double-stage three-phase grid-integrated solar PV system with fast zero attracting normalized least mean fourth based adaptive control. IEEE Trans Ind Electron 65(5):3921–3931
5. Karami N, Moubayed N, Outbib R (2017) General review and classification of different MPPT Techniques. Renew Sustain Energy Rev 68:1–18
6. Ponnaluri S, Linhofer GO, Steinke JK, Steimer PK (2008) Comparison of single and two stage topologies for interface of BESS or fuel cell system using the ABB standard power electronics building blocks, p 9
7. Singh B, Chandra A, Al-haddad K. Power quality problems and mitigation techniques. Wiley
8. Pradhan S, Hussain I, Singh B, Panigrahi BK (2017) Modified VSS-LMS-based adaptive control for improving the performance of a single-stage PV-integrated grid system. IET Sci Measure Technol 11(4):388–399
9. Albert TR, Abusalem H, Juniper MD (1991) Experimental results: detection and tracking of low SNR sinusoids using real-time LMS and RLS lattice adaptive line enhancers. In: 1991 International conference on acoustics, speech, and signal processing, ICASSP-91. IEEE, pp 1857–1860
10. Kazemi R, Farsi A, Ghaed MH, Karimi-Ghartemani M (2008) Detection and extraction of periodic noises in audio and biomedical signals using Kalman filter. Sig Process 88(8):2114–2121
11. Ding H, Soon Y, Koh SN, Yeo CK (2009) A spectral filtering method based on hybrid wiener filters for speech enhancement. Speech Commun 51(3):259–267
12. Widrow B, Hoff ME (1960) Adaptive switching circuits. In: IRE WESCON convention record 1960, vol 4, no 1, pp 96–104
13. Vaseghi SV (2008) Advanced digital signal processing and noise reduction. Wiley
14. Paulo SD (2008) Adaptive filtering algorithms and practical implementation. In: The international series in engineering and computer science, pp 23–50
15. Chulajata T, Kwon HM, Min KY (2000) Adaptive antenna array with no phase calibration for CDMA reverse link. In: 52nd 2000 vehicular technology conference. IEEE-VTS Fall VTC 2000, vol 1. IEEE, pp 127–134
16. Mayyas K, Aboulnasr T (1997) Leaky LMS algorithm: MSE analysis for Gaussian data. IEEE Trans Sig Process 45(4):927–934
17. Im S, Powers EJ (1997) A block LMS algorithm for third-order frequency-domain Volterra filters. IEEE Sig Process Lett 4(3):75–78
18. Xiong K, Wang S (2019) Robust least mean logarithmic square adaptive filtering algorithms. J Franklin Inst 356(1):654–674
19. Kwong RH, Johnston EW (1992) A variable step size LMS algorithm. IEEE Trans Sig Process 40(7):1633–1642
20. Chern SJ, Horng JC, Wong KM (1995) The performance of the hybrid LMS adaptive algorithm. Sig Process 44(1):67–88
21. Beniwal N, Hussain I, Singh B (2017) Hybrid VSS–LMS–LMF based adaptive control of SPV-DSTATCOM system under distorted grid conditions. IET Renew Power Gener 12(3):311–322
22. Bermejo JF, Fernández JFG, Polo FO, Márquez AC (2019) A review of the use of artificial neural network models for energy and reliability prediction. A study of the solar PV, hydraulic and wind energy sources. Appl Sci (Switzerland) 9
23. Saxena N, Hussain I, Singh B, Vyas AL (2018) Implementation of a grid-integrated PV-battery system for residential and electrical vehicle applications. IEEE Trans Ind Electron 65(8):6592–6601

# Modular Multilevel Converter Based HVDC System Using PD PWM Algorithm


**Richa, Abdul R. Beig, R. Jayashree, and Mohd Tariq**

**Abstract** The modular multilevel converters (MMC) are gaining popularity in grid-connected systems such as HVDC systems, renewable energy systems. This paper primarily focusses on high power application specially HVDC system. MMC has many advantages because of its high modularity, scalability and high power quality. Because of these features, this paper presents a MMC based HVDC system for large power exchange between two areas. The rotating d-q reference based vector control algorithm is used for the control and operation of above HVDC system. PWM plays a very major role for switching the power semiconductor devices of multi levels converter. Here PD-PWM has been used because of its simple structure and easy to implement for high number of levels. The proposed PD-PWM based HVDC system is verified through simulation and experiment. The simulation as well as experimental results are presented.

**Keywords** HVDC · Modular multilevel converter · Pulse width modulation · Phase disposition PWM · Field oriented control · Grid-connected systems

## 1 Introduction

High Voltage Direct Current (HVDC) transmission is proven to be most economical for transmission of high power over long distances. HVDC system also plays an important role in better energy management. In the electricity industry, in view

Richa · R. Jayashree
EEE, B.S. Abdur Rahman Crescent Institute of Science and Technology, Chennai, India
e-mail: richasrii@gmail.com

R. Jayashree
e-mail: jayashree@bsauniv.ac.in

A. R. Beig
ECE, Advanced Power and Energy Center, ECE, Khalifa University, Abu Dhabi, UAE
e-mail: balanthi.beig@ku.ac.ae

M. Tariq (✉)
Department of Electrical Engineering, ZHCET, Aligarh Muslim University, Aligarh, India
e-mail: tariq.ee@zhcet.ac.in



F. Shahnia and S. Deilami (eds.), *ICPES 2019*, Lecture Notes in Electrical Engineering 669, https://doi.org/10.1007/978-981-15-5374-5_6

of the liberalization and demand to conserve energy and reduce pollution, HVDC solutions have become more desirable due to: (1) Reduced pollution (2) low cost (3) Asynchronous connections (4) Power flow control with better stability, power quality etc. [1]. Conventional HVDC system uses thyristor bridge inverter known as Line Commutated Inverter (LCC) based HVDC systems. However, conventional HVDC system suffers from commutation failure when connected to weak grid, lack of control over reactive power, slow dynamic response and unable to work with loads with insufficient local generation posed major limitation for modern power system [2, 3]. Due to advancement in fully controlled high voltage high power semiconductor devices, an improved topology called Voltage Source Converter (VSC) gained a popularity in HVDC system. This has resulted in the development of VSC based HVDC systems [2, 4, 5]. The VSC-HVDC system offers a solution to control active and reactive power simultaneously which helps to achieve stability under fault conditions, fast reversal of the direction of power flow, multi-terminal connections, weak grid interface and improved dynamic response [6, 7]. VSC uses a fully controlled and voltage controlled fast semiconductor switches. Insulated Gate Bipolar Transistor (IGBT) due to its desirable features such as simple gate drives, voltage control capability, high switching frequencies and bidirectional voltage blocking capability has made it to be an attractive for VSC [7]. The Pulse Width Modulation (PWM) technologies are used to create the desired sinusoidal voltage waveform. However, the performance of VSC based HVDC system is limited in high voltage rating and high power applications that needs to handle few KVAs to MVAs. The solution to these problems is solved by the development of simpler Multi-Level Converters (MLCs). In MLCs the conventional VSC structure is connected in cascade to generate high voltage levels. Advancement in the field of MLCs, contributed several topologies such as diode clamp converters, flying capacitor converter, Cascaded H-Bridge converters (CHB) and Modular Multilevel Converters (MMC). The flying capacitor and diode clamp convertrs use non-isolated DC bus. But these topologies are suitable only for medium and low voltage level applications because the power circuit becomes very complex as the number of voltage levels increase and have problems such as voltage variation and dynamic voltage sharing [8]. The MMC and CHB topologies are highly reliable for high power applications because they have simple power circuit and have modular structure. These topologies are made by cascading identical modular units called Sub-Modules (SM) to obtained the desired number of levels. However, the CHB topology requires isolated separate DC for each of the module whereas MMC has common DC bus. So in CHB, isolation transformer for each module is required at the ac side, which makes the CHB based system bulk and expensive. In addition, the CHB based system requires complicated arrangement for power reversal. The MMC topology has common DC bus and does not require isolated DC for its SM units hence isolation at the ac side is not needed. Also MMC topology do not have large capacitors across DC bus. So that, the MMC topology is gaining popularity in grid-connected applications such as grid integration of renewable energy sources and HVDC systems. The higher level MMC can generate near sinusoidal voltages, so filters can be eliminated in many applications [9]. MMC faces few technical challenges that need to be addressed. The MMC has circulation current in the arms of

converter resulting in (1) additional losses in power circuit, (2) voltage ripple in SM DC bus (3) voltage variation and unequal voltages across each SM DC bus. Additionally MMMC has uneven loading of the SMs requires arm inductors. The PWM plays an important role in overcoming some of the above limitations. So, the careful selection of PWM algorithms is required. Phase-Shifted PWM (PSC-PWM) [8, 10, 11], Level-Shifted (LS-PWM) or Phase-Displacement PWM (PD PWM) [12] and space vector PWM (SVPWM) [13, 14] are the three main carrier based modulation strategies used to get near sinusoidal voltages. Out of these PSC-PWM and PD-PWM are widely used in the system because it is simple to implement when the number of levels are high [15]. Multilevel converters need multiple carrier signals with same frequency and amplitude, they fully occupy the range of $+V_{dc}$, and $-V_{dc}$.

PSC-PWM are have certain advantages over PD-PWM, these are (1) shifting the harmonic contents due to higher voltage levels in the output voltages (2) higher switching frequency, resulting in reduced filters size and cost (3) better THD (4) equal load distribution between sub-modules. Because of above-mentioned advantages, design and modification of PS-PWM has been carried out and implemented on the variety of converter topologies. Mostly, PSC-PWM produces $2N + 1$ output voltage levels and upper and lower arm are switched independently. This results in higher number of levels but also large circulation current resulting in increased SM capacitor voltage ripple and increased loss in power circuit. So this method requires additional circulation current controller which will make overall control complex for higher level of SM such as in the case of MMC [16, 17]. Compared to PSC-PWM, PD-PWM is easy, simple to implement and has better THD [12], also results in uniform loading of all the submodules. Therefore, PD-PWM technique is used in this paper. The PD-PWM carrier signals are shifted vertically and maintain same amplitude. The total number of carrier signals required for PD-PWM modulation is $(M - 1)$ with magnitude $V_{dc}/(M - 1)$, where M is the number of level at the output [12]. For Nine-level $(M = 9)$converter, the number of carrier signal required is 8. PD-PWM uses $N + 1$ modulation scheme, where the lower arm switching states are complementary of upper arm switching states. This results in low circulation current thus low SM capacitor voltage ripple eliminated additional controller [16]. Since the phase current flows in the SM capacitors resulting in SM capacitor voltage variation so it is important to balance the SM capacitor voltage. The methods used to balance the SM capacitor voltages are (1) sorting algorithm, (2) closed loop SM voltage control and (3) pulse rotation [11, 16]. Among all the three methods sorting algorithm gives good results and it requires only SM capacitor voltage information to balance the SM voltages [16, 18]. While closed loop SM voltage control loop needs dedicated DC bus voltage control loop for each SM and voltage needs to be sensed every time which makes the system complex for large number of SMs. The pulse rotation method results in beat frequency oscillations in the output and capacitor balancing is similar to the other two methods. Hence in this research work, sorting algorithm is used to balance the SM voltages.

The paper is organized as follows. Section 2 illustrates mathematical modeling of MMC based HVDC system. Closed Loop Control of HVDC System is discussed in

Sect. 3. The simulation results are given in Sect. 4. Experimental results are given in Sect. 5 The Sect. 6 concludes the paper.

## 2 System Modelling

The basic structure of a three phase MMC based VSC-HVDC system shown in Fig. 1. The system is capable of bidirectional power flow between area-1 and area-2. For illustration and analysis, the power flow from sending end converter (Conv-1) to receiving end (Conv-2) is considered in this paper. The two M-level three-phase converters are assumed to be identical. Let us assume the MMC related with area-1 and area-2 is denoted as Conv-1 and Conv-2 respectively. Each phase of MMC consists of upper arm and lower arm ($k \in Upper(U), Lower(L)$). Both the upper and lower arms are formed by $N = M - 1$ series connected HB (Half Bridge)-SMs as shown in Fig. 1. DC terminals are connected through a long cable and its equivalent model is represented by π model as shown in Fig. 1. In HB-SM when SM is ON, the switches T1 is turned ON and for the positive current (negative), the DC bus capacitor is charged (discharged). When SM is OFF, the switch T2 is turned ON

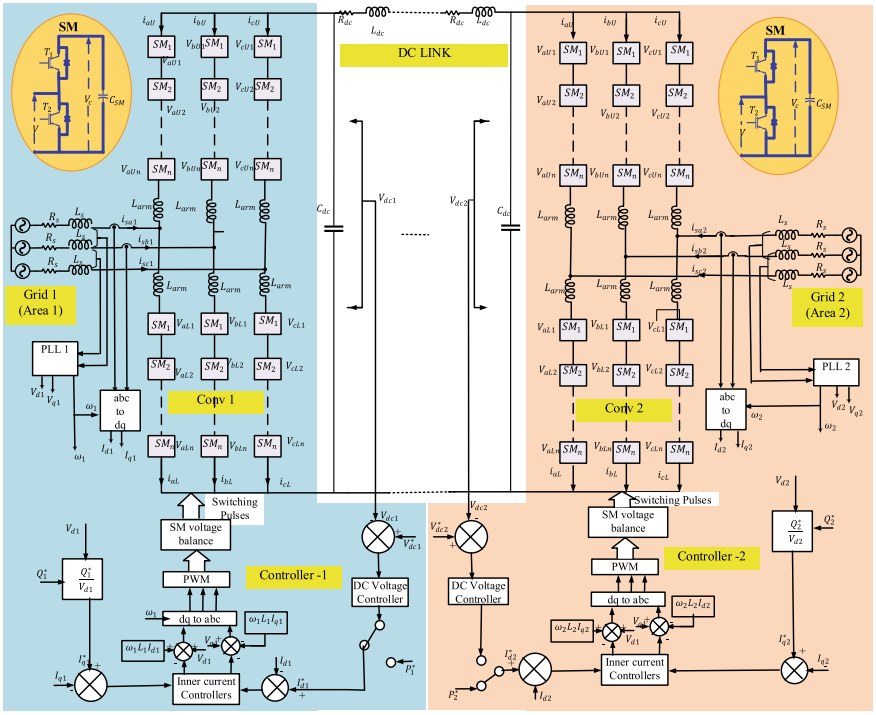


**Fig. 1** Functional block diagram of the HVDC system with controller

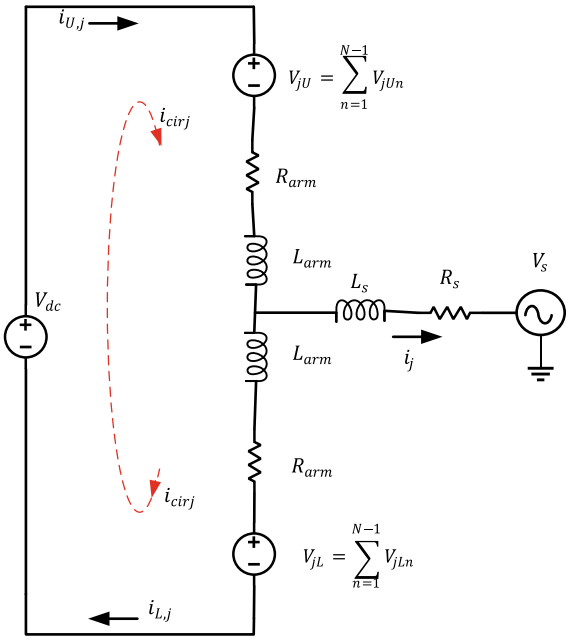


**Fig. 2** Equivalent circuit for MMC

while T1 is OFF, no current in the DC bus capacitor, the SM DC bus voltage does not change.

The simplified per phase equivalent circuit of three-phase MMC powered from AC source is shown in Fig. 2. Here $V_s, i_j, R_s, L_s$ represents grid side AC voltage, current at grid side, line resistance and line inductance of phase $j$; $v_{jU}$ and $v_{jL}$ is the equivalent upper arm and lower arm voltage; and $R_{arm}$ and $L_{arm}$ are the resistance and inductance of arm inductor; $V_{dc}$ is the DC-bus voltage. $i_{Uj}$ and $i_{Lj}$ is the upper arm and the lower arm current; $i_{circ,j}$ is the circulating current which flow only in the loop formed by the each phase and DC-bus. The $v_{jU} = \sum_1^N v_{jkn}$ and $v_{jL} = \sum_1^N v_{jkn}$ are the upper arm and lower arm voltages generated by the MMC in phase j.

The dynamic equations of MMC can be expressed as:

$$\frac{V_{dc}}{2} - v_{jU} - R_{arm} i_{Uj} - L_{arm} \frac{di_{Uj}}{dt} + R_s i_j + L_s \frac{di_j}{dt} - v_{s,j} = 0 \tag{1}$$

$$-\frac{V_{dc}}{2} + v_{jL} + R_{arm} i_{Uj} + L_{arm} \frac{di_{Uj}}{dt} + R_s i_j + L_s \frac{di_j}{dt} - v_{s,j} = 0 \tag{2}$$

Ideally, the upper arm and lower arm are symmetrical so, the AC side current will be equally divided into upper and lower arm respectively. Hence, the arm current can be expressed as:

$$i_{Uj} = \frac{i_j}{2} + i_{circ,j} \tag{3}$$

$$i_{Lj} = -\frac{i_j}{2} + i_{circ,j} \tag{4}$$

The grid current $i_j$ and circulating current $i_{circ,j}$ can be described from Eqs. (3) and (4):

$$i_j = i_{Uj} - i_{Lj} \tag{5}$$

$$i_{circj} = \frac{i_{Uj} + i_{Lj}}{2} \tag{6}$$

The dynamics of phase current ($i_j$) is given by

$$\frac{di_j}{dt} = \frac{v_{jU} - v_{jL} + 2v_{sj} - (-R_{arm} + 2R_s)i_j}{(-L_{arm} + 2L_s)} \tag{7}$$

The dynamic equations of the circulation current ($i_{cirj}$) is given by,

$$\frac{di_{circj}}{dt} = \frac{\frac{V_{dc}}{2} - \frac{(v_{jU}+v_{jL})}{2} - R_{arm}i_{circj}}{L_{arm}} \tag{8}$$

Ideally, the $V_{cjkn} = \frac{V_{dc}}{N}$, but the arm current flowing through the SM capacitor makes this voltage to deviate from the ideal value and cause capacitor voltage variation and ripple which results in circulation current ($i_{cir}$). So, the SM capacitor and $L_{arm}$ are calculated as per [19].

## 3 Closed Loop Control of HVDC System

The rotating d-q model of the The MMC based converter enables the independent control of active and reactive power [20]. A cascaded control system with inner current controller and outer power control loop are designed. The inner current controller ($I_{d1}$, $I_{q1}$, $I_{d2}$, $I_{q2}$) has higher bandwidth than outer power and voltage controller because its dynamics are faster than ($V_{dc1}$,$P_2$, $Q_1$, $Q_2$) dynamics. The proportional-integral controllers are used for inner current controllers and outer controllers. The $I^*_{q1}$ and $I^*_{q2}$ are computed from $Q^*_1 = V_{q1}I^*_{q1}$ and $Q^*_2 = V_{q2}I^*_q$ respectively. The dynamic model of MMC of three phase system can be written as:

$$v_{sa} = R_s i_a + L_s \frac{di_a}{dt} + v_{ca} \tag{9}$$

$$v_{sb} = R_s i_b + L_s \frac{di_b}{dt} + v_{cb} \tag{10}$$

$$v_{sc} = R_s i_c + L_s \frac{di_c}{dt} + v_{cc} \tag{11}$$

Applying Clark transformation to Eqs. (9)–(11)

$$\begin{bmatrix} v_{s\alpha} \\ v_{s\beta} \end{bmatrix} = R_s \begin{bmatrix} i_\alpha \\ i_\beta \end{bmatrix} + L_s \frac{d}{dt} \begin{bmatrix} i_\alpha \\ i_\beta \end{bmatrix} + \begin{bmatrix} v_{c\alpha} \\ v_{c\beta} \end{bmatrix} \tag{12}$$

Transforming alpha-beta to dq reference frame, we get

$$\begin{bmatrix} v_{sd} \\ v_{sq} \end{bmatrix} = R_s \begin{bmatrix} i_d \\ i_q \end{bmatrix} + L_s \frac{d}{dt} \begin{bmatrix} i_d \\ i_q \end{bmatrix} + \omega L_s \begin{bmatrix} 0 & -1 \\ 1 & 0 \end{bmatrix} \begin{bmatrix} i_d \\ i_q \end{bmatrix} + \begin{bmatrix} v_{cd} \\ v_{cq} \end{bmatrix} \tag{13}$$

$$v_{sd} = R_s i_d + L_s \frac{di_d}{dt} - \omega L_s i_q + v_{cd} \tag{14}$$

$$R_s i_d + L_s \frac{di_d}{dt} = v_{sd} - v_{cd} + \omega L_s i_q = v_{xd}$$

$$v_{cd} = v_{sd} + \omega L_s i_q - v_{xd} \tag{15}$$

Similarly, for q-axis

$$v_{sq} = R_s i_q + L_s \frac{di_q}{dt} + \omega L_s i_d + v_{cq} = v_{xq} \tag{16}$$

$$v_{cq} = v_{sq} - \omega L_s i_d - v_{xq} \tag{17}$$

$$\begin{cases} v_{cd} = -\left(K_{pc} + \dfrac{K_{ic}}{s}\right)\left(i_d^* - i_d\right) \\ v_{cq} = -\left(K_{pc} + \dfrac{K_{ic}}{s}\right)\left(i_q^* - i_q\right) \end{cases} \tag{18}$$

where $K_{pc}$ $v_{ab}$ and $K_{ic}$ indicates the PI parameters of the current controller, As the dynamics of $i_q$ and $i_d$ are the same, in current controller, the PI controller parameters of d-axis and q-axis are equal.

The voltage and current vector in d-q axis can be expressed as:

$$\overrightarrow{V} = v_d + jv_q \quad and \quad \overrightarrow{I} = i_d + ji_q \tag{19}$$

Hence the active and reactive power is given as:

$$P = V_{sd} i_d + V_{sq} i_q \quad and \quad Q = V_{sq} i_d - V_{sd} i_q \tag{20}$$

Here d axis is aligned to the grid voltage so $V_{sd} = V_s$ and $V_{sq} = 0$; so Eq. (20) can be rewritten as:

$$P = V_{sd} i_d \quad and \quad Q = -V_{sd} \tag{21}$$

From Eq. (21), it is observed that independent control of active and reactive power can be done using different controller design.

## 4 Simulation Results

The system in Fig. 1 is simulated using MATLAB Simulink toolbox. A MMC based HVDC system with M = 9 is used. The simulation parameters are given in Table 1. PD-PWM is used. PDPWM, the carriers are level shifted by $n \in \left\{-\frac{N-Nf}{2}, 0, \frac{N-Nf}{2}\right\}$ as shown in Fig. 3. These carrier signals are compared with

**Table 1** Rating and parameters of system used in simulation

| Parameters | Value | Parameters | Value |
|---|---|---|---|
| $S_{rated}$ | 15 MVA | $F_1 = F_2$ | 50 Hz |
| $V_{dc1} = V_{dc2}$ | 13 kV | $V_{sa}$ (RMS) | 11 kV |
| $L_s$ | 6 mH | $R_s$ | 0.5 Ω |
| $L_{arm}$ | 5 mH | $R_{arm}$ | 0.5 Ω |
| $C_{SM}$ | 75 μF | $c_{dc}$ | 0.23 μF/Km |
| $r_{dc}$ | 14 mΩ/Km | $l_{dc}$ | 0.16 mH/Km |

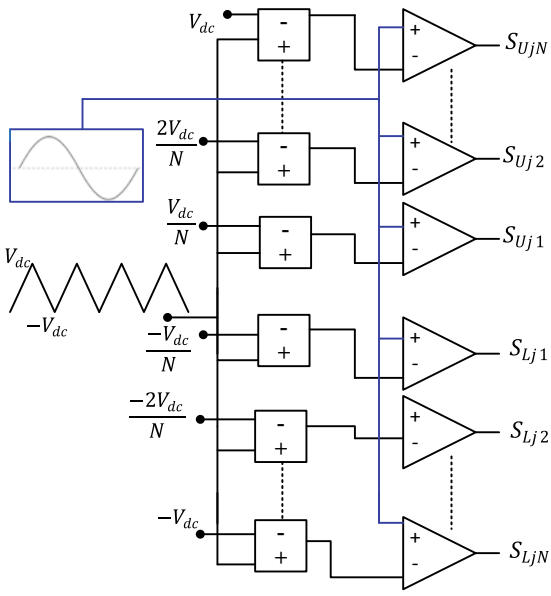


**Fig. 3** PD PWM pulse genration

the modulation signal $m \sin(\omega_1 t)$, where $\omega_1$ is the fundamental frequency of the system and $m \in \{1, -1\}$ is the modulation index in the linear modulation range. For $N + 1$ level modulation strategy, the corresponding lower arm SM switching states are obtained by complementing the switching state of the corresponding upper arm SM. Figures 4 and 5 show simulation waveforms of steady state operation of conv-1 and conv-2 at unity power factor respectively. The SM capacitor voltages of all the sixteen SMs of phase-A and phase-B are shown in Fig. 4f, g respectively. The SM capacitor voltages are $\frac{13\,\text{kV}}{8} = 1.6\,\text{kV}$ and ripple is less than 10%. The dc bus voltage ($V_{dc1}$), the active power ($P_1$) and reactive power ($Q_1$) of area-1, remain constant as seen from Fig. 4a, b which validates the effectiveness of controllers. The AC side grid currents are sinusoidal for both converters as shown in Figs. 4c and 5c and unity power factor is maintained as both voltage and current are in phase. The converter output voltages have nine levels and are very close to sinusoidal as in Fig. 4d. The $i_{cira1}$ of phase-A is plotted in Fig. 4e and it has second order component. The simulation waveform of receiving end converter (Conv-2) under typical full load operating conditions are given in Fig. 5. The $P_2$ and $Q_2$ controllers maintain the commanded active power and reactive power as decided by the grid-2. The SM capacitor voltages of conv-2 are shown in Fig. 5f, g respectively. These capacitor voltages are settled at 1.6kV with ripple less than 10%. The voltage ripple in Conv-1 and Conv-2 is within the designed values. Unity power factor is commanded because $Q_2^* = 0$ so the line currents are in pahe with the voltages and are sinusoidal as shown in Fig. 5c. The converter terminal voltages of conv-2 is shown in Fig. 5d. The $i_{cira2}$ of phase-A is plotted in Fig. 5e.

## 5 Experimental Verification and Results

A scaled down experimental prototype of HVDC system between two grids is fabricated in the lab. The area-2 consist of utility grid and converter-2 is made up of three-phase five-level ($M = 5$, $N = 4$) MMC, designed and fabricated in the lab. The $V_{dc}$ is derived from area-1 (grid-1) from a grid emulator using conventional two-level AC to DC PWM converter, controlled using closed loop vector control algorithm in rotating d-q reference frame. Each of the converters have separate independent dSPACE based digital controllers. Autotransformers are used to step down the voltages. The parameters are $V_{dc} = 100\,\text{V}$, Rated power $= 500\,\text{VA}$. Input voltage is 80 V RMS L-L. The SM capacitor is 1000 μF, arm inductor is 2 mH. The experimental results are given in Fig. 6. The line voltage in Fig. 6a shows 9 levels, the capacitor voltage ripples in Fig. 6b are within the design limits and these voltages are balanced. Figure 6c shows the sinusoidal line current ($i_a$) and the ac component of the circulation current ($i_{cira}$)is low. The $V_{dc}$ is kept constant as shown in Fig. 6d. The experimental results are in line with the simulation results.

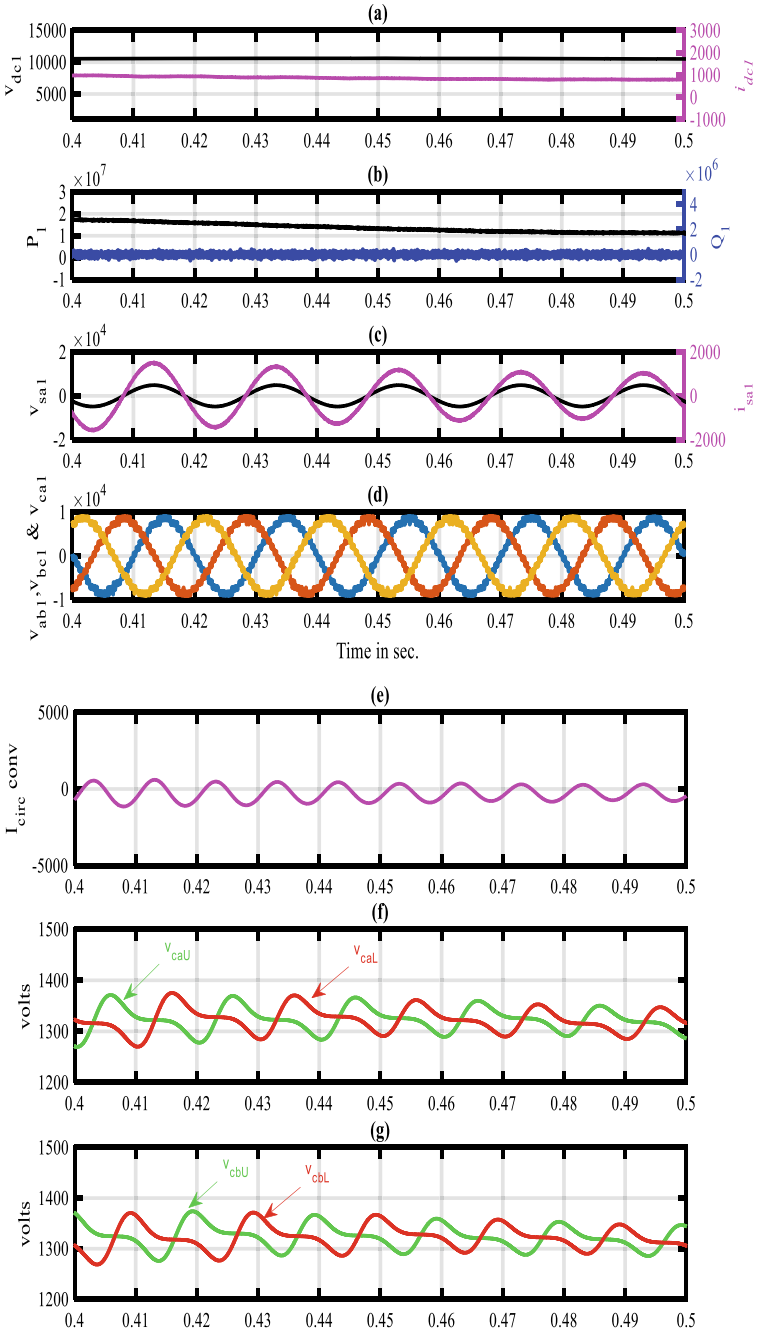


**Fig. 4** **a** Simulation waveforms of $V_{dc1}, I_{dc1}$, **b** $P_1$ and $Q_1$, **c** $V_{sa1}$ and $I_{sa1}$, **d** $V_{c1}$, **e** $i_{cir}$ and **f** $V_{sm\_a}$, **g** $V_{sm\_b}$ of conv-1 for full load operation at unity power factor

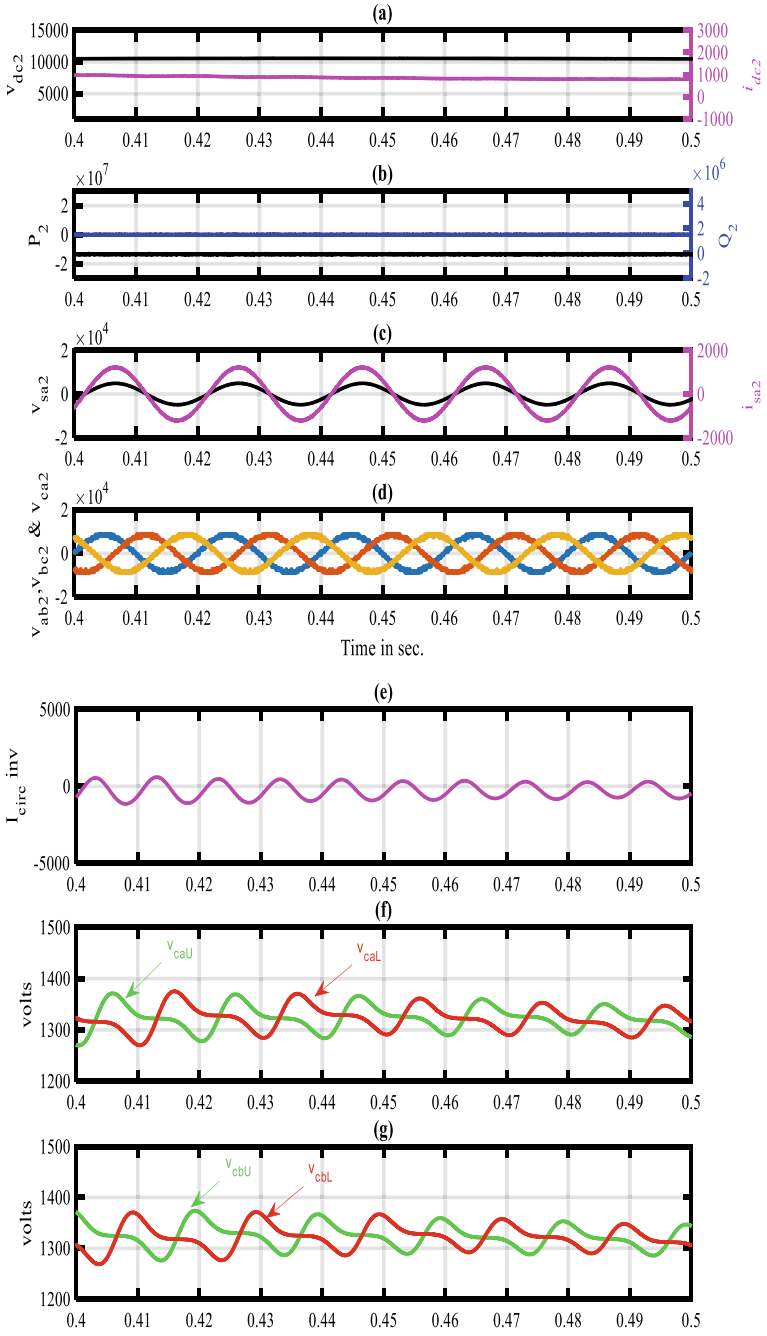


**Fig. 5** **a** Simulation waveforms of $V_{dc2}$, $I_{dc2}$, **b** $P_2$ and $Q_2$, **c** $V_{sa2}$ and $I_{sa2}$, **d** $V_{c2}$, **e** $i_{cir}$ and **f** $V_{sm\_a}$, **g** $V_{sm\_b}$ of conv-2 for full load operation at unity power factor

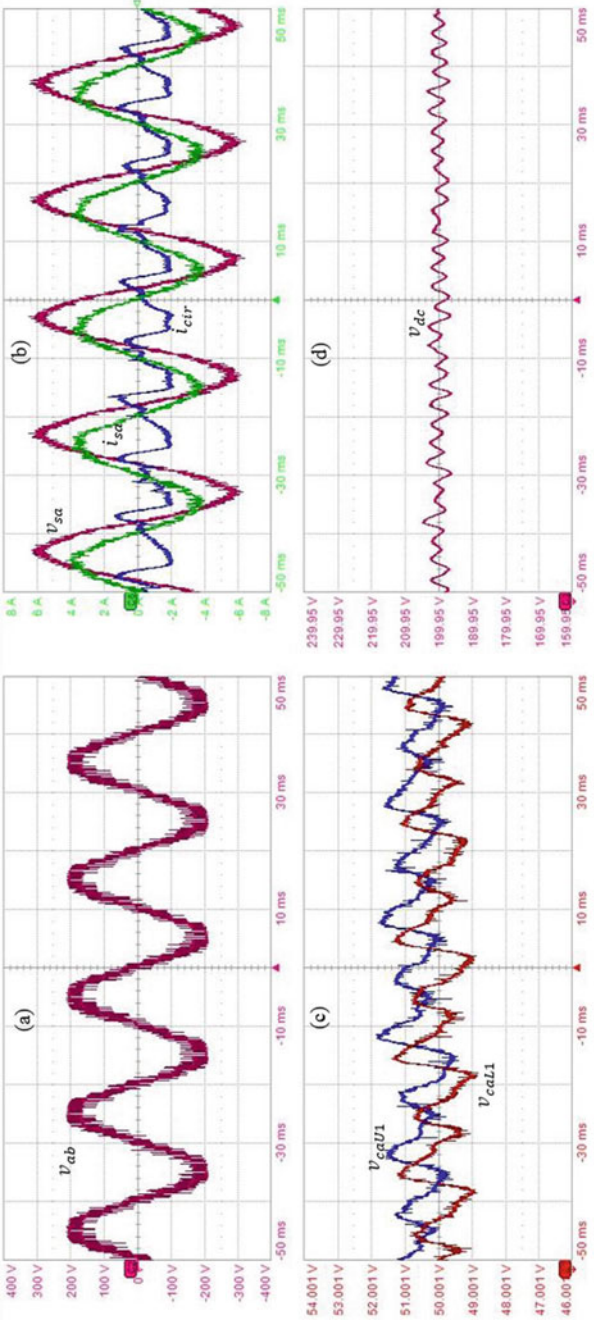


**Fig. 6** The experimental results at UPF, 500 W load. **a** Converter line to line voltage $v_{ab}$ (100 V/div). **b** $v_{sa}$ (40 V/div) and $i_a$ (2 A/div) and $i_{cir}$ (2 A/div). **c** SM Capacitor voltage $v_{caU1}$ and $v_{caL1}$ (1 V/div). **d** $v_{dc}$ (10 V/div)

## 6 Conclusions

The paper shows a novel PWM technique for the operation of MMC based unipolar HVDC system. PD-PWM technique has been used for switching the semiconductor devices of nine level MMC. The vector control method is used. The controllers maintain constant dc bus voltage during disturbances. The sorting algorithm keeps all the SM capacitor voltages equal around their nominal value. The grid currents are near sinusoidal and have low THD. Stable operation of the HVDC system is demonstrated. Overall the proposed algorithm works as desired and is capable to maintain the power flow between two areas.

## References

1. Bahrman MP, Johnson BK (2007) The ABCs of HVDC transmission technologies. IEEE Power Energy Mag 5:32–44
2. Xue Y, Zhang X-P (2016) Reactive power and AC voltage control of LCC HVDC system with controllable capacitors. IEEE Trans Power Systems 32:753–764
3. Zhang X-P (2004) Multiterminal voltage-sourced converter-based HVDC models for power flow analysis. IEEE Trans Power Syst 19:1877–1884
4. Richa, Beig AR, Al Jaafari K, Jayashree R, (2019) Operation of MMC based HVDC under SM failure at sending end converter. In: 2019 IEEE energy conversion congress and exposition (ECCE), Baltimore, MD, USA, pp 1040–1046
5. Guo J, Wang X, Bie Z, Hou Y (2014) Reliability modeling and evaluation of VSC-HVDC transmission systems. In: 2014 IEEE PES general meeting, conference & exposition, pp 1–5
6. Li Y, Guo J, Zhang X, Wang S, Ma S, Zhao B et al (2019) Over-voltage suppression methods for the MMC-VSC-HVDC wind farm integration system. IEEE Trans. Circ. Syst. II: Exp. Briefs
7. Sun K, Yao W, Fang J, Ai X, Wen J, Cheng S (2019) Impedance modeling and stability analysis of grid-connected DFIG-based wind farm with a VSC-HVDC. IEEE J. Emerg. Sel. Top. Power Electron.
8. Kartick JC, Sujit BK, Suparna K (2016) Dual reference phase shifted pulse width modulation technique for a N-level inverter based grid connected solar photovoltaic system. IET Renew Power Gener 10:928–935
9. Dekka A, Beig AR, Kanukollu S, Al Rahis MS (2014) Retrofitting of harmonic power filters in onshore oil drilling rigs: challenges and solutions. IEEE Trans Ind Appl 50:142–154
10. Liu X, Lv J, Gao C, Chen Z, Guo Y, Gao Z et al (2017) A novel diode-clamped modular multilevel converter with simplified capacitor voltage-balancing control. IEEE Trans Ind Electron 64:8843–8854
11. Sepahvand H, Liao J, Ferdowsi M, Corzine KA (2012) Capacitor voltage regulation in single-DC-source cascaded H-bridge multilevel converters using phase-shift modulation. IEEE Trans Ind Electron 60:3619–3626
12. Carrara G, Gardella S, Marchesoni M, Salutari R, Sciutto G (1992) A new multilevel PWM method: a theoretical analysis. IEEE Trans Power Electron 7:497–505
13. Veeranna S, Yaragatti U, Beig A (2012) Space vector-based synchronised bus-clamping pulse width modulation algorithms for three-level voltage source inverter in overmodulation region. IET Power Electron. 5:493–500
14. Ronanki D, Williamson SS (2019) A simplified space vector pulse width modulation implementation in modular multilevel converters for electric ship propulsion systems. IEEE Trans Transp Electr 5:335–342

15. Beig AR, Ranganathan V (2003) Influence of placement of small space vectors on the performance of PWM techniques for three level inverters. In: IECON'03. 29th Annual conference of the IEEE industrial electronics society (IEEE Cat. No. 03CH37468), pp 2764–2770
16. Richa, Jayashree R, Tariq M (2019) Vector control of modular multilevel converter based unipolar HVDC system. In: 2019 International conference on electrical, electronics and computer engineering (UPCON), Aligarh, India, pp 1–6
17. Yang X, Li J, Wang X, Fan W, Zheng TQ (2011) Circulating current model of modular multilevel converter. In: 2011 Asia-Pacific power and energy engineering conference, pp 1–6
18. Richa, Tariq M (2019) Vector control of modular multilevel converter based regenerative AC to DC converter. In: 2019 International conference on electrical, electronics and computer engineering (UPCON), Aligarh, India, pp 1–5
19. Zygmanowski M, Grzesik B, Nalepa R (2013) Capacitance and inductance selection of the modular multilevel converter. In: 2013 15th European conference on power electronics and applications (EPE), pp 1–10
20. Taha W, Beig AR, Boiko I (2018) Quasi optimum PI controller tuning rules for a grid-connected three phase AC to DC PWM rectifier. Int J Electr Power Energy Syst 96:74–85

# Single-Inductor Dual Outputs Buck-Boost Converter with Dual Switches


**Tzung-Je Lee and Chih-Yuan Chang**

**Abstract** This paper presents a single-inductor dual outputs buck-boost converter with only dual switches. The power distributive control and peak current control are used to improve the performance of load regulation and cross regulation. The proposed design is implemented with a typical 0.25 μm BCD process. The peak efficiency is simulated to be 87.69% at load current of 436 mA. The load regulation is 0.81 and 2.01 mV/mA for 1.0 V and 5.0 V, respectively. Besides, the cross regulation is 0.66 and 3.89 mV/mA for 1.0 V and 5.0 V modes, respectively. Moreover, the maximum load current is 2.234 A.

**Keywords** SIDO · Buck-buck converter · Dual switches

## 1 Introduction

With the fast development of portable devices, IoT (Intelligence-of-things), and Li-ion battery, DC/DC converter IC becomes a key component for the power management system. In a complex integrated system with different voltages, the buck-boost converter is needed for delivering power for dual outputs [1–7]. There are various types of buck-boost converters presented in several prior works. Figure 1a shows a dual switches buck-boost converter, which could transfer energy bi-directionally [1]. However, the output voltage is inverted, which is difficult to be used in IC design due to the ground issue. Figure 1b shows a non-inverting 4 switches buck-boost converter design [3]. Although the ground issue is avoided, it is not preferred for the IC design because of the large area penalty of the 4 power switches, especially for large current applications.

A 3 switches buck-boost converter with dual outputs is revealed in Fig. 2a [4–7]. The voltage is boosted for the output, $V_{sys32}$. $V_{sys31}$ could be bucked or boosted dependent on the loads, as shown in Fig. 2b. In the second phase, the inductor is charging and the inductor current keeps rising, if $V_{sys31} < V_{bat}$. For $V_{sys31} > V_{bat}$, the

T.-J. Lee (✉) · C.-Y. Chang
Department of Computer Science and Information Engineering, Cheng Shiu University, 83347 Kaohsiung, Taiwan
e-mail: tjlee@gcloud.csu.edu.tw



F. Shahnia and S. Deilami (eds.), *ICPES 2019*, Lecture Notes in Electrical Engineering 669, https://doi.org/10.1007/978-981-15-5374-5_7

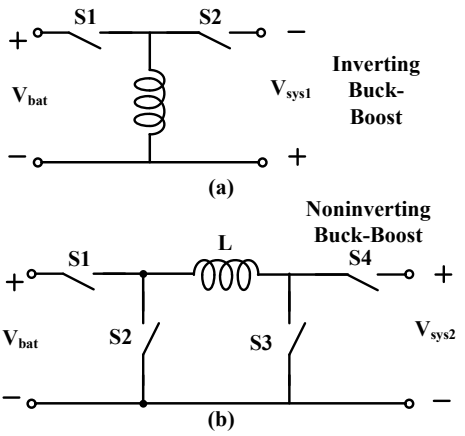


**Fig. 1** Topologies of **a** 2 switches and **b** 4 switches buck-boost converters

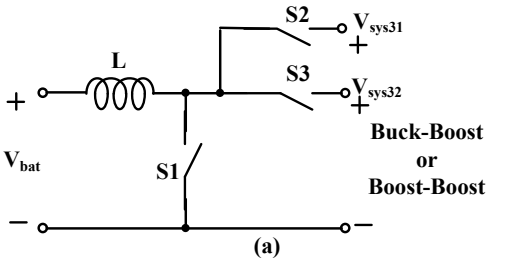


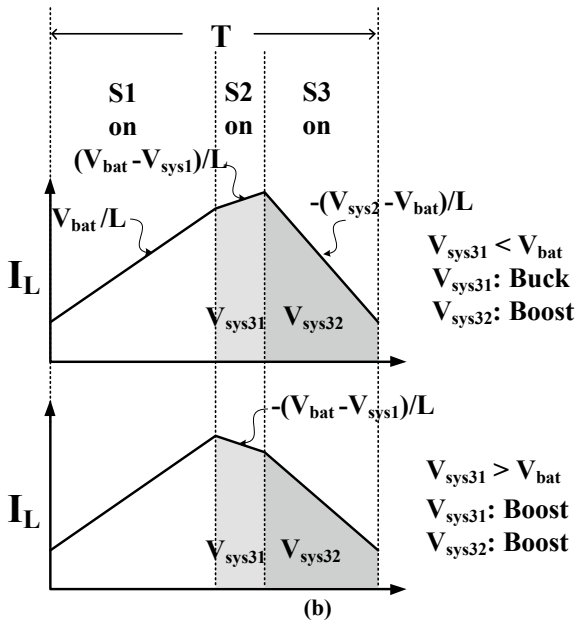


**Fig. 2** **a** Topology and **b** operating waveforms of the 3 switches buck-boost converter

inductor current becomes falling to deliver the required energy. Moreover, because the voltage mode control [4–6] and the type III compensation [7] could not provide small load regulation, the peak current control with type II compensation is used in this work to improve the load regulation.

To reduce the system cost, a dual output buck-boost converter with only dual switches is proposed in this paper. By using the power distributive and peak current control, the load regulation is 0.81 and 2.01 mV/mA for 1.0 V and 5.0 V modes, respectively. Besides, the cross regulation is 0.66 and 3.89 mV/mA for 1.0 V and 5.0 V outputs, respectively.

## 2 SIDO Buck-Boost Converter with Dual Switches

According to Fig. 2, the switch, S1, could be removed for the application of $V_{sys31} < V_{bat}$. It becomes a 2 switches dual outputs buck-boost converter, as shown in Fig. 3a, which is the proposed design. Only two phases are required for this topology. In the

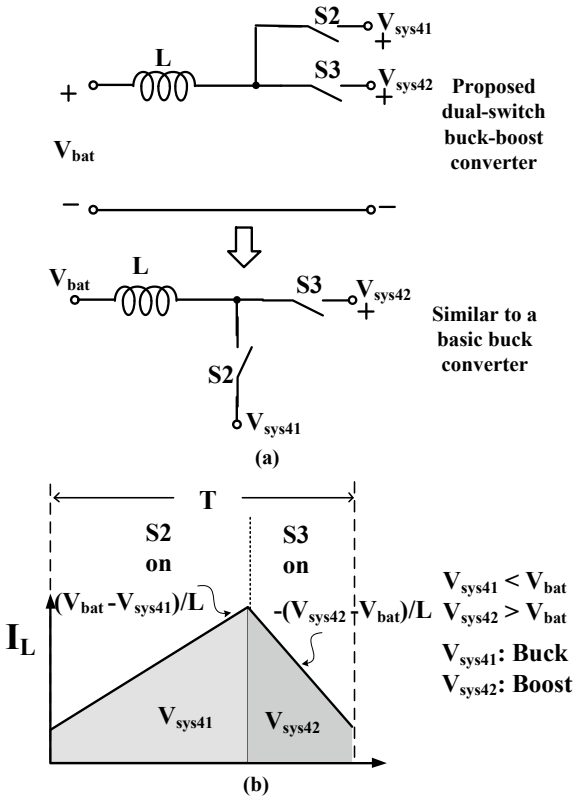


**Fig. 3** **a** Topology and **b** waveform of the proposed dual switches buck boost converter

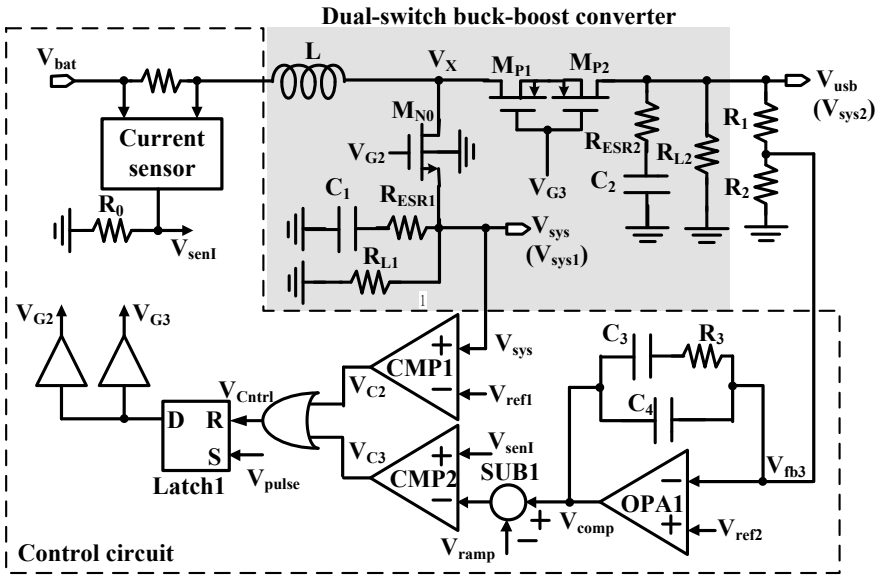


**Fig. 4** Block diagram of the proposed design

first phase, S2 is turned on to charging the inductor and the output, $V_{sys41}$. Notably, $V_{sys41}$ must be less than $V_{bat}$, thus, the circuit operates in the buck mode. In the second phase, the inductor delivers the energy to the second output, $V_{sys42}$, which is in the boost mode, as shown in Fig. 3b. Because $V_{sys41} < V_{bat}$, the circuit operates like a basic buck converter.

Figure 4 shows the block diagram for the proposed design. The circuit possesses a 3.6 V input, $V_{bat}$, from the li-ion battery and dual outputs, $V_{sys}$ and $V_{usb}$, for the 1.0 V and 5.0 V systems, respectively. The design is composed of a dual-switch buck-boost converter stage and a Control circuit. The dual switch buck-boost converter is comprised of an inductor, L, two capacitors, $C_1$ and $C_2$, a low-side switch, $M_{N0}$, and a highside switch, $M_{P1}$ and $M_{P2}$. The Control circuit includes two control loops, the power distributive control and peak current control loops. The power distributive control circuit, CMP1, senses the output signal, $V_{sys}$, and generates the control signal, $V_{C2}$, which is combined with the output of the peak current control circuit, $V_{C3}$. The peak current control circuit includes a feedback resistor string, a compensation circuit, as well as a comparator, CMP2, and a subtraction circuit, SUB1. The feedback resistor string consists of $R_1$ and $R_2$, to sense the output, $V_{usb}$ and generates a signal, $V_{fb3}$ for the compensation circuit. The compensation circuit is a Type II compensator, including OPA1, $R_3$, $C_3$, and $C_4$, to provide the required phase for the stable operation. The output of the compensation circuit, $V_{comp}$, is then subtracted by a ramp signal, $V_{comp}$, to eliminate the sub-harmonic oscillation. The subtraction result is compared to the signal, $V_{senI}$, which is the output of the current sensor, and generates the output signal, $V_{C3}$, for the peak current control. The control signals, $V_{C2}$ and $V_{C3}$, are

combined by OR gate to obtain the control signal, $V_{Cntrl}$. $V_{Cntrl}$ is coupled to the reset terminal of the SR latch, Latch1. The set terminal of Latch1 is a 1 MHz periodic pulse signal, $V_{pulse}$. The output of Latch1 is followed by two buffers to generate the control signals, $V_{G2}$ and $V_{G3}$, for the low-side switch and the high-side switch, respectively.

Notably, because the output, $V_{sys}$, is less than $V_{bat}$, the NMOS transistor, $M_{N0}$, is used as the power switching MOS transistor. For the second output, $V_{usb}$, the serial $M_{P1}$ and $M_{P2}$ are used to prevent the leakage current through the parasitic diodes. Besides, there are two control loops in the design, including the power distributive control [4] and the peak current control, for the two phase operation. In the first phase, $V_{sys}$ is compared to a target reference voltage, $V_{ref1}$. When $V_{sys} > V_{ref1}$, it indicates that $V_{sys}$ reaches its target voltage and the first phase is stopped. In the second phase, $V_{usb}$ is feedback in a peak current control with a Type II compensation circuit. $V_{C3}$ is obtained for the second phase operation. The output $V_{C3}$ is then combined with $V_{C2}$ to determine the final switching.

## 3 Implementation and Simulation

The proposed design is implemented using a typical 0.25 μm BCD process. The 5.0 V devices are used in this design. Figure 5 shows the layout of the design, where the area is 878.8 × 1266.3 $\mu m^2$. As shown in Fig. 6, the output ripple is simulated to be 130 mV and 150 mV for $V_{sys}$ and $V_{usb}$, respectively. Besides, $V_{pulse}$ is used to trigger the control signal $V_{G2}$ and $V_{G3}$. $V_{Cntrl}$ is to deactivate $V_{G2}$ and $V_{G3}$.

Figures 7 and 8 show the simulation results of the load regulation and the cross regulation. $I_{L1}$ and $I_{L2}$ are the load current through the outputs, $V_{sys}$ and $V_{usb}$, respectively. Based on the simulation results, the load regulation is 0.81 and 2.01 mV/mA for 1.0 V and 5.0 V, respectively. The cross regulation is 0.66 and 3.89 mV/mA for $V_{sys}$ and $V_{usb}$, respectively.

Figure 9 reveals the simulated efficiency. The peak efficiency is 87.69% at load current of 436 mA. Table 1 shows the comparison with several prior works. The proposed design possess the large output current and only 2 switches is used. By

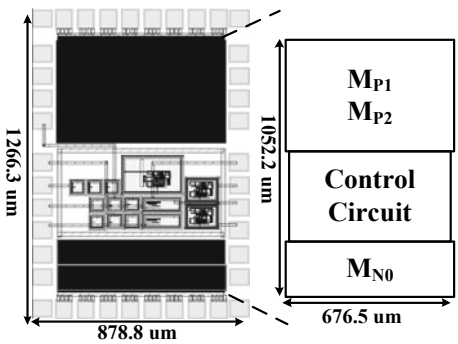


**Fig. 5** Layout of the proposed design

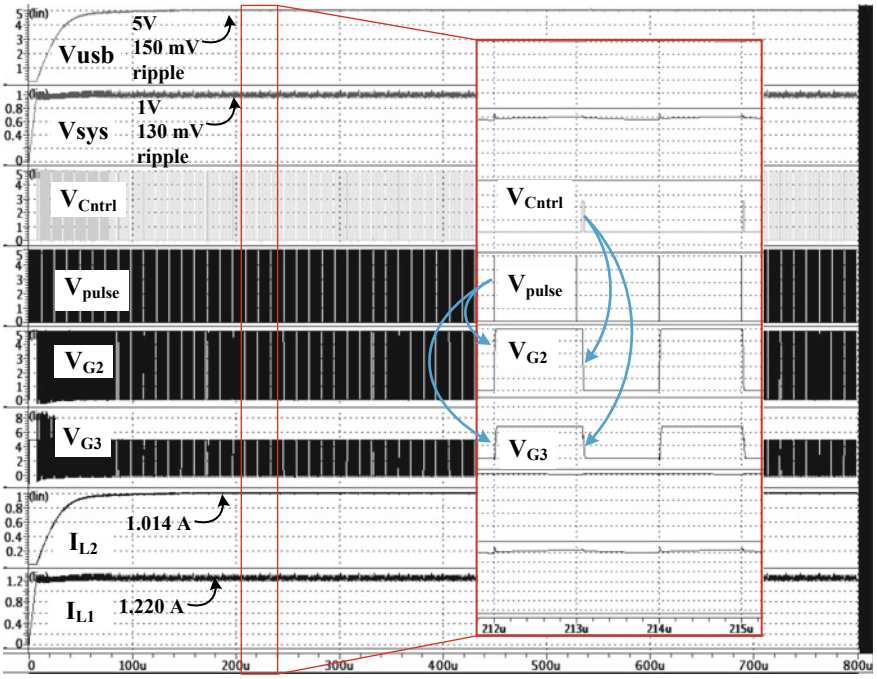


**Fig. 6** Simulated waveforms in steady state

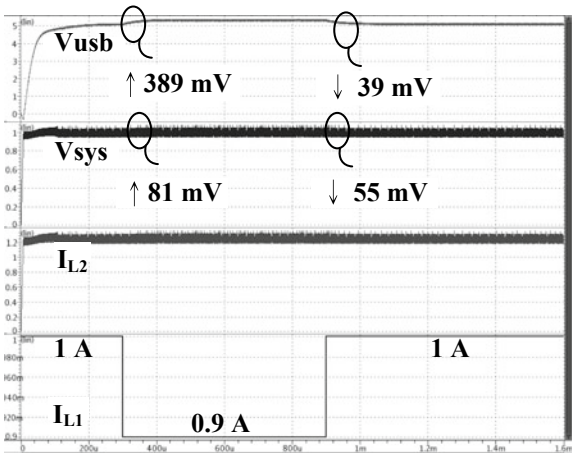


**Fig. 7** Simulated waveforms of the load regulation and cross regulation with the load current, $I_{L1}$, varied from 900 to 1000 mA

considering the FOM (Figure-of-Merit) of the cross regulation, switches and output channel quantity, as well as the max. output current, the proposed design possesses the best performance.

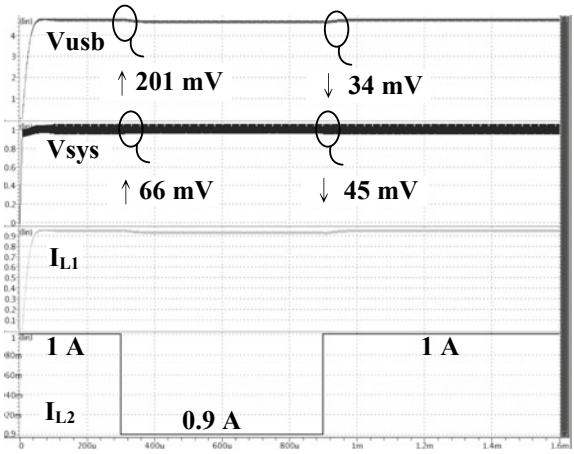


**Fig. 8** Simulated waveforms of the load regulation and cross regulation with the load current, $I_{L2}$, varied from 900 mA to 1000 mA

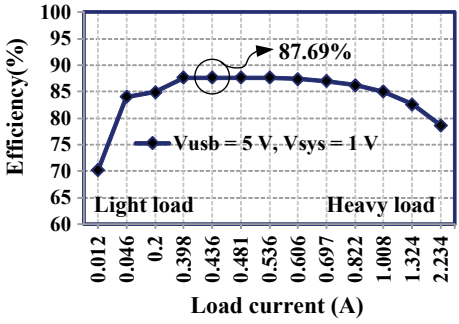


**Fig. 9** Simulated efficiency with the output current from 0.012 A to 2.234 A

## 4 Conclusion

This paper proposes a dual switches SIDO buck-boost converter. With the power distributive control and peak current control, the performance of load regulation and cross regulation is improved with a large output current. Besides, the system cost is also reduced because of only 2 switches used.

**Table 1** Comparison with several prior works

| | This work | [4] | [7] | [8] | [9] | [10] |
|---|---|---|---|---|---|---|
| Year | 2019 | 2009 | 2013 | 2017 | 2019 | 2017 |
| Publication | ICPES | PEDS | ISNE | EDSSC | MEJ | TCAS-II |
| Process (μm) | 0.25 | 0.35 | 0.18 | 0.18 | 0.18 | 0.35 |
| Switching Freq. (kHz) | 1000 | 400 | 1000 | N/A | 1000 | 40 |
| L (μH) | 9 | 10 | 10 | 10 | 10 | 22 |
| C (μF) | 33/22 | 4.7 | 4.7 | 6.9/47 | 4.7/4.7 | 4.7 |
| Input voltage (V) | 3.6 | 2.7–3.3 | 1.6–3.3 | 0.5–1.8 | 0.5–1.0 | 3.3 |
| Output voltage (V) | 1.0/5.0 | 2.5/3.6 | 2.5/3.3 | 1.8/3.0 | 1.8/1.2 | 1.8 |
| Max. output current (mA) | 1220/1014 | 50/90 | 180/100 | 120 | 40/40 | 12 |
| Peak/worst efficiency (%) | 87.69 | 90.6 | 91.5 | 88.6 | 91 | 84.6 |
| Core area ($mm^2$) | 0.712 | 1.87 | 3.0 | 1.369 | 0.52 | 2.42 |
| Load regulation (mV/mA) | 0.81/2.01 | N/A | 2/2.7 | N/A | N/A | N/A |
| Cross regulation (mV/mA) | 0.66/3.89 | N/A | 0.1/2.4 | N/A | 0.2/0.11 | N/A |
| Output ripple (mV) | 130/150 | 50/50 | 16/18 | N/A | N/A | 100 |
| Modes | Buck-boost | Buck-boost | Buck-boost | Boost | Boost | Buck-boost |
| Outputs | 2 | 2 | 2 | 2 | 2 | 2 |
| Switches | 2 | 3 | 3 | 3 | 3 | 7 |
| FOM | 1.74 | N/A | 9.64 | N/A | 3.75 | N/A |

*Note* FOM = (Worst cross regulation × Switches No. × 1000)/(Max. output current × output no.)

**Acknowledgements** This research was partially supported by the Ministry of Science and Technology under grant no. MOST 108-2221-E-230-008- as well as Cheng Shiu University under grant CS-2-108-19. Moreover, the authors would like to express their deepest appreciation to TSRI (Taiwan Semiconductor Research Institute) of NARL (National Applied Research Laboratories), Taiwan, for the assistance of thoughtful chip fabrication.

## References


1. Moo C-S, Jian J-Y, Wu T-H, Yu L-R, Hua C-C (2013) Battery power system with arrayed battery power modules. In: 2013 International conference on system science and engineering (ICSSE), pp 437–441
2. Lee Y-H, Huang S-C, Wang S-W, Wu W-C, Huang P-C, Ho H-H, Lai Y-T, Chen K-H (2012) Power-tracking embedded buck-boost converter with fast dynamic voltage scaling for the soc system. IEEE Trans Power Electron 27(3):1271–1282
3. Wu K-C, Wu H-H, Wei C-L (2015) Analysis and design of mixed-mode operation for noninverting buck-boost DC-DC converters. IEEE Trans Circuits Syst II Express Briefs 62(12):1194–1198
4. Chang H-W, Chang W-H, Tsai C-H (2009) Integrated single-inductor buck-boost or boost-boost DC-DC converter with power-distributive control. In: International conference on power electronics and drive systems, 2009 (PEDS 2009), pp 1184–1187
5. Li G-L, Chen Y-C, Chang Y-T, Tsai C-H, Chen H-S (2012) A single-inductor dual-output DC-DC converter with output voltage mode switching. In: 2012 IEEE 13th workshop on control and modeling for power electronics (COMPEL), pp 1–4
6. Huang C-S, Chen D, Wu T-H, Chen Y-J (2011) Mix-voltage power conversion for single-inductor dual-output (SIDO) boost converters and SIDO bipolar converters. In: Proceedings of the 2011 14th European conference on power electronics and applications, pp 1–10
7. Huang C-Y, Chen Y-C, Tsai C-H (2013) Integrated single-inductor dual output DC-DC converter with power-distributive control. In: 2013 international symposium on next-generation electronics, pp 33–36
8. Sheu M-L, Tsao L-J, Liang K-C (2017) A single-inductor dual-output boost DC-DC converter with 0.5 V start-up. In: 2017 international conference on electron devices and solid-state circuits (EDSSC), pp 1–3
9. Liu L-N, Chen C, Liao X-F, Huang W-B, Mu J-C, Zhu Z-M (2019) A low cross-regulation and high-efficiency SIDO boost converter with near-threshold start-up. Microelectron J 87(2019):22–32
10. Qian Y, Zhang H, Chen Y, Qin Y, Lu D, Hong Z (2017) A SIDIDO DC-DC converter with dual-mode and programmable-capacitor-array MPPT control for thermoelectric energy harvesting. IEEE Trans Circuits Syst II Express Briefs 64(8):952–956

# Voltage Unbalance Mitigation Using Controlled Vehicle to Grid (V2G) Strategy


**Trinnapop Boonseng, Anawach Sangswang, and Sumate Naetiladdanon**

**Abstract** In the near future, electric vehicles (EV) will play an important role in society around the globe and affect the electrical power system. For instance, there would sometimes be a period of electric shortage in a case of high volume of electric consumption. This sample issue might be prevented by enacting a policy of charging EV during the peak time of electric consumption. Apart from the electric shortage during the peak hours, voltage unbalance could also be another concern due to the fact that most EV stations are supplied by single phase electricity. Many previous researches have used V2G as an ancillary source supporting peak demand and frequency regulation. This research presents a method to mitigate the problem of voltage unbalance by utilizing vehicle to grid technology management. The EVs are tested IEEE 14 Bus model using DigSILENT PowerFactory Programming. The results show that when V2G mode in EVs is managed by discharging them at selected for a suitable number of EV customers. The Voltage Unbalance Factor (VUF) decreases and satisfies the IEC standard.

**Keywords** V2G · Voltage unbalance · Distribution system · EV demand · Charging/discharging · Power quality

## 1 Introduction

Nowadays, plug-in hybrid electric vehicles (PHEV) and battery electric vehicle (BEV) are playing essential roles in transportation system in most of the countries worldwide. There are many advantages of PHEV and BEV such as reduction of the level of carbon dioxide emission which causes pollution issues and cheaper

T. Boonseng (✉) · A. Sangswang · S. Naetiladdanon
Department of Electrical Engineering, King Mongkut's University of Technology, Thonburi, Thailand
e-mail: trin_eng@hotmail.com

A. Sangswang
e-mail: Anawach.san@kmutt.ac.th

S. Naetiladdanon
e-mail: sumate.nae@kmutt.ac.th



F. Shahnia and S. Deilami (eds.), *ICPES 2019*, Lecture Notes in Electrical Engineering 669, https://doi.org/10.1007/978-981-15-5374-5_8

maintenance cost than traditional vehicles which consume fuel and petrol. However, the increasing in number of using electric vehicles (EVs) can cause many impacts in the distribution system. As a result, the electric consumption of EVs is controlled using the charging regimes [1]. This may have an adverse impact on power quality phenomenon such as voltage drop, harmonics and voltage imbalance etc. [2].

The proliferation of EVs also causes the DSO to adjust demand. Furthermore, Vehicle to Grid (V2G) is a new technology that can be installed at charging stations to return electrical energy from PHEV's and BEV's battery to the distribution system. This will help to stabilize voltage. However, the station must be a bidirectional charging system. as well as the PHEV and BEV must be equipped with state of charge (SOC) controller system to alleviate any incident during plugging in to charge or return the electrical power into the system to meet this purpose. Furthermore, The V2G Technology [3, 4] can stabilize the electrical system and frequency in distribution system and can act as spare electrical power for the distribution system in the vehicles when the power consumption level is high. Some previous researches have used V2G with ESS(Energy Storage System) to store energy during the off-peak time and then generate during the peak time to mitigate impacts in stability and power quality.

By considering the research gaps outlined in the above paragraphs, this research paper presents a simple and efficient strategy based on combination of selective phase discharging and allowance of controlled numbers of V2G customers for participation to mitigate the Voltage Unbalance Factor without ESS. The theories related to the developed methodology is described in Sect. 2 followed by the analysis results in Sect. 3. Finally, Sect. 4 describes the conclusions derived from our study.

## 2 Theories

### *2.1 Smart Grid and EV Charging*

Smart grid system is critical to plug-in electric vehicles in terms of monitoring distribution system and signaling to control the distribution system for charging the vehicles efficiently by grid to vehicle technology (G2V) and for returning the power into the electric system by vehicle to grid technology (V2G) as show in Fig. 1.

Distribution System Operators (DSOs) are primarily responsible to distribute the electrical power to the local grid. The recent-increase in number of EVs relatively raises the power demand as well. To prevent this issue, DSOs must balance the load properly, especially during the peak time of the power consumption or when there is any fault in the power system.

Aggregator service is mainly responsible for aggregating the EV volumes (MW until a certain level) in V2G mode and supply the electric power into the system whenever necessary. However, DSOs and Aggregator must suitably communicate with each other to meet this purpose [5].

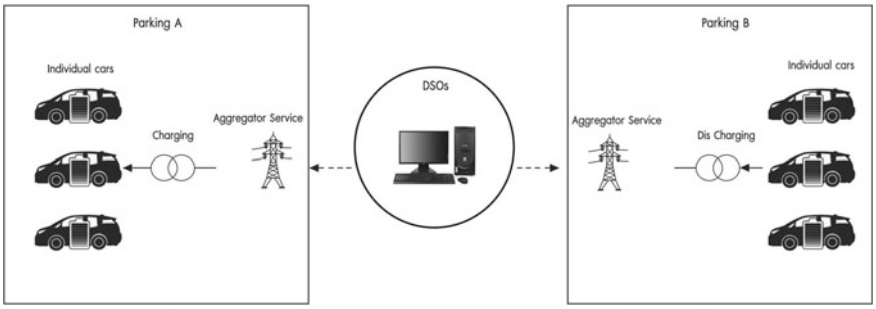


**Fig. 1** DSO and aggregator system controlling EV charging

A difference between PHEV and BEV is that PHEV is a hybrid technology which is mainly driven by fuel and can switch to be driven by power in its battery, while BEV is exclusively driven only by the battery power. Consequently, PHEV and BEV will be used to explain in the research paper as "EV".

The charging power into the vehicles for this study is taken from the standard of North America and Europe as shown in Tables 1 and 2 [6]. The charging standard in the United States of America is normally at 120 V Level 1 or 240 V Level 2 as can be seen from Table 1. Also, there is a controlling standard of power quality which is ANSIC84.1 2011 [7]. In Europe, 230 V single phase and 400 V three phase power systems are being used broadly with the standard of power quality EN50160 [8] as given in Table 2. Apart from this, IEC 62196 [9] and SAE J1772 [10] standards define that charging type 1 is using in North America and Japan, but charging type 2 is used in Europe as per Table 2.

**Table 1** North America standard charging

| Charging level type | Voltage level | Power level |
|---|---|---|
| Level-1 | 120 VAC | Up to 1.8 kW |
| Level-2 | 208–240 VAC | Up to 19.2 kW |
| Level-3 (DC charging) | 480 VDC | 50–150 kW |

**Table 2** Europe standard charging

| Charging level type | Voltage level | Power level |
|---|---|---|
| Level-1 | Single-phase 230 VAC | Up to 4.6 kW |
| Level-2 | Tri-phase 400 VAC | Up to 44 kW |
| Level-3 (DC charging) | 480 VDC | 50 W–150 kW |

The power demand of EV can be calculated

$$P_{Demand}(t) = P_{\max}\left\{n - \sum_{i=1}^{n} e^{-\left(\alpha_i \eta_r \cdot \frac{t_i}{t_{\max}}\right)}\right\} \quad (1)$$

where

$P_{\max}$ is Maximum battery capacity of EV
$\alpha$ is Battery Charging Constant
$\eta_r$ is Charger rectifier efficiency
$t$ is Charging time
$t_{\max}$ is Maximum Charging time.

## 2.2 V2G Technology

There are two types of EV charging station: namely, unidirectional charging and bidirectional charging. The unidirectional charging station refers to charge the power in the same direction of EV by receiving the power from grid to store in the battery, while the bidirectional charging statio refers to charging the power both directions which consist of receiving the power from grid, called Grid to Vehicle (G2V) and returning the power from a battery to grid, called Vehicle to Grid (V2G). V2G is a challenge of DSOs because they have to become more active and flexible to control the use of power between grid and EV. From the study, it is found that 95% of the electric vehicles are parked without using, V2G will be activated. V2G can be separated into 2 groups which are Vehicle to Home (V2H), returning the power to accommodations, and Vehicles to Building (V2B), returning the power to buildings [11]. In this case, V2G will provide the power as a spare source for accommodations and buildings through being triggered by a signal when there is a shortage of the power for the accommodations and building or when there is any defect in the power system. However, the EVs can become V2G mode depending on the permission of EV owner if their condition such as sufficient state of charge(SOC) for next travel can be met.

The V2G power can be calculate [12]

$$P_{Export}(t) = \sum_{i=1}^{n} P_{Initial}\left\{1 - e^{-\left(\beta_i \eta_r \cdot \frac{t_i}{t_{\max}}\right)}\right\} \quad (2)$$

$P_{Initial}$ is Initial Power in EV
$\beta$ is Battery Discharging Constant
$\eta_i$ is Inverter efficiency
$t$ is Charging time
$t_{\max}$ is Maximum Charging time.

State of charge (SOC) can be calculate [13]

$$SOC_k = SOC_{in} + \frac{t_k - t_{in}}{t_{out} - t_{in}}(SOC_{out} - SOC_{in}) \tag{3}$$

$SOC_{in}$ is State of Charge at Plug in time
$SOC_{out}$ is State of Charge at Plug out time
$t_{in}$ is Time of Plug in
$t_{out}$ is Time of Plug out
$t_k$ is Current time.

### 2.3 Voltage Unbalance

Voltage unbalance in the three phase power is a case where the voltages of A phase, B phase and C phase are different from the standard of Voltage Unbalance Factor (VUF) by more than 2% (refer to the standard of IEC 61000-2-4:2000-06) can be calculate [14]

$$VUF = \sqrt{\frac{1 - \sqrt{3 - 6\beta_{VUF}}}{1 + \sqrt{3 - 6\beta_{VUF}}}} \times 100 \tag{4}$$

$$\beta_{VUF} = \frac{|V_{ab}|^4 + |V_{bc}|^4 + |V_{ca}|^4}{|(V_{ab}|^2 + |V_{bc}|^2 + |V_{ca}|^2)^2} \tag{5}$$

$V_{ab}$ is line voltage between phase a and b.
$V_{bc}$ is line voltage between phase b and c
$V_{ca}$ is line voltage between phase c and a

## 3 Simulation and Case Study

The IEEE 14 Bus is used to simulate the impacts of EVs on VUF. The Bus 14 has a feeder where the EVs are installed as can be seen from Figs. 2 and 3. The function of the Feeder is to receive the power from the Bus 14 [15]. Loads in the Feeder are separated into 2 types: namely Base Load and EV Load. The simulation of charging EV Load is computed using Eq. (1) and Time of Use [16] is for controlling the charging power into the EVs. All the EVs are assumed to be charged in the off-peak time. Yet, it will begin charging in phase A, phase B and phase C in Fig. 4. This is a behavior of charging that may occur in reality. The parameters used for simulation is shown in the Table 3.

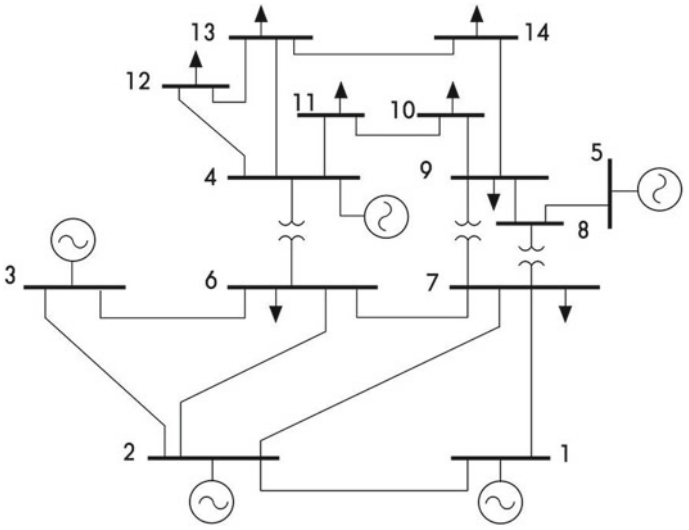


**Fig. 2** IEEE 14 BUS

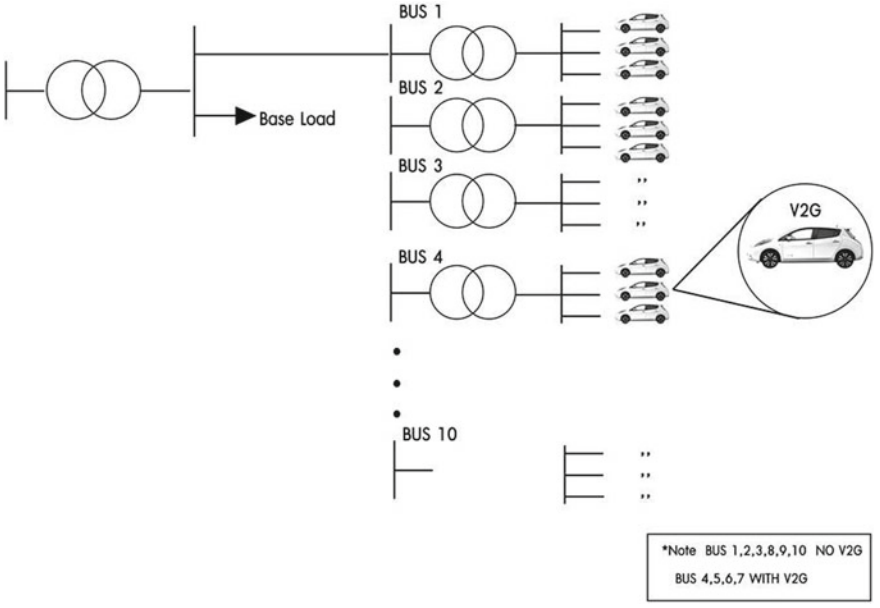


**Fig. 3** EV feeder with connected in BUS14 in IEEE14 BUS

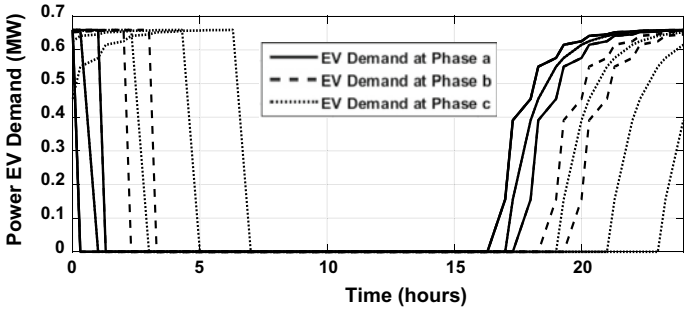


**Fig. 4** Power EV demand each phase

**Table 3** Parameter for simulation

| Parameter | Value |
|---|---|
| EV' brand | Nissan leaf (NLEV) |
| Travel range at SOC 100% | 250 km |
| Charging type | Single phase level 2 |
| Number of EV each phase | 400 cars |
| Number of BUS | 10 Bus |
| $P_{\max}$ | 6.6 kW |
| $P_{Initial}$ | 6.6 kW |
| $\alpha$ | 8.443 |
| $\eta_r$ | 85% |
| $\beta$ | 9.2103 |
| $\eta_i$ | 85% |
| $t_{\max}$ | 8 h |

The analysis is carried out for 2 scenarios according to the charging profile shown in Fig. 4. It is assumed that all incident can occur in the future and cause power quality issues. In each scenario, the EVs which can switch from G2V mode to V2G are assumed to have owners have permission and sufficient state of charge (SOC) for the next trip as shown in Fig. 5. The EVs in buses 1, 2, 3, 8, 9, 10 following charging Model 2 and the EVs connected in buses 4, 5, 6, 7 follows the Charging Model 1. Furthermore, the owner of the 2 charging model uses only 12% of SOC and stores 88% of SOC a day therefore, DSOs and Aggregator will not drain the SOC below 12%.

In the first scenario, all EVs are directly connected to EV charging station without V2G mode. The second scenario is divided into two cases. Case 1 considers the situation where some of the EVs from scenario 1 is turned on to be V2G mode

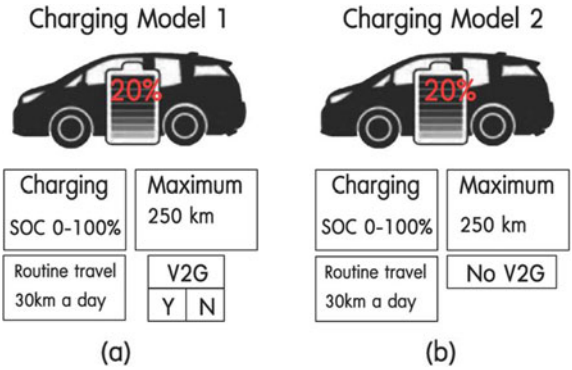


**Fig. 5** Charging model behavior for each bus

without controlled phase discharging whereas case 2 considers controlled selective phase discharging and different maximum number of EV consumers connection.

**Scenario 1**

By charging profile using TOU technique, it is to avoid charging during peak hours of the power consumption in Fig. 4 it can be seen that chargings power of A phase, B phase and C phase are different in association with periods that user begins charging the power. After EV 400 cars in each phase have been fully charged during 4.30 pm to 6.30 am next day (every car in Feeder). The results from DIGSILENT programming language (DPL) simulation as. show in Fig. 6 a comparison between base load demand versus total EV demand. Figure 7 shows VUF (%) at Bus 14 of IEEE 14 Bus. It shows that the starting time charging between 4.30 pm to 1 am. VUF (%) increased and is obvious that hours between 1.30 am and 4.30 am there is unbalance phase among a, b and c of the power which goes over 2% of VUF for certain periods of time. Figure 8 shows Maximum Different EV Power of $P_{ab}$, $P_{bc}$, $P_{ca}$.

**Scenario 2**

As can be seen from scenario 1, VUF is over the IEC standard value of 2%. Hence,

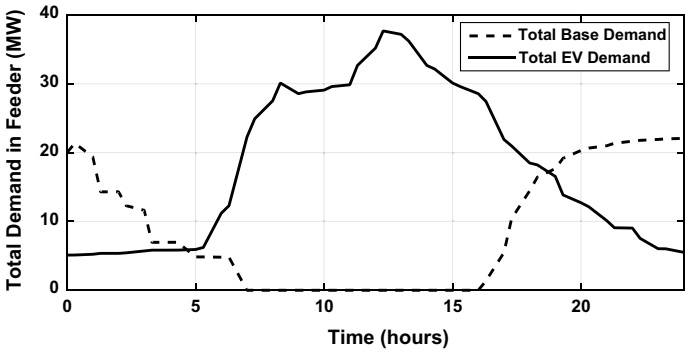


**Fig. 6** Total demand in EV feeder

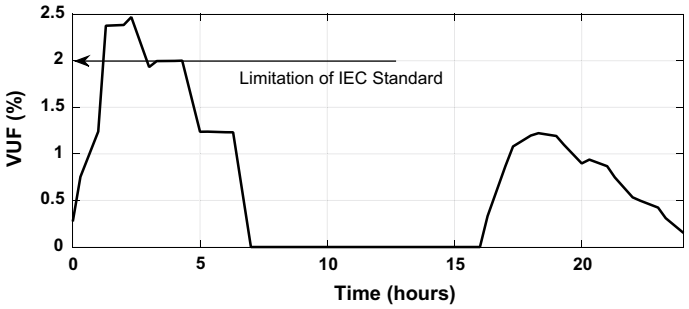


**Fig. 7.** VUF (%) for Scenario 1

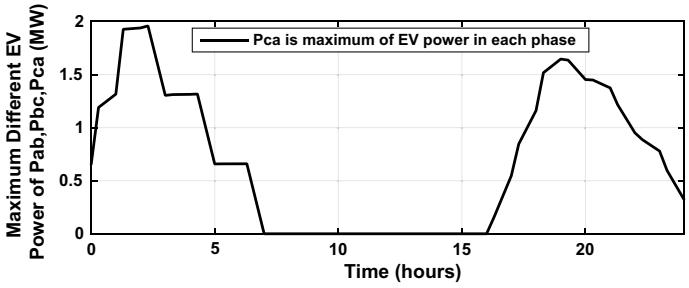


**Fig. 8.** Maximum different EV power of $P_{ab}$, $P_{bc}$, $P_{ca}$

V2G technology will be installed in this scenario for compensating the power into the system during 1.30 am to 4.30 am. Assume that DSO needs V2G to activate for compensation during that time. EVs could be noticed in each car during 8 h of charging (maximum capacity: SOC = 100%) which is calculated in Eq. (3). In each phase and in each Bus of Feeder, EV will fully charge 400 cars. In the scenario 2 is separated to two case. First case is uncontrolled V2G each Phase, V2G is activated by selecting EV which obtained user's permission to return the power. A concern is that returning the power must not impact on battery for next day. The permission of EV to become V2G is populated 60,150,200 cars of each phase at Bus 4, 5, 6, 7 and the power of V2G can be calculate in Eq. (2). In this case will activate every ready V2G which DSO require to compensate during the problem in the period of time. Then, DPL simulation analyze its results in Fig. 9. As a result, EV in a mode of V2G without control each phase properly cause the fact that VUF gets worse. Figure 10 Shows Maximum Different EV Power of $P_{ab}$, $P_{bc}$, $P_{ca}$ as the result shows that V2G can maintain the maximum of different phase which is decreased with increasing of the number of EV in V2G mode but VUF (%) is still not satisfied with IEC standard during that time

Second case is controlled V2G each phase, According to scenario 1 and 2 (case 1), VUFs are over 2% of the standard. This leads to use V2G technology with controlled in each phase for compensating the power during 1.30 am to 4.30 am from charging

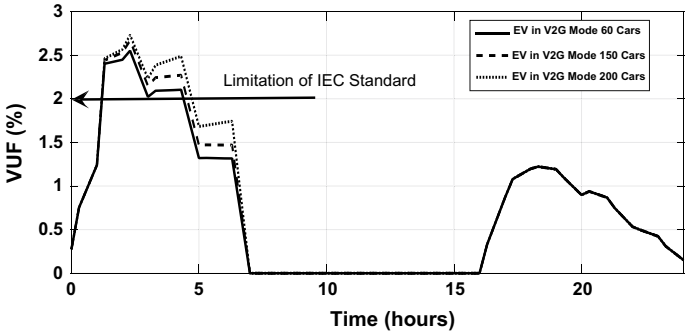


**Fig. 9** VUF (%) For Scenario 2 case 1

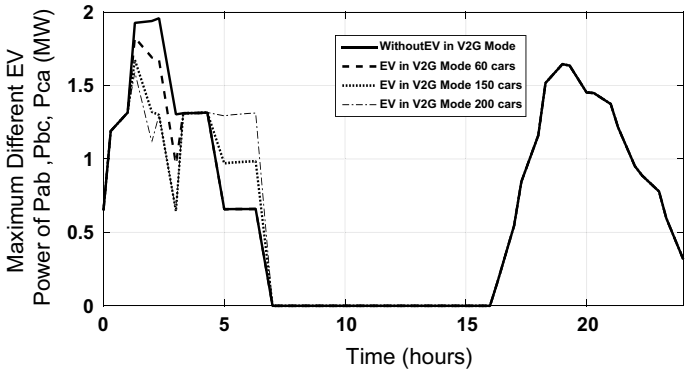


**Fig. 10** Maximum different EV power of $P_{ab}$, $P_{bc}$, $P_{ca}$

profile Phase a has fully charged and stopped at 1 am and there is an issue that phase b and phase c still need 1.30 h and 5 h respectively to get charged until SOC = 100%. Also, V2G is required users to permit for returning the power into the system. Figure 8 shows the maximum of different EV Power each phase is $P_{ca}$ then the V2G will be activated only Phase c. V2G is selected from The permission of EV to become V2G is populated 60,150,200,300 cars of phase c at Bus 4, 5, 6, 7 as Scenario 2 (case 1). Moreover, V2G is analyzed its results in each phase properly. In this case will activate ready V2G by control only maximum different phase during the problem in the period of time The results from DPL simulation in Fig. 11 show that if V2G is activated with the controlled in each phase suitably (300 cars at BUS 4, 5, 6, 7 in Phase c in the Feeder), VUF value is in a range of acceptance. Figure 12 Shows Maximum Different EV Power of $P_{ab}$, $P_{bc}$, $P_{ca}$ as the result shows that V2G can maintain the maximum of different phase as scenario 2 case 1. If V2G mode is controlled by activating only phase c the maximum different EV power will be decreased during that time and the VUF (%) is satisfied with IEC standard.

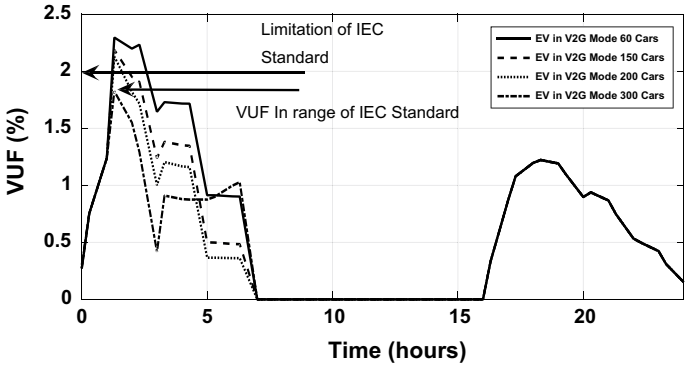


**Fig. 11** VUF (%) For Scenario 2 case 2

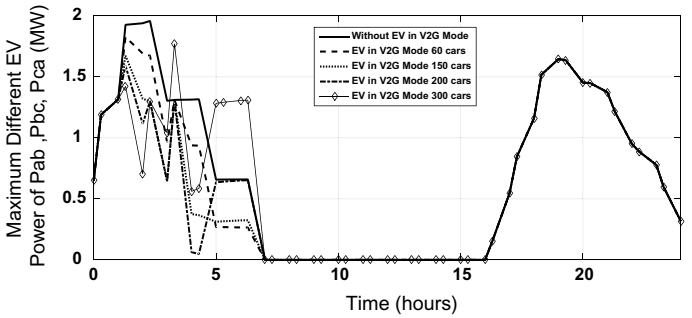


**Fig. 12** Maximum different EV power of $P_{ab}$, $P_{bc}$, $P_{ca}$

## 4 Conclusion

Due to the upward trend of EV connection in the distribution system worldwide, it is certain that there will be an adverse impact on the power. This research analyzes the impact V2G techology on VUF as well as provides the mitigation strategy to improve it.The following results are observed from our analysis:

1. The VUF increases over IEC standard when the EVs are charged between 1:30 am and 4:30 am.
2. The VUF is well over the limit of IEC standard when V2G mode is activated and are discharged charging through all the phases. This condition worsens with the increase in number of customers (Highest with 200 cars).
3. The VUF falls below the IEC standard when the EVs are only discharged through phase c for the given test system. Furthermore, the VUF is highest when the number of V2G is low (60 cars) and low when the number of V2G is high (300 cars) when they are only discharged through phase c.

Our future work will use probabilistic method to model in the charging/discharging and state of charge of the battery of V2G and use stochastic optimization to schedule them for mitigation of power quality issues.

## References

1. McCarthy, D., Wolfs, P.: The HV system impacts of large scale electric vehicle deployment in a metropolitan area. In: 20th Australasian Universities Power Engineering Conference, Dec 2010
2. Aljanad, A., Mohamed, A (2015) Impact of plug-in hybrid electric vehicle on power distribution system considering vehicle to grid technology: a review. J Appl Sci Eng Technol 1404–1413
3. Panich S, Govind Singh J (2015) Impact of plug-in electric vehicles on voltage unbalance in distribution system. Int J Eng Sci Technol 7(3):76–93
4. Hassan Mohamed T, Ahmed Hassan H (2018) Terminal voltage and power regulation using vehicle-to-grid (V2G) schemes connected to a two area power system. In: 20th international Middle East power system conference (MEPCON), Dec 2018
5. Kaufmann A (2017) Vehicle-to-grid business model entering the swiss energy market. Master Thesis, Institute of Economy and Environment, Univ. St Gallen
6. Dubey A, Santoso S (2015) Electric vehicle charging on residential distribution system: impacts and mitigations. IEEE Access 3:1871–1893
7. American National Standard for Electric Power System and Equipment Voltage Ratings (2011) ANSI Standard C84.1–2011
8. Voltage Characteristics of Public Distribution System (2011) ISO Standard IN EN 50160
9. IEC Standard 62196 (2014) Plugs, socket-outlets, vehicle connectors and vehicle inlets conductive charging of electric vehicles
10. SAE Standard J1772 (2013) SAE electric vehicle and plug in hybrid electric vehicle conductive charge coupler
11. Berthold F, Ravey A (2015) Design and development of a smart control strategy for plug-in hybrid vehicles including vehicle-to-home functionality. IEEE Trans Transp Electr 3:168–177
12. Uwakwe C, Mahajan M (2017) Modeling of V2G net energy injection into the grid. In: 6th international conference on clean electrical power (ICCEP), Aug 2017
13. Han H, Huang D, Liu D, Li Q (2017) Autonomous frequency regulation control of V2G (vehicle to grid) system. In: 29th Chinese control and decision conference (CCDC), May 2017
14. Klayklueng T, Dechanupaprittha S (2013) Impact analysis of EVs charging in low voltage system using DIgSILENT. EECON-36, 11–13, Dec 2013
15. Klayklueng T, Dechanupaprittha S (2015) Impact analysis on voltage unbalance of plug-in electric vehicle home charging in thailand distribution system. In: 23rd international conference on electricity distribution, June 2015
16. Ranathunga RMGD, Samaliarachchi LA (2017) Impact of electric vehicle load on the system load profile of Sri Lanka. J Inst Eng Sri Lanka

# Research on Digital Voltage Regulation Technology of Diesel Generator Set Based on DSP


**Qin Lv, Shanshui Yang, Li Wang, and Dafeng Fu**

**Abstract** Generator voltage regulator is an indispensable part of maintaining the normal operation of diesel generator set, which plays an important role in the safe and stable operation of the generator set. At present, there are mainly two types of regulator named transistor-based analog voltage regulator and microprocessor-based digital voltage regulator. In view of the advantages that the digital voltage regulator has incomparable with the traditional analog voltage regulator, this paper designs a digital voltage regulator based on the TMS320F28335 chip for a certain type of vehicle diesel generator. The input and output interface circuit of the digital voltage regulator is designed, including the analog conditioning circuit, the digital conditioning circuit, the excitation main circuit and the excitation driving circuit, etc., to fabricate the power board. The software minimum control system is designed by using the DSP minimum system with TMS320F28335 as the core controller, and the voltage and excitation current double loop adjustment mode is adopted. Set up a system experiment platform to test the regulator to meet the expected functional requirements.

**Keywords** Diesel · Generator set · Analog voltage regulator · Digital voltage regulator · TMS320F28335

Q. Lv · S. Yang (✉) · L. Wang · D. Fu
Department of Electrical Engineering, Nanjing University of Aeronautics and Astronautics, Nanjing, China
e-mail: yshanshui@nuaa.edu.cn

Q. Lv
e-mail: lvqin87@163.com

L. Wang
e-mail: liwang@nuaa.edu.cn

D. Fu
e-mail: 13813814961@139.com



F. Shahnia and S. Deilami (eds.), *ICPES 2019*, Lecture Notes in Electrical Engineering 669, https://doi.org/10.1007/978-981-15-5374-5_9

## 1 Introduction

The performance of the voltage regulator is directly related to the operation safety and stability of the power system. The voltage regulator affects the steady-state accuracy and dynamic characteristics of the output voltage of the alternator [1]. It is an important part of the power system. With the development of voltage regulation technology, while realizing its own steady-state voltage regulation accuracy, it can often complete some important protection functions [2] such as limiting the load current of the generator, the soft start function, and the excitation current limit, etc.

At present, most of the voltage regulators used in generators are analog. There are several control modes, such as voltage single loop regulation, voltage and load current double loop regulation, voltage and excitation current double loop regulation [3, 4], output voltage feedback combined with excitation current regulation. For example, the reference [2] designed an analog voltage regulator for a 45 kVA alternator. Analog regulators are difficult to debug, adjust, and modify in the face of synchronous alternators with nonlinear characteristics. At the same time, it is difficult to implement advanced algorithms, and its dynamic response accuracy is not high, and the dynamic performance is poor in the variable frequency power system. Compared with analog voltage regulator, digital voltage regulator has the advantages of strong anti-interference, flexible control strategy, easy adjustment of control parameters, and recordable data.

There are several digital control strategies of alternator voltage regulator, such as digital control strategy [5], adaptive control strategy [6], fuzzy control strategy [7], fuzzy control strategy based on T-S model [8], multivariable excitation blur control strategy [8]. References [4, 9] have carried out research on the digital voltage regulation technology of brushless generators, which can meet the requirements of steady state performance and transient performance of voltage regulator. Reference [10] studies the digital voltage regulation technology of hybrid excitation synchronous motors. In [11], the digital voltage regulator is designed by fuzzy filtering algorithm and field current limiting method, which verifies the feasibility of the voltage regulator in the variable speed constant frequency (VSCF) system. Reference [12] uses FPGA to adjust and control the power output. However, most of the regulators on the market today are analog voltage regulators, and digital regulators have fewer applications.

This paper designs a digital voltage regulator based on TMS320F28335 chip for a certain type of vehicle diesel generator. In the Altium Designer environment, the input and output interface circuit of the digital voltage regulator is designed, including the analog conditioning circuit, the digital conditioning circuit, the excitation main circuit and the excitation driving circuit to make the power board. The DSP minimum system based on TMS320F28335 is adopted, and the software control algorithm is designed by means of voltage and excitation current double loop adjustment. Set up a system experiment platform to test the regulator to meet the expected functional requirements.

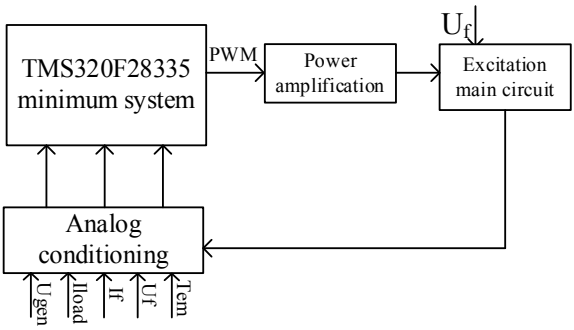


**Fig. 1** Digital voltage regulator block diagram

## 2 Regulator Structure and Working Principle

The block diagram of the digital voltage regulator is shown in Fig. 1. It mainly includes the following parts: TMS320F28335 minimum system, analog quantity detection and conditioning circuit, digital input and output interface, power amplification and excitation main circuit.

The working principle of the digital voltage regulator is: the output voltage $U_{gen}$ and the excitation current $I_f$ of the generator are detected by the power board conditioning circuit and then output to the A/D conversion module of the DSP to convert the analog signal into a digital signal. The DSP generates a PWM wave according to the digital signal obtained by sampling, and then uses a drive circuit to control the switching state of the MosFET in the excitation main circuit. The software algorithm is used to track the change of the generator output voltage in real time, change the duty cycle of the PWM, and change the excitation current to achieve the purpose of stabilizing the output voltage of the generator. Similarly, the load current $I_{load}$ passes through the detection conditioning circuit, and is sampled and converted into a digital signal by the A/D conversion module, and the software judges whether there is an overload or not. The output voltage adjustment function is mainly realized by controlling the PWM duty cycle of the MosFET.

## 3 Voltage Regulator Hardware Design

The regulator detects the following analog quantities such as three-phase AC voltage, load current (generator output current), excitation current, excitation voltage, and generator stator temperature signal, etc.

### 3.1 Non-similar Double Redundancy Voltage Detection Circuit

Regardless of the control mechanism of the generator voltage regulator, it is necessary to timely and effectively detect the control object. The regulator regulates the generator output voltage by adjusting the generator excitation current. The performance of the generator voltage detection circuit has a decisive influence on the accuracy and stability of the voltage regulation.

First, the three-phase AC output of the generator is stepped down, and the voltage is divided by a resistor to make the voltage value acceptable to the operational amplifier. As shown in Fig. 2, taking the phase A as an example, when the generator outputs a rated voltage of 220 V, the output after the step-down is a sine wave with an amplitude of about 7.73 V.

Two forms of voltage detection conversion circuits are used:

One is the average value detection, as shown in Fig. 3. When the generator is rated for output, the $U_{TABC}$ output is about 2.1 V DC.

Another way is to detect the voltage of each phase, as shown in Fig. 4, taking the phase A as an example. The booster circuit is used to raise the converted alternating current of each phase to a positive value, and then the voltage value is read by the

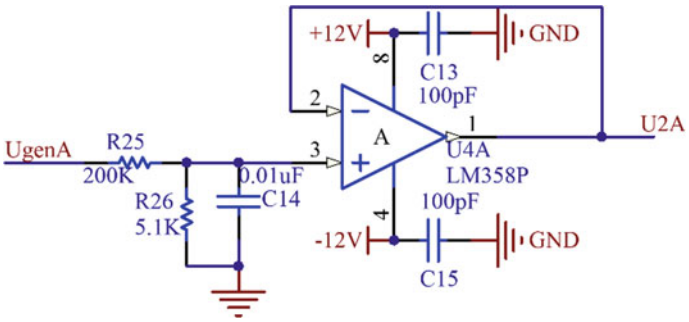


**Fig. 2** Buck converter circuit (take phase A as an example)

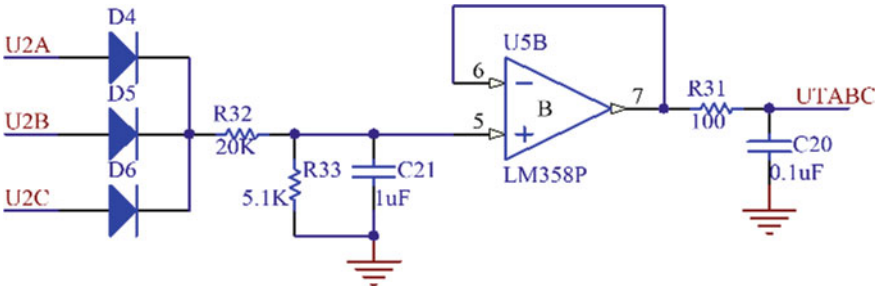


**Fig. 3** Voltage average detection circuit

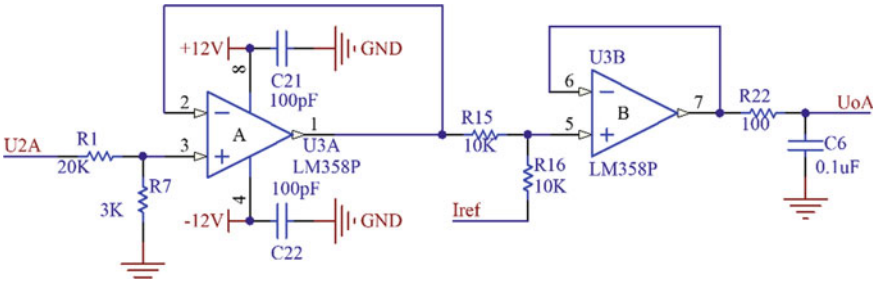


**Fig. 4** Voltage boost circuit (take phase A as an example)

DSP for the effective value calculation. When the generator is rated for output, the voltage after lifting is between 0.2455 and 1.2545 V.

These two voltage detection circuits constitute a non-similar double redundancy detection circuit. The average detection circuit has a fast response speed and a small lag time, and can be used as a voltage adjustment feedback detection circuit, so that the dynamic response of the system is good. The voltage RMS detection circuit can truly reflect the effective value of the voltage, and can be used as a reference indicator for generator protection, which can effectively protect the generator and also serve as a backup for the average voltage detection circuit.

## *3.2 Excitation Current Detection Circuit*

The excitation current detection circuit is shown in Fig. 5. The sensor ACS714LLCTR-20A-T is selected, the operating temperature is −40–85 °C, the sensitivity is 100 mV/A, the power supply of the sensor is 5.0 V, and the response speed is 5 μs. The output voltage of the chip is:

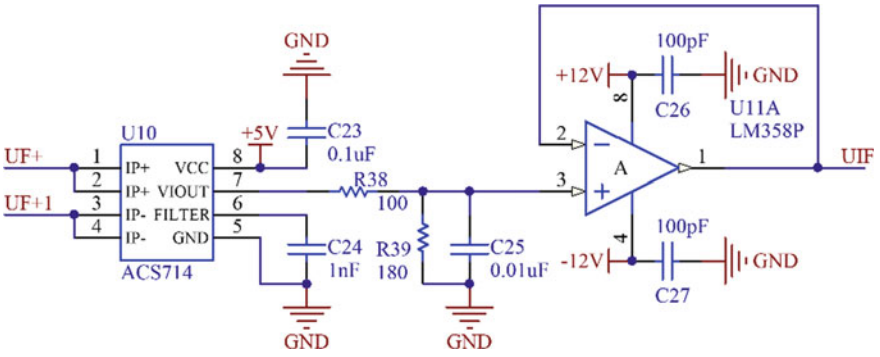


**Fig. 5** Excitation current detection circuit

$$V_{out} = 0.1I_f + 2.5\,(\mathrm{V}) \tag{1}$$

In the indicator, the excitation current is 6 A continuously and the maximum is 10 A. When the excitation current is greater than 12 A (duration 1 s), the output is directly turned off and an excitation overcurrent alarm is issued. Leave a margin, take the maximum excitation current of 20 A, the maximum output voltage of this circuit is 4.5 V. UF+ and UF + 1 are connected between the excitation power supply output and the field winding. When the output of ACS714 is 4.5 V, the UIF is 2.89 V.

## 4 Voltage Regulator Software Design

DSP is the control core of the digital voltage regulator. It collects the output voltage, output current, frequency and other parameters of the generator, and completes the voltage regulation algorithm. The output PWM wave controls the excitation current of the main generator.

In order to complete the above functions, this article selects TMS320F28335 high-performance microcontroller. The TMS320F28335 digital signal processor is a 32-bit floating point DSP controller. Compared with the previous fixed-point DSP, the device has high precision, low cost, low power consumption, high performance, high peripheral integration, large data and program storage, and more accurate and fast A/D conversion. Powerful data processing capabilities enable real-time operations on very complex control algorithms, ensuring real-time control of digital regulators.

The DSP minimum system structure diagram is shown in Fig. 6, including the DSP and its peripheral circuits.

### *4.1 Software Overall Process*

The overall process of the regulator software is shown in Fig. 7. Whether the regulator works depends on whether the speed of the generator reaches the specified value. When the output voltage value is lower than the safe value, turn off the voltage regulation system.

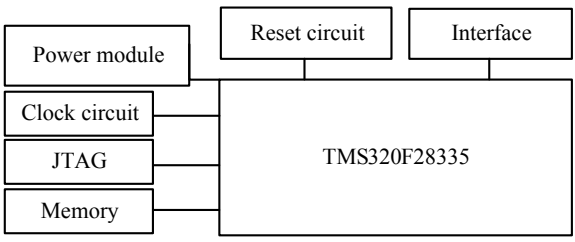


**Fig. 6** DSP minimum system structure

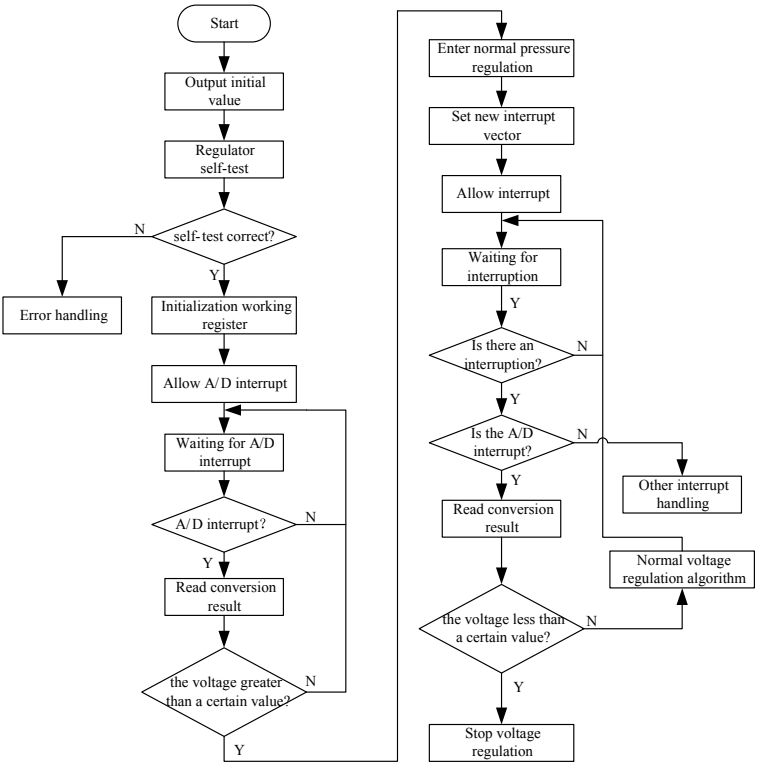


**Fig. 7** Digital regulator software flow chart

First set the initial value of the regulator and perform a self-test. When the self-test is correct, initialize the working register and allow the A/D interrupt. After waiting for A/D conversion, the digital value is used to judge the magnitude of the output voltage. When it is greater than a certain value, normal voltage regulation can be performed. If the condition is not met, the A/D interrupt is continuously waited. After entering the normal voltage regulation, set a new interrupt vector. When the output voltage value is lower than the set value, turn off the voltage regulation system, otherwise continue the voltage regulation step.

## *4.2 Control Algorithm Structure*

In this paper, the voltage and excitation current double loop regulation system is selected. The block diagram of the structure is shown in Fig. 8.

Diesel set may need to be loaded and unloaded with different loads during operation. The digital voltage regulator uses a composite PID control algorithm. The

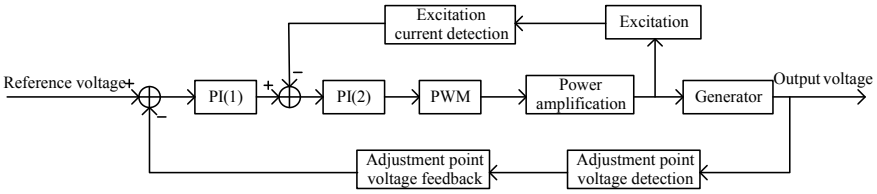


**Fig. 8** Block diagram of voltage and excitation current double loop regulation system

voltage of the main generator is controlled by adjusting the excitation current. The sampled feedback signal contains harmonic ripple components that affect the stability of the controller. To this end, the smoothing filter is eliminated by the whole period.

When the system requires a step load of the full load amplitude to be applied to the generator, the adjustment time and overshoot need to meet the corresponding requirements. The general PI algorithm accumulates too large points in large deviations, which is likely to cause excessive overshoot, which not only prolongs the adjustment time, but also does not meet the system requirements. In order to improve the speed of the voltage regulator, this paper uses a composite PID control algorithm. The PID algorithm is an algorithm controlled by the ratio of deviation (P), integral (I) and differential (D). Compared to analog voltage regulators, it has the characteristics of simple principle, easy implementation, independent control parameters, and simple selection of parameters.

## *4.3 Data Acquisition Interrupt Module*

The ADC interrupt is started by the periodic interrupt of the event manager EVA timer T1, and the frequency of the sampling is changed by adjusting the value of the T1 period register. The function of the data acquisition interrupt service subroutine is mainly to read the data of the AC voltage collected from the ADC register, digitally filter the data, and finally rewrite the flag bit to inform the main program that the AD sampling has been completed.

## *4.4 Frequency Capture Interrupt Module*

Set the transition detection mode of CAP1 of the event manager EVA to the rising edge capture. When the rising edge adjacent to the square wave signal output by the zero-crossing comparator is captured, it will cause a capture interrupt. In the frequency capture interrupt service subroutine, the difference between the two count

values represents the period of the square wave signal with the count period of the timer as the time reference, that is, the period of the generator output voltage signal.

## 5 Experiment

After testing the hardware circuit and software algorithm of the voltage regulator, build a system experiment platform, as shown in Fig. 9. The generator has a rated output of 20 kVA, a rated output phase voltage of 230 V and a frequency of 50 Hz.

### *5.1 Step-by-Step Loading and Unloading Experiment*

Three programmable electronic loads were used for step-by-step loading and unloading experiments. Due to the limitations of the experimental equipment, the maximum output of the three programmable electronic loads is 12.9 kVA, so the maximum load can be 50–65%, that is, from 10–12.9 kVA.

The test results of steady-state voltage, steady-state voltage change, excitation current, stabilization time and peak change under U = 230 V and PF = 1 are shown in Table 1.

### *5.2 Sudden Loading and Unloading Experiment*

The experiments of sudden loading and unloading 12.9 kVA resistive load were carried out respectively. The test results are shown in Table 2. The waveforms of the generator output voltage are shown in Figs. 10 and 11. It can be seen that the voltage regulator completes the voltage regulation process with 212.5 ms and 431.25 ms respectively.

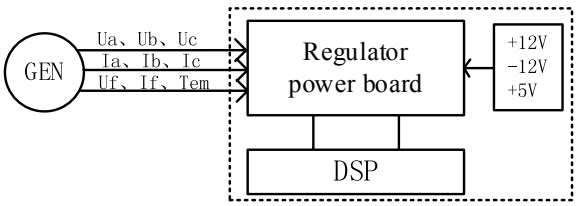


**Fig. 9** System experiment platform framework

**Table 1** Step-by-step loading and unloading experimental test results (U = 230 V PF = 1)

| P (three phase kVA) | | Steady-state voltage (V) | Steady state voltage change (V) | Excitation current(A) | Stabilization time (ms) | Peak change(V) |
|---|---|---|---|---|---|---|
| 0 | No load | 230.2 | | 0.24 | | |
| 5 (25%) | Load | 229.94 | 0.26 | 0.28 | 121.875 | 7.5 |
| 10 (50%) | Load | 229.65 | 0.29 | 0.38 | 181.25 | 10 |
| 12.9 (65%) | Load | 229.33 | 0.32 | 0.48 | 121.875 | 6.875 |
| 10 (50%) | Unload | 229.53 | 0.2 | 0.39 | 340.625 | 8.125 |
| 5 (25%) | Unload | 229.75 | 0.22 | 0.28 | 203.125 | 11.875 |
| 0 | No load | 229.96 | 0.21 | 0.23 | 212.5 | 11.0 |

**Table 2** Sudden loading and unloading experimental test results (U = 230 V PF = 1)

| P (three phase kVA) | | Steady state voltage (V) | Steady state voltage change (V) | Excitation current (A) | Stabilization time (ms) | Peak change (V) |
|---|---|---|---|---|---|---|
| 0 | No load | 229.96 | 0.21 | 0.23 | 212.5 | 11.0 |
| 12.9 (65%) | Load | 229.03 | 0.78 | 0.47 | 212.5 | 24.6 |
| 0 | No load | 229.90 | 0.72 | 0.23 | 431.25 | 27.5 |

## 6 Conclusion

This paper designs a digital voltage regulator based on TMS320F28335 chip for a certain type of vehicle diesel generator. The two voltage detection circuits and excitation current detection circuits in the hardware circuit are mainly introduced. The software minimum control system is designed by using the existing DSP minimum system with TMS320F28335 as the core, and the voltage and excitation current double loop adjustment mode is adopted. The system experimental platform is built, and the voltage regulator is loaded and unloaded step by step, and the sudden loading and unloading test is performed to meet the expected functional requirements.

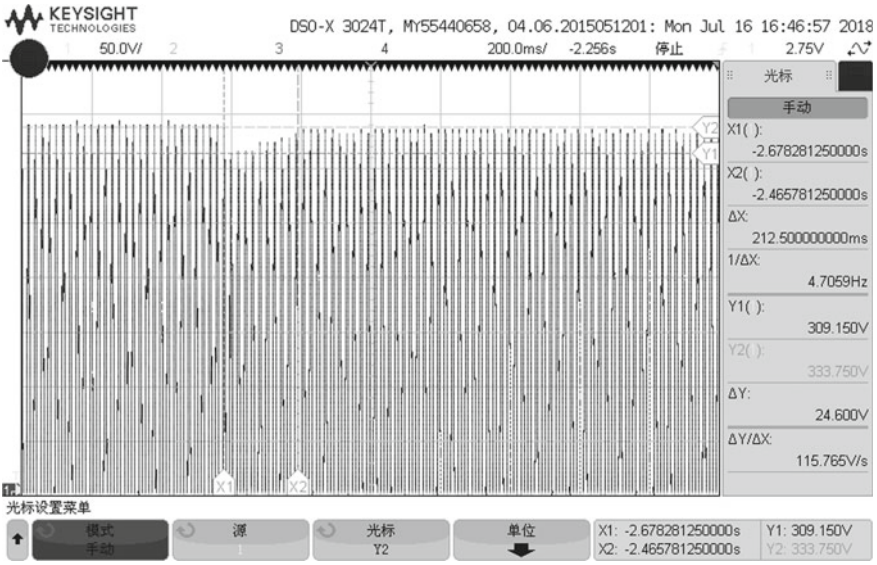


**Fig. 10** Voltage waveform when a 12.9 kVA resistive load is added

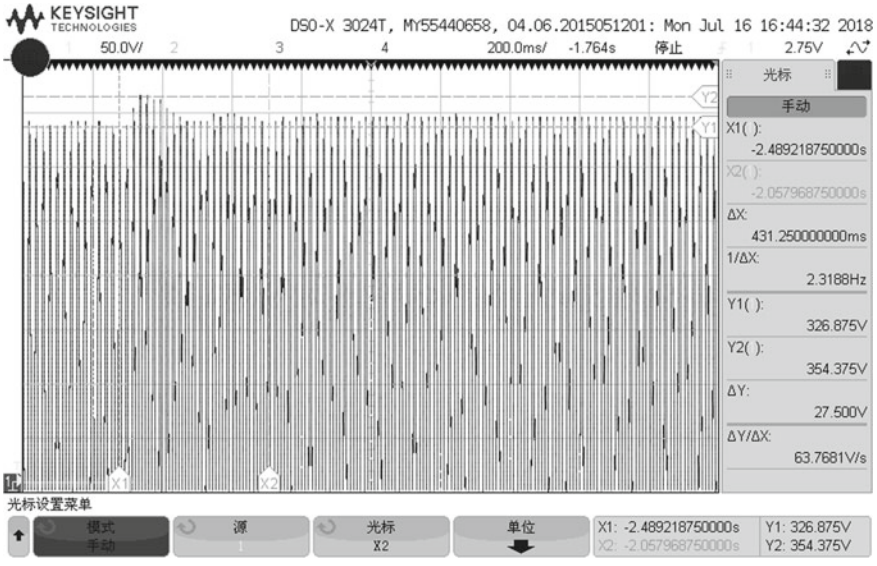


**Fig. 11.** Voltage waveform when bumping 12.9 kVA resistive load

## References

1. Wang Y (2007) Hardware design and implementation of universal development platform for digital generator controller. Northwestern Polytechnical University, Xi'an
2. Xijian Dong (2008) Research on AC generator control unit of aeroplane. Nanjing University of Aeronautics and Astronautics, Nanjing
3. Xuqiang Qiu (2007) Research on the voltage regulation system of doubly salient electromagnetic generator. Nanjing University of Aeronautics and Astronautics, Nanjing
4. Zhihui Chen (2000) Research on digital voltage regulation technology of brushless generator. Nanjing University of Aeronautics and Astronautics, Nanjing
5. Sedaghati A (2014) A PI controller based on gain-scheduling for synchronous generator. Turkish J Electr Eng Comput Sci 14(2):241–251
6. Cheng C-H, Hsu Y-Y (1991) Excitation control of a synchronous generator using a lookup table. IEEE Transactions on Aerospace and Electronic Systems 27(2):247–254
7. Chen T-C, Chen T-R, Chang W-T (2001) Implementation of AC line voltage regulator (AVR) with fuzzy control theory. IEEE 422–424
8. Pengfei Sun (2005) Fuzzy PID control method for the excitation of synchronous generator based on T-S model. Tianjin University, Tianjin
9. Dingzhen Guan, Xiaobin Zhang, Xiancheng Zheng (2011) Design of digital voltage regulator based on DSP. Mechatronics 17(7):65–68
10. Yang C (2010) Research on digital voltage regulation technology of rotor magnet-shunting hybrid excitation synchronous generator. Nanjing University of Aeronautics and Astronautics
11. Chen Z, Changsheng J (2001) Research on the digital voltage regulator on a VSCF AC power system. In: International conference on electrical machines & systems. IEEE
12. Yuzhen Huang (2010) Research and design of digital power conditioner based on FPGA. Nucl Electr Detect Technol 30(10):1334–1336

# Differentiation of High Impedance Faults from Other Distribution Network Events Using Microsynchrophasor Measurements


**Lady Joelle C. Dela Torre and Michael Angelo A. Pedrasa**

**Abstract** High impedance faults (HIFs) are faults with currents of low magnitude which appear like a nonlinear load from the system's perspective. Because this fault is an anomaly that the system might see as part of normal operations, it is important to differentiate it from actual normal distribution network events, such as capacitor and load switching. The development of the microsynchrophasor (μPMU), a device that provides current and voltage magnitudes and angles for distribution networks gives operators a different view during distribution level events. This paper aims to provide an interpretation of μPMU measurements to discern HIFs from other distribution network events. Simulations were focused on these events: high impedance faults, low impedance faults, and capacitor and load switching. It has been found that the HIF can be differentiated with the LIF using the current angle, this would not be enough to discern the HIF from capacitor switching events.

**Keywords** High impedance fault · Microsynchrophasor · Event classification

## List of Abbreviations

| | |
|---|---|
| HIF | High Impedance Fault |
| μPMU | Microsynchrophasor |

L. J. C. Dela Torre (✉) · M. A. A. Pedrasa
Electrical and Electronics Engineering Institute, University of the Philippines Diliman, Quezon City, Philippines
e-mail: lady.joelle.dela.torre@eee.upd.edu.ph

M. A. A. Pedrasa
e-mail: mapedrasa@up.edu.ph



F. Shahnia and S. Deilami (eds.), *ICPES 2019*, Lecture Notes in Electrical Engineering 669, https://doi.org/10.1007/978-981-15-5374-5_10

## 1 Introduction

High impedance faults (HIFs) are faults that have a low current magnitude and are often accompanied by arcing. They are commonly formed by connecting a phase of the network to the ground through a high impedance material, such as a tree branch. The detection and subsequent immediate action to extinguish these faults are important as it may cause fire and safety hazards due to the arc which could endanger the equipment and personnel. However, these faults are hard to discern using measurements because (1) the small current value makes it hard for traditional overcurrent relays to detect, and (2) the system sees the fault as a nonlinear load due to the nonlinearity and randomness of the arc. While there have been technologies developed to detect HIFs by observing irregularity on measurements such as the High Impedance Fault Analysis System (HIFAS), Digital Feeder Monitor (DFM), and Open Conductor Detection [1], these methods are outdated and not cost effective to just detect a specific type of fault. With the availability of the microsynchrophasor (μPMU), it is possible to see behavior that can be investigated in detecting HIFs. The microsynchrophasor was developed by the University of California in conjunction with the Power Standards Laboratory (PSL) and the Lawrence Berkeley National Laboratory (LBNL), with the goal of producing a measurement device that is able to capture the small angle differences in a distribution network, given that distribution network measurements are subject to more noise [2].

A comprehensive review of the different methods of HIF modeling and detection was presented in [3], which mentioned the different measurements that can be used to detect the HIF such as using the current harmonics or the magnetic signature of the event, to name a few. Aside from these, PMU measurements has also been used to detect high impedance faults. In [4] the pre- and during fault PMU samples were used to compute for a time domain estimate of the event, which was subsequently compared to the actual time domain measurement through a matrix index. If the index yields a nonzero value, a HIF is detected or the estimate contains both pre- and during fault samples, which should not be used to compute for the estimate. This work, however, did not consider other network events. On the other hand, [5] used the phase difference of the voltage and the current phasors to differentiate the normal to the faulted or new condition (e.g. load and capacitor switching) before differentiating the high impedance fault from other events using discrete wavelet transform. However, as the HIF was only represented as a fault with a high impedance, it did not model the arc and neglected to consider the nonlinear nature of the fault. In [6], it was found that a high impedance fault introduces an angle jump in the measured current due to the additional real power it consumes, thereby changing the measured power angle by the μPMU. No further observation about how it can be differentiated from other transient events were presented in the mentioned work.

This work builds upon [6], where the high impedance fault was found to add real power consumption and is seen as a resistor by the μPMU, and presents how a high impedance fault was discerned from other network transient events, such as load and capacitor switching and low impedance faults, using μPMU measurements.

The paper is organized as follows: the modeling of the high impedance fault and the microsynchrophasor are detailed, followed by the simulation setups and descriptions of the considered distribution network transient events. The findings and analysis of the results are presented, and finally possible applications and more insights are discussed.

## 2 Discussion on the Models and Simulations

In this section, details about the events and the microsynchrophasor blocks used in the simulation are discussed. Characteristics for each simulated event is explained in the next subsections. A brief discussion on the microsynchrophasor model used is also presented.

### *2.1 Block Models: HIF and μPMU*

The models mentioned in this subsection are all recovered from [6], and further discussion can be found in the aforementioned work. The model for the high impedance fault shown in Fig. 1 is a modified form of [7]. The randomly changing resistance $R_p$ and $R_n$ represents the randomness; the decaying resistance $R_b$ provides the current buildup; and the diodes and sources (which are dependent on the nominal voltage and expected load of the network) further increase the randomness of the signal and

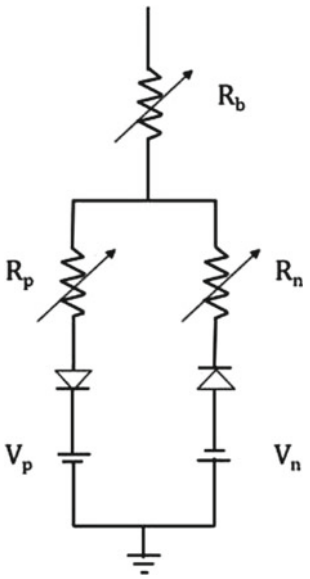


**Fig. 1** High impedance fault model used in this work

**Table 1** Values for HIF model

| Component | Minimum | Maximum | Variation through time |
|---|---|---|---|
| $R_p$, $R_n$ | 5000 | 6000 | Random every 0.1 ms |
| $R_b$ | 1600 | 0 | Decays after 0.05 ms |
| $V_p$ | 3600 V | 4400 V | Random every 0.1 ms |
| $V_n$ | 1800 V | 2200 V | Random every 0.1 ms |

accounts for the asymmetry. Table 1 lists down the values for each of the components throughout the simulations.

On the other hand, the μPMU model is a modified three phase PLL-based synchrophasor model in the Simscape Power Systems Toolbox [8] to make it consistent with the actual μPMU specifications produced by PSL [9].

## *2.2 Events Considered*

Aside from the high impedance fault, other events that were included in the simulations for this work are capacitor switching, load switching, and low impedance faults. The goal is to also see how these events manifest in μPMU measurements. Table 2 lists down the details for the events. As presented in [6], the HIF consumes an additional real power of 68 kW if the values in Table 1 are used in the test network. As for the other events, built in models are available in the Simulink Toolbox and were just modified for the simulations. For the capacitor, the value was based on the actual capacitor value of the system where the test network is based on. The real and reactive power for the load used in load switching was deliberately made equal to introduce the same change in the P and Q of the network. For the two types of low impedance fault simulated, the default values in the simulation platform were used.

**Table 2** Event details

| Event | Characteristic |
|---|---|
| High impedance fault | Equivalent P of 68 kW |
| Three phase fault | Fault resistance of 0.001 |
| Single line to ground fault | Fault resistance of 0.001 |
| Capacitor bank switching | Q of 21 kVar |
| Three phase load switching | P and Q of 68 kW and 68 kVar (inductive) |

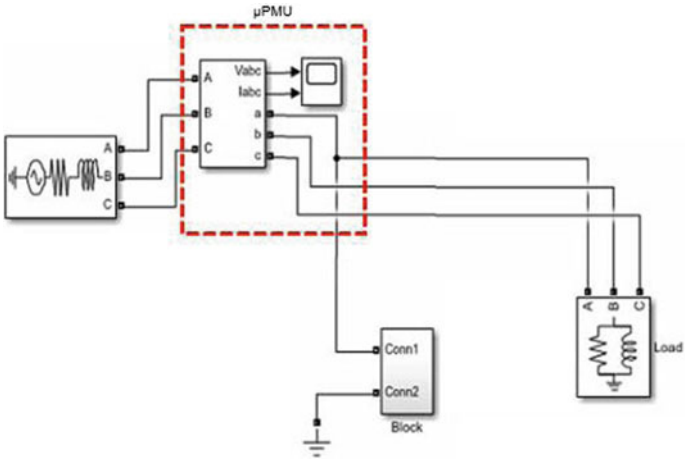


**Fig. 2** Simulation setup

### *2.3 Simulations*

The simulations were all carried out in MATLAB/Simulink. Except for the three phase fault, all events are only simulated in phase A. Each simulation records for 1.3 s, with each event occurring from 0.4 to 0.6 s. The voltage and current magnitudes and angles were gathered for each event.

The setup for the simulation is shown in Fig. 2. The μPMU model is placed near the event block to allow for better observation and characterization of the events being considered. In the setup, the bulk inductive load has a value of 63 kW and 40.693 kVar, respectively.

## 3 Results and Discussions

Voltage and current phasors were gathered for each of the events and subsequently compared to one another. Three phase plots are shown in the results of the next subsections.

### *3.1 Comparing High Impedance Faults to Low Impedance Faults*

We compare high impedance fault to its low impedance counterparts; specifically, single line to ground and three phase faults, which are faults having a connection to

ground, just like a high impedance fault. Shown in Fig. 3 are the voltage and current phasors of the HIF events and the low impedance fault events considered in this paper. The most notable difference is that the effects of the low impedance faults are significantly larger than that of the HIF. From Fig. 3, we can see that overcurrent relays that are used to detect low impedance fault will not work for detecting high impedance faults because the scale of how it affects the current is not the same.

An important observation about high impedance faults is how the biggest observable change that it contributes is in the current angle because of the HIF consuming additional real power, which explains why it is often seen as a nonlinear load instead of a fault. Finally, we can see through the measurements that while low impedance faults and high impedance faults both add in the current magnitude and introduce a dip in the voltage angle, the only observable quantity for a HIF is the current angle, which differs from the low impedance faults.

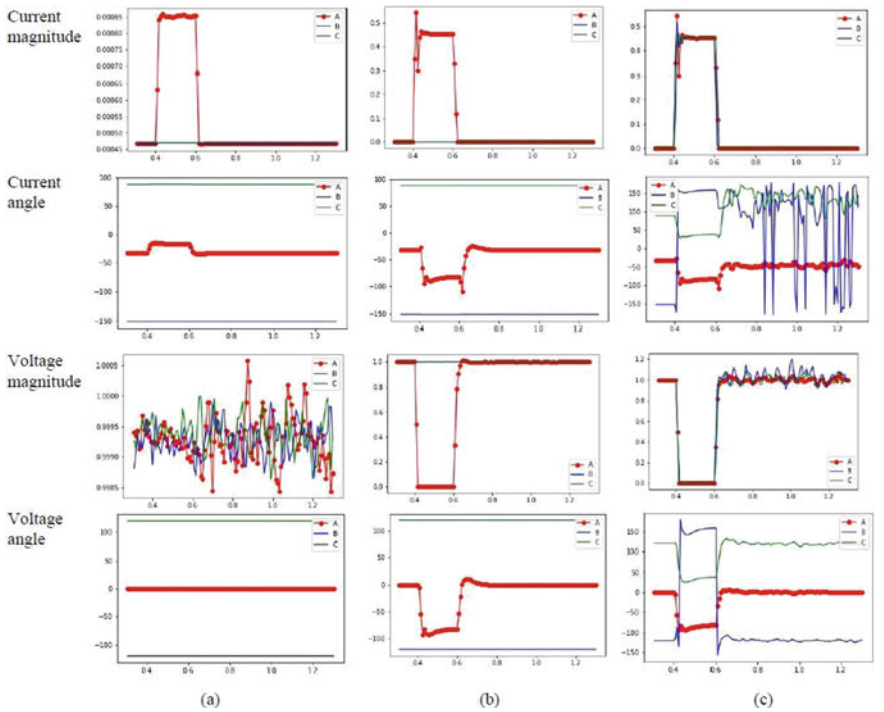


**Fig. 3** Current and voltage phasors for **(a)** a high impedance fault event, **(b)** a single line to ground fault and **(c)** a three phase fault

### 3.2 *Comparing High Impedance Faults to Load Altering Events*

We have established that the HIF affects the real power, so it is also imperative that we compare it to events altering the power of the network. Figure 4 shows the voltage and current phasors of HIF events and load and capacitor switching events, which are events that alter the real and/or reactive power of the system. Unlike low impedance faults, the scale of how load and capacitor switching events affect the measurements are very small. Except for its effect on the current angle, the events are barely noticeable in the other measurement streams, much like the high impedance fault. We can also see that both capacitor and load switching are events affecting all three phases, while a high impedance fault usually only involves one phase. Observing the current angle, we can see that the HIF and the capacitor switching introduce almost the same angle jump. The load switch also exhibits an angle jump but is noticeably different than the other two events. To better make sense of this, we can draw the power triangle before and during the occurrence of the different events.

Figure 5 shows the power triangles of the different events compared to the normal system power triangle. It has been previously mentioned that the HIF consumes

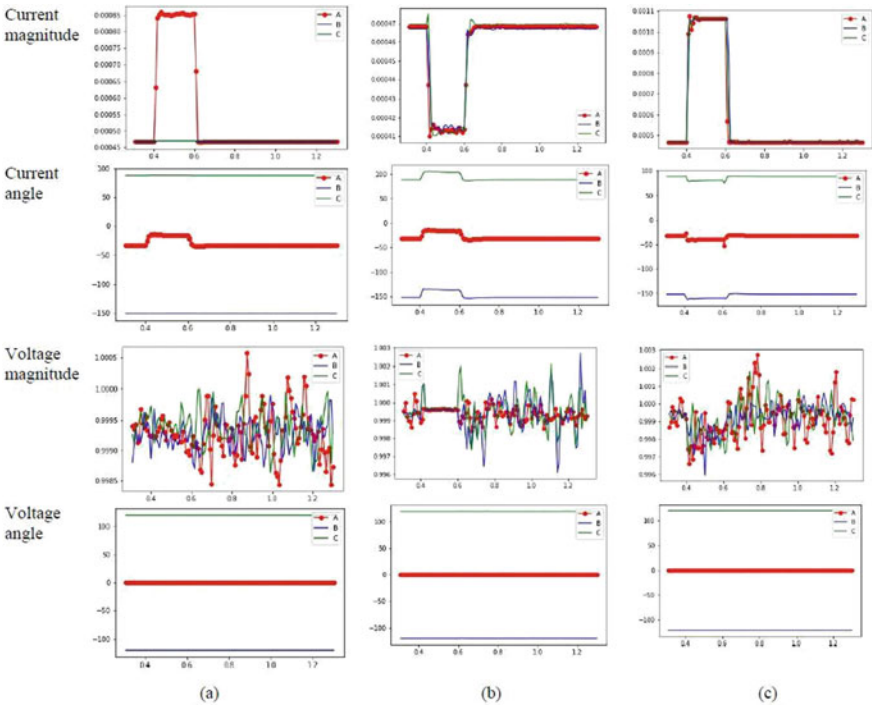


**Fig. 4** Current and voltage phasors for **(a)** a high impedance fault event, **(b)** a capacitor switching event and **(c)** a load switching event

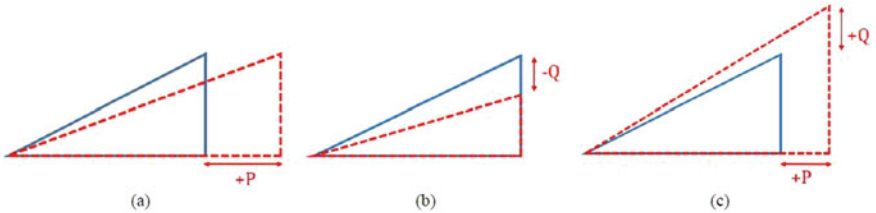


**Fig. 5** Power triangles for **(a)** a high impedance fault event, **(b)** a capacitor switching event and **(c)** a load switching event

additional real power, and for the same reactive power consumed in the network, will result in a smaller power angle (shown in Fig. 5a). Similarly, we know that a capacitor supplies reactive power and is commonly used in power factor correction, also reducing the power angle (Fig. 5b). Lastly, the inductive load introduced in the network have equal P and Q values, both adding additional real and reactive power consumption and increasing the power angle. Given that the voltage angle is almost close to zero, and knowing that $\theta_p = \theta_v - \theta_i$, the current angle is the negative of the power angle. This explains the angle jump in these measurements.

### *3.3 Detecting the High Impedance Fault Against the Other Events*

Each event can be discerned from each other by looking at the general event signatures in each of the phasor measurements. However, this may still be hard to do in an actual event classification standpoint; for one, the very small changes in the current magnitude and voltage phasor for a high impedance fault event may not be recognized by a classifier, and behavior of the capacitor switching may not be the same if the network operating voltage and its placement are considered. However, what is clear is that angle measurements from a microsynchrophasor may be used to differentiate one event from another, and the actual classification based from measurements may be explored.

## 4 Conclusion and Recommendations

This work presented how high impedance faults differ from some distribution-level events. It also discussed how it relates to its low impedance fault counterpart and other load altering events such as load and capacitor switching. It has been shown that the HIF is very similar to the capacitor switching event because both events decrease in different ways the power angle of the system. Through microsynchrophasor measurements, it was shown that high impedance faults greatly differ from low impedance

faults even if both events include contact of a conductor and ground. It has also been confirmed that high impedance faults do not appear as a significant increase in current magnitude measurements which explains why it does not trigger overcurrent protective devices like low impedance faults. Moreover, it was observed that the HIF behaves like a device that alters the power of the system, as seen in its similarities with load and capacitor switching such that all these events only appear in current angle measurements due to the change in power angle.

While the event signatures presented in this work may be too small for an actual classifier to differentiate, the importance of using a microsynchrophasor in a distribution network was highlighted because the current angle information given by the μPMU provides differentiation from the events. It is important to note that the current angle information may not be enough to differentiate the HIF from a capacitor switching event and should be investigated in further studies. Moreover, the authors are currently working on modeling and simulating the events considered in this work on a three-phase, unbalanced system to verify if the current results are consistent in a larger and more realistic network, as well as to investigate further applications of these findings.

**Acknowledgements** The authors acknowledge the research project PCARI-CHED IIID 2015-10 for funding and supporting this research study.

## References

1. Tengdin J et al (1996) Report of IEEE PSRC working group. Online
2. von Meier A et al (2014) Micro-synchrophasors for distribution systems. In: ISGT 2014, pp 1–5
3. Ghaderi A et al (2017) High impedance fault detection: a review. Electr Power Syst Res 143:376–388
4. Zanjani MGM et al (2012) High impedance fault detection of distribution network by phasor measurement units. In: 2012 proceedings of 17th conference on electrical power distribution, pp 1–5
5. Myint S et al (2018) A simple high impedance fault detection method based on phase displacement and zero sequence current for grounded distribution systems. In: 2018 IEEE PES Asia-Pacific power and energy conference (APPEEC), pp 118–122
6. Dela Torre L, Pedrasa MA (2019) High impedance fault characterization on microsynchrophasor measurements. In: 2019 IEEE PES Asia-Pacific power and energy conference (APPEEC)
7. Gautam S, Brahma SM (2013) Detection of high impedance fault in power distribution systems using mathematical morphology. IEEE Trans Power Syst 28(2):1226–1234
8. PMU (PLL-based, Positive Sequence), (1994–2020). Mathworks.com. https://www.mathworks.com/help/physmod/sps/powersys/ref/pmupllbasedpositivesequence.html. Retrieved 12 Mar 2019
9. Power Standards Laboratory. "microPMU" microsynchrophasor datasheet (2018). https://www.powerstandards.com/download/micropmu-data-sheet

# Linguistic Hesitant Fuzzy Sets and Cloud Model Based Risk Assessment of Gaseous Hydrogen Storage in China


**Liqi Yi and Tao Li**

**Abstract** Gaseous hydrogen storage has been paid high attention as a promising storage method with low carbon cleaning properties. This paper analyzes the risk of gaseous hydrogen storage in China from a serious of points of view. At first, linguistic hesitant fuzzy sets (LHFSs) is utilized to describe the risk of application of gaseous hydrogen storage in China under the perspective of sustainable development. Then, in order to ensure the integrity of information and fully describe the fuzziness and randomness in the evaluation process, cloud model is utilized to convert LHFS into a more comprehensive way. At last, the final risk degree of current gaseous hydrogen storage in China is determined by CCPA operator. The calculation result shows that the risk of applying gaseous hydrogen storage is between medium high and high. At the same time, some suggestions are proposed for better extension of gaseous hydrogen in China.

**Keywords** Gaseous hydrogen storage · LHFSs · Cloud model · Risk assessment · China

## 1 Introduction

The utilization of clean energy is becoming more and more important due to the shortage of fossil fuels and the demand of ecological environment sustainable development [1]. Among many energy raw materials, hydrogen energy has been widely concerned and applied due to its advantages of abundant resources, no pollution, and high thermal power.

The main processes of application of hydrogen energy includes the extraction, storage, transportation and consumption. Among them, the storage of hydrogen energy is a main factor that restricts the utilization of hydrogen energy. At present, hydrogen energy storage methods include compressed gaseous hydrogen method,

L. Yi (✉) · T. Li
Institute of Economics and management, North China Electric Power University, Beijing, China
e-mail: kg1995538530@163.com

T. Li
e-mail: Litao@ncepu.edu.cn



F. Shahnia and S. Deilami (eds.), *ICPES 2019*, Lecture Notes in Electrical Engineering 669, https://doi.org/10.1007/978-981-15-5374-5_11

cryogenic liquid storage method, metal hydride hydrogen storage and hydrogen storage of carbonaceous materials [2]. The compressed gaseous hydrogen storage method is based on the physical properties of the gas. At a constant temperature, the volume can be reduced by increasing pressure for a certain amount of gas. The compressed gaseous hydrogen method is based on above principle. This method is widely used because it is simple and convenient in operating, low price in storage, fast in charging and discharging gas, easy to use in transportation and operation. However, the characteristics of low hydrogen storage capacity and insecurity restrict the use of compressed gaseous hydrogen. At present high-pressure gas hydrogen storage is a promising method widely used in hydrogen battery vehicles, chemical industry, gas stations and other directions in the current stage.

At present, hydrogen energy is listed as a critical component of the national energy supply in many countries and regions. In Europe, Germany firstly led the introduction of hydrogen energy into the EU energy system; the United States and Japan invested a lot of time and money to develop hydrogen fuel cells. In the field of hydrogen fuel cell vehicle, Japan and Germany has entered the commercialization stage. In China, the technology of hydrogen production by electrolysis of water has matured. However, the development of gaseous hydrogen storage possesses great uncertainty and risk in China due to the high technical barriers in hydrogen storage, unstable electricity price and so on. Relying on the cost advantage of China's hydrogen production and subsidies for renewable energy sources such as wind power and photovoltaic, it is worthwhile to study the feasibility of gaseous hydrogen storage development in China.

Because of the ambiguity and limitation of human emotions, it is difficult for decision makers to express their assessment through crisp values. Fortunately, the linguistic terms as "high", "slightly high", "low", "slightly low" and some others are utilized for expressing the decisions from decision makers (DMs). In addition, DMs usually provide their information over alternatives with hesitancy or anonymity, linguistic hesitant fuzzy set (LHFSs) proposed by Meng et al. [3] can effectively solve above problems. In general, the difference between LHFSs is not stable. Thus, cloud model proposed by Zhu et al. [4] can convert the hesitant language fuzzy set with a stable and reasonable distance on the basis of ensuring complete information. Cloud model can describe the fuzziness and randomness of language evaluation through three numerical characteristics, which has been widely utilized in renewable energy risk assessment. Considering the diversity and uncertainty of risk factors, this paper adopts Linguistic Hesitant Fuzzy Sets (LHFSs) and Cloud model to assess the gaseous hydrogen storage risk degree in China.

The contribution of this paper has three aspects. (i) The risk of gaseous hydrogen storage in China is firstly comprehensively investigated under the perspective of sustainable development. (ii) This paper proposes a comprehensive gaseous hydrogen storage risk criteria system which divides risk evaluation index into internal technical index and external environmental index. (iii) The application risk of gaseous hydrogen storage in China is evaluated by LHFSs and cloud model.

The reminder of this paper is arranged as follows. A comprehensive risk criteria system is determined in Sect. 2. Section 3 introduces the overall risk assessment process. Finally, the conclusion and suggestion are proposed in Sect. 4.

## 2 Risk Factors Identification

The main technical obstacle to the large-scale application of hydrogen energy is to find a hydrogen storage system that can meet sufficient hydrogen storage capacity and a safe operating environment. At present, some standards have been proposed internationally to evaluate the technical risks of different hydrogen storage systems, including hydrogen storage density (weight and volume), cost, operational safety and hydrogen recovery rate. According to current technological developments and applicable conditions, high-pressure gaseous hydrogen storage, liquid hydrogen storage and metal hydride hydrogen storage may be the best way to store hydrogen in the future [5]. In this paper, the risk factors of gaseous hydrogen storage are studied, and combined with its own characteristics, the technical factors that can reflect the risk of gaseous hydrogen storage are selected.

Establishment of risk indicators is the basis of risk management. A good risk indicator system can accurately and efficiently reflect the risks of various aspects of the project and improve the scientific of risk management [6]. In order to comprehensively reflect the application risk of gaseous hydrogen storage in China, the technical characteristics of gaseous hydrogen storage itself, and the external environmental factors that affect the risk of gaseous hydrogen storage including economic environmental risks, ecological environmental risks and social environmental risks are considered. Finally, a comprehensive risk criteria as shown in Table 1 is formulated under the perspective of sustainable development through expert meeting

**Table 1** Risk criteria system of gaseous hydrogen storage

| First-criteria | Symbol | Sub-criteria | Symbol |
|---|---|---|---|
| Technical risk | C1 | Operational safety | C11 |
| | | Operating cost | C12 |
| | | Hydrogen storage density | C13 |
| | | Charging speed | C14 |
| Economic environment risk | C2 | Inflation | C21 |
| | | Change in tax | C22 |
| | | Financial subsidy | C23 |
| Natural environment risk | C3 | Environmental pollution | C31 |
| | | Energy consumption | C32 |
| Social and political environment risk | C4 | Public acceptance | C41 |
| | | Government supervision | C42 |

with a scale of seven whose academic backgrounds are energy economy, gaseous hydrogen, renewable energy production, energy policy and so on.

## 2.1 Technical Risk

The technical risk factors of high-pressure gaseous hydrogen storage are the factors that determine the promotion of gaseous hydrogen storage. It mainly includes three aspects: cost, safety and hydrogen storage efficiency in the process of gaseous hydrogen storage [7]. This paper specifically divides it into the following four factors:

1. *Operational safety*: Refers to the safety and reliability during the whole process of compressing hydrogen, storing hydrogen, releasing hydrogen and hydrogen transportation.
2. *Operating cost*: Operating costs mainly include the cost of compressing hydrogen which consumes a large amount of compression work and the cost of hydrogen storage container [8]. The container of compressed hydrogen needs to be able to withstand large pressures, and is generally made of heavy pressure-resistant materials.
3. *Hydrogen storage density*: Hydrogen storage density refers to the hydrogen content stored per unit volume. When the hydrogen storage density is high, per hydrogen storage unit volume can store more hydrogen, which is beneficial to improve the efficiency of hydrogen energy utilization [9].
4. *Charge and discharge speed*: The charge and discharge speed refers to the speed at which hydrogen is compressed into and discharged from the hydrogen storage container, which is related to the efficiency of hydrogen usage.

## 2.2 Economic Environment Risk

The economic environment of gaseous hydrogen storage refers to the macroeconomic factors affecting the application of gaseous hydrogen storage, and is a key factor affecting the application of gaseous hydrogen storage in China.

1. *Inflation*: Inflation affects the stability of the economy environment, causing uncertainties such as currency depreciation, increase transaction cost and rising prices.
2. *Tax changes*: The government's changes in new energy tax policies such as hydrogen storage will largely affect the realization of the expected benefits of the projects.
3. *Financial subsidies*: At present, the Chinese government has certain financial subsidies for wind energy and photovoltaic. Using the state's financial support to generate electricity and using hydrogen energy for energy storage can provide projects with additional economic benefits.

### 2.3 Natural Environment Risk

The natural environmental risks of gaseous hydrogen storage include two aspects, one is the problem of pollution caused by gaseous hydrogen storage to the environment, and the other is the consumption of energy by gaseous hydrogen storage.

1. *Environmental pollution*: The environmental pollution of compressed gaseous hydrogen storage mainly comes from the process of compressing hydrogen, hydrogen storage and usage. At the same time corporate environmental pollution emissions increase the likelihood of receiving social penalties.
2. *Energy consumption*: The energy consumption of the high-pressure gaseous hydrogen storage method occurs mainly in the process of hydrogen production and hydrogen compression. At the same time the energy consumption of the hydrogen storage process will affect the cost of the enterprise.

### 2.4 Social and Political Environment Risk

The risks of the social and political environment mainly come the public and the government.

1. *Public acceptance*: Hydrogen storage energy has not yet been widely used in China, and the public's adaptability to hydrogen storage energy remains to be seen.
2. *Government regulation*: The supervision and regulation of hydrogen storage energy by government regulatory authorities will also affect the application of gaseous hydrogen storage in China [6].

## 3 Methodology

In this section we establish the linguistic hesitant fuzzy sets (LHFSs) based cloud model to solve this comprehensive MCDM problem. Several basic concepts are introduced first.

### 3.1 LHFSs

The linguistic hesitant fuzzy sets can help DMs to give their evaluation in natural language in the environment of complexities and limitation of human cognition. Set as a linguistic term set, and t is an odd number. A LHFS is a set of appending the

hesitation level valuing in as, where is a set with valuing in representing the possible membership degrees of the element to the set LH [10].

For example, Let linguistic term set be $S = \left\{ \begin{array}{l} s_0 : very\ poor,\ s_1 : poor,\ s_2 : slightly\ poor,\ s_3 : fair, \\ s_4 : slightly\ good,\ s_5 : good,\ s_6 : very\ good \end{array} \right\}$. In the evaluation process, the expert commission may give a value of 0.6 for "low" and a value of 0.3 for "medium", but hesitate to give a value of 0.2 or 0.3 for "very low". In this situation, the evaluated value can be represented as:

**Definition 1** [10]. For LH in a LHFS, $E(LH) = s_{e(LH)}$ is called the expectation function of LH with $e(LH) = 1/|index(LH)|\left\{\sum_{\theta(i):\theta(i)\in index(LH)} \left(\theta(i)/\left|lh(s_{\theta(i)})\right|\right)\left(\sum_{r\in lh(s_{\theta(i)})} r\right)\right\}$, and $D(LH) = s_{v(LH)}$ is called its variance function with $v(LH) = 1/|index(LH)|\left(\sum_{\theta(i):\theta(i)\in index(LH)} \left(\left(\theta(i)/\left|lh(s_{\theta(i)})\right|\right)\left(\sum_{r\in lh(s_{\theta(i)})} r\right) - e(LH)\right)^2\right)$, where $\left|lh(s_{\theta(i)})\right|$ is the count of real numbers in $lh(s_{\theta(i)})$, and $|index(LH)|$ is the cardinality of $index(LH)$; $index(LH) = \left\{\theta(i)\middle|(s_{\theta(i)}, lh(s_{\theta(i)})) \in LH, lh(s_{\theta(i)}) \neq \{0\}\right\}$ with $s_{\theta(i)} \in S$.

For two LHFSs, $LH_1$ and $LH_2$, if $E(LH_1) < E(LH_2)$, then $LH_1 < LH_2$; if $E(LH_1) = E(LH_2)$, then

$$D(LH_1) > D(LH_2),\ LH_1 < LH_2;$$
$$D(LH_1) = D(LH_2),\ LH_1 = LH_2.$$

## 3.2 Cloud Model

**Definition 2** [11]. $U$ is Quantitative domain of exact numerical representation, $C$ is the qualitative concept of $U$. If $x \in U$ and $x$ is a random implementation of $C$, and the certainty is $\mu(x) \in [0, 1]$, thus $\mu : U \to [0, 1], \forall x \in U, x \to \mu(x)$ is called cloud.

**Definition 3** [12]. Supposing $S = \{s_0, s_1, \ldots, s_{t-1}\}$ is the linguistic term set, $t$ is an odd number, a valid universe $X_{\min}, X_{\max}$ is given by experts. Correspondingly, the cloud $A_i(Ex_i, En_i, He_i)$ is utilized to denotes the linguistic value $s_i$.

A golden method for generating five clouds was proposed by Wang and Feng [12] based on $3\sigma$ principle of the normal distribution curve. Zhu et al. [4] extended the five clouds into seven clouds by applying the golden ratio method as follows:

Let linguistic term set be $S = \left\{ \begin{array}{l} s_0 : very\ poor,\ s_1 : poor,\ s_2 : slightly\ poor,\ s_3 : fair, \\ s_4 : slightly\ good,\ s_5 : good,\ s_6 : very\ good \end{array} \right\}$,

where the universe is $[X_{\min}, X_{\max}]$, then seven clouds can be formulated by the golden radio method, where the universe is $[X_{\min}, X_{\max}]$, then seven clouds can be formulated by the golden radio method.

$$
\begin{aligned}
&Ex_3 = (X_{\min} + X_{\max})/2,\ Ex_0 = X_{\min},\ Ex_6 = X_{\max},\\
&Ex_2 = Ex_3 - 0.382(X_{\max} - X_{\min})/4,\ Ex_4 = Ex_3 + 0.382(X_{\max} - X_{\min})/4,\\
&Ex_1 = Ex_3 - (X_{\max} - X_{\min})/4,\ Ex_5 = Ex_3 + (X_{\max} - X_{\min})/4\\
&En_2 = En_4 = 0.382(X_{\max} - X_{\min})/12,\ En_3 = 0.618En_4,\\
&En_1 = En_5 = En_4/0.618,\ En_0 = En_6 = En_5/0.618\\
&He_2 = He_4 = He_3/0.618,\ He_1 = He_5 = He_4/0.618\\
&He_0 = He_6 = He_5/0.618
\end{aligned}
$$

**Definition 4** [13]. Let $S = \{s_0, s_1, \ldots, s_{t-1}\}$ be a linguistic term set. The valid universe is $[X_{\min}, X_{\max}]$. The cloud $A_i(Ex_i, En_i, He_i)$ represents $s_i$. Let $LH = \{s_{\theta(i)}, lh(s_{\theta(i)}) \big| s_{\theta(i)} \in S\}$ be a LHFS, where $A^*_{LH}(Ex^*_{LH}, E^*_{LH}, He^*_{LH})$ is called the comprehensive cloud of LH.

$$
Ex^*_{LH} = \sum_{\theta(i)\in index(LH)} \left( \left( \frac{\sum_{relh(s_{\theta(i)})} r}{\left|lh(s_{\theta(i)})\right|} \Big/ \sum_{\theta(i)\in index(LH)} \frac{\sum_{relh(s_{\theta(i)})} r}{\left|lh(s_{\theta(i)})\right|} \right) Ex_{\theta(i)} \right) \tag{1}
$$

$$
En^*_{LH} = \frac{\sum_{\theta(i)\in index(LH)} \left( \left( \frac{\sum_{r\in lh(s\theta(i))} r}{\left|lh(s_{\theta(i)})\right|} \Big/ \sum_{\theta(i)\in index(LH)} \frac{\sum_{r\in lh(s\theta(i))} r}{\left|lh(s_{\theta(i)})\right|} \right) Ex_{\theta(i)} En_{\theta(i)} \right)}{\sum_{\theta(i)\in index(LH)} \left( \left( \frac{\sum_{r\in lh(s\theta(i))} r}{\left|lh(s_{\theta(i)})\right|} \Big/ \sum_{\theta(i)\in index(LH)} \frac{\sum_{r\in lh(s\theta(i))} r}{\left|lh(s_{\theta(i)})\right|} \right) Ex_{\theta(i)} \right)} \tag{2}
$$

$$
He^*_{LH} = \sqrt{\sum_{\theta(i)\in index(LH)} (He_{\theta(i)})^2} \tag{3}
$$

where $\left|lh(s_{\theta(i)})\right|$ represents the total membership numbers to $s_{\theta(i)}$ of $lh(s_{\theta(i)})$. And $index(LH) = \left\{\theta(i) \big| \left(s_{\theta(i)}, lh(s_{\theta(i)})\right) \in LH, LH(s_{\theta(i)}) \neq \{0\}\right\}$ is tenable in the situation of $s_{\theta(i)} \in S$.

### 3.3 Risk Assessment Framework

In this section, the risk assessment framework of gaseous hydrogen storage in China is established.

Step 1. Select the critical risk criteria for gaseous hydrogen storage in China as shown in Sect. 2.

Step 2. Construct standard clouds based on the $3\sigma$ principle.

Step 3. Collect the value of risk criteria in the form of LHFSs by expert decision group. And convert the expert decision into cloud model by Definition 4.
Step 4. Obtain the finial risk values by CCPA operator [13].

$$
\begin{aligned}
CCPA(A_{\alpha_1}, A_{\alpha_2}, \ldots, A_{\alpha_n}) &= \prod_{i=1}^{n} \left(A_{\alpha_i}\right)^{\frac{1}{n}} \\
&= \left( \prod_{i=1}^{n} (Ex_i)^{\frac{1}{n}}, \prod_{i=1}^{n} (Ex_i)^{\frac{1}{n}} \sqrt{\sum_{i=1}^{n} \left( \frac{1}{n} \times \left( \frac{En_i}{Ex_i} \right)^2 \right)}, \right. \\
&\quad \left. \prod_{i=1}^{n} (Ex_i)^{\frac{1}{n}} \sqrt{\sum_{i=1}^{n} \left( \frac{1}{n} \times \left( \frac{He_i}{Ex_i} \right)^2 \right)} \right) \\
&= (Ex, En, He) \qquad (4)
\end{aligned}
$$

### 3.4 Application of the Proposed Framework

Firstly, by referring to the description of the evaluation grades of the relevant indicators in the literature and the views of expert committee, seven rating levels of "EH", "H", "MH", "N", "ML", "L" and "EL" as $S = \{s_0, s_1, s_2, s_3, s_4, s_5, s_6\}$ are established for the index system through the golden radio method as shown in Table 2 with a universe of [0, 10], and $He_3 = 0.1$ is given by expert committee [12].

This article seeks to help experts in various fields to assess the application risks of gaseous hydrogen storage in China. The results of the expert's hesitant language score are shown in Table 3.

According to the results of the hesitant language score given by the experts, the EX of each influencing factor and the comprehensive influencing factor is calculated

**Table 2** Grading system

| Linguistic term | Level | EX | EN | HE |
|---|---|---|---|---|
| s0 | EL | 0 | 0.833 | 0.424 |
| s1 | L | 2.5 | 0.515 | 0.262 |
| s2 | ML | 4.045 | 0.318 | 0.162 |
| s3 | N | 5 | 0.197 | 0.1 |
| s4 | MH | 5.955 | 0.318 | 0.162 |
| s5 | H | 7.5 | 0.515 | 0.262 |
| s6 | EH | 10 | 0.833 | 0.424 |

**Table 3** Experts hesitate language score results

| Criteria | Linguistic term | | |
|---|---|---|---|
| C11 | s2; 0.2 | s4; 0.6 | s6; 0.3 |
| C12 | s2; 0.3 | s4; 0.6 | s5; 0.5 |
| C13 | s2; 0.2 | s4; 0.6 | s6; 0.5 |
| C14 | s1; 0.1 | s3; 0.5 | s5; 0.7 |
| C21 | s1; 0.1 | s5; 0.9 | |
| C22 | s2; 0.1 | s3; 0.1 | s5; 0.5 |
| C23 | s1; 0.1, 0.2 | s3; 0.3 | s6; 0.6 |
| C31 | s1; 0.2 | s3; 0.3 | s5; 0.8 |
| C32 | s1; 0.2 | s4; 0.4 | |
| C41 | s3; 0.1 | s5; 0.7 | |
| C42 | s3; 0.1, 0.2 | s5; 0.7 | |

by the contents of Definitions 3 and 4 above. The specific numerical values are listed in Table 4.

Table 4 shows that among the technical risk factors, the gaseous hydrogen storage density is the biggest risk factor, the operational safety risk is second, and the operational cost and the charging speed are relatively low. In terms of economic and environmental risks, government financial subsidies are the biggest uncertainty. It's risk rating is high risk. Inflation and tax changes have relatively low impact; in terms of environmental risks, energy consumption risk is low, significantly lower than the risk of emissions; in terms of social and political environmental risks, the

**Table 4** Evaluation results of each risk indicator

| Criteria | Hesitant language result | Hesitant language score and its scoring interval |
|---|---|---|
| C11 | Close to MH | MH(5.955) < 6.71 < H(7.5) |
| C12 | Close to MH | MH(5.955) < 6.10 < H(7.5) |
| C13 | Close to H | MH(5.955) < 7.22 < H(7.5) |
| C14 | Close to MH | MH(5.955) < 6.15 < H(7.5) |
| C21 | Close to H | MH(5.955) < 7.00 < H(7.5) |
| C22 | Close to MH | MH(5.955) < 6.65 < H(7.5) |
| C23 | Equal to H | H(7.5) = 7.50 = H(7.5) |
| C31 | Close to MH | MH(5.955) < 6.15 < H(7.5) |
| C32 | Close to N | ML(4.045) < 4.80 < N(5) |
| C41 | Close to H | MH(5.955) < 7.19 < H(7.5) |
| C42 | Close to H | MH(5.955) < 7.06 < H(7.5) |
| Comprehensive risk | Close to MH | MH(5.955) < 6.550 < H(7.5) |

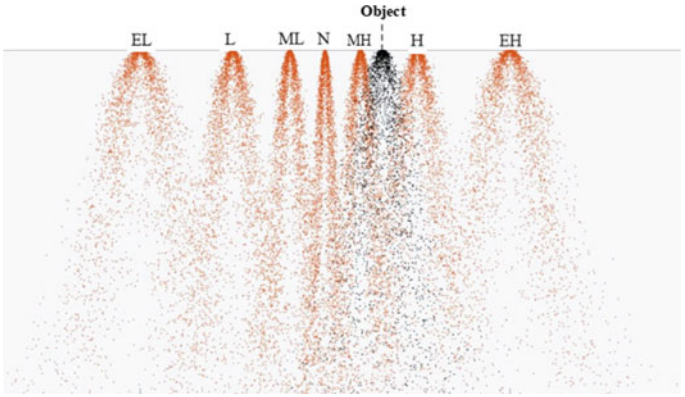


**Fig. 1** Results of cloud model

risks of government regulation and public acceptance are high. The overall risk level is between middle high and high (Fig. 1).

## 4 Conclusion and Suggestion

In this paper, we use LHFSs and cloud model to evaluate the risk of gaseous hydrogen storage in China, and find that the risk of gaseous hydrogen storage in China is moderately high. The higher risk factors include gaseous hydrogen storage density, fiscal subsidy policy, government regulation, and public acceptance and so on.

The storage density of gaseous hydrogen is a key factor that restricts the development of hydrogen storage, and it is the main factor affecting the cost of hydrogen storage. China should increase its R&D [14] investment in gaseous hydrogen storage density. The improvement of technology can make gaseous hydrogen storage widely used in China. Chinese government's financial subsidies for hydrogen energy and government regulatory policies will also have a significant impact on the expected benefits of the project. In the environment where potential gaseous hydrogen storage operators cannot influence government policies, they need to make full use of their own resources to prepare for risk prevention [15], and identify and control the main risk factors in the whole process of production and operation.

**Acknowledgements** Project supported by the North China Electric Power University Domestic and Foreign Joint Training Postgraduate Program.

## References


1. Zhao J et al (2012) Current situation and prospect of hydrogen storage technology with new organic liquid. Chem Ind Eng Prog 39(30):17442–17451
2. Zhang YH et al (2015) Development and application of hydrogen storage. J Iron Steel Res 22(9):457–464
3. Meng F, Chen X, Zhang Q (2014) Multi-attribute decision analysis under a linguistic hesitant fuzzy environment. Inf Sci 287–305
4. Zhu C, Zhu L, Zhang X (2016) Linguistic hesitant fuzzy power aggregation operators and their applications in multiple attribute decision-making. Inf Sci 367:809–826
5. Barthélémy H (2012) Hydrogen storage—industrial prospectives. Int J Hydrogen Energy 37(22):17364–17372
6. Wu Y et al (2018) Risk management of public-private partnership charging infrastructure projects in China based on a three-dimension framework. Energy
7. Shao H et al (2018) Progress and trends in magnesium based materials for energy-storage research: a review. Energy Technol
8. Li X et al (2016) Review of hydrogen storage technology and its application prospects in hydrogen storage. Smart Grid 4(2):166–171
9. Adametz P, Müller K, Arlt W (2014) Efficiency of low-temperature adsorptive hydrogen storage systems. Int J Hydrogen Energy 39(28):15604–15613
10. Meng F, Chen X, Zhang Q (2014) Multi-attribute decision analysis under a linguistic hesitant fuzzy environment. Inf Sci 267:287–305
11. Grabisch M (1996) The application of fuzzy integrals in multicriteria decision making. Eur J Oper Res 89(3):445–456
12. Wang H-L, Feng Y-Q (2005) On multiple attribute group decision making with linguistic assessment information based on cloud model. Control Decis 20(6):679
13. Hu S (2018) Multi-attribute group decision making based on comprehensive cloud under linguistic hesitant fuzzy environment and its application in ERP selection. Jiangxi University of Finance and Economics
14. Sim J, Kim CS (2019) The value of renewable energy research and development investments with default consideration. Renew Energy 143:530–539
15. Nguyen DT, Le LB (2014) Risk-constrained profit maximization for microgrid aggregators with demand response. IEEE Trans Smart Grid 6(1):135–146

# A Voltage Based Communication-Free Demand Response Controller


**Saifullah Shafiq, Ahmed Al-Asmar, Bilal Khan, and Ali Taleb Al-Awami**

**Abstract** Demand response (DR) is the promising feature in smart grids to enable the consumers' active participation in scheduling the overall residential demand to avoid voltage violations during peak hours. Usually, DR strategies are implemented using centralized control schemes which require extensive communication infrastructure. However, this paper proposes a decentralized DR strategy. The proposed controller compares the voltage at the point of control (POC) with a preset reference voltage to adjust the power consumption of several residential loads such as electric vehicle, air conditioner, water heater, and clothes dryer while taking users' requirements into account. In addition, a controller is provided with the function to assign priority levels to these loads if needed. A test distribution system having 18 nodes, where each node has 60 houses, is used to validate the proposed controller. Furthermore, the controller is tested under light and heavy loading conditions. The results showed the effectiveness of the proposed controller and its ability to mitigate voltage drops during peak hours.

**Keywords** Decentralized strategy · Demand response · Distribution system · Electric vehicle

S. Shafiq (✉)
Electrical Engineering Department, Prince Mohammad Bin Fahd University (PMU), Khobar, Saudi Arabia
e-mail: sshafiq@pmu.edu.sa

A. Al-Asmar · B. Khan · A. T. Al-Awami
Electrical Engineering Department, King Fahd University of Petroleum and Minerals (KFUPM), Dhahran, Saudi Arabia
e-mail: s201375790@kfupm.edu.sa

B. Khan
e-mail: g201707470@kfupm.edu.sa

A. T. Al-Awami
e-mail: aliawami@kfupm.edu.sa

A. T. Al-Awami
K. A. CARE Energy Research and Innovation Center, Dhahran, Saudi Arabia



F. Shahnia and S. Deilami (eds.), *ICPES 2019*, Lecture Notes in Electrical Engineering 669, https://doi.org/10.1007/978-981-15-5374-5_12

## 1 Introduction

Technology has been bringing us new devices every day. The increasing number of these electric devices introduces a new challenge to the power grid in terms of power consumption. Peak consumption hours of the day have been a problem for a long time, but this problem would become more critical considering the present and the future challenging electric loads. To show an example, let us consider a house with an average monthly electricity bill of 400 Saudi Riyals (SR). With the current tariff of 0.10 SR per kWh [1], this house is consuming a monthly average of 4000 kWh or approximately 5.6 kW each hour of the day. However, a commercial electric vehicle (EV) charger consumes around 3.3 kW. A regular water heater (WH) and an air conditioner (AC) can consume up to 3.8 kW and 1.92 kW, respectively [2]. For a transformer that is currently supplying power to 10 houses, the addition of an EV in two of these houses will enforce the transformer to supply for an equivalent of 11 houses which may cause new peaks into the system and, in critical cases, blackouts in certain areas.

There are two ways to solve this kind of problem. One way is to change the whole infrastructure of the power system like installing new power plants, new transformers, and more distribution lines. This solution is considered as a cumbersome because of its very high cost and the amount of time and labor it requires. The other way is to control the loads in the houses by reducing their consumption during the peak hours which is known as "Demand Response" (DR) [3, 4]. DR is much better than the former in terms of cost, time, and efficiency especially if the DR controller is adaptive to the changing number of loads as well as to the changes in the network topology. There are several methods that were previously introduced to implement such controllers like the Artificial Neural Network (ANN) based controller proposed in [5] which considers the priorities of the loads' operation and a signal from the utility company. The signal and the priorities are then processed by the ANN and an on/off signal is sent to each load as the output. Another method is proposed in [6] which uses a controller that reschedules the operation of high consumption loads in the house to off-peak hours after receiving the data about the peak hours as an input from the utility company. Until this moment, a well-established channel of communication between the houses and the utility companies does not exist which makes previous methods impractical. In [7, 8], a voltage-based feedback (VBF) controller is introduced which does not require communication, between the house and the utility, making it the most convenient method of controlling the residential loads. The work in [7] is focused on controlling the EV load only. The authors have designed and implemented a controller in MATLAB/Simulink.

In this research, a residential responsive demands controller, based on the VBF method, is proposed to control different loads. It maintains the voltage at the point of control (POC) within the range of $\pm 5\%$ of nominal voltage while considering the loads priorities set by user. Four different loads, i.e., AC, the WH, the clothes dryer (CD), and the EV are considered. The controller is tested on 18 bus distribution system where each load node has 60 houses.

The rest of the paper is organized as follows: Sect. 2 discusses the proposed demand response controller. The test distribution system is provided in Sect. 3. The simulated results are presented in Sect. 4. Section 5 concludes the paper.

## 2 Residential Responsive Demands Controller

The proposed residential responsive demands controller (RRDC) is designed to maintain the voltage at POC within the safety margins while ensuring the satisfaction of the users. It considers the operation priorities of the responsive demands, from the user, as an input along with the voltage at POC. After that, the controller calculates the difference between the voltage at POC and a preset voltage reference every one-minute. When the voltage at POC goes below the reference voltage, the controller starts turning off the lowest priority loads one by one until the difference is compensated and the voltage is restored to the acceptable range. The turned off device cannot turn back on unless the voltage reaches a certain level where the device's power consumption will not cause it to drop below the safety limit.

The percentage change in voltage is calculated by monitoring the voltage response to a 1 kW change in the total power consumption which is 0.7% per kW. This is done to prevent the controller from hunting. The output of the controller is the on/off signal which is sent to the controlled devices. A block diagram for the RRDC is shown in Fig. 1. The output of hysteresis comparator and device state logic block are shown in Figs. 2 and 3, respectively.

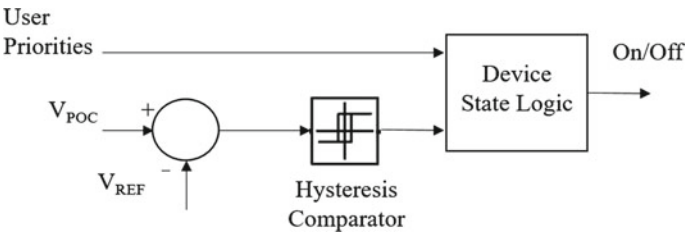


**Fig. 1** A block diagram of RRDC

**Fig. 2** Hysteresis comparator's output

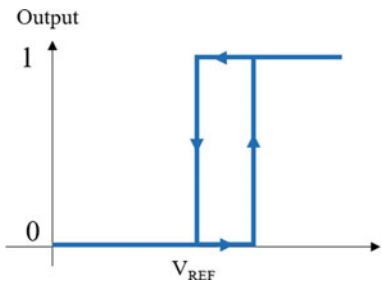

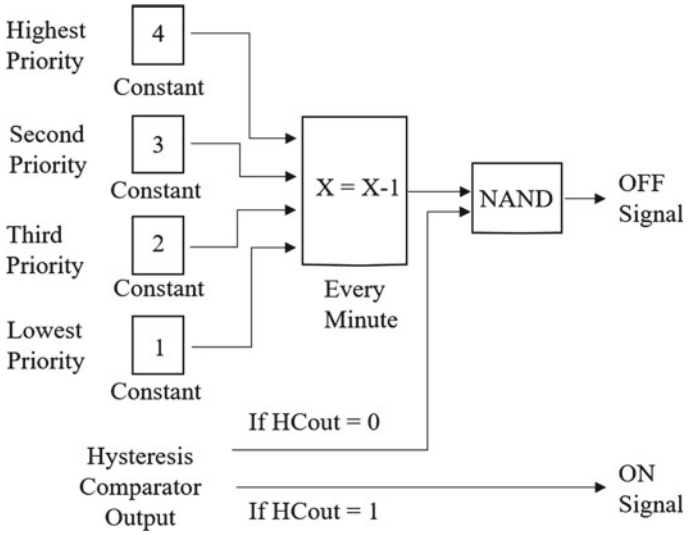


**Fig. 3** Device state logic block

## 3 Test Distribution System

To test the efficacy of the RRDC, a test distribution system is used as shown in Fig. 4. Every load node has 60 houses where each house has controllable and uncontrollable loads. In addition to the controllable EV load, three uncontrollable loads are modeled which are the AC, the WH, and the CD. The specifications of different loads are provided in Table 1. The AC is assumed to operate at its maximum power for 5 min to decrease the room's temperature by 2 °C until the temperature set by the user is reached. Then, it consumes 80 W for 10 min where only the fan and the sensors are working, and the room's temperature will be increased by 2 °C and the cycle repeats over and over again during its operation time. The WH is assumed to operate at maximum power for 2 min to raise the water's temperature by 2 °C until the required water temperature is reached. Then, it remains off for 20 min and the water's temperature will decrease by 2 °C. This cycle repeats to maintain the ±2 °C temperature difference [9]. The EVs are assumed to be connected through the charging controller proposed in [7] which decides a regulated charging rate for the EV based on the voltage at POC.

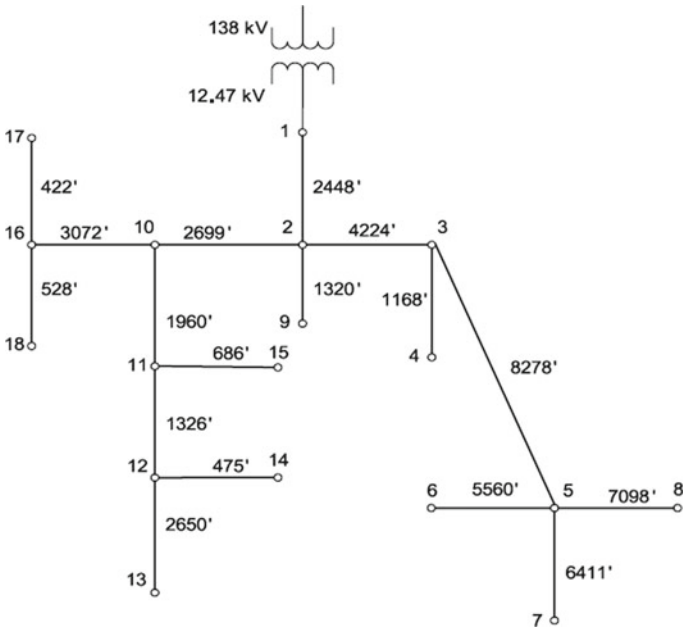


**Fig. 4** Test distribution system. Load buses are 2–18

**Table 1** Specifications of loads

| Devices | Maximum Power (kW) | Allowed temperature difference ($\Delta T$) |
|---|---|---|
| AC | 1.0 | $\pm 2$ °C |
| WH | 2.0 | $\pm 2$ °C |
| CD | 1.3 | – |
| EV | 3.3 | – |

## 4 Simulations and Results

The proposed controller takes the voltage at POC and priorities of different loads as inputs. It then decides the status of each device. The test distribution system having 18 nodes is used to validate the efficacy of the controller.

The simulation is done between 4:00 pm and 11:00 pm since peak hours usually occur in this time interval. It is assumed that the user has set priority order as shown in Table 2. The user is assumed to use the AC from 4:00 pm to 10:00 pm with a temperature choice set at 24 °C and the WH from 7:00 pm to 8:00 pm with a temperature setting of 45°C. The initial temperature in the two rooms, one at upstream node (Node-2a) and second at downstream node (Node-6a), is assumed to be 30 °C. The CD is assumed to be used from 6:00 pm to 8:00 pm and the EV is assumed to start charging at 5:00 pm. The controller is tested for heavy loading condition, i.e.,

**Table 2** Priorities of loads

| Devices | Priority level |
|---|---|
| CD | 1 (lowest) |
| EV | 2 |
| WH | 3 |
| AC | 4 (highest) |

4–7.3 kW per house as well as for light loading condition, i.e., 1–4 kW per house. The voltage, controllable and uncontrollable loads profiles at node 2a are shown in Fig. 5 while the load profiles of AC, WH, EV, and CD are shown in Fig. 6. It can be seen from figures that the voltage remains within the allowable range from 4:00 pm to 7:00 pm. After the WH gets started at 7:10 pm, the voltage drops below 0.95 p.u. and the controller responds by turning off the lowest priority (the CD in this case). The CD is turned on again at 7:15 pm after the WH heating cycle ended and the voltage goes above 0.968 p.u. At 7:35 pm, the WH is turned on again to compensate for the water's temperature loss and this causes the voltage to again drop below 0.95 p.u. and the CD to turn off. The voltage does not go above 0.968 p.u. this time and therefore, the CD is not turned on again. At 7:55 pm the WH is again turned on for 2 min and in the meanwhile the controller tried to respond by turning off the second priority

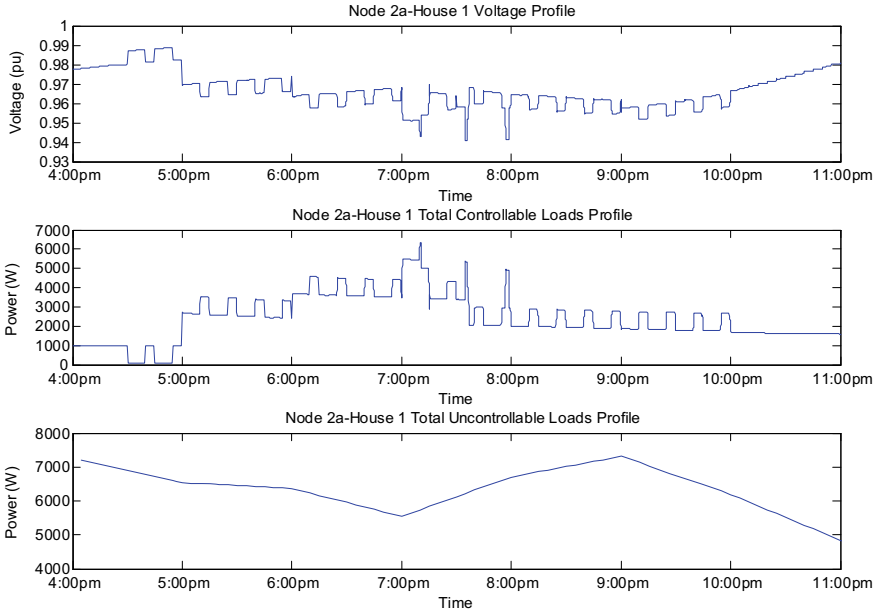


**Fig. 5** Voltage, controllable, and uncontrollable load profiles at node 2a during heavy loading condition

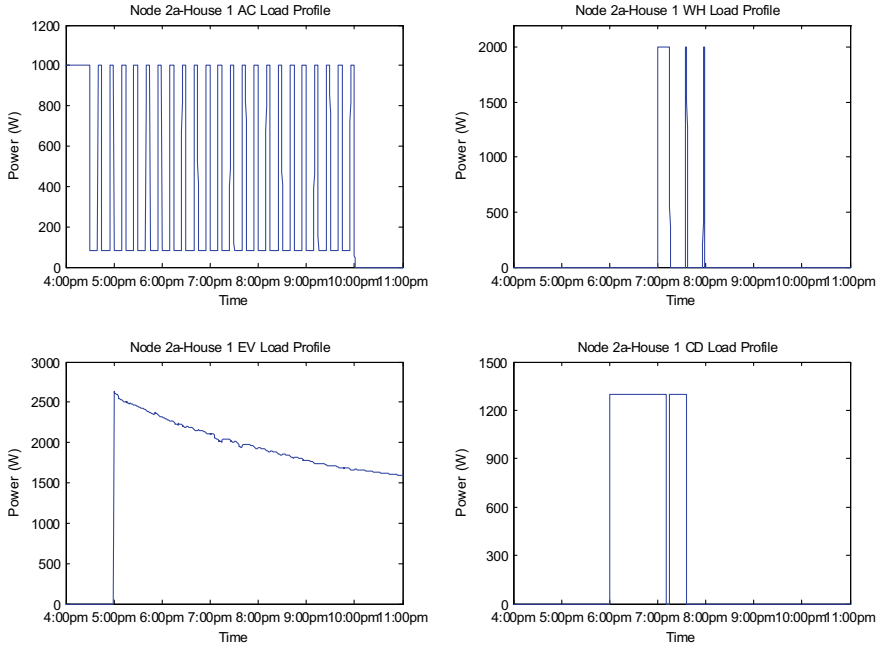


**Fig. 6** The AC, WH, EV, and CD load profiles at node 2a during heavy loading condition

device (the EV), the WH finished the heating cycle and the voltage went back above 0.95 p.u. so there was no need for turning it off.

The controller is also installed in the house at node 6a. Voltage profile, controlled and uncontrolled load profiles for node 6a are shown in Fig. 7. However, the load profiles of AC, WH, EV, and CD are shown in Fig. 8. The voltage is within the allowable range from 4:00 pm to 5:00 pm. At around 5:15 pm, the EV has been turned off since CD (lowest priority) is already off. The voltage goes below 0.95 p.u. again at around 6:25 pm and the controller sends signal to turn off CD. At 7:00 pm, the WH is turned on and voltage violation occurs. Therefore, the controller responds by turning it off just three minutes after it was started. The AC (highest priority) remains on for almost three hours from 4:00 pm. However, it turns off at 7:20 pm because voltage goes below 0.95 p.u. and it was the only controllable device operating at that time.

The controller is also tested for light loading cases on both the upstream and downstream nodes. The voltage profile, controllable and light uncontrollable load profiles of node 2a are shown in Fig. 9. The voltage is always above 0.95 p.u. during the simulation time and there is no need to turn off any of the controllable devices which can be seen in Fig. 10.

The voltage profile, controllable and uncontrollable load profiles of node 6a, for light loading condition, are shown in Fig. 11 whereas the load profiles of controllable devices are shown in Fig. 12. Around 6:40 pm, the voltage drops below 0.95 p.u.

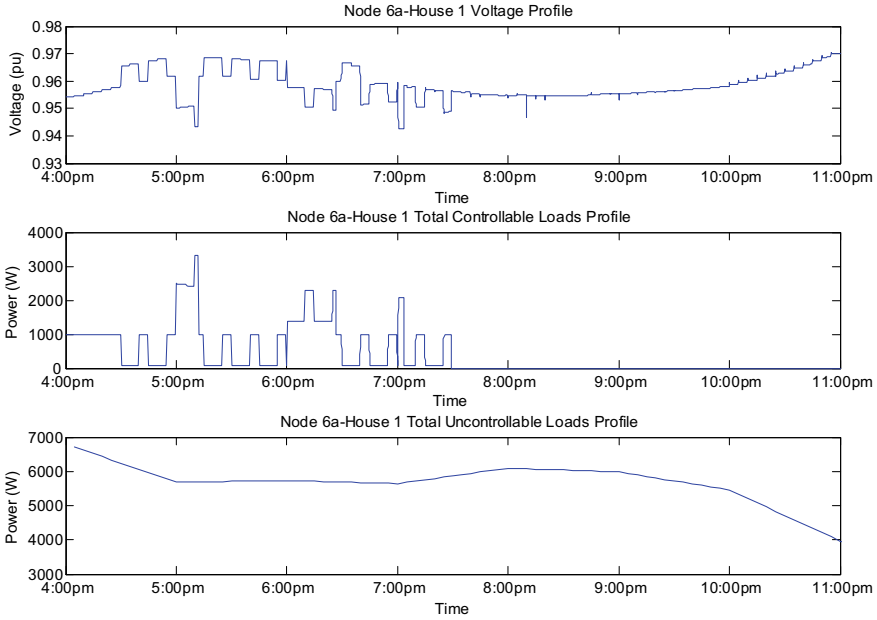


**Fig. 7** Voltage, controllable and uncontrollable load profiles at node 6a during heavy loading condition

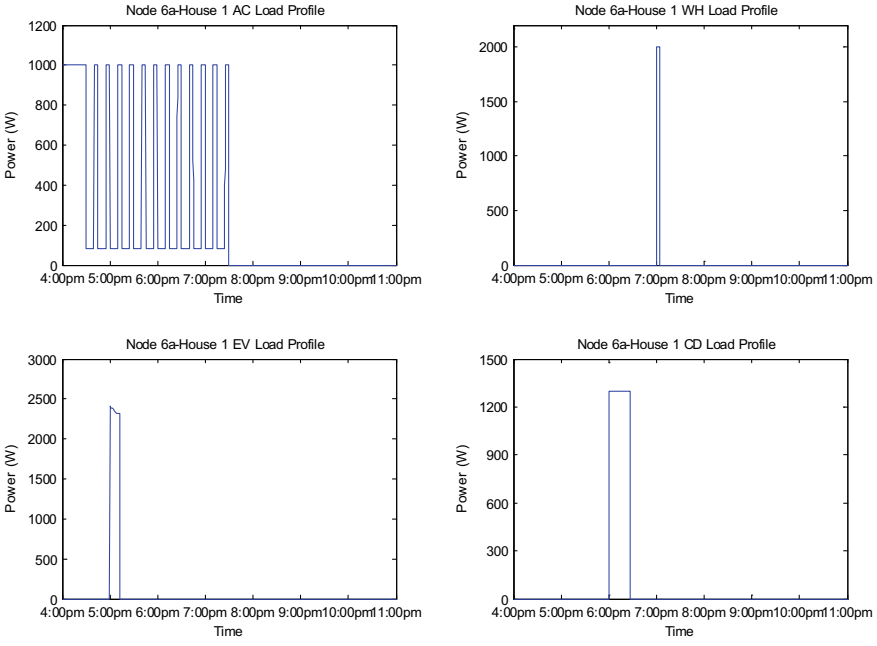


**Fig. 8** The AC, WH, EV, and CD load profiles at node 6a during heavy loading condition

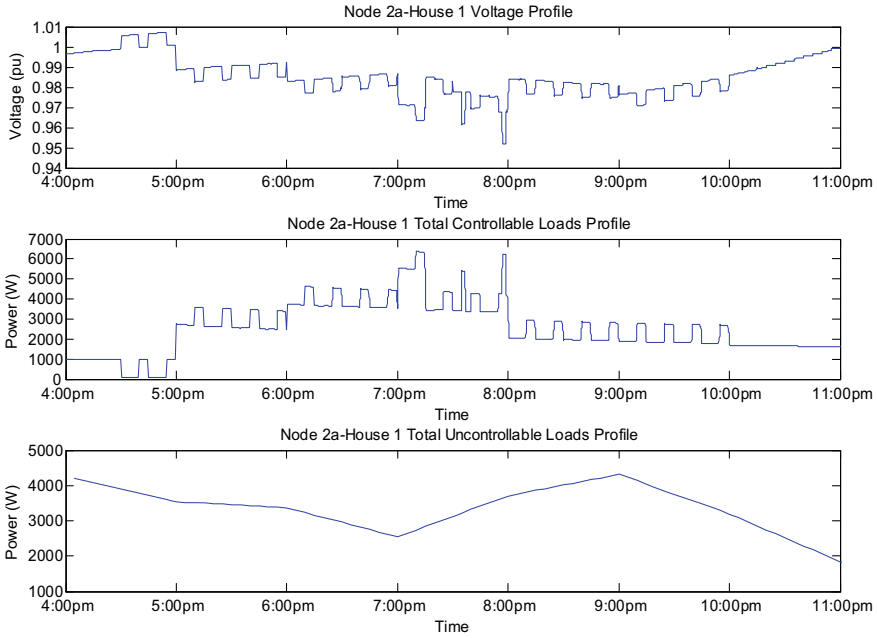


**Fig. 9** Voltage, controllable and uncontrollable load profiles at node 2a during light loading condition

hence, CD is turned off which restores the voltage to allowable range. Similarly, the voltage drops below the minimum allowed voltage around 7:10 pm and EV is turned off since CD was already turned off. At 7:15 pm, the WH finished its heating cycle and tuned off. Thus, the voltage becomes 0.968 p.u. which is not enough to turn on the EV, however, the CD can be turned on. At 7:55 pm, the WH turns on for two minutes causing the CD to turn off during that time but CD gets turned on again at 7:57 pm. The EV can charge at 10:20 pm when the voltage reaches to 0.98 p.u.

## 5 Conclusion

In this paper, a communication-free voltage-based controller for residential responsive demands has been proposed. The user is given the option to set the priorities of the selected devices, i.e., air conditioner (AC), water heater (WH), clothes dryer (CD), and electric vehicle (EV). The proposed controller is tested on 18-bus test distribution system. It maintains the voltage at the point of control (POC) within the allowable range by turning on/off devices based on the priorities set by user. The controller is further tested under different loading conditions. The results prove the effectiveness of the proposed controller.

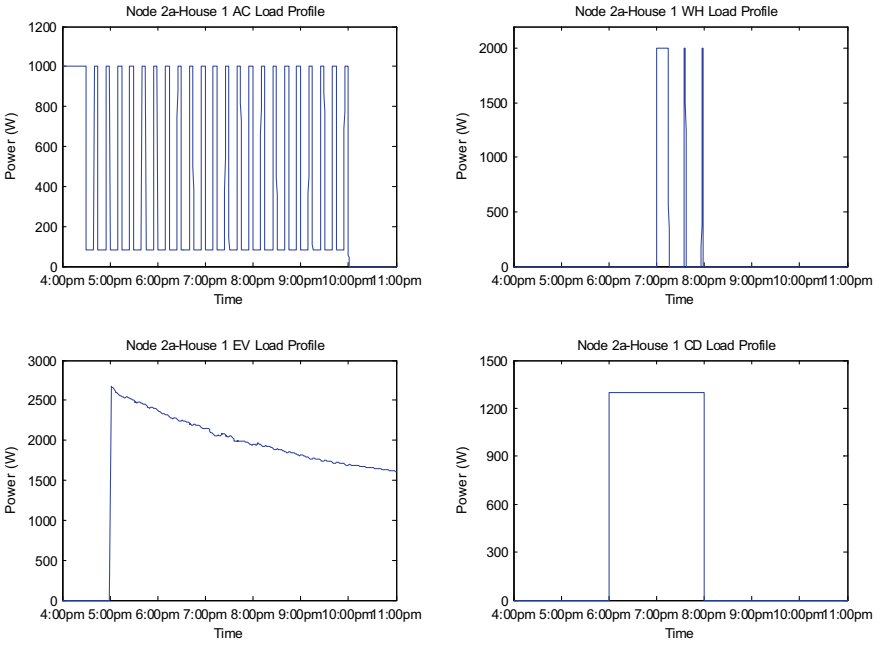


**Fig. 10** The AC, WH, EV, and CD load profiles at node 2a during light loading condition

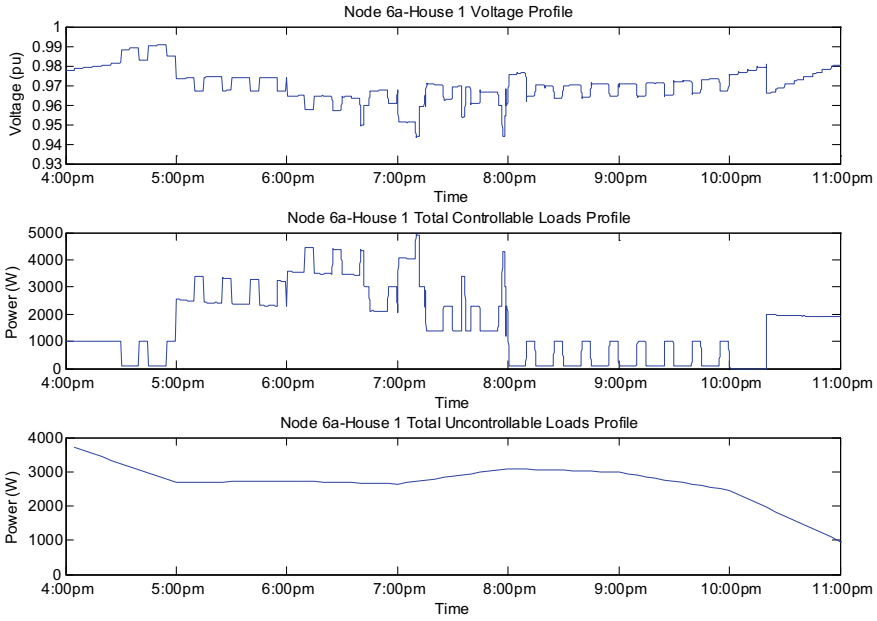


**Fig. 11** Voltage, controllable and uncontrollable load profiles at node 6a during light loading condition

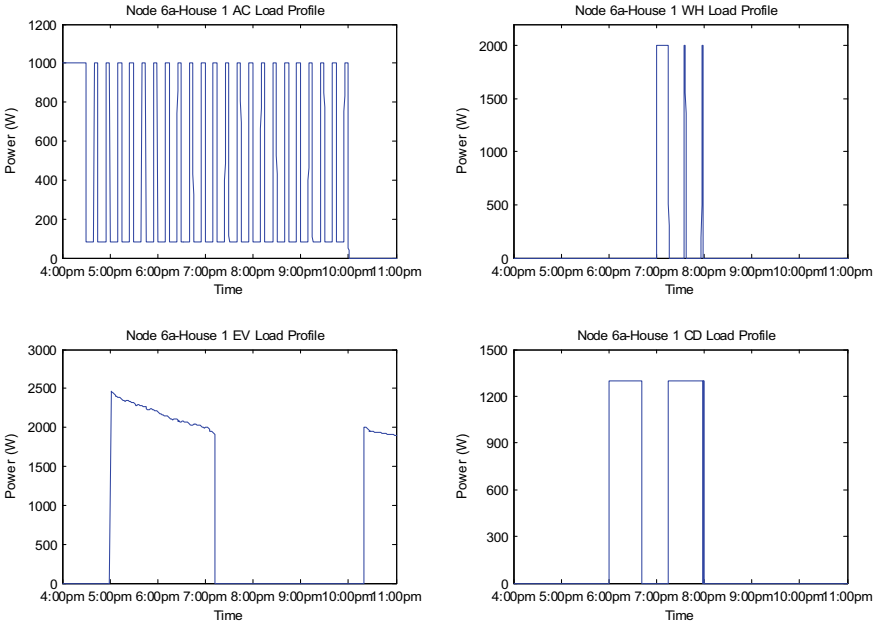


**Fig. 12** The AC, WH, EV, and CD load profiles at node 6a during light loading condition

**Acknowledgements** S. Shafiq would like to acknowledge the support provided by Prince Mohammad Bin Fahd University (PMU), Al-Khobar, Kingdom of Saudi Arabia. B. Khan and A. Al-Awami would like to acknowledge the support provided by the Deanship of Research at King Fahd University of Petroleum and Minerals (Project No. RG1404) and King Abdullah City for Atomic and Renewable Energy (K. A. CARE).

## References

1. Saudi Electricity Company (2015) Electricity consumption tariff. https://www.se.com.sa/en-us/customers/Pages/TariffRates.aspx
2. Khamphanchai W, Pipattanasomporn M, Kuzlu M, Zhang J, Rahman S (2015) An approach for distribution transformer management with a multiagent system. IEEE Trans Smart Grid 6(3):1208–1218
3. Albadi MH, El-Saadany EF (June, 2007) Demand response in electricity markets: an overview. In: Proceeding on IEEE power engineering society general meeting, pp 1–5
4. Stepanov VS, Suslov KV, Chebotnyagin LM, Moskalenko NS, Styczynski ZA (October, 2012) The market approach of demand management in the power system. In: Proceeding on 3rd IEEE PES innovative smart grid technology (ISGT Europe), pp 1–4
5. Ahmed MS, Mohamed A, Shareef H, Homod RZ, Ali JA (November, 2016) Artificial neural network based controller for home energy management considering demand response events. In: International conference on advances in electrical, electronic and system engineering (ICAEES), pp 506–509

6. Sarris T, Messini G, Hatziargyriou N (November, 2016) Residential demand response with low cost smart load controllers. In: Mediterranean conference on power generation, transmission, distribution and energy conversion (MedPower), pp 1–8
7. Al-Awami AT, Sortomme E, Akhtar GMA, Faddel S (2016) A voltage-based controller for an electric-vehicle charger. IEEE Trans Veh Tech 65(6):4185–4196
8. Al-Awami A, Sortomme E (July, 2013) Electric vehicle charging modulation using voltage feedback control. In: Proceeding on IEEE power energy society general meeting (PES), pp 1–5
9. Ghosh P, Bhattacherjee D, Datta S (August, 2010) Adaptive intelligent controller for household cooling systems. In: 1st International conference on integrated intelligent computing, pp 96–101

# Renewable Energy Installation: Challenges and Benefits in Oil/Gas Drilling Rigs


**Abdul Hasib Siddique and Braham Barkat**

**Abstract** Use of renewable energy in standalone system has started to develop and continually becoming a lucrative approach to the new electrical network. Lately, in many countries the combination of solar power photovoltaic (PV) and diesel generator hybrid system has become quite popular. This type of hybrid system is very reliable and works in all types of climate. Especially in an environment such as desert (Middle East) or forest (Africa) where the reliability is a major concern. The diesel generation system has been installed and has been operating in the oil rigs for ages and the introduction of the solar photovoltaic will give a new dimension to operation and reliability as well as fetch environmental and economic benefits. This paper proposes a PV-Diesel hybrid system and focuses on challenges in implementing hybrid (PV-Diesel-Battery) powered rig system and the benefits of such system. A brief discussion on the challenges in health and safety, unpredictable weather and other electrical issues has been done. All the data used for this paper have been taken from real rig data and used for analysis of the system.

**Keywords** Oil · Gas · Drilling · PV · Economic · Hybrid

## 1 Introduction

The energy sector in the world today is very much open regarding the hybrid energy integration in the energy system. Considering the fact that UAE has such a vast potential to harness its solar irradiation, it is utmost important to incorporate that in drilling sector as well. Many other industries in the world today are much more proactive with regards to drilling industry. There is a common saying in the drilling industry that "Don't put your figure into something which is running". This is the reason why drilling industry is lacking behind in smart integration of renewable energy.

A. H. Siddique (✉)
Industrial Engineering Department, Khalifa University, Abu Dhabi, UAE
e-mail: ahnion.ahs@gmail.com

B. Barkat
Electrical Engineering Department, Khalifa University, Abu Dhabi, UAE
e-mail: braham.barkat@ku.ac.ae



F. Shahnia and S. Deilami (eds.), *ICPES 2019*, Lecture Notes in Electrical Engineering 669, https://doi.org/10.1007/978-981-15-5374-5_13

Recently, the concept of smart grid has been successfully applied to many countries electric power systems. So it is time that similar approach should be implemented in the drilling industry as well. The companies have now beginning to see integration of renewable resources as a positive thing rather a burden on them. Certainly there are challenges in developing renewable generation technologies, such as reducing the capital costs and improving energy efficiencies of the various types of renewable resources such as PV. But the positive does out weight the challenges by huge factor.

This paper has been divided into five main subsections. The subsections are hybrid system description, challenges in integration of PV in the rig electrical system, the benefits of PV system in the rig and how beneficial it is for western region of UAE to install it. For this study past 30 years solar irradiation data have been studied [1] to look at the potentiality of PV installation in the rig site. Even the vision 2030 of UAE tries to promote renewable energy integration in the system and reducing the carbon foot print [2]. Beside this also an economic study of the proposed system has been done. Challenges and benefits from HSE prospective have also been briefly discussed in this paper.

## 2 Proposed Rig Electrical System

In this section a detailed description of the new proposed system has been given. The proposed system has additional PV array included in the LV lighting area, which also includes a battery room and a DC bus. The design have been done keeping in mind the Integrity of the system.

In this section a segmented description have been done where firstly the generation unit and AC bus have been described. Followed by the inverter, VFD and DC bus and lastly the load side with other auxillary equipment has been discussed. The sections are clearly segmented in Fig. 1. A clear border line is drawn around the sections to be discussed.

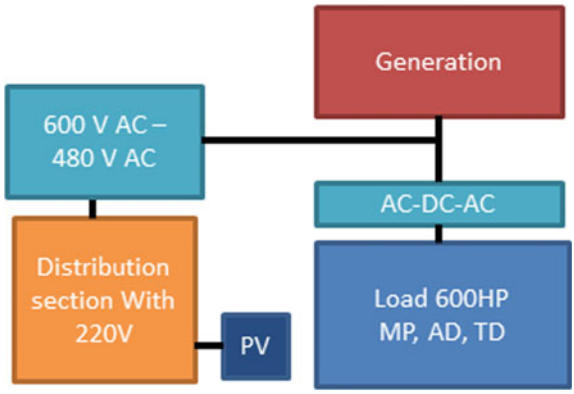


**Fig. 1** Block diagram of hybrid rig electrical system

In generation sensation four 3512 or 3516 CAT engine have been proposed to carry out all operation which are connected to four generators SR4B or Kato with 1750 kVA capacity. The system is rated at 600 V, 60 Hz AC. A 0–200 A rated CT (Current Transformer) is connected to the output of the generator. Control module is connected for syncing purpose between the DG (Distributed Generation) units. An UV relay has also been added for protection. All the Engines are connected via AC bus of 600 V, 60 Hz.

Figure 2 shows the generation section with proposed control system. The picture shows other auxiliary subsystem. Figure 3 demonstrates a detailed diagram of Inverter, DC bus and the rectifiers. Three Inverters are connected to the AC bus which feeds a DC bus of 800 V. Inverters are connected to the DC bus which feeds the loads

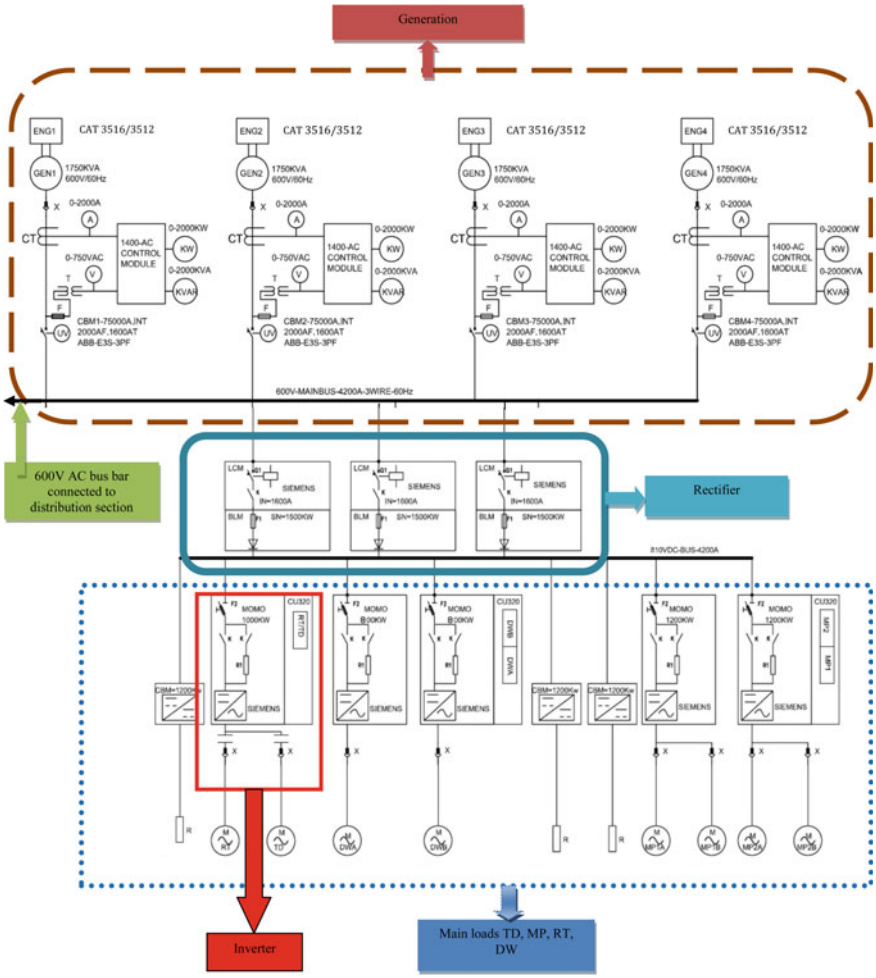


**Fig. 2** SLD of generation, rectifier, inverter and main loads

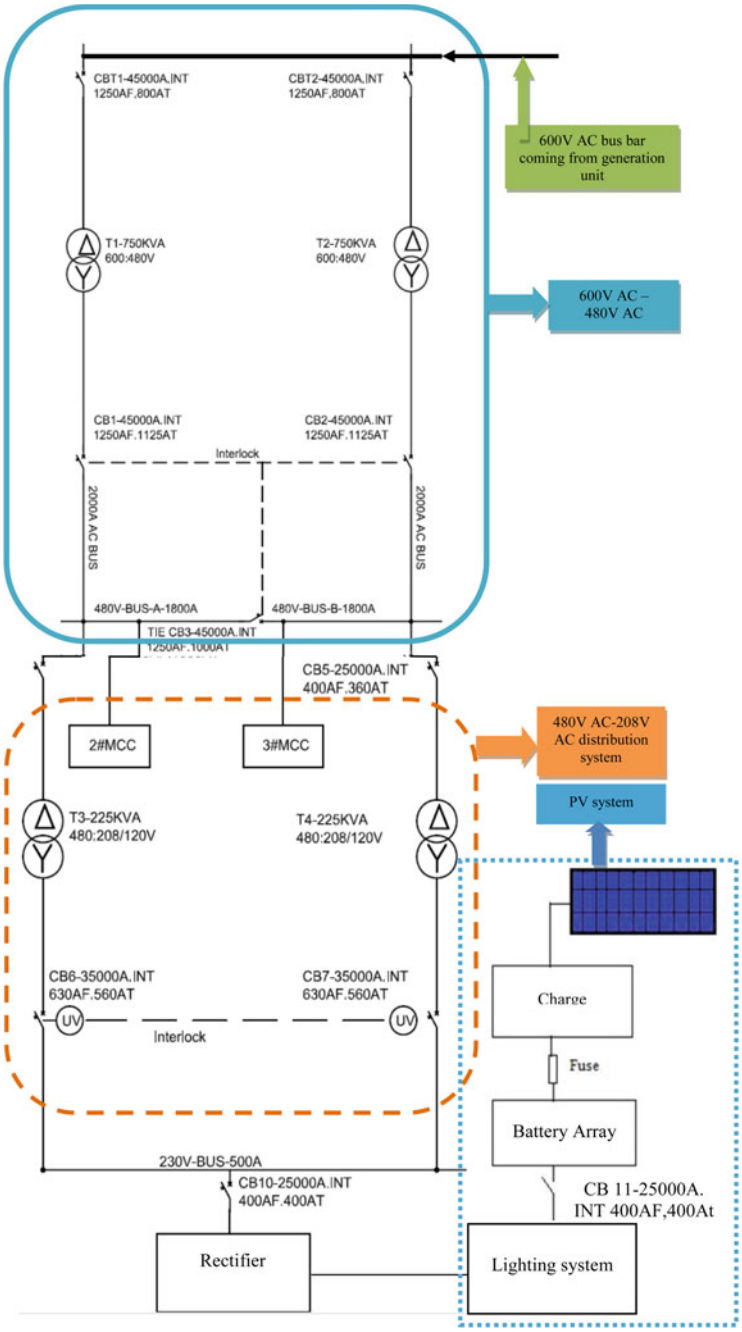


**Fig. 3** SLD of 600–208 V distribution network and PV system

which are connected. For a typical Rig usually the loads are Rotary Table (RT), Draw Works (DW), Mud Pump (MP) and Top Drive (TD) [3].

The load side has been designed to integrate PV to the system. Usually Photo voltaic systems are designed to operate on voltages of 12, 24 or 48 V DC. For the proposed system is a 24 V DC operating system. 600 V AC is stepped down to 480 V AC and further stepped down at 230 V AC. This is then connected to AC/DC rectifier to convert it to 24 V DC. In Fig. 1 the orange rectangular box denotes this section. The system is connected to a PV system which is then connected to lighting system. PV arrays are connected to the 24 V DC bus which is connected to the charge controller. Charge controller is the main control of the PV part. Two circuit breakers (CB10 and CB11) are connected which are manually operated. At a time both should not be on. A fuse has been connected between the charge controller and battery array to save guard the controller in case of any malfunction. The fuse used for protection is rated at 40 A. CB 10 and CB 11 have been connected to the 230 V line and battery array respectively. So in case of any emergency situation we can use either of the system.

## 3 Renewable Energy Potential of UAE

This section deals with detailed the geographical location of UAE and its potential to generate electricity from solar irradiation (Fig. 4).


**Fig. 4** The area where solar mapping has been done by ReCREMA

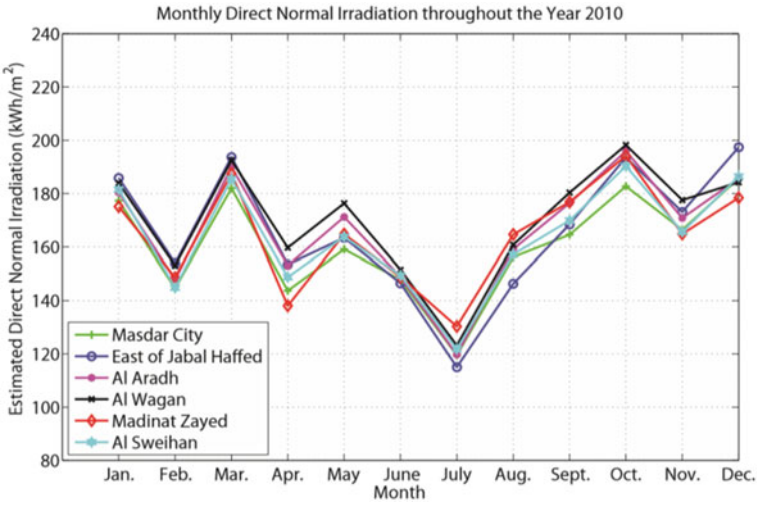


**Fig. 5** Monthly irradiation in kWh/m$^2$ [4]

The United Arab Emirates is situated in the Middle East/southwest Asia, bordering the Gulf of Oman and the Persian Gulf, between Oman and Saudi Arabia. Abu Dhabi's location-latitude 240′ 00″ N and longitude 540′ 00″ E is perfect for solar irradiation harvesting. The long hours of available sunshine have made it possible to utilize this bounty of nature to promote distributed generating units all across the UAE. Especially in the desert area of the UAE the potentiality of energy from solar is huge [4].

A detailed study was conducted by ReCREMA in Masdar city in Abu Dhabi, Western region (AL mirfa, Madinat Zayed and Sir bani yas Island) and Eastern region (Al Sweihan, East of Jabal Haffed, Al Aradh and Al Wagan). The potential of solar energy harvesting in the UAE is significant, with an average annual sunshine hours of 3568 h (i.e., 9.7 h/day), which corresponds to an average annual solar radiation of approximately 2285 kWh/m$^2$, that is, 6.3 kWh/m$^2$ per day [5].

Figure 5 gives a detailed solar irradiation of the six observation areas in UAE. Most of the rigs are present in Madinat Zayed, and mirfa region So this study has been of great importance to this paper. It indicates the potential of the western region to harvest electricity from sun. From Fig. 6 it can also be seen that the average solar irradiation is about 450 W/m$^2$ [1] which indicates the potential that the UAE has to generate electricity from solar throughout the year.

## 4 System Construction

In the proposed system full tank area has been covered with PV panels. A movable panel has been proposed so that during rig moves this will not hamper or delay the

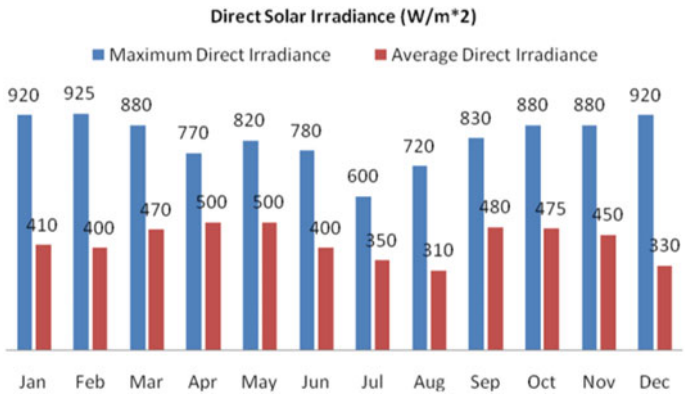


**Fig. 6** Solar irradiation on monthly basis in UAE [1]

operation. The height of the panel is set at 9 ft in accordance to international residential code R305.1 for sloped ceilings. Minimum headroom of 7 ft is maintained so as to accommodate free movement (Figs. 7 and 8).

**Fig. 7** Mud tank area with proposed PV structure

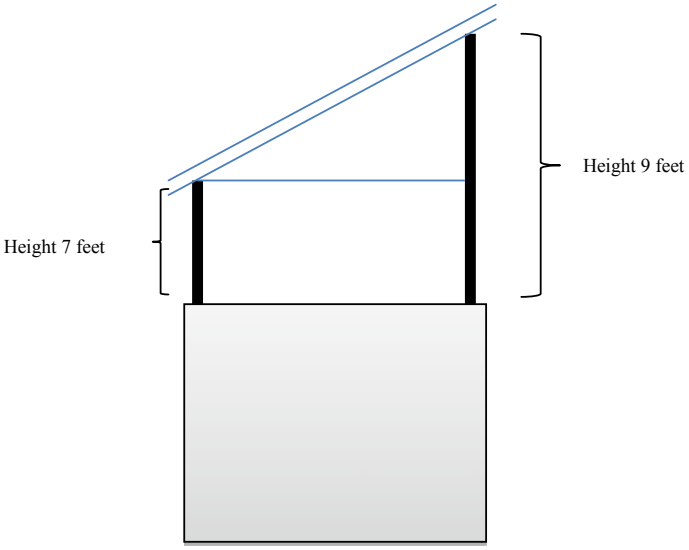


**Fig. 8** Mud tank side view with PV panel

## 5 Challenges of Renewable Energy Integration

Although solar energy is derived from nature and it is in abundance in the Middle East, yet its predictability and availability is of great concern. High initial cost, variability, space for installation, efficiency, daily and seasonal effect are some of the concerns related to PV [6]. Integration of PV in the existing AC system also brings about technical challenges. For a rig electrical system another challenge is to store battery where flammable gas might be present. Last but surely on the least are HSE, Power quality issue which needs to be taken care off.

### *5.1 High Initial Cost*

usually Photo voltaic has high initial cost. The capital cost, operating cost, management cost and also construction cost have been considered while designing the system. This system costs up to 1.5 times of the conventional generation. But with constant development of the technology this cost is reducing day by day.

## 5.2 Variability

Due to the variation of solar irradiation throughout the day, solar energy is one of the most unpredictable sources of energy. Even when cloud passes over the PV cell there is variation of output power. With could seeding in UAE there is good chance of having rain in November to March, this will also effect the output of PV array.

## 5.3 Space for Installation

Finding suitable space for installation is another big concern for the drilling industry. The place where solar irradiation is good might have shade which makes the output variable. PV array have been located on top of offices, VFD room and Mud tank area for the proposed system efficiency.

Efficiency of PV is on an average 25% [7] which is quite low as compared to any other type of conventional energy source. A lot of research is going on with new materials to see how the efficiency can be improved keeping into consideration the commercial viability.

## 5.4 Technical Challenges

Integrating DC system to an AC system does require modification as well as robust system algorithm. The control panel of DC system needs to feed on the solar power and an auxiliary system from AC main. Many times there are ripples from the main system, uneven generation from PV and in case inverter is used then issue related to frequency arises as well. In the proposed system two manually charged circuit breakers are proposed. The lighting system can be fed by both the rig generators and also by the PV array.

## 5.5 HSE Consideration

Usually solar panels are enclosed in heavy-duty glass or plastic so the risk of releasing semiconductor material into the environment is very acute. But in the case of fire it poses a great threat as it can release hazardous fumes which if inhaled by human can be of great risk. Beside this acid from the battery does pose a environmental hazard. So it is important to have a proper disposal method. From the HSE point of view these PV shades also affect the TWL by reducing the temperature by almost 5°C, Hence a worker can work for longer period of time.

### *5.6 Power System Quality*

Power quality ensures constant voltage, phase angle adjustment and removal of extraneous harmonic content from the rig electric system. The common problem is voltage sag in the rig, in which the UPS can supply the energy to shoot the voltage to the desired level.The heavy loads of around 600 HP motors does create ripple in the system and when the motor move in the other direction it creates regenerative voltage. For this reason a brake resister have been taken into account.

## 6 Benefits of Renewable Energy in the Rigs

The UAE is one of the leading countries contributing towards the carbon footprint. The report of WWF 2010 revealed that "if everyone in the world lived like an average resident of the United States or the United Arab Emirates, then a bio capacity equivalent to more than 4.5 Earths would be required to keep up with humanity's consumption and $CO_2$ emissions". The report also revealed that the UAE residents contributed to a carbon footprint of 8.1 global hectors per person (gha/person) [8]. Therefore, it is the duty of the government as well as the non-governmental institutes to look for alternative resources for energy which will not only be a benefit towards the environment but will also help the country economically.

One of the major parts of the operating costs for the oil operation companies is the cost of electricity production given the fact that the only way of electrification the projects is to use diesel driven generators. By using a hybrid system the cost of generating electricity could be reduced by a big number.

NPV of the system has been calculated to be $1,540,845.26. Rate of return, inflation rate of UAE, average increase in diesel price and operating and maintenance cost have been considered while calculating the NPV. Beside all these benefits, PV system is going to bring about a good reduction of Greenhouse Gas (GHG) emissions. For GHG reduction calculation $CO_2$, HFCs, $CH_4$, $N_2O$ emission data has been taken into account. Then total emission is being multiplied by the emission factors. A total GHG reduction of about 135 kt/year has been calculated. 1650 tons are directly produced by oil extraction industry, which accounts of 3.4% of the GHG production (Greenhouse gas inventory 2012). Most of the contribution is being from carbon dioxide which is about 95% of the total GHG, and about 17 kt/year is emitted in the form of $CH_4$. This will help countries like the UAE reduce its GHG emission to meet the world challenge to reduce the carbon foot print (Table 1).

**Table 1** Values considered for NPV calculation

| | |
|---|---|
| Rate of return: | 7.6 |
| Inflation rate | 0.07 |
| Diesel and PV maintenance cost | $5189 |
| Diesel price increase | 10% |

## 7 Conclusion

Even though the world is moving toward sustainable energies but drilling field is far more reluctant than other industries. Looking at the energy potential of UAE it is quite evident that UAE is not utilizing its full potential of harnessing energy from the sun. After analyzing the challenges and benefit it is quite clear that benefit out weights the challenges by a long margin. On the other hand the concern of GHG has been a talking point for the world for quite some time now and being in the oil business if a bold step can be taken to integrate renewable energy for energy production in the rig it will be exemplary move for the other countries in the similar business. Hence it is demand of the hour that the drilling industry start to adopt DG in their rig power system.

## References

1. Islam MD, Alili AA, Kubo I, Ohadi M (2010) Measurement of solar-energy (direct beam radiation) in Abu Dhabi, UAE. Renew Energy, Elsevvier 35:515–519
2. Siddique AH, Al Bloushi HK, Lamont LA (2012) Distributed generation and smart power grid UAE vision for 2030. In: 2012 3rd IEEE PES innovative smart grid technologies Europe (ISGT Europe). Berlin
3. National Oil Well Verco (9th September, 2013) Introduction to drilling basic operations and tools
4. Ghedira H, Ouarda T, Gherboudj I, Marpu PR, Munawwar S, Eissa Y, Estima J, Al Sharif I, Al Meqbali N (April, 2013) The UAE solar atlas research center for renewable energy mapping and assessment (ReCREMA)
5. Assi A, Jama M (September, 2010) Predicting global solar radiation on horizontal using sunshine duration in al Ain, UAE. In: Proceedings of the 25th European photovoltaic solar energy conference and exhibition/5th world conference on photovoltaic energy conversion. Valencia, Spain, pp 508–512
6. Kaur T (July, 2015) Solar PV integration in smart grid—issues and challenges. Int J Adv Res Electr Electron Instrum Eng 4(7):5861–5865. ISSN (Print): 2320–3765, ISSN (Online): 2278–8875
7. PVeducation Solar cell efficiency record PV education. Available: https://www.pveducation.org/pvcdrom/appendices/solar-cell-efficiency-results2
8. WWF (2010) Living planet report 2010" WWF. Available: http://d2ouvy59p0dg6k.cloudfront.net/downloads/lpr_summary_booklet_final_feb_2011.pdf